Designing a Quantum Computer based on Pulsed Electron Spin Resonance

Gavin W. Morley
Wolfson College



A thesis submitted for the degree of
Doctor of Philosophy
at the
University of Oxford
Hilary Term 2005

Designing a Quantum Computer based on Pulsed Electron Spin Resonance

Gavin W. Morley
Wolfson College, Oxford University
Hilary Term 2005

Abstract of Thesis Submitted for the Degree of Doctor of Philosophy

Electron spin resonance (ESR) experiments are used to assess the possibilities for processing quantum information in the electronic and nuclear spins of endohedral fullerenes.

It is shown that $^{15}N@C_{60}$ can be used for universal two-qubit quantum computing. The first step in this scheme is to initialize the nuclear and electron spins that each store one qubit. This was achieved with a magnetic field of 8.6 T at 3 K, by applying resonant RF and microwave radiation. This dynamic nuclear polarization technique made it possible to show that the nuclear T_1 time of $^{15}N@C_{60}$ is on the order of twelve hours at 4.2 K. The electronic T_2 is the limiting decoherence time for the system. At 3.7 K, this can be extended to 215 μs by using amorphous sulphur as the solvent. Pulse sequences are described that could perform all single-qubit gates to the two qubits independently, as well as CNOT gates. After these manipulations, the value of the qubits should be measured. Two techniques are demonstrated for this, by measuring the nuclear spin.

$Sc@C_{82}$ could also be useful for quantum computation. By comparing ESR measurements with density functional theory calculations, it is shown how the orientation of a $Sc@C_{82}$ molecule in an applied magnetic field affects the molecule's Zeeman and hyperfine coupling. Hence the g- and A-tensors are written in the coordinate frame of the molecule. Pulsed ESR measurements show that the decoherence time at 20 K is 13 μs, which is 20 times longer than had been previously reported.

Carbon nanotubes have been filled with endohedral fullerenes, forming 1D arrays that could lead to a scalable quantum computer. $N@C_{60}$ and $Sc@_{82}$ have been used for this filling in various concentrations. ESR measurements of these samples are consistent with simulations of the dipolar coupling.

Acknowledgments

I thank G. D. W. Smith for extending to me the use of the Materials Department and its facilities. I thank R. A. Cowley, K. Burnett, R. J. Nicholas and A. T. Boothroyd for extending to me the use of the Physics Department and its facilities.

I have been fortunate enough to have two excellent D.Phil. supervisors. Andrew Briggs lead the QIP group and suggested that endohedral fullerenes in nanotubes could be used for QC. His awareness of the wide field of QIP research provided motivation, and his attention to detail added focus to my experiments. Arzhang Ardavan's approach to physics has inspired me to think new thoughts and sharpen my expression of them. His intellectual contributions to this thesis include suggesting that DNP could be useful for ESR QIP, and the general calculation (Section 2.4.2) showing that the amplitude of pseudo-pure states decays exponentially with the number of qubits.

Kyriakos Porfyrakis and Andrei Khlobystov lead the preparation of all of the samples studied here. Our close interactions sparked central ideas such as Andrei's suggestion that sulphur could be used as a fullerene solvent. Andrei found a way to fill SWNTs with endohedral fullerenes at moderate temperatures, allowing him to synthesize $N@C_{60}$ peapods. The $N@C_{60}$ that was used for these peapod experiments was produced by C. Meyer and W. Harneit with A. Weidinger at HMI in Berlin. Jinying Zhang did most of the purification of the $^{15}N@C_{60}$ that was used for the DNP experiments. Kyriakos made and purified all of the other endohedral fullerenes that are the basis of this thesis. John Dennis in Queen Mary College at the University of London showed us how to make and purify endohedral fullerenes and helped to make the $Sc@C_{82}$ that was used in Chapter 7.

Hans van Tol and Louis-Claude Brunel showed me how to use some of the world's best ESR equipment at the National High Magnetic Field Laboratory in Tallahassee, Florida. Their ESR expertise is complemented by their European appreciation of a good meal. The experiments on DNP, $Sc@C_{82}$ and $Sc@C_{82}$ peapods in solution were carried out with their spectrometers. Hans' program was used to fit the anisotropic spectra of $Sc@C_{82}$.

Mark Newton in the Physics Department at the University of Warwick advanced my understanding of ESR while the spectrum of $N@C_{60}$ peapods was being collected.

Most of my ESR time was provided by the Biology Department at University College London (UCL). Johnathan Nugent got us started and Mike C. W. Evans kept us going. These facilities made it possible for me to characterize a wide range of samples and prepare for trips to Florida. Richard Ball was always available to help out with the Jeol spectrometer and the cryogenics. The spectra of concentrated $Sc@C_{82}$ peapod powders were collected with the Jeol and the relaxation times of $N@C_{60}$ in amorphous sulphur were measured with the Bruker pulsed X-band spectrometer.

I benefited from discussions with Simon Benjamin about QC in general and also the two-qubit scheme in Chapter 5.

Many people in Oxford University performed DFT modeling to interpret and understand the $Sc@C_{82}$ spectra. Seung Mi Lee, Duc Nguyen-Manh, Roberto Scipioni and David Pettifor found the geometric structure in the Materials Modeling Laboratory. Ben Herbert and Jenny Green in the Inorganic Chemistry Laboratory used the resources of the Oxford Supercomputing Centre to find the spin density and hence the hyperfine coupling. Also, Andrew Horsfield carried out the spherical atom calculation in the Department of Physics and Astronomy at UCL. The paper on $Sc@C_{82}$ was drafted with the help of these modelers as well as my supervisors and Kyriakos.

The appendix is a neat way to show that perfect π pulses exist in a spin $\frac{3}{2}$ system, due to Arzhang, John Morton and Brendon Lovett.

Martin Austwick and John joined me on the early trips to Tallahassee. Mark Jones helped to find Bruker's sleep command, enabling us to have lunch breaks. Martin, John, Mark, Jinying, Ahsan Nazir, Dave Britz, Dave Leigh, Daniel Gunlycke and Kwan Lee made 12/13 Parks Road a place in which you could relax with a DVD or convene for trips further afield. Outings to Dublin, Amsterdam, Japan, Cambridge and Sheringham were most stimulating.

The Correlated Electrons Group in the Clarendon were my regular tea-time companions. Ali Bangura and I share more than just a birthday. James Analytis, Sonia Sharmin, Tom Lancaster, Alessandro Narduzzo, Mick Brooks, Fox Liang, Paul Goddard, Moon Sun Nam, Amalia Coldea, Steve Blundell, Bill Hayes and occasionally John Singleton have all joined me in watching the last three years fly past.

Wolfson is so international that it's like traveling without moving. Mark, Ville, Davide, Sarah, Evy, Matteo, Charlie and Nick traveled with me to Rome and Milton Keynes, as well as snowboarding, rowing, playing football and pool.

Tania, Jen, Laura and all of the 11 Norham Gardeners created a warm community in which cake and tea were always on offer. Laura is an inspirational source of love for me.

My family have given me support and love during the last 27 years. Oliver and Jake are my beloved brothers and friends. This thesis is dedicated to Ros and Colin, my beloved parents and friends. The way Colin lived is a shining example of how to find great new things and share them with others. Ros's intelligent positivity makes everyone around her happy.

I thank all of these people and everyone I have interacted with during my research.

Abbreviations

$\|\psi\rangle$	Vector representing the quantum mechanical wavefunction,ψ; also known as a ket
$\langle\psi\|$	Dual vector of $\|\psi\rangle$; also known as a bra
α	Boltzmann factor between equilibrium populations of two states
π, $\frac{\pi}{2}$ pulse	A pulse that flips the direction of a spin by π, $\frac{\pi}{2}$ radians
1D, 2D, 3D	One, two, three-dimensional
ADF	Amsterdam Density Functional
Amp	Amplitude
A-tensor	Hyperfine tensor
B	Magnetic Field
CNOT	Controlled NOT, a logic gate
CW	Continuous-wave
DJ	Deutsch-Jozsa
DFT	Density functional theory
DMF	N,N-Dimethylformamide
DNP	Dynamic nuclear polarization
D.Phil.	Doctor of Philosophy
Edfs	Echo-detected field-sweep
EELS	Electron energy loss spectroscopy
ENDOR	Electron nuclear double resonance
EPR	Electron paramagnetic resonance
ESR	Electron spin resonance
ESEEM	Electron spin echo envelope modulation
FCC	Face-centered cubic
FFT	Fast Fourier transform
FID	Free induction decay
FT	Fourier transform
FT-ESR	Fourier transform electron spin resonance
FWHM	Full width at half-maximum
G_i^θ	A pulse at the resonant GHz frequency labeled as G_i for $i = 1, 2$ in Figure 5.1, rotating the electron spins through an angle θ degrees (radians) when θ is expressed as a number (multiple of π)
GGA	Generalized gradient approximation
HFHF	High-field, high-frequency

Hfs	Hyperfine splitting
HMI	Hahn-Meitner Institute
HPLC	High performance (or pressure) liquid chromatography
HRTEM	High-resolution transmission electron microscopy
IPR	Isolated-pentagon rule
IR	Infrared
JEOL	Japan Electron Optics Laboratory Co.
LDA	Local density approximation
M_i^θ	A pulse at the resonant MHz frequency labeled as M_i for $i = 1, 2, 3, 4$ in Figure 5.1, rotating the nuclear spins through an angle θ degrees (radians) when θ is expressed as a number (multiple of π)
MALDI	Matrix-assisted laser desorption ionization
MRFM	Magnetic resonance force microscopy
N/A	Not applicable
N@C_{60}	A molecule of C_{60} fullerene containing a nitrogen atom
NMR	Nuclear magnetic resonance
$P[\psi]$	Equilibrium population of state $\|\psi\rangle$
PLATO	Programme for the linear combination of atomic orbitals
QC	Quantum computation
QEC	Quantum error correction
Q-Factor	Quality factor
QIP	Quantum information processing
Qubit	Quantum bit
RF	Radio Frequency: Electromagnetic radiation below 1000 MHz
Sc@C_{82}	A molecule of C_{82} fullerene containing a scandium atom
$scCO_2$	Super-critical carbon dioxide
SCF	Super-critical fluid
SOMO	Semi-occupied molecular orbital
SQUID(s)	Superconducting quantum interference device(s)
Srt	Shot repetition time
STM	Scanning tunneling microscopy
SWAP	Quantum logic gate that swaps the wavefunctions of two qubits
SWNT(s)	Single-walled carbon nanotube(s)
T_1	Spin-lattice relaxation time
T_2	Spin-spin dephasing time
T_2^*	Inhomogeneous dephasing time of FID
T_1^e, T_2^e	Electronic T_1, T_2
T_1^n, T_2^n	Nuclear T_1, T_2
TEM	Transmission electron microscopy
TEMPO	2,2,6,6-Tetramethylpiperidine 1-oxyl
UV	Ultraviolet
UV-vis-NIR	Ultraviolet-visible-near infrared
W-Band	Radiation with frequency around 95 GHz
X-Band	Radiation with frequency around 9.5 GHz

Contents

Acknowledgments iii

Abbreviations v

1 Introduction 1
- 1.1 Historical Background . . . 1
  - 1.1.1 Quantum Computing . . . 1
  - 1.1.2 ESR . . . 2
  - 1.1.3 Fullerenes and Nanotubes . . . 2
- 1.2 This Thesis . . . 3

2 Quantum Computing 4
- 2.1 Overview . . . 4
- 2.2 Qubits . . . 5
  - 2.2.1 Decoherence . . . 6
- 2.3 Density Matrices . . . 7
- 2.4 Experiments . . . 9
  - 2.4.1 Experimental Requirements for QC . . . 9
  - 2.4.2 Pseudo-Pure States for NMR QC . . . 10
  - 2.4.3 The Deutsch-Jozsa Algorithm . . . 12
  - 2.4.4 Manipulating Electron Spins in the Solid State . . . 14
  - 2.4.5 Advantages of Qubits . . . 16

3 Varieties of ESR Experiment 17
- 3.1 Polarization . . . 17
- 3.2 Continuous-Wave . . . 19
- 3.3 Spin Hamiltonian . . . 22
- 3.4 Pulsed ESR . . . 24

4 Fullerenes and Nanotubes 27
- 4.1 Fullerenes . . . 28
  - 4.1.1 Endohedral Fullerenes . . . 29
- 4.2 Nanotubes . . . 42
  - 4.2.1 Peapods . . . 44

5 ^{15}N@C$_{60}$ QC Scheme 47
- 5.1 Qubits . . . 48
- 5.2 Initialization . . . 51
  - 5.2.1 CW DNP . . . 52
  - 5.2.2 Pulsed DNP . . . 56

5.2.3 Flip-Flop Transitions . . . 60
5.2.4 Summary of Initialization Techniques . . . 61
5.3 Decoherence . . . 62
5.4 Quantum Logic Gates . . . 63
5.4.1 CNOT Gates . . . 63
5.4.2 Wavefunction Swaps . . . 64
5.4.3 Single-Qubit Gates . . . 65
5.4.4 Implementing the Deutsch-Jozsa Algorithm . . . 67
5.5 Readout . . . 69
5.5.1 CW Readout . . . 70
5.5.2 Pulsed Readout . . . 70
5.6 Sources of Error . . . 72
5.7 Scaling Up . . . 74
5.7.1 Dimers: Potential Four-Qubit Systems . . . 75
5.7.2 Fully Scalable QC . . . 78

6 $N@C_{60}$ ESR Measurements **81**
6.1 $^{15}N@C_{60}$ QC Scheme . . . 82
6.1.1 Initializing the Nuclei with DNP . . . 82
6.1.2 Nuclear T_1 . . . 92
6.1.3 Qubit Readout . . . 94
6.2 $N@C_{60}$ Decoherence . . . 97
6.2.1 Sources of Decoherence . . . 97
6.2.2 Spin Dephasing: T_2 Time . . . 101
6.2.3 Spin-Lattice Relaxation: T_1^e Time . . . 102
6.3 Conclusions . . . 104

7 $Sc@C_{82}$ **107**
7.1 Sample Preparation . . . 107
7.2 Electronic T_1 and T_2 Decoherence . . . 109
7.2.1 Room Temperature . . . 109
7.2.2 A Frozen Solution . . . 114
7.3 Understanding Anisotropy with DFT . . . 117
7.3.1 Summary . . . 128

8 Two Spin-Active Peapods **130**
8.1 Nanotubes . . . 131
8.1.1 Solution ESR . . . 133
8.2 $N@C_{60}$ Peapods . . . 134
8.2.1 Modeling the Dipolar Interaction between $N@C_{60}$ molecules in SWNTs . . . 141
8.3 $Sc@C_{82}$ . . . 143
8.3.1 ESR of $Sc@C_{82}$ Powders . . . 144
8.3.2 Peapod Synthesis . . . 145
8.3.3 Pure $Sc@C_{82}$ Peapod Powders . . . 147
8.3.4 Samples Dispersed in CCl_4 . . . 156
8.4 Conclusions . . . 162

9 Conclusions **165**
9.1 $^{15}N@C_{60}$ Two-Qubit Scheme 165
9.2 $Sc@C_{82}$ 166
9.3 Peapods 166
9.4 Future Research 167

A Spin $\frac{3}{2}$ System **168**
A.1 Pauli Matrices 168
A.1.1 Pauli Matrices for Spin $\frac{3}{2}$ 169
A.2 Time Evolution 171

Bibliography **182**

Chapter 1

Introduction

The quantum mechanical spin states of atoms trapped inside fullerenes can be used to store quantum information. Pulsed electron spin resonance (ESR) can be used to process this information.

1.1 Historical Background

1.1.1 Quantum Computing

Paul Benioff wrote in 1980 about a computer based on the laws of quantum physics [1]. Five years later, the specifications and implications of such a machine were laid out by David Deutsch [2]. He showed that a quantum computer might be able to solve some problems faster than its classical counterpart. This was demonstrated by the algorithms for quantum computation (QC) invented by Peter Shor [3, 4] and Lov Grover [5, 6]. At the time of writing, these ideas have been realized experimentally on a small scale only. Nuclear magnetic resonance (NMR) QC has been used to demonstrate Shor's algorithm [7] with seven quantum bits (qubits). However, the techniques used for NMR QC so far are unsuitable for scaling up to computers with many qubits. Several other experimental approaches to QC are being developed, but it is not yet clear if any of these will develop into fully scalable quantum computers. Chapter 2 gives a well-known checklist that is useful

for assessing how close different approaches are to realizing a scalable quantum computer.

1.1.2 ESR

The possibility of ESR was discussed by physicists for about twenty years before the effect was seen experimentally by Evgeny Zavoisky in 1944 [8]. Pulsed ESR is an extension of this technique that can study the dynamics of electron spins. Pulsed NMR had already been demonstrated when Richard Blume reported the first observation of an electron spin echo in 1958 [9]. Pulsed ESR machines are now available commercially, largely due to their applications in biochemical research. Chapter 3 is an introduction to ESR principals and techniques.

1.1.3 Fullerenes and Nanotubes

Fullerenes such as C_{60} are ball-shaped molecules composed of carbon atoms. Various sizes of these closed cages were spotted in the 1980's, with the structure being correctly deduced in 1985 [10]. In the same year came the first report of C_{60} and C_{70} molecules containing an atom of lanthanum [11]. La@C_{60} and La@C_{70} illustrates the most common labeling convention for these 'endohedral fullerenes'. N@C_{60} was first produced in 1996 [12]. ESR characterization showed that the C_{60} cage isolates the electron spin of the nitrogen atom from its environment. In the language of QC, this isolation is responsible for the long decoherence time.

Carbon nanotubes are long cylinders of rolled-up graphene [13] that can have multiple or single walls. The electronic properties of each single-walled carbon nanotube (SWNT) depend sensitively on its diameter and structure. Nanotubes can be filled with fullerenes, producing structures called peapods that were first reported in 1998 [14]. Chapter 4 provides a more detailed introduction to carbon nanostructures.

1.2 This Thesis

Chapters 2 - 4 describe relevant ideas from the literature.

- Chapter 5 presents a theoretical scheme for two-qubit QC with $^{15}N@C_{60}$. This uses pulsed ESR and pulsed NMR at the same time, which is a technique called ENDOR (electron-nuclear double resonance).

- Chapter 6 describes the partial experimental realization of this QC scheme. A glassy solvent is used to increase the decoherence time of $N@C_{60}$'s electronic spin to 215 μs at 3.7 K.

- Chapter 7 presents ESR experiments on $Sc@C_{82}$. By comparing these measurements with density functional theory (DFT) calculations, it is shown how the orientation of a $Sc@C_{82}$ molecule in an applied magnetic field affects the molecule's properties. Pulsed ESR measurements show that the decoherence time at 20 K is 13 μs, which is 20 times longer than had been previously thought. This demonstrates that $Sc@C_{82}$ is a promising qubit.

- Chapter 8 begins by reviewing two ways to use 1D chains of endohedral fullerenes for large-scale QC. This structure has been realized by using carbon nanotubes as a 1D container for fullerenes. Samples have been produced of nanotubes filled with dilute $N@C_{60}$. Identically prepared SWNT samples have been filled with pure $Sc@_{82}$, as well as $Sc@C_{82}$ diluted by empty C_{82} cages. ESR measurements on these samples are presented and compared. All of these data are consistent with simulations of the dipolar interactions.

- Chapter 9 offers some overall conclusions as well as outlining future directions for this research.

Chapter 2

Quantum Computing

Contents

2.1 Overview 4

2.2 Qubits 5

2.2.1 Decoherence 6

2.3 Density Matrices 7

2.4 Experiments 9

2.4.1 Experimental Requirements for QC 9

2.4.2 Pseudo-Pure States for NMR QC 10

2.4.3 The Deutsch-Jozsa Algorithm 12

2.4.4 Manipulating Electron Spins in the Solid State 14

2.4.5 Advantages of Qubits 16

2.1 Overview

The ability to do QC increases the range of things that can be computed in a finite universe [15]. Even so, there are functions that are uncomputable by a universal quantum computer [2]. Computer science generally receives funding by focusing on less abstract topics than these.

Shor's Algorithm for factorizing large numbers [3, 4] allows a quantum computer to solve problems that would be classically intractable. It is thought that the time taken by a classical computer to factorize a number must increase exponentially with the size of the number. This means that no classical computer is realistically able to find the prime factors of a number with many digits. Shor's Algorithm factorizes in a time that increases polynomially with the number of digits.

Grover's search algorithm [6, 5] is another algorithm that demonstrates the usefulness of a quantum computer. Certain problems require a classical computer to search through N possible cases, and this takes a time that is proportional to N. Grover showed how a quantum computer can perform some of these tasks in a time proportional to $\sqrt{N}$.

The simulation of quantum systems is a third problem that could be solved faster on a quantum computer than with a classical computer [16]. Indeed this was the job that Feynman was considering in his well-known 1982 paper [17].

These advances in quantum algorithms have spurred research into possible physical realizations of a quantum computer.

2.2 Qubits

A qubit can be defined as a two-level quantum system, and the Bloch sphere is a convenient way to visualize this. The surface of this sphere contains all of the possible quantum states of a single qubit, as shown in Figure 2.1 a). The north pole represents the state $|0\rangle$ and the south pole corresponds to $|1\rangle$. All possible states can be written as

$$|\psi\rangle = \cos\frac{\theta}{2}|0\rangle + \mathrm{e}^{i\phi}\sin\frac{\theta}{2}|1\rangle\,, \tag{2.1}$$

using the spherical polar coordinates shown in Figure 2.1 b). This picture was originally used by Bloch to represent the states of a spin-half system in a magnetic

field. For a field pointing upwards, the $|0\rangle$ state is the lower energy state in which the spin is aligned with the applied field. The behavior of spins in an applied field will be discussed further in Chapter 3.

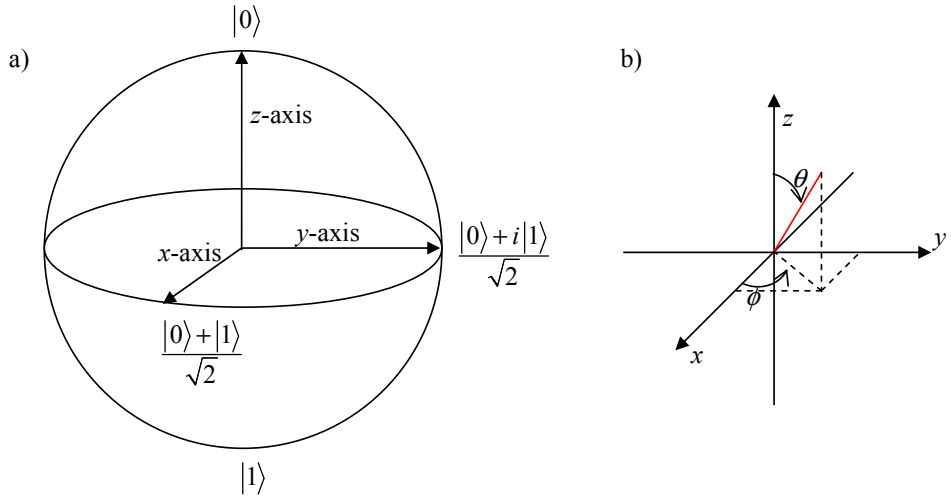


Figure 2.1: a) The surface of the Bloch sphere is a convenient way to visualize the possible states of a single qubit. Unfortunately there is no equivalent picture of a two-qubit system. b) Spherical polar coordinates are useful because T_1 decoherence processes change θ while T_2 processes change ϕ. The length of the qubit vector is always equal to 1.

2.2.1 Decoherence

The spin dephasing time, T_2, is the characteristic time for which a spin qubit remains coherent. If the desired manipulations can be performed on an ensemble of spins in this time then the signal will decay to $\frac{1}{e}$ of its initial value, which should be large enough to measure. Fully scalable QC has much stricter requirements: Current techniques for quantum error correction demand that $\sim 10,000$ gate operations be performed during the decoherence time [18].

The spin-lattice relaxation time, T_1, is the timescale on which the qubit must be measured at the end of the quantum computation. There are only two measurement outcomes: '0' and '1', so the spin coherence is not relevant here. Measuring the magnetic field due to a single electron spin is technologically very challenging

because of the small signal to noise ratio. This can be improved by averaging for a long time, but after a time T_1 there is a $\frac{1}{e}$ chance of the spin flipping its value. The T_2 time can be seen as the characteristic time for storing quantum information and the T_1 can be seen as the characteristic time for storing classical information.

For quantum information processing (QIP), it is important that qubits do not change their value except according to the computational operations. Any unwanted movement on the Bloch sphere is a decoherence process. T_1 processes are defined as those that affect θ: They change the z-component of the qubit vector so the system's energy changes. T_2 processes affect ϕ: The z-component of the vector is unchanged, so the system's energy remains the same.

2.3 Density Matrices

The Bloch sphere is used to describe a single qubit, but a more powerful approach is needed to consider the possible states of a quantum system containing more than one qubit. Density matrices are a way to do this for any number of qubits. Statistical classical information about the ensemble of particles can be represented independently of the quantum coherence (superposition or entanglement) that may be present.

The *density operator* of a wavefunction $|\psi\rangle$ is defined as

$$\rho(\psi) = |\psi\rangle \langle\psi| . \tag{2.2}$$

This density operator can be written as a matrix in some basis of quantum states $|\phi_i\rangle$ with the matrix entries taking the values

$$\rho(\psi)_{ij} = \langle\phi_j| \psi\rangle \langle\psi| \phi_i\rangle . \tag{2.3}$$

Statistical classical information about an ensemble can now be represented with

a sum of density operators. Consider a system of N particles whose eigenstates $|\phi_i\rangle$ have energy E_i. The density operator of this system at thermal equilibrium with temperature T is

$$\rho(T) = N\frac{\sum_{i=0}^{\infty} \mathrm{e}^{-\frac{E_i}{k_B T}} |\phi_i\rangle \langle\phi_i|}{\sum_{i=0}^{\infty} \mathrm{e}^{-\frac{E_i}{k_B T}}}. \tag{2.4}$$

The corresponding density matrix in the eigenstate basis is diagonal, with the i^{th} entry giving the average number of particles in state i. For $N = 1$ this is the probability of finding the particle in state i. The density matrix of a single qubit in thermal equilibrium can be written as

$$\rho_{\text{thermalized qubit}} = \frac{1}{P_0 + P_1}\begin{pmatrix} P_0 & 0 \\ 0 & P_1 \end{pmatrix}, \tag{2.5}$$

where P_0 and P_1 are the classical probabilities (Boltzmann factors) of the system being in the states $|0\rangle$ and $|1\rangle$. This system is in a mixed state, so it cannot be described with a single wavefunction. The wavefunction

$$|\psi\rangle = \frac{1}{P_0 + P_1}(\sqrt{P_0}\,|0\rangle + \sqrt{P_1}\,|1\rangle) \tag{2.6}$$

would refer to a pure quantum state in a superposition of eigenstates, with density matrix

$$\rho_{\text{superposition}} = \frac{1}{P_0 + P_1}\begin{pmatrix} P_0 & \sqrt{P_1 P_0^*} \\ \sqrt{P_0 P_1^*} & P_1 \end{pmatrix} \tag{2.7}$$

where the complex conjugates are needed as the P's can be complex. The off-diagonal terms in the density matrix are the quantum coherences between the eigenstates.

2.4 Experimental Realizations of QC

2.4.1 Experimental Requirements for QC

In 1985, Deutsch described what is now meant by quantum computation [2]. Fifteen years later, DiVincenzo published a checklist that can be used to assess many schemes for experimental QC [19][1]. His five criteria are:

1. Qubits. There must be a scalable physical system with well characterized qubits. The first systems to be used for quantum computation involve either NMR on a large number of identical molecules [7] or 'ion trap' experiments [22]. These experimental approaches have succeeded in demonstrating some of the basic ideas discussed above with seven and three qubits respectively. However, many challenges would need to be overcome before these technologies could be scaled up to many qubits. Scalability may be less challenging in the solid state. The leading candidates include superconducting systems [23], where simple two-qubit experiments have been demonstrated [24], and the spin associated with donor atoms in silicon [25]. These spins would be manipulated by pulsed ESR, with nano-electrodes applying a controlled magnetic field to each qubit.

2. Initialization. It must be possible to bring the array of qubits to a given state before the calculation.

3. 'Universal' set of quantum gates. Logic gates such as 'NOR' are used to process classical information and there is a minimum amount of control that is necessary to be able to perform all possible quantum calculations. One universal set of quantum logic gates comprises all possible operations on the individual qubits as well as the two-qubit 'control-NOT' (CNOT) gate. A CNOT gate leaves one qubit unchanged but flips the other if the first was in the $|1\rangle$ state.

[1] One-way QC is an alternative approach that does not follow this checklist [20, 21]. Instead, entanglement is generated initially which is then used up during the course of the computation.

4. Decoherence. Each qubit's interactions with the outside world must be much weaker than the interactions used to manipulate the qubits. The ratio of the decoherence time to the gate operation time is known as the 'figure of merit'. As long as this figure is greater than about 10^4, the decohered qubits can be fixed by quantum error correction codes [18]. These codes work by encoding each 'logical qubit' in up to ten 'physical qubits' in such a way that an error in any one of the physical qubits can be spotted and fixed.

5. Readout. At the end of the computation, the state of each qubit must be measured. For some solid state schemes, this would require the measurement of the states of an array of single electron spins.

2.4.2 Pseudo-Pure States for NMR QC

Liquid-state NMR QC has been demonstrated with more qubits than any other technology. However, the nuclear magnetic moments are too weak to be initialized by merely cooling the sample down and applying a strong magnetic field. Instead, a 'pseudo-pure' state can be prepared at room-temperature for just a few qubits that satisfies the initialization criterion above.

Consider a computer made up of an ensemble of N molecules that each have m computational eigenstates. The equilibrium state at room temperature is described by the density matrix

$$\rho_{\text{thermalized}} = N \begin{pmatrix} p_1 & 0 & 0 & \cdots & 0 \\ 0 & p_2 & 0 & \cdots & 0 \\ 0 & 0 & p_3 & \cdots & 0 \\ \vdots & \vdots & \vdots & \ddots & 0 \\ 0 & 0 & 0 & 0 & p_m \end{pmatrix}, \tag{2.8}$$

where the populations are the Boltzmann factors of each quantum computational

state normalized by the partition function:

$$p_i = \frac{\mathrm{e}^{\frac{-E_i}{k_\mathrm{B}T}}}{\sum_{j=1}^{m} \mathrm{e}^{\frac{-E_j}{k_\mathrm{B}T}}}. \tag{2.9}$$

The ground state population is

$$p_1 = \frac{\mathrm{e}^{\frac{-E_1}{k_\mathrm{B}T}}}{\sum_{j=1}^{m} \mathrm{e}^{\frac{-E_j}{k_\mathrm{B}T}}} \approx \frac{1 - \frac{E_1}{k_\mathrm{B}T}}{m}, \tag{2.10}$$

where the approximation is valid because $E_i \sim g_\mathrm{N}\mu_\mathrm{N}B << k_\mathrm{B}T$ at room temperature. Pulses can then be applied that equalize all of the populations to $\bar{p}$ except for the ground state, which keeps its slightly higher population, p_1. This leads to the density matrix

$$\rho_\mathrm{pseudo} = N \begin{pmatrix} p_1 & 0 & 0 & \cdots & 0 \\ 0 & \bar{p} & 0 & \cdots & 0 \\ 0 & 0 & \bar{p} & \cdots & 0 \\ \vdots & \vdots & \vdots & \ddots & 0 \\ 0 & 0 & 0 & 0 & \bar{p} \end{pmatrix}, \tag{2.11}$$

which can be rewritten as

$$\rho_\mathrm{pseudo} = N\bar{p} \begin{pmatrix} 1 & 0 & 0 & \cdots & 0 \\ 0 & 1 & 0 & \cdots & 0 \\ 0 & 0 & 1 & \cdots & 0 \\ \vdots & \vdots & \vdots & \ddots & 0 \\ 0 & 0 & 0 & 0 & 1 \end{pmatrix} + N(p_1 - \bar{p}) \begin{pmatrix} 1 & 0 & 0 & \cdots & 0 \\ 0 & 0 & 0 & \cdots & 0 \\ 0 & 0 & 0 & \cdots & 0 \\ \vdots & \vdots & \vdots & \ddots & 0 \\ 0 & 0 & 0 & 0 & 0 \end{pmatrix}. \tag{2.12}$$

The first term is the identity, which is not affected by the pulses applied for computation, or measured at the end. The second term is the zero-temperature pure state: The perfect state from which to begin a quantum computation. The

amplitude of the pure term is

$$N(p_1 - \bar{p}) = N\left(p_1 - \frac{1-p_1}{m-1}\right) = \frac{N(p_1 m - 1)}{m-1} \approx \frac{-\frac{NE_1}{k_B T}}{m-1} \tag{2.13}$$

using Equation 2.10. Now, a system with q qubits contains 2^q distinct eigenstates, so $m = 2^q$. Hence the pure state amplitude can be written as

$$N(p_1 - \bar{p}) \approx \frac{-\frac{NE_1}{k_B T}}{2^q - 1} \tag{2.14}$$

showing the exponential decay of signal with number of qubits. This analysis is quite general as it does not depend on the way in which the pseudo-pure state is prepared. There was enough signal to do liquid-state NMR QC with seven qubits, but there would be about half as much signal for eight qubits. This problem makes pseudo-pure NMR QC unscalable.

An alternative route for NMR QC is to use nuclear-spin polarized *para*-hydrogen as a reactant to form a spin-polarized molecule suitable for QC. This has been demonstrated with two-qubits [26]. Scalable NMR QC schemes have also been suggested in the solid-state [27, 28].

2.4.3 The Deutsch-Jozsa Algorithm

QC speedup can be demonstrated with a two-qubit computer using the Deutsch-Jozsa (DJ) algorithm. This proof-of-principle experiment is generally carried out to demonstrate that an experimental system is suitable for QC [29].

The simplest version of the DJ algorithm distinguishes between constant and balanced functions of a single bit. A function $f(x)$ that maps one input bit onto one output bit is constant if the output is always 1 or always 0. If the output is 0 for exactly half of the inputs then the function is said to be balanced. There are four possible one-bit functions, which are shown in Table 2.1. Two function calls are always required for a deterministic classical computer to distinguish between the balanced and constant functions in this case. The same problem can be solved

by calling the function just once with a two-qubit quantum computer [30, 31].

x	$f_{00}(x)$	$f_{01}(x)$	$f_{10}(x)$	$f_{11}(x)$
0	0	0	1	1
1	0	1	0	1

Table 2.1: The four possible binary functions that map one bit (x) onto another.

Figure 2.2 shows schematically a version of the DJ algorithm [32]. Both qubits start (on the left) in state $|0\rangle$, after the initialization described above. They then 'travel' along the 'wires' to boxes that represent quantum logic gates. The $\frac{\pi}{2}$ gate acts on a single qubit, mapping $|0\rangle \rightarrow \frac{|0\rangle+|1\rangle}{\sqrt{2}}$ and $|1\rangle \rightarrow \frac{|0\rangle-|1\rangle}{\sqrt{2}}$. This corresponds to a rotation on the Bloch sphere of 90° about the y-axis. The $-\frac{\pi}{2}$ gate maps $|0\rangle \rightarrow \frac{|0\rangle-|1\rangle}{\sqrt{2}}$ and $|1\rangle \rightarrow \frac{|0\rangle+|1\rangle}{\sqrt{2}}$.

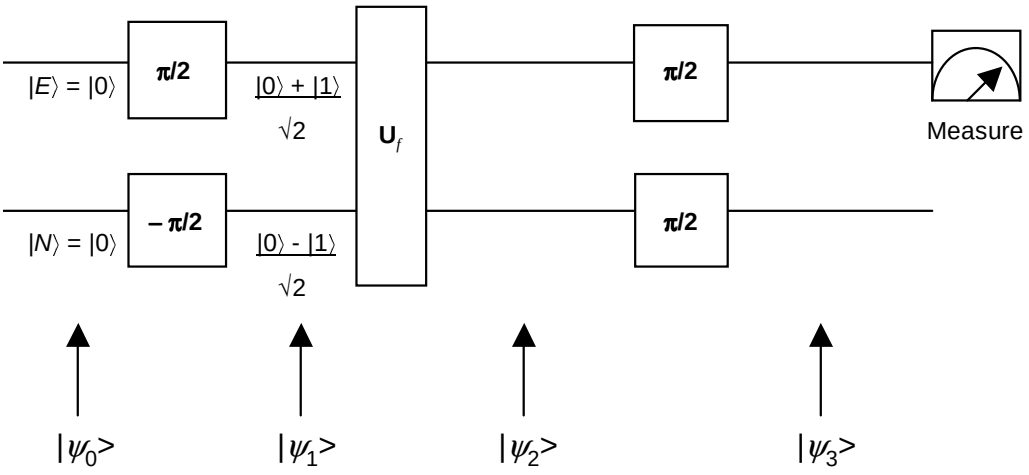


Figure 2.2: An implementation of the two-qubit Deutsch-Jozsa algorithm shown as a circuit diagram.

After the two qubits have been prepared with the $\frac{\pi}{2}$ gates, the QC version of the function $f(x)$ is called using the reversible two-qubit gate $\mathbf{U}_f$. QC gates must be reversible so this gate implements the functions $f(x)$ as follows:

$$|E\rangle\,|N\rangle \xrightarrow{\mathbf{U}_f} |E\rangle\,|N \oplus f(E)\rangle\,, \tag{2.15}$$

where $\oplus$ indicates addition modulo two. After this two-qubit gate, the two-qubit

wavefunction is

$$|\psi_2\rangle = \pm\left[|0\rangle + |1\rangle\right]\left[|0\rangle - |1\rangle\right] \qquad \text{if} f(0) = f(1) \tag{2.16}$$

$$\pm\left[|0\rangle - |1\rangle\right]\left[|0\rangle - |1\rangle\right] \qquad \text{if} f(0) \neq f(1). \tag{2.17}$$

Two more $\frac{\pi}{2}$ gates lead to the wavefunction

$$|\psi_3\rangle = \pm\,|1\rangle\,|0\rangle \qquad \text{if} f(0) = f(1) \tag{2.18}$$

$$\pm\,|0\rangle\,|0\rangle \qquad \text{if} f(0) \neq f(1), \tag{2.19}$$

and a measurement of the qubit initially labeled as $|E\rangle$ reveals whether $f(0) = f(1)$. $|\psi_3\rangle$ can be written more concisely as

$$|\psi_3\rangle = \pm\,|f(0) \oplus f(1)\rangle\,|0\rangle\,. \tag{2.20}$$

Measuring $|E\rangle = |0\rangle$ means that $f(0) \oplus f(1) = 0$ so the function is constant, while if the result is $|E\rangle = |1\rangle$ then the function is balanced.

An experiment that would implement this algorithm is described in Chapter 5 using an electron spin and a nuclear spin as the two qubits. The two-qubit DJ algorithm has been performed with NMR QC [29] and some of the techniques used are also useful in ESR QC.

2.4.4 Manipulating Electron Spins in the Solid State

One example of the published proposals for quantum computing in the solid state uses the spin on a nitrogen atom inside C_{60} as a qubit [33, 34]. In a similar scheme [35], the endohedral fullerenes are aligned inside single-walled nanotubes. Electron spins have a larger magnetic moment than that of nuclei. This makes them easier to polarize with a magnetic field, and their stronger interactions permit faster two-qubit manipulations. These advantages improve the figure of merit but this is usually offset by the shorter decoherence time of an electron spin. For N@C_{60}

this is found to be exceptionally long, as measured with pulsed ESR in Chapter 6.

Individual qubits could be addressed by local gating [35, 25] which is technologically challenging. A pulsing scheme for implementing a universal set of gates has been proposed [34] that makes use of nuclear spins and their hyperfine interactions with the electron spin. This requires a large local magnetic field gradient to enable the addressing of individual qubits.

Proposals have been made for applying a universal set of quantum gates without addressing individual qubits. For example, this can be arranged if an 'ABABA...' chain of alternating qubits is available [36, 37, 38]. Each gate operation involves manipulating the 'A' qubits and then the 'B' qubits, in turn, several times. This process increases the gate operation time and also requires eight physical qubits to describe each logical qubit.

DiVincenzo's final requirement for a quantum computer is readout, and for many spin based proposals in the solid state, it will be necessary to measure whether single electronic spins are pointing 'up' or 'down'. Single spin magnetic resonance has been observed with optical detection [39, 40], and has been used to perform two-qubit quantum computations using nitrogen vacancies in diamond. This technique might be applicable to endohedral fullerenes if a molecule were found with accessible optical transitions that depend on the state of an unpaired electronic spin.

Potassium magnetometers [41] have reached a magnetic field sensitivity below 1 fT $\mathrm{Hz}^{-\frac{1}{2}}$, but are much larger than a molecule of $\mathrm{N@C_{60}}$. A 20 micron magnetoresistive sensor has been built with a sensitivity of 32 fT $\mathrm{Hz}^{-\frac{1}{2}}$ [42]. Nano-SQUIDs have reached a sensitivity of 40 electron spins per root hertz inside a SQUID loop 3.5 microns wide [43]. A micro-SQUID has been used to measure the flipping of 1000 electron spins [44].

Another approach is magnetic resonance force microscopy (MRFM), which uses a ferromagnetic particle as a probe on the end of an oscillating micro-

mechanical cantilever [45, 46]. The cantilever is driven by a combination of pulsed fields that also excite resonant transitions in a spin at a particular distance from the probe. The magnetic resonance of the spins is measured as a change in the resonant frequency of the cantilever. MRFR has been used to detect the presence of a single spin, making use of a 13 hour measurement [47]. To readout the quantum state of a spin-half it is necessary to decide if it pointing 'up' or 'down' before a relaxation event occurs.

In another technique for single-spin detection, the Pauli exclusion principle is used to provide spin-selective tunneling of electrons through a quantum dot [48]. A single electron transistor could then be used to measure the single electronic charge witnessing a particular spin state.

2.4.5 Advantages of Qubits

People have considered what it is about quantum computers that enables them to outperform their classical counterparts. The advantages of using a quantum computer arise from the unique properties of quantum information. When a qubit is involved in a computation, there is a possibility that its measured value would be $|0\rangle$ and and a chance of it being $|1\rangle$. This means that N qubits can explore the enormous phase space of 2^N possibilities simultaneously. Contrastingly, a classical computer is always in a particular state so 2^N such computations would be required to consider 2^N possibilities. All of these possibilities would add up to a big quantum mess, were it not for the care with which quantum algorithms are constructed.

Quantum entanglement is a key resource for applications such as 'super-dense coding' and teleportation [32]. It is not clear whether entanglement is required for the operation of quantum algorithms, but Shor's algorithm was demonstrated on an NMR QC that used pseudo-entangled states. These states are mathematically equivalent to entangled states despite the fact that they contain no true entanglement [49].

Chapter 3

Varieties of ESR Experiment

Contents

3.1	**Polarization**	**17**
3.2	**Continuous-Wave**	**19**
3.3	**Spin Hamiltonian**	**22**
3.4	**Pulsed ESR**	**24**

3.1 Polarization

In electron spin resonance[1] (ESR) experiments a polarization is imposed on unpaired electron spins and deviations from this polarization are measured. The initial polarization can be generated by applying a magnetic field, $\mathbf{B}$, because each electron spin has a lower energy when its magnetic moment is aligned with the applied field. This behaviour is expressed by the Zeeman term in the Hamiltonian operator

$$H_{\text{Zeeman}} = \mu_{\text{B}} \mathbf{B} \cdot \mathbf{g} \cdot \mathbf{S}, \tag{3.1}$$

for an electron spin operator $\mathbf{S}$ with a magnetic moment

$$\boldsymbol{\mu} = -\mu_{\text{B}} \mathbf{g} \cdot \mathbf{S} \tag{3.2}$$

[1] Also called electron paramagnetic resonance (EPR).

where the Bohr magneton

$$\mu_{\mathrm{B}} = \frac{e\hbar}{2m} \tag{3.3}$$

sets the scale of the electron's magnetic moment in terms of the electronic charge (e) and rest mass (m), as well as Plank's constant ($h = 2\pi\hbar$). The g-tensor, $\mathbf{g}$, contains information about the electron's environment. In an isotropic environment, this tensor reduces to a scalar value, g, and the Zeeman term simplifies to

$$H_{\mathrm{Zeeman}}^{\mathrm{isotropic}} = g\mu_{\mathrm{B}} B_z S_z, \tag{3.4}$$

where S_z is the component of the spin, S, that is in the direction of the applied magnetic field, which defines the z-axis. S_z must take one of ($2S$+1) quantized values S, S-1, S-2, $\cdots$ -(S-2), -(S-1), -S. For example, a single electron with $S = \frac{1}{2}$ has two possible states $S_z = \pm\frac{1}{2}$ in a magnetic field.

The expectation value of the energy, E_A, of a quantum state $|\mathrm{A}\rangle$ due to the Hamiltonian H is

$$E_A = \langle A| \, H \, |\mathrm{A}\rangle \,, \tag{3.5}$$

so the energy of an isotropically-placed spin in a magnetic field[2] is

$$E(S_z) = g\mu_{\mathrm{B}} B_z S_z. \tag{3.6}$$

The polarization of two quantum states, $|\mathrm{A}\rangle$ and $|\mathrm{B}\rangle$, is defined here[3] as the ratio of their populations in an ensemble:

$$\text{Polarization} \equiv \alpha^{-1} \equiv \frac{\text{Population of } |\mathrm{A}\rangle}{\text{Population of } |\mathrm{B}\rangle}. \tag{3.7}$$

[2]When unqualified, the word 'field' will always be used to refer to the applied magnetic field.

[3]Other authors define the polarization of two states as the difference in their populations divided by the sum of their populations.

The inverse polarization, α, is called the Boltzmann factor of the two-level system. The equilibrium (eqm) polarization depends on the Boltzmann distribution for two states separated by energy E_A-E_B, at temperature T:

$$\alpha^{-1}_{\mathrm{eqm}}(T) \equiv \frac{P[A]}{P[B]} = \mathrm{e}^{-\frac{(E_A - E_B)}{k_\mathrm{B} T}}, \tag{3.8}$$

where P[A] is the notation used for the equilibrium population of state $|\mathrm{A}\rangle$.

3.2 Continuous-Wave ESR

Continuous-wave (CW) ESR is described in the textbook by Poole [50]. In the most simple experiments, a microwave field of frequency f is applied to a sample while a strong magnetic field is swept slowly. Equation 3.6 shows that the energy difference between levels with adjacent values of S_z is

$$\Delta E(B_z) = g\mu_\mathrm{B} B_z. \tag{3.9}$$

Conservation of energy requires that the spin must absorb (lose) this much energy for S_z to increase (decrease) by 1. These transitions occur resonantly when the magnetic field produces an energy difference that is equal to the energy of each microwave photon, $E_{\mathrm{photon}} = hf$. Energy is resonantly exchanged between the spin and the microwave field when the magnetic field is

$$B_{\mathrm{res}} = \frac{hf}{g\mu_\mathrm{B}}. \tag{3.10}$$

Before reaching this resonance condition, the system is polarized: Equations 3.8 and 3.9 show that the polarization is

$$\alpha^{-1}(T) = \mathrm{e}^{-\frac{g\mu_\mathrm{B} B_z}{k_\mathrm{B} T}}. \tag{3.11}$$

The net effect of resonance is that the spin ensemble absorbs energy from the

microwave field and the population of the higher S_z state increases. This loss of energy from the microwave field is detected by the spectrometer. Plotting the absorption against magnetic field produces an absorption spectrum as shown in Figure 3.1 (a) containing a single resonance[4].

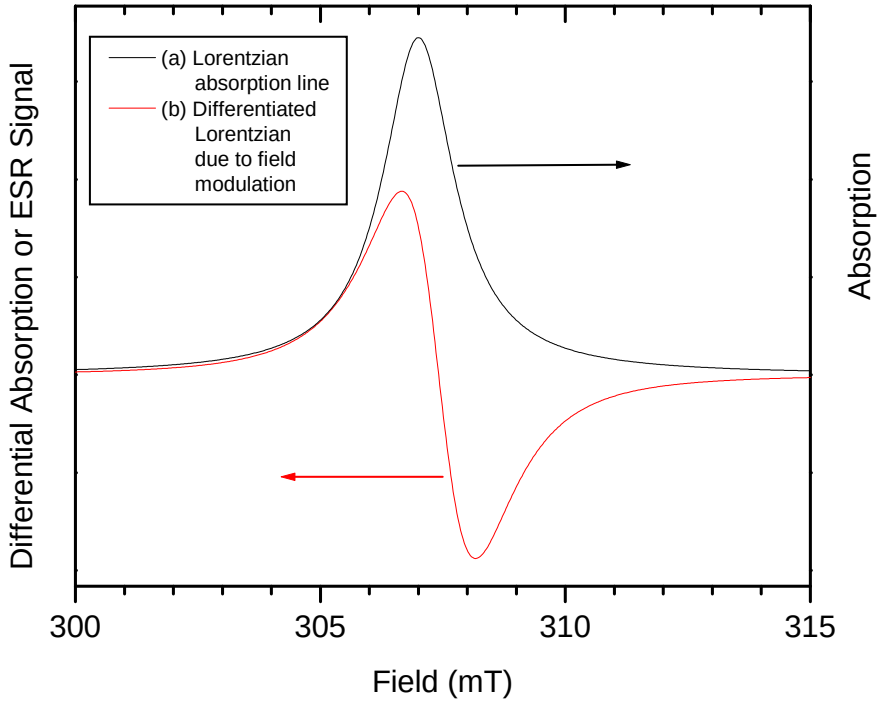


Figure 3.1: (a) Characteristic Lorentzian absorption spectrum. (b) Characteristic differentiated Lorentzian that would be found in an ESR experiment with field modulation. The absolute size of the signal is not used when analyzing these data, so the y-axis generally has arbitrary units or none.

In many experiments the signal to noise is improved by adding a small modulation to the applied field, and measuring the change in the absorption that occurs with the same frequency as the modulation. This technique produces a differential absorption spectrum as shown in Figure 3.1 (b). As a general rule, the size of the modulation needs to be three times smaller than the width of a resonance to avoid artificial line-broadening called modulation broadening. The samples studied in Chapters 5 and 6 have very small linewidths, so field modulation improves their signal to noise greatly. It is not generally possible to measure the intrinsic

[4]Spectra are also referred to as scans, and resonances can be referred to as lines.

linewidth of these samples in CW ESR, because of the inhomogeneity of the applied magnetic field. The field across the sample commonly varies by at least 2 μT, so all resonances sharper than this will have a measured width of 2 μT.

The resonance due to a single, isolated spin system has a width that is referred to as the homogeneous linewidth. The CW ESR spectrum of an ensemble sample is the sum of the spectra from each constituent spin system. If each of these constituent spectra contain a sharp resonance at slightly different magnetic fields, the measured spectrum is inhomogeneously broadened. Magnet inhomogeneity is one such process that can hide the intrinsic linewidth of each individual spin system. Pulsed ESR enables inhomogeneous line-broadening effects to be studied separately from intrinsic linewidths.

Using a resonant microwave cavity increases the microwave power and provides a known microwave field geometry. The most common microwave frequency used in ESR spectrometers is around 9.5 GHz, and this region is called X-band. The corresponding wavelength is $\sim$ 30 mm, so the resonant cavity, and hence the sample, have about this size. Each time a new sample is inserted, the resonant cavity must be tuned by changing the microwave frequency slightly. This difference in frequencies must be allowed for when comparing the CW spectra of different samples. The most simple way to do this is to scale the field axis of one of the scans to agree with the other (reference) scan by the factor $\frac{f_{\text{reference}}}{f_{\text{scaled}}}$.

To produce spectra that can be straightforwardly interpreted, the spin system should always be at quasi-equilibrium, which defines the reference level of polarization throughout the scan. This is achieved by scanning slowly: Each resonance should be swept in a time that is long compared with the longitudinal spin relaxation time, T_1. After absorbing microwave energy, the spin system returns to equilibrium mainly by non-radiative transitions such as spin-lattice transitions involving phonons. In simple cases, there is a single exponential decay time, T_1. Scanning too fast produces 'passage effects' in which the recorded spectrum depends on whether the field is swept up or down.

A related condition is that the spin system should not be saturated. With high microwave powers, spins with long T_1's can absorb energy faster than they lose it, and when they can absorb no more they are completely saturated. The polarization $\alpha^{-1} = 1$ because there is no population difference. This regime must be avoided by reducing the power, but partial saturation may remain. The resonances of a partially saturated spin system are weakened by an unknown amount, which prevents them being compared with unsaturated spins. In the absence of saturation, the area under a resonance in an absorption spectrum is proportional to the number of spins that produced the resonance. These calculations are called spin counts.

The most simple way to avoid saturation effects is to look at the power dependence of the resonant amplitude. In the absence of saturation, the signal intensity is proportional to the square root of the microwave power. After recording the spectrum of a resonance, another can be recorded with four times greater power, and half as much receiver gain. If the two scans have the same size and shape then neither is saturated.

3.3 Effective Spin Hamiltonian

Simulating the behaviour of ESR samples generally involves fitting a model Hamiltonian to the data. Three of the most common terms describe the electronic Zeeman energy, the nuclear Zeeman energy and the hyperfine coupling between electronic and nuclear spins. The Hamiltonian operator due to these terms is

$$H_{\text{model}} = \mu_{\text{B}}\mathbf{B}\cdot\mathbf{g}\cdot\mathbf{S} - g_{\text{N}}\mu_{\text{N}}\mathbf{B}\cdot\mathbf{I} + \mathbf{I}\cdot\mathbf{A}\cdot\mathbf{S}. \tag{3.12}$$

The first term is due to the electronic Zeeman interaction described in Section 3.1. The g-tensor is usually symmetric, in which case it contains up to six independant

quantities[5]. Fewer parameters are needed if the probe spin is in a symmetric environment. A free electron has $g = 2.0023$ for any applied field direction.

The second term represents the nuclear Zeeman energy which is analogous to the electronic version. A nuclear spin $\mathbf{I}$ has $(2I+1)$ quantum states in a magnetic field. The big difference here is that the nuclear magneton, μ_{N}, is on the order of 1000 times smaller than μ_{B} because electrons are so much lighter than nucleons. The nuclei are so weakly coupled to their environment that the nuclear Zeeman interaction can generally be assumed to be isotropic.

The third term describes the hyperfine coupling between the nuclear spin and the electronic spin, via the hyperfine tensor, $\mathbf{A}$. This is made up of the Fermi contact interaction and the electron-nuclear dipole-dipole interaction. The Fermi contact interaction is described by an isotropic (scalar) coupling which is proportional to the electron spin density at the nucleus. This is often dominated by s-orbitals. In an isotropic environment, the A-tensor reduces to a scalar, A. The hyperfine and nuclear Zeeman coupling can be positive or negative.

Other terms that are commonly used include a zero-field splitting term of the form $\mathbf{S} \cdot \mathbf{D} \cdot \mathbf{S}$. This can be found in systems with electron spin greater than $\frac{1}{2}$; like the hyperfine term, it does not depend on field. The nuclear quadrupole interaction can be relevant for $I \geq 1$, taking the form $\mathbf{I} \cdot \mathbf{Q} \cdot \mathbf{I}$.

The electron spins that are being probed can also be coupled to each other. In this case, the full Hamiltonian consists of the individual terms described already, added to coupling terms describing the dipole-dipole interaction, and the exchange interaction.

The dipolar coupling experienced by the probe spin can be simply modeled as the result of an extra magnetic field due to some other spin (magnetic dipole). This falls off with the third power of the spins' separation.

Direct exchange is relevant whenever there is significant overlap of two elec-

[5]These could be the three principal values: g_x, g_y and g_z as well as the three (Euler) angles that describe the orientation of the principal axis in the coordinate frame of the molecule.

tronic wavefunctions. This coupling can be defined as

$$H_{\text{exchange}} = -\mathbf{S_1} \cdot \mathbf{J} \cdot \mathbf{S_2}, \tag{3.13}$$

so that a negative exchange constant encourages the two spins to point in opposite directions, leading to antiferromagnetism [51]. The anisotropic part of $\mathbf{J}$ is due to spin-orbit coupling and can usually be neglected for organic radicals. The exchange term then simplifies to $-J\mathbf{S_1} \cdot \mathbf{S_2}$.

3.4 Pulsed ESR

The textbook by Schweiger and Jeschke [52] provides a thorough introduction to the principles and applications of pulsed ESR.

Pulsed ESR employs a static magnetic field (along the z-axis) that is chosen to satisfy the resonance condition of equation 3.10. This provides some magnetization that can be thought of as a vertical vector of variable length in the Bloch sphere, Figure 2.1. Microwave radiation is then applied for periods of time on the order of 10-1000 ns. These pulses rotate the magnetization by an amount that is proportional to the duration of the pulse.

The simplest such experiment consists of applying a pulse that moves the magnetization to the equator of the Bloch sphere: This is called a 90° pulse or a $\frac{\pi}{2}$ pulse. From here, the spins will precess about the z-axis due to the only remaining (static) field. This precession is a consequence of the conservation of the angular momentum associated with a magnetic moment. All of these spins rotate at about the electronic Zeeman frequency (9.5 GHz at 0.3 T). This fast precession is subtracted in calculations by moving to the rotating frame.

As they precess, the spins emit characteristic microwave radiation, called the free induction decay (FID). This comparatively tiny signal is measured by sensitive detectors that can be switched on only after the high-intensity applied pulse has died away. In this way, the x- and y-components of the magnetization are

measured; they decay as the spins lose phase coherence with each other. This happens over a characteristic dephasing time called T_2^* that contains dephasing due to inhomogeneous line-broadening effects such as the inhomogeneity of the static magnet. Nearby spins such as nuclear spins can provide some extra magnetic field, changing the precession frequency slightly. In the rotating frame, this corresponds to a slow rotation of the magnetization, making the FID oscillate as it decays. Taking the Fourier transform (FT) of the FID reveals a spectrum that is analogous to a CW scan, with frequency replacing magnetic field on the x-axis. This technique is called FT-ESR.

When a sample has a T_2 time that is longer than T_2^*, a two-pulse 'Hahn echo' can be used to measure the sample's intrinsic T_2. This begins with the same $\frac{\pi}{2}$ pulse. The spins are then left to precess for a time τ about the z-axis at speeds that are dominated by the inhomogeneous linewidth (in the rotating frame). A π pulse is then applied that mirror flips the slow spins ahead of the fast spins, so that those that are still phase-coherent reconvene a time τ after the π pulse, forming an echo. This echo is two FIDs back to back. Its intensity depends on τ and T_2, but not on the inhomogeneous linewidth, so T_2 is measured by plotting the echo intensity against τ. Oscillations can also be present in this plot which are referred to as ESEEM (electron spin echo envelope modulation). This signal can be used to measure hyperfine interactions.

Spin echoes can also be used for spectroscopy by holding τ constant and sweeping the field. This echo-detected field-sweep (Edfs) produces spectra that are directly comparable to a CW scan. The advantage of this technique over Fourier transforming the FID is that some of the FID is always lost during the 'deadtime' before the detector can be turned on. However, an Edfs broadens narrow lines unless very long pulses are used, and FT ESR is faster.

The spin-lattice relaxation time, T_1, can be measured with the 'inversion recovery' pulse sequence. This uses a π pulse to flip the net magnetization into the -z direction from where it is left to decay back to the lower energy +z state for a

time τ. A $\frac{\pi}{2}$ pulse is then applied as a readout to rotate onto the y-axis those spins that have decayed so far. The FID emitted reveals the z-magnetization decay as a function of time (τ), allowing the characteristic decay time to be extracted. The free evolution takes place with no magnetization in the x-y plane, so T_2-type processes are not involved. If an echo can be measured, this can be used as the readout instead of the FID.

In more advanced experiments, the nuclear spin is also excited. This technique is known as electron-nuclear double resonance (ENDOR). CW or pulsed radio-frequency (RF) radiation is applied to change the nuclear spin state, and the effects on the electron spin system can be measured with pulsed or CW ESR[6]. This opens the possibility of a two-qubit experiment using the nuclear and electronic spins of a single atom inside a fullerene.

[6]A superscript is used here to differentiate electronic relaxation times, T_1^e and T_2^e from nuclear relaxation times, T_1^n and T_2^n.

Chapter 4

Fullerenes and Nanotubes

Contents

4.1 Fullerenes 28

4.1.1 Endohedral Fullerenes 29

4.2 Nanotubes 42

4.2.1 Peapods 44

Materials composed entirely of carbon can have several different forms. Diamond, soot and graphite are the most common of these and their structures are well understood. Graphite is composed of layered graphene sheets with weak van der Waals forces binding the sheets together. Each sheet is made of strongly covalently bonded carbon atoms at the vertices of regular, tessellating hexagons.

In the last twenty years new allotropes of carbon have been discovered: Fullerenes and nanotubes. The structure of these materials can be visualized as sheets of graphene that are curled over and seamlessly joined on the nanometer scale. They have unusual electronic and mechanical properties that make them promising building blocks for various nano-structures.

4.1 Fullerenes

The first fullerene to be discovered was the football-shaped C_{60}, named Buckminsterfullerene in 1985 by the researchers who correctly guessed at its structure [10]. The very high symmetry of this geodesic ball had earlier been used by the architect R. Buckminster Fuller in the design of domes. As shown in Figure 4.1, there are twelve pentagons linked to each other by twenty benzene-like hexagons. This structure was verified in 1990 when sufficient quantities of C_{60} had been produced to measure the ^{13}C NMR spectrum. A single resonance line was seen, demonstrating the high molecular symmetry: Each carbon atom is in an equivalent position. Infra-red (IR) and ultra-violet (UV) spectroscopy confirmed this high symmetry [53], and X-ray analysis of crystalline samples measured the cage diameter as about 0.7 nm.

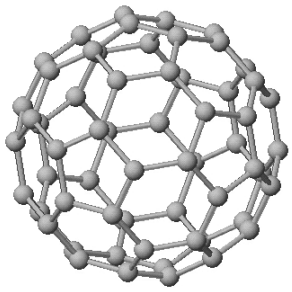


Figure 4.1: Structure of C_{60} [54].

Mass spectroscopy was the first tool used to characterize fullerenes and has revealed a large family from C_{20}^+ through the more stable ions C_{2n}^+ (where $2n > 32$) to the stable molecules such as $C_{60,70,74...}$.

For fullerenes with more than 70 carbon atoms, several structural isomers are possible, with different patterns of five and six-membered rings. Calculations suggest that the stable structures are those in which each pentagon is surrounded by five hexagons. This is called the isolated-pentagon rule (IPR) and is obeyed by all of the fullerenes that have so far had their structures characterized.

Insights have come from studying the dc conductivity of thin fullerene films. A simple model has been proposed to explain the observation that the conductance of solid C_{60} is one hundredth that of its relative, graphite [55]. C_{60} is a semiconductor with a band gap of about 2.3 eV [56]. Exposing the films to oxygen or air at room temperature causes a fast decrease in the dark conductivity and the photoconductivity, which is partially reversible by heating to 180°C [57]. Simultaneous exposure to white light and oxygen causes larger and faster irreversible reductions in the conductivity. These effects have been ascribed to significant drops in the carrier mobilities [56].

Several investigators have seen ESR signals from both anions and cations of C_{60} and C_{70} [58, 59, 60, 61]. This technique has been used to show that the oxidation of C_{60} is enhanced by exposure to light [62].

4.1.1 Endohedral Fullerenes

Endohedral fullerenes are composed of one or more atoms trapped inside a carbon cage. Trapping metal atoms produces metallofullerenes that were reviewed by Shinohara [63]. N@C_{60} has different properties that will be described separately.

Metallofullerenes

Just days after finding C_{60} [10] came the first indication that atoms had been trapped inside these molecular cages [11]. The mass spectra showed that a molecule with 60 carbon atoms and a lanthanum atom had been produced, as well as similar complexes with higher, even numbers of carbon atoms. Three years later, the same group of researchers showed that these ions did not react with H_2, O_2, NO or NH_3. This suggested that the carbon cage was chemically protecting the reactive metal atom, supporting the initial idea of encapsulation.

Only later, in 1991, were macroscopic quantities of these endohedral fullerenes produced, again by the group at Rice University [64]. They used high-temperature laser vaporisation of graphite rods containing La_2O_3. However, when they tried

to extract the lanthano-fullerenes from the soot that was produced, only La@C_{82} survived. This shows that it is stable in air and solvents (such as toluene and carbon disulphide), while La@C_{60} and La@C_{70} are not. Metalofullerenes with C_{82} cages are more stable than those based on C_{60} or C_{70}. The converse is true of empty cages: Empty C_{60} and C_{70} are more stable than C_{82}.

The separation and purification of endohedral fullerenes has been a difficult and important part of their study. After the production stage in an arc discharge experiment, and the solvent extraction from soot, many species remain mixed up. There will be empty carbon cages as well as various filled fullerenes, but many characterization techniques require a pure sample to provide clear results. Liquid chromatography is a standard chemical tool for separating different molecules, which was used successfully with empty fullerenes.

A more powerful technique is HPLC: High performance (or pressure) liquid chromatography. The dissolved species are passed through a column that is packed with porous material. With a good choice of stationary (packing) material and solvent, similar molecules will move through the system at slightly different speeds. For example, if all of the C_{82} and nothing else emerges during a two minute period, it can be completely separated from the other molecules. Alternatively, if the La@C_{82} starts to come out before the C_{82} has finished emerging, the purification will be incomplete. In this case, multi-stage separations can be used that may benefit from the use of differing packing materials. These approaches eventually succeeded in isolating and purifying the metallofullerenes described here, even separating cage isomers, which have alternative arrangements of the carbon atoms. This in turn allowed techniques such as absorption spectroscopies and X-ray diffraction to unambiguously identify the properties of specific molecules. HPLC will be described further with reference to N@C_{60}.

ESR spectroscopy was used to measure the hyperfine splitting (hfs) of La@C_{82}, allowing the electronic structure to be inferred [65]. It was suggested that three electrons are transfered from the metal atom to the cage, producing $La^{3+}@C_{82}^{3-}$.

This picture was later modified by density functional theory (DFT) simulations showing that the La-C_{82} bond has a significant covalent character [66]. Soon after these experiments, Y@C_{82} was produced and found to have very similar electronic structure [66]. Another Group 3 metal to have been encaged is scandium, for which an abundance of species were found to be stable in solvents. These include Sc_n@C_{82} for n=1,2,3,4 as well as Sc_2@C_{74} and Sc_2@C_{84}. Several electronic structures have been proposed for Sc@C_{82} in experimental and theoretical studies [67, 68, 66, 69, 70, 71, 72, 73, 74]. Results are presented in Chapter 7 that resolve many of these problems by comparing ESR data with density functional theory (DFT) calculations.

ESR spectroscopy provided evidence that the metal atoms are sited close to the cage wall. Group 3 endohedral fullerenes such as La@C_{82}, Y@C_{82} and Sc@C_{82} are ESR active. Their hyperfine spectra are characteristic of the unpaired electronic and nuclear spins of the trapped ion. However, these spectra also show smaller splittings due to interactions of the electrons with some of the carbon nuclei in the cage. 99% of carbon atoms are ^{12}C which is nuclear-spin-silent and so invisible to ESR and NMR. However, the remaining carbon atoms have an extra, unpaired neutron, resulting in a nuclear spin of $\frac{1}{2}$. It is therefore likely that most fullerene molecules will contain at least one ^{13}C nucleus. The observation of ^{13}C hyperfine satellite lines demonstrates that the unpaired electron is spending some time close to the carbon atoms in the cage.

Sc_3@C_{82} shows an ESR hyperfine signal due to the three independent Sc atoms in equivalent positions [67, 68]. Di-metallofullerenes such as La_2@C_{80} are always ESR-silent, having no unpaired electronic spins [63]. C_{82} cages containing an atom of gadolinium [75], holmium [76], thulium [76] or lutetium [77] all show ESR signals.

Endohedral Nitrogen: N@C_{60}

Many people were surprised when N@C_{60} was created in 1996, by accelerating nitrogen atoms towards a sample of C_{60} [12]. It was correctly deduced that the N atom is in an almost atomic state, shielded from its environment by the fullerene which was latter described as a 'chemical Faraday cage'. Nitrogen atoms are generally highly reactive, but experimental [78] and theoretical [79, 80, 81] studies have found that they are quite stable right in the centre of Buckminsterfullerene (see Figure 4.2). It seems that, unlike the outer surface, the concave inner surface of the carbon cage is inert [82, 83]. The interesting properties of this unexpected molecule complement its geometry.

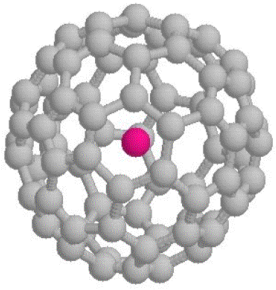


Figure 4.2: Structure of N@C_{60} [54] with the nitrogen atom shown in pink.

N@C_{60} powder is stable in air, but will irreversibly polymerize, like empty C_{60}, if left in air for a month in daylight. Kept in the dark, dissolved in deoxygenated CS_2, N@C_{60} is stable on timescale of at least a year. The stability in deoxygenated toluene solvent is a much worse; the solution becomes ESR-silent over a period of days [84]. Heating N@C_{60} up to 220°C for a minute does not cause significant decomposition and adding functional groups to the outside of the cage was found to increase the molecule's heat-stability [78]. Functionalization does not destroy the atomic nature of the nitrogen, and has been used to further understand the molecular structure [82]. Inert noble gas atoms inserted into C_{60} are much more stable to heating, escaping only above 1000°C, when it is thought that the cage

opens due to breakage of some C-C bonds. Thermal decomposition of $N@C_{60}$ must occur via a different mechanism, as it takes place at much lower temperatures. There is evidence [85] to support a two-step process beginning with the excited nitrogen atom leaving its central position and binding to the inside of the carbon cage. Once attached to the cage the N atom has a chance of flipping onto the outside, from where it escapes. The stability of $N@C_{60}$ in ambient conditions is evidence for the weak host-guest interaction that is further demonstrated by ESR spectroscopy. In contrast, thermal decomposition begins with the formation of a bond between the nitrogen atom and its cage, prior to escape.

As well as ion bombardment of C_{60} with a Kaufman ion source, $N@C_{60}$ can be produced in a glow discharge reactor [86]. This uses the same principle of accelerating positive nitrogen ions with a few hundred volts towards empty C_{60} cages. These methods can provide mixed samples of $N@C_{60}$ and C_{60} in the ratio of about 1:10,000. Purification is thus highly desirable, but made difficult by the similarity of these two fullerenes. As before, HPLC is the best method, but $N@C_{60}$ and C_{60} move through the column at almost the same speed due the weakness of the interaction between the trapped atom and its cage. There is almost no charge transfer and the cage size is not noticeably modified, so the extra mass of $N@C_{60}$ may be responsible for its slightly slower passage through the packing material. Even with a good choice of solvent and packing material, there is considerable overlap with both species emerging at similar times (see Figure 4.3).

This problem can be reduced by using a longer HPLC column, or an arbitrary length can be simulated by feeding the output back into the entrance of the column. This technique is called recycling HPLC and allows the concentration of $N@C_{60}$ in C_{60} to be increased to over 95% [87, 88].

Pure $N@C_{60}$ is required for some QC applications, but the dilute samples made initially contained enough spins to be characterized by ESR. This is because C_{60} and most of the other impurities are diamagnetic and hence ESR-silent. For CW ESR, the quantum mechanics of an atom with nuclear and electronic spin in a

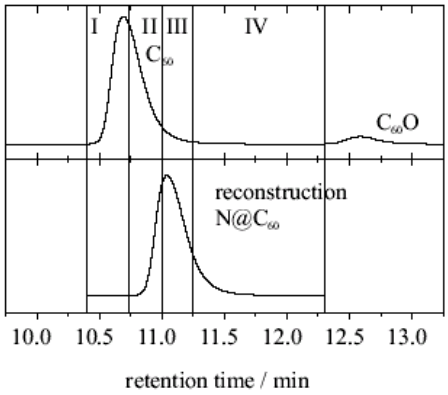


Figure 4.3: Upper part is UV absorption during HPLC of dilute $N@C_{60}$ [78], which was cut as shown by the vertical lines to separate the C_{60}. Lower part is the peak due to $N@C_{60}$ infered from the measured quantities in each of the four fractions.

magnetic field $\mathbf{B}$ must be considered. The Hamiltonian operator for an atom with electronic spin operator $\mathbf{S}$ and nuclear spin operator $\mathbf{I}$ is written

$$H = \mu_{\mathrm{B}}\mathbf{B}\cdot\mathbf{g}\cdot\mathbf{S} - \mu_{\mathrm{N}}\mathbf{B}\cdot g_{\mathrm{N}}\mathbf{I} + \mathbf{S}\cdot\mathbf{A}\cdot\mathbf{I} + \mathbf{S}\cdot\mathbf{D}\cdot\mathbf{S} + \mathbf{I}\cdot\mathbf{Q}\cdot\mathbf{I}. \tag{4.1}$$

The five terms represent the following interactions: The electronic and nuclear Zeeman, the hyperfine, the fine structure and the nuclear quadrupole. These terms were introduced in Section 3.3.

This equation can be considerably simplified for $N@C_{60}$ because the centrally placed nitrogen atom experiences isotropic interactions due to the high symmetry of the carbon cage. For an isotropic system, there is no fine structure or quadrupole interaction and both $\mathbf{g}$ and $\mathbf{A}$ reduce to scalar values g and A. In addition, the external magnetic field applied for ESR is at least 0.3 T, so the electronic Zeeman energy is at least 300 times larger than the next largest term: The hyperfine coupling to the ^{14}N nucleus provides an effective field of 0.6 mT. Hence the electrons and nuclei are (almost) decoupled from each other, precessing (almost) independently about the applied field (which defines the z-axis). The Hamiltonian can then be written as

$$H = \mu_{\mathrm{B}}B_z g S_z - \mu_{\mathrm{N}}B_z g_{\mathrm{N}} I_z + S_z A I_z, \tag{4.2}$$

where S_z and I_z are the magnetic spin quantum numbers of the electrons and the nuclei respectively. The energy level diagram can thus be drawn as shown in Figure 4.4 for atomic ^{14}N which has $S = \frac{3}{2}$ and $I = 1$.

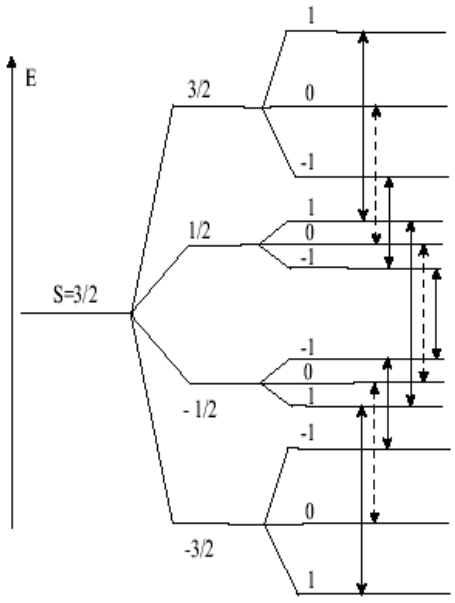


Figure 4.4: Energy level diagram for isotropic atomic ^{14}N in a strong external magnetic field [78]. The first split shows the four possible values of the total electronic spin, S_z, and then these are each split into the the three possible values of I_z. The splitting of the nuclear energy levels has been shown greatly exaggerated for clarity: The nuclear splitting is three orders of magnitude smaller than the splitting of the electronic energy levels.

The allowed ESR transitions are those indicated for which

$$\Delta S_z = \pm 1 \quad \text{and} \quad \Delta I_z = 0. \tag{4.3}$$

In the high-field limit, these nine transitions form a triplet of lines with three transitions making up each line. This is the origin of the measured ESR spectrum shown in Figure 4.5.

Therefore, CW ESR supports the assumptions used in these calculations of the electronic structure of N@C_{60}. Specifically, the ^{14}N atoms are in their atomic ground states having an unpaired electron in each of the three $2p$-orbitals. These electron spins are parallel, forming a total electronic spin of $\frac{3}{2}$. The nitrogen atom

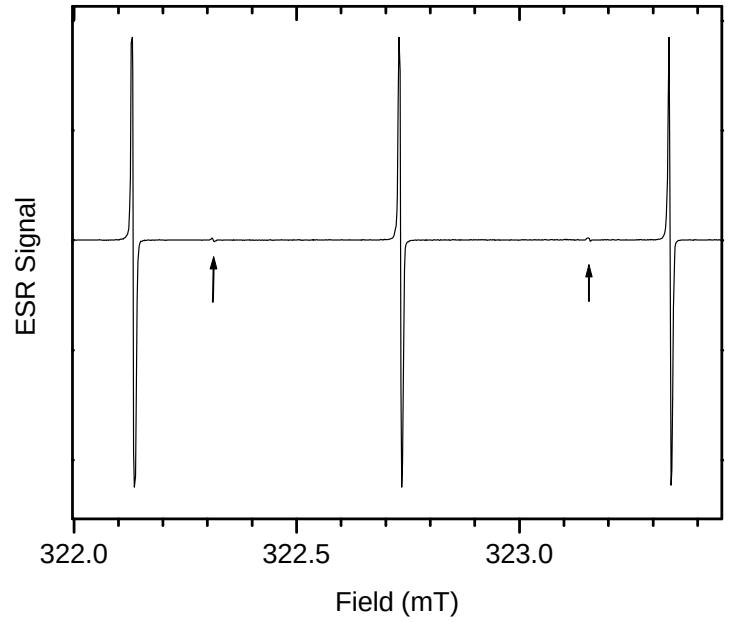


Figure 4.5: Measured X-band CW ESR signal of N@C_{60} in deoxygenated toluene solution. The three large resonances are due to ^{14}N@C_{60}, as described in the text. The arrows indicate the two resonances due to the natural abundance of ^{15}N@C_{60}, which has a nuclear spin of $\frac{1}{2}$.

is likely to be in the centre of the cage because of the observed isotropy, which permits the simplification to Equation 4.2. This interpretation could be made confidently when more precise results from pulsed ESR were available [89]. In particular, the molecular isotropy was confirmed when these results were checked by low-temperature pulsed measurements of N@C_{60} powder [90]. This excluded the possibility that the dissolved molecules were anisotropic, but tumbling so fast that this was averaged out. Separate evidence for the central location of the N atom is provided by the weakness of the hyperfine interaction with the ^{13}C atoms in the C_{60} cage [90].

Three papers are devoted to theoretical simulations of the electronic structure of N@C_{60}. They all use density functional theory (DFT), and they all confirmed the following key ideas:

1. N@C_{60} is stable under ambient conditions.

2. The system can be considered as having two parts that interact only weakly:

An atom of nitrogen in its $^4S_{\frac{3}{2}}$ ground state[1], and a molecule of C_{60}.

3. The nitrogen is located in the centre of the cage.

The first of these papers [79] found that adding the nitrogen atom caused a very slight increase in the fullerene energy levels. The nitrogen atom energy levels were placed higher still and a small amount of electron transfer away from the cage was reported. The second study [80] reported essentially no change in the fullerene energy levels and no electron transfer. Addition of the nitrogen atom was found to cause very little strain in the carbon cage, with the bonds stretching by only one part in 10^4. However, the charge cloud of the nitrogen atom was found to be significantly contracted as a result of confinement, leading to much increased hyperfine coupling between the nitrogen nucleus and its electrons. A 50% increase has been quoted [91] of the ESR hfs constant measured for N@C_{60}, as compared to the value calculated for a free nitrogen atom. ESR measurements cannot be performed on free N atoms because they immediately react, forming N_2. Confining atoms in a fullerene can be compared to the confining effects of a lattice, as well as with low temperatures and high pressures [91]. A nitrogen atom in a C_{70} cage is less compressed so the hfs constant is slightly smaller [82].

The third theoretical paper [81] repeated the calculations in both of the previous papers for P@C_{60} and As@C_{60} as well as their relative, N@C_{60}. This revealed that the different results arose from the choice of theoretical model: Molecular orbitals were used initially, but the second paper used Hartree-Fock wavefunctions.

Width of N@C_{60} ESR Lines

As its name suggests, ESR is a resonant phenomenon, which means that the measured signal can be very sensitive to parameters such as the applied magnetic fields. The ESR of N@C_{60} is quite exceptional for the narrow range of applied fields for which transitions can be excited by a particular microwave frequency.

[1]This notation is the atomic term $^{2S+1}L_J$ for total spin quantum number S, total orbital quantum number L (with S=0, P=1, D=2 etc.) and $J = L + S$.

The linewidths in solution are ten times smaller than in any other dissolved species [89][2]. Analysis of the width of the absorption lines can reveal a lot about the environment experienced by the spins, but standard CW ESR measurements are not normally precise enough to measure the intrinsic linewidth of $N@C_{60}$. This is because the applied static magnetic field is never perfectly constant across the sample. This inhomogeneity leads to 'field broadening' because identical spins in different parts of the sample experience different magnetic fields and go through resonance separately.

ESR linewidths can be influenced by the lifetime of the excited spin states, which is characterized by the decay time called T_1^e. When a spin is anti-aligned with an applied magnetic field, T_1^e is the exponential relaxation time required for the spin to return to its ground state. Heisenberg's uncertainty principle states that the energy of the excited state has some uncertainty associated with it, as it only exists for a finite time. For shorter lifetimes, the uncertainty in the energy of the transition grows proportionally. Uncertainty in the energy required to excite transitions translates directly into a broadening of the resonance. The strength of a spin's interaction with its environment describes how easily it can lose energy and return to its ground state. Therefore, a system with a long T_1^e is only weakly coupled to its environment.

There are other sources of line broadening in a CW ESR experiment, and the next lower limit arises from the spin dephasing time, T_2^e. This is a measure of the interactions between spins and can be understood in the CW setup as the direct analog of electronic band-structure in a crystal. In solid state physics, the environment felt by an electron in a lattice can be attributed to the coupling of many quantized atomic energy levels into a smeared out energy band. Similarly, two interacting spins in a magnetic field experience a modified local field as a result of their magnetic dipole-dipole interactions with each other. This turns the single ESR line into two, equally split about the original position. A group of

[2]Electron bubbles in liquid helium can have equally sharp resonances [92].

many interacting spins shows a broad band of such overlapping lines. The width is quantified by the characteristic time for the net magnetization to decay due to spins precessing at differing speeds about the applied field. This T_2^e time, as well as the T_1^e time, can be independently measured with pulsed ESR.

In the quantum computing literature, it is common to consider all of the T_1 and T_2 processes together as the decoherence time, and this is sometimes refered to simply as the T_2 time.

At room temperature, the T_2^e time for the central $I_z = 0$ resonance of a dilute solution of N@C_{60} has been measured as 120 μs, with the T_1^e time taking the same value [89]. Another paper [33] quotes $T_2^e = 50$ μs in solution, and $T_2^e = 20$ μs for powders, as well as $T_1^e = 120$ μs in the solid state, all at room temperature. At 5 Kelvin a T_1^e time of greater than one second has been quoted [33]. Measurements at 3.7 K in Chapter 6 reveal that in amorphous sulphur the T_1^e time is 4.5 minutes, and the T_2^e time reaches 215 μs.

The widths of the three hyperfine lines enable some spin relaxation mechanisms to be ruled out at room temperature [89]. Hyperfine interactions with the ^{13}C nuclei in the carbon cage are very weak, limiting the N-cage transferred spin density to $\sim 3\%$ of an electronic spin. Therefore this cannot be the dominant relaxation mechanism. No nuclear quadrupole interaction has been measured because of the central site of the nitrogen atom. In very dilute samples, the concentration of N@C_{60} spins is too low for dipolar broadening to be significant. It has therefore been suggested that decoherence in these solutions is dominated by collision-induced deformations of the carbon cage leading to a fluctuating zero-field splitting [89, 77].

In the absence of molecular collisions, the high symmetry of N@C_{60} means that no zero-field splitting (ZFS) occurs. Collisions that deform the carbon cage break this symmetry, introducing ZFS terms into the spin Hamiltonian, as mentioned in Section 3.3. The ZFS tensor, $\mathbf{D}$, can be different for each molecule in the sample, particularly as the orientations can vary. This corresponds to different N@C_{60}

spins seeing different local magnetic fields, and hence precessing at different rates. A variation in the precession rates of different molecules can be refocused with a spin-echo experiment only if the variations are constant for the duration of the experiment. However, the timescale for molecular collisions in these low-viscosity solvents is a few picoseconds [77] while the spin-echo experiment takes hundreds of nanoseconds. It is therefore expected that molecular collisions could induce T_2^e and T_1^e relaxation in solutions of N@C_{60}.

The measurements described so far were made with very dilute samples of N@C_{60}, where dipole-dipole moments are negligible in solution. More recent CW ESR experiments on almost pure powder samples have found quite different results [93, 88]. In solution the linewidths of these samples were limited by magnet inhomogeneity as before. However, solid state ESR linewidths corresponded to interaction times of 6 ns for a highly concentrated sample. This is evidence of strong interactions between the spins of closely-packed N@C_{60} molecules, which could be useful for constructing two-qubit gates. Strong interactions between the qubits are not a source of decoherence because information is not lost to the environment.

Breaking the Symmetry of N@C_{60}

N@C_{70} and N@C_{60} have similar properties, but N@C_{70} has lower symmetry, taking the approximate shape of a rugby-ball rather than a football. This anisotropy may be useful for QC because the resulting quartet of energy levels now are permitted by symmetry to have different energy gaps. Aligning N@C_{60} within nanotubes will enforce the same uniaxial symmetry-breaking which may be convenient for quantum computing.

Pulsed ENDOR has been used to study N@C_{70} powders [94]. ENDOR spectroscopy uses a combination of microwaves and radio-waves to excite transitions between states with specific combinations of nuclear and electronic spin. The ENDOR linewidth of N@C_{70} was found to be broadened compared to N@C_{60} by the

anisotropy of the hfs. The anisotropic coupling constants for the hyperfine interaction and the nuclear quadrupole interaction were measured for the transitions within each of the four electronic spin states.

The anisotropy of C_{70} has also been investigated by aligning N@C_{70} inside a liquid crystal matrix [95]. Each of the three ESR lines were split into three, by lifting the approximate degeneracy in the transition energies.

When the liquid crystal experiment was repeated with N@C_{60}, each line again became three, but the splitting was smaller. This was attributed to a deformation of the fullerene's electronic shell, citing evidence from a synchrotron X-ray study that found this in a crystal of C_{60} [96]. The anisotropy of the C_{60} electronic shell would then need to be noticeable by the endohedral nitrogen atom. The nitrogen atom is in its atomic state, unbound, and centrally placed, implying that it is unaffected by changes to the fullerene. However, the electronic cloud is significantly compressed by the fullerene cage resulting in a 50% increase in the hfs constant [91]. Anisotropy in the cage is experienced by the N atom as a change in this compression. An alternative explaination for these experiments is that the liquid crystal supplied the anisotropic crystal field.

Anisotropy is also relevant in the formation of dimers from N@C_{60} and C_{60}, because the linking axis breaks the spherical symmetry of the cage[3]. Hence the ESR spectrum of N@C_{60}-C_{60} shows some broadening of the three-line hyperfine structure, attributed to fine structure [97]. Many approaches have been described for making $(C_{60})_2$ dimers, including high pressures with heating (1.5 GPa and 100-200°C) and photochemistry. Mechano-chemical synthesis is a more gentle method, so this was used with N@C_{60} to avoid decomposition. A mortar and pestle are used to grind up the dilute N@C_{60} in C_{60}, together with stainless steel grinding balls (5mm diameter) and an inorganic additive that catalyzes the reaction.

These dumb-bell shaped dimers contained just one N atom; new pulsed ESR experiments could be performed using dimers with spins in both cages: $(N@C_{60})_2$.

[3]This effect was initially investigated by adding simple functional groups to N@C_{60} [82].

The exchange and dipolar couplings may allow controlled entanglement of the two electron spins, with applications in simple quantum computing. Such a sample in solution may be suitable for two-qubit QC, by analogy with an NMR quantum computer. These possibilities are explored further toward the end of Chapter 5.

4.2 Nanotubes

Carbon nanotubes can be thought of as nanoscale wires. Their free electrons can form a 1D system of fermions which may display some features of a Luttinger liquid [98]. Further motivation for studying the many kinds of nanotubes has come from their potential technological usefulness. They are very strong cylinders that can reach micrometer lengths with diameters as small as 4 Å [99]. Each tube is either metallic or semiconducting so they might find applications as wires in nanoscale electronic circuits and devices. Nanotubes have also been used as molecular containers providing a new environment for growth of crystals and polymers [100].

The first nanotubes to be reported [13] were multi-walled, having between two and fifty concentric tubes. The structure of each tube consists of a rolled sheet of graphene. These have been seen to grow helically from the negative graphite electrode in arc discharge experiments. Different tubes have a different helical pitch that is called the chirality, as can be seen in Figure 4.6. The catalytic production of single-walled carbon nanotubes (SWNTs) was a significant step [101] because individual tubes with a specific diameter and chirality could then be studied. This allowed theoretical predictions regarding their electronic structure to be confirmed [102], and the dependence of a tube's band structure on the diameter and chirality is now well understood [103, 104]. Nanotube research is described in much more detail in the textbook by Saito *et al.* [105].

It has been predicted that applying a magnetic field changes the bandgap of all nanotubes, leading to a metal-insulator transition [106]. However, magnetic

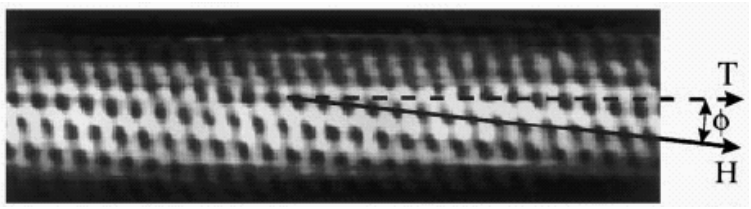


Figure 4.6: Atomically resolved scanning tunneling microscopy (STM) image of a single-walled carbon nanotube from reference [103]. T is the tube axis and ϕ is the chiral angle between T and H: The direction of nearest neighbour hexagon rows.

fields on the order of 10 GT would be needed to produce a 10% bandgap change. This dependence is approximately linear with the applied field, and ESR fields are never larger than $\sim$ 10 T so this effect can be neglected in ESR measurements.

ESR studies on single-walled nanotubes have brought contradicting results. The first paper measured the ESR of unoriented bundles of solid SWNTs in the temperature range 4-300 K [107]. A large signal was seen centred on $g \sim 2$ that arose from residual catalytic particles and this was subtracted in the analysis. The signal that was attributed to the tubes had an asymmetric Dysonian lineshape with a linewidth of about 2.6 mT (as shown in Figure 4.7). Conduction electrons in graphite show this lineshape, that goes up higher than it goes down, so that A > B in Figure 4.7. On this basis, it was concluded that at least some of the tubes are intrinsically metallic, rather than semiconducting with a small band gap.

The next paper on this subject found no ESR signal from SWNTs in bulk or in solution [108]. However, this was attributed to experimental problems: The bulk sample may have constituted too large a perturbation of the resonant cavity in the ESR spectrometer. The sample that was dissolved in hexane suffered from a large background signal due to residual ferromagnetic catalyst particles. The ESR results on SWNTs in this paper should therefore be viewed with some caution.

A third group published different results in 1999 on dissolved SWNTs [109]. They found no SWNT ESR signal until the catalytic metal particles had been removed by chemical purification. The purified sample had a weak ESR signal

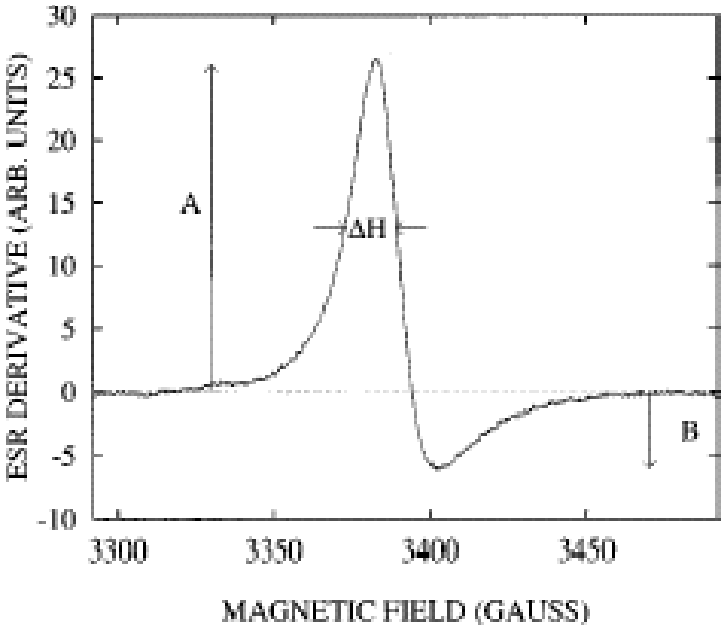


Figure 4.7: ESR spectrum of as-grown bulk (low density) SWNTs recorded at 100 K [107]. The asymmetric line has a classic Dysonian shape.

that was almost symmetrical. This was around $g = 2$ with a smaller linewidth of 0.20 mT. The purified tubes were then shortened which resulted in a stronger, more symmetrical ESR signal with the same g-value. Finally, soluble solutions of SWNTs were chemically prepared by adding organic amide functionalities to the ends. This sample gave a strong ESR signal with a linewidth of 0.21 mT at g=2.003 $\pm$ 0.001. This was identified as the signature of conduction electrons. It was suggested that the first results (Dysonian line with a width of $\sim$ 3 mT) were due to the vacuum annealing process at 1000-1500°C.

A separate study confirmed that unpurified SWNTs in solution are ESR-silent [110]. Another group reported the effects of various parameters on the ESR signal of nanotubes [111] without specifying if the tubes studied were single-walled.

4.2.1 Peapods

Pulsed laser vaporisation of graphite in the presence of certain catalysts produces both fullerenes and nanotubes. However, it was not until 1998 that the first observation of fullerenes inside nanotubes was reported [14]. High resolution

transmission electron microscopy (HRTEM) provided pictures of tubes filled with circles 0.7 nm across, spaced 0.3 nm from the tube walls. These measurements are consistent with the expectations for C_{60} in SWNTs. The electronic structure of these peapods has been studied with scanning tunneling microscopy [112]. Doping of peapods with potassium was found to polymerize the C_{60} molecules inside the nanotube [113]. This process changed the electronic structure from semiconducting to metallic.

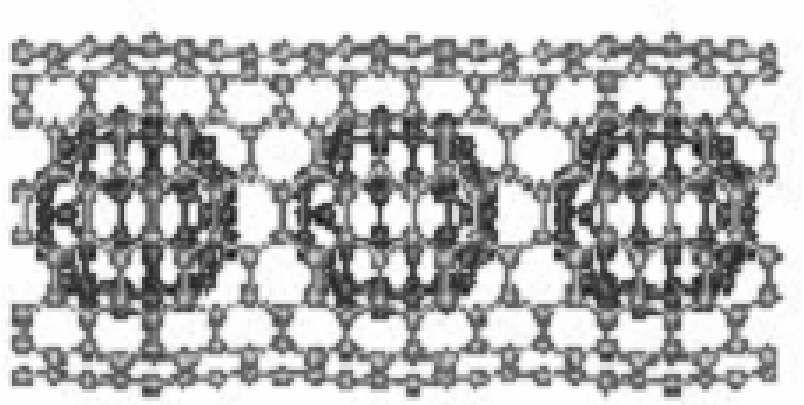


Figure 4.8: Structure of a segment of a C_{60}@SWNT peapod.

Some fairly crude chemistry was used to demonstrate that peapods really do contain C_{60} [114] and this study predicted that it was unlikely that the peas were formed already inside the pods. Molecular dynamics simulations [115] suggest that the most plausible formation process is for the C_{60} molecules to first stick to the tube walls along which they can move laterally until entering through a hole in the tube. The optimum temperature for this process was found to be around 400°C, which agrees well with experiments. Entry through the open ends was found to be much less common and unlikely to explain the high degree of filling seen in many tubes.

Pictures of individual peapods tend to show complete filling and experiments on larger samples have broadly supported this. Electron energy-loss spectroscopy (EELS) provided an estimate of 85% filling of those tubes that are large enough

to contain a C_{60} molecule [116]. These experiments also showed the electronic and optical properties of the encaged fullerenes to be very similar to those of free C_{60}, pointing to weak van der Waals interactions between the two species. A universal graphitic potential has been proposed describing the van der Waals forces between graphite, nanotubes and fullerenes [117]. This estimates the binding energy for a C_{60} molecule entering a tube as 2.7 eV. The molecular dynamics calculations mentioned above arrived at a value of 0.36 eV. Both of these numbers are very large compared to thermal fluctuations at room temperature ($k_B T_{293} \approx 0.025$ eV) in agreement with the very high thermal stability of peapods.

Endohedral fullerenes have also been inserted into nanotubes. These 'endohedral peapods' include Gd@C_{82}@SWNT [118]. Low temperature STM demonstrated a spatial modulation of the bandgap in these materials [119]. The tubes can be thought of as a one dimensional chain of quantum dots. A series of high resolution TEM images of Ce@C_{82}@SWNT, such as the one in Figure 4.9, shows the endohedral atoms moving and rotating.

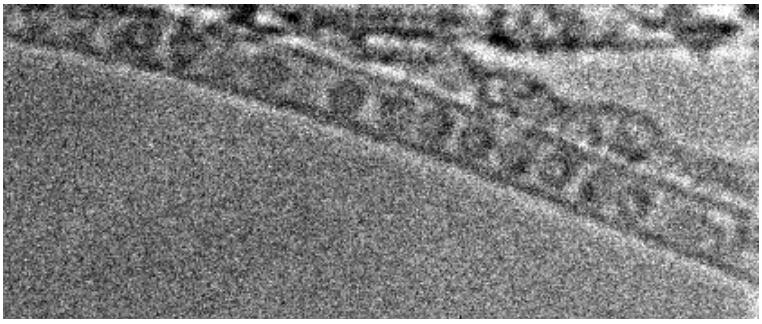


Figure 4.9: HRTEM image of Ce@C_{82}@SWNT: An endohedral peapod [120]. The cerium atoms can be seen as dots in the C_{60} molecules. This picture is courtesy of A. N. Khlobystov.

N@C_{60} has been inserted into SWNTs using n-hexane solvent at temperatures of just 69°C [121]. An alternative technique is described in Chapter 8 using supercritical fluids [122, 100]. The electronic interactions between the endohedral species and the SWNTs can be probed with ESR. Chapter 8 shows how this can depend strongly on the choice of endohedral molecule and their spacing in the nanotube.

Chapter 5

A Complete Scheme for Performing Two-Qubit QC with ^{15}N@C$_{60}$

Contents

5.1 Qubits 48

5.2 Initialization 51

5.2.1 CW DNP 52

5.2.2 Pulsed DNP 56

5.2.3 Flip-Flop Transitions 60

5.2.4 Summary of Initialization Techniques 61

5.3 Decoherence 62

5.4 Quantum Logic Gates 63

5.4.1 CNOT Gates 63

5.4.2 Wavefunction Swaps 64

5.4.3 Single-Qubit Gates 65

5.4.4 Implementing the Deutsch-Jozsa Algorithm 67

5.5 Readout 69

5.5.1 CW Readout 70

5.5.2 Pulsed Readout 70

5.6 Sources of Error 72

5.7 Scaling Up 74

5.7.1 Dimers: Potential Four-Qubit Systems 75
5.7.2 Fully Scalable QC 78

A detailed method is presented for using a pulsed ESR machine to perform two-qubit quantum computations with $^{15}N@C_{60}$. It is shown that the current state-of-the-art is adequate to realize this scheme [123]. In Chapter 6, key parts of this proposal are demonstrated experimentally.

Chapter 2 described the five DiVincenzo criteria [19] for making a full quantum computer. This chapter shows how these criteria can be met with two qubits and briefly assesses the possibilities for scaling up to more qubits. One route to scaling up this scheme will be described further in the chapter on peapods.

5.1 Qubits

A molecule of $^{15}N@C_{60}$ in a strong magnetic field has eight energy levels as shown in red in Figure 5.1. The electronic and nuclear spins precess (almost) independently about the strong field, so they are both good quantum numbers. In the current scheme, these quantum numbers are used to store quantum information, with the nuclear and electronic spins each representing one qubit. The state names given in Figure 5.1 identify the eigenstates corresponding to the four computational basis states, with $|01\rangle$ meaning that the electron is in state $|0\rangle$ and the nucleus is in state $|1\rangle$. States $|A\rangle$, $|B\rangle$, $|C\rangle$ and $|D\rangle$ are not used to store information. The physical system that embodies the quantum information is a single molecule of $^{15}N@C_{60}$. In practice, an ensemble of these molecules is used to get a measurable signal. Between 10^{11} and 10^{16} molecules are used to have a good signal to noise ratio. Each of these molecules can be thought of as a two-qubit computer. The average result from 10^{16} computers is useful as long as each computer is identical.

Each molecule of $^{15}N@C_{60}$ is identical, except that some will contain one or

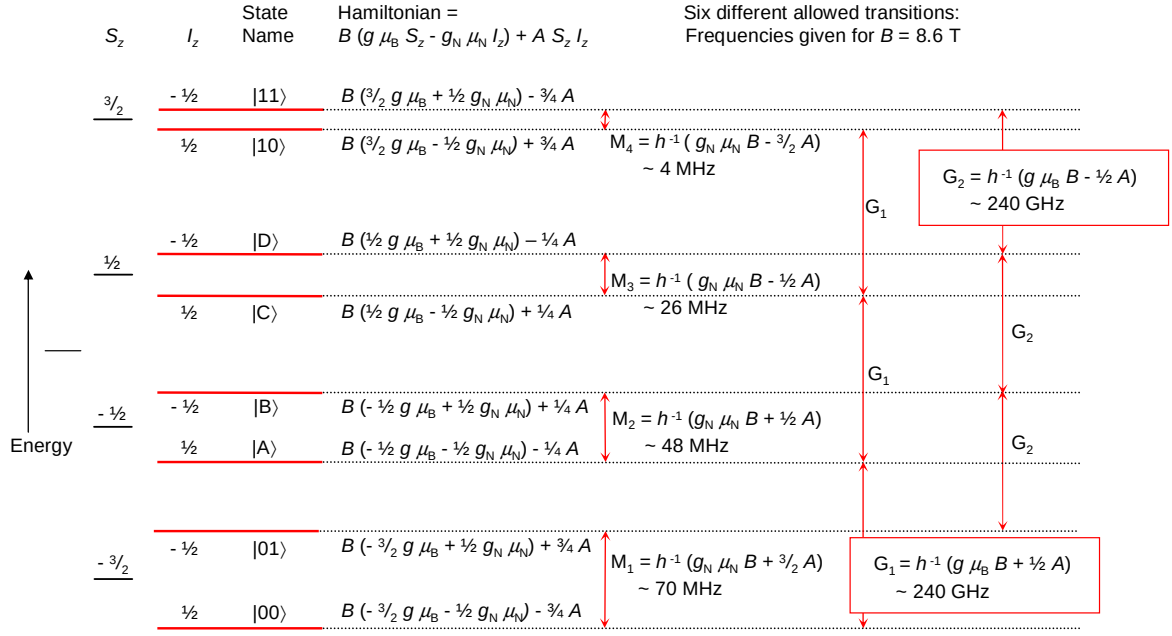


Figure 5.1: Energy levels of $^{15}N@C_{60}$ in a strong magnetic field from Equation 4.2. The nitrogen atom has electron spin $S = \frac{3}{2}$ and nuclear spin $I = \frac{1}{2}$. The hyperfine coupling of $^{15}N@C_{60}$ is $\frac{A}{h} = 22$ MHz. Transition frequencies are given for an applied magnetic field of 8.6 T. The splitting of the nuclear energy levels has been shown greatly exaggerated for clarity.

more ^{13}C molecules in the place of the more common ^{12}C. 1% of carbon atoms are ^{13}C, with a nuclear spin of $\frac{1}{2}$, so almost half of the C_{60} molecules will have one or more of these defects. This has a very small but measurable effect on the CW ESR spectrum of $N@C_{60}$. The hyperfine splitting due to one ^{13}C atom is about 1 μT which is less than the magnetic field inhomogeneity of a standard ESR magnet. The hyperfine splitting due to the ^{15}N nucleus is 787 μT. The quantum information will be manipulated in Section 5.4 with ESR pulses that will be chosen to be just selective enough to apply to a particular ^{15}N hyperfine line. Therefore these pulses will excite all transitions within their bandwidth of, say 800 μT. A cage containing one, two or three ^{13}C atoms, will produce an alteration in the resonant frequency of one, two or three times a few μT. This will produce an off-resonance error in the response of the electron spin to the applied ESR pulse. However, this error will be negligible because the bandwidth of the pulses used is

so much greater than the ^{13}C hyperfine splitting.

The nuclear spin $I = \frac{1}{2}$ has two quantum states in a magnetic field, so is conceptually straightforward to use as a qubit. The ^{15}N isotope is 100 times less common than the $I = 1$ ^{14}N nucleus which has three equally split levels in a magnetic field. In Figure 5.1, $I_z = \frac{1}{2}$ is identified with the computational basis state $|0\rangle$ and $I_z = -\frac{1}{2}$ is called $|1\rangle$. The electronic spin $S = \frac{3}{2}$ has four distinct energy levels which are used here as one qubit. A four-level quantum system can contain two qubits of information if it is possible to completely control the quantum state of the system. If the state cannot be controlled at all, then no information can be stored, and the system contains no qubits.

The resonant frequency of the ^{14}N nucleus in an NMR experiment is 7.23% that of a proton, while for ^{15}N this percentage is 10.14%.

The dipolar selection rules for the electronic spin are $\Delta S_z = \pm 1$ and $\Delta I_z = 0$. For moderate microwave powers, forbidden transitions are so weak that they can be ignored. For each value of I_z, there are three allowed transitions, which are effectively degenerate. They are split by the second-order hyperfine interaction which is just 0.07 μT for ^{15}N@C$_{60}$ at 8.6 T. This degeneracy makes it difficult to controllably move between levels as the transitions cannot be excited individually. The experimenter can only choose between exciting all of these transitions equally, or none. (Section 5.7 describes a three-qubit QC scheme that makes use of the second-order interaction with pseudo-pure states.)

Appendix A shows that it is possible to apply a pulse that controllably changes the sign of every electron spin, swapping the populations of levels $-\frac{3}{2}$ and $+\frac{3}{2}$, as well as swapping the populations of levels $-\frac{1}{2}$ and $+\frac{1}{2}$. The first of these pairs are more useful for QIP because the larger energy gap makes them easier to polarize. Polarization is the first step in a quantum computation, as described in the following section. It is quite acceptable to define some subsystem as a qubit and ignore the rest of the levels as long as these have no effect on the measured signal. This will be the case if the system is perfectly initialized and the manipulations

are perfectly accurate. The errors introduced by imperfect initialization and manipulations are considered throughout and specifically in Section 5.6. It will be shown that these errors can be made small enough to do reliable QIP.

The ability to scale up to many qubits was included in DiVincenzo's first criteria, but is difficult in this scheme, as in many others. This important topic will therefore be discussed in a separate section after the two-qubit scheme has been described.

5.2 Initialization

Initialization of the system begins by cooling the sample and applying a magnetic field. This polarizes the spin system shown in Figure 5.1. Equation 3.11 gives the relative equilibrium populations of adjacent electronic energy levels as

$$\alpha_{\text{electronic}} \equiv \frac{P[S_z = -\frac{1}{2}]}{P[S_z = -\frac{3}{2}]} = \mathrm{e}^{-\frac{g\mu_{\mathrm{B}}B}{k_{\mathrm{B}}T}}, \tag{5.1}$$

where $P[\psi]$ is the equilibrium population of a quantum state $|\psi\rangle$. With a temperature of $T = 3$ K and a magnetic field of $B = 8.6$ T (240 GHz radiation for $g = 2$), the Boltzmann factor, $\alpha_{\text{electronic}} = 0.02$. This means that 98% of the electron spins are in the $S_z = -\frac{3}{2}$ level. There are just 0.001% of the electron spins in the $S_z = \frac{3}{2}$ level. This polarization is high enough to assume that there are no electronic qubits in the $|1\rangle$ state. However, the polarization of the nuclei is much lower because the nuclear magnetic moment is about 1000 times smaller than that of the electron. The equivalent expression for the nuclei is

$$\alpha_{\text{nuclear}} \equiv \frac{P[I_z = \frac{1}{2}]}{P[I_z = -\frac{1}{2}]} = \mathrm{e}^{-\frac{g_{\mathrm{N}}\mu_{\mathrm{N}}B}{k_{\mathrm{B}}T}}. \tag{5.2}$$

Applying 8.6 T at 3 K produces a Boltzmann factor $\alpha_{\text{nuclear}} = 0.9995$. This means that only 50.01% of the nuclear spins are in the $I_z = \frac{1}{2}$ state.

To initialize the nuclear spins, dynamic nuclear polarization (DNP) is used

after the electrons have been polarized. This technique begins by transferring polarization from the electrons to the nuclei with resonant ESR and NMR radiation. The electrons are then left to relax back to their equilibrium polarization. The electronic T_1 is much shorter than the nuclear T_1 so the nuclei remain polarized while the electrons repolarize. CW or pulsed radiation can be used, producing slightly different results.

5.2.1 CW DNP

DNP with CW ESR consists of simultaneously applying microwave radiation with frequency G_2 and RF radiation with frequency M_4 (see Figure 5.1). The G_2 radiation changes the electron spin of those molecules with nuclear spin $I_z = -\frac{1}{2}$. The RF radiation changes the nuclear spin of those molecules with electron spin $S_z = \frac{3}{2}$. At equilibrium, the combined effect of these radiations is to equalize the populations of levels $|01\rangle$, $|\mathrm{B}\rangle$, $|\mathrm{D}\rangle$, $|10\rangle$ and $|11\rangle$. The time required to reach this equilibrium is a few times the length of the nuclear π pulse. A nuclear π pulse typically takes 20-200 μs, depending on instrumental factors such as the applied power.

The system now has more molecules in the state $|10\rangle$ than would be expected at thermal equilibrium. There will be a net decay of these molecules via allowed transitions to the state $|\mathrm{C}\rangle$ which has a lower energy. These processes are spin-lattice relaxations, where excitations in the lattice (such as phonons) remove the excess energy. Angular momentum is conserved by flipping some coupled spin in the environment. Alternatively, T_1^e relaxations can be accompanied by the spontaneous emission of a photon. As the population of state $|\mathrm{C}\rangle$ increases, a net T_1^e decay begins to state $|\mathrm{A}\rangle$ and then on to state $|00\rangle$. The overall rate of this three-step decay is the electronic T_1^e time that has been measured with pulsed ESR as described in Chapter 6. This T_1^e time is of the order of minutes at 3 K. It is necessary to perform DNP for several T_1^e before the nuclei are close to their maximum polarization. The time required is much shorter than the characteristic

time for the nuclei to depolarize: Experiments presented in the following chapter found this nuclear T_1 to be on the order of twelve hours.

The maximum polarization is determined by the thermal equilibrium of molecules with nuclear spin $I_z = \frac{1}{2}$. This depends on the Boltzmann factor between the $S_z = -\frac{3}{2}$ and $S_z = \frac{3}{2}$ levels, $\alpha^3_{\text{electronic}}$. The nuclear polarization of the $|00\rangle$ and $|01\rangle$ states can be defined as the ratio of their populations, $\frac{P[00]}{P[01]}$. CW DNP makes this ratio equal to the electronic polarization $\alpha^{-3}_{\text{electronic}}$.

To show this, the equilibrium populations of all of the levels in Figure 5.1 will be considered[1]. The microwave radiation at frequency G_2 equalizes the equilibrium populations of four levels:

$$P[01] = P[\text{B}] = P[\text{D}] = P[11], \tag{5.3}$$

and the RF radiation leads to the equation

$$P[11] = P[10], \tag{5.4}$$

so these five populations are equal. Next, the Boltzmann relation describes the relative populations of the levels with $I_z = \frac{1}{2}$:

$$P[10] = \alpha P[\text{C}] = \alpha^2 P[\text{A}] = \alpha^3 P[00], \tag{5.5}$$

where $\alpha_{\text{electronic}}$ has been abbreviated to α. Combining equations 5.3 - 5.5 gives all of the equilibrium populations in terms of the total number of molecules. In particular,

$$P[01] = P[11] = P[10] = \alpha^3 P[00]. \tag{5.6}$$

This shows that the nuclear polarization of the levels that will be used for QIP is the same as that of the original electronic polarization. Also, this electronic

[1]Again writing $P[\psi]$ as the equilibrium population of state $|\psi\rangle$

polarization is maintained.

This simple analysis neglects the spontaneous decay of nuclear spins because this process is known to be slow: The order of magnitude of the nuclear T_1 of this system has been measured as 12 hours at 4.2 K, as described in the following chapter. In fact, the next most important transitions to consider are the 'flip-flop' transitions which conserve angular momentum by changing nuclear spin by ± 1 and electronic spin by ∓ 1. The rate of these transitions has not been measured for $^{15}N@C_{60}$, but experiments in the following chapter show that this rate is considerably higher than the rate of other spontaneous nuclear spin flips. Differential equations could be set up to describe the level populations as a function of time, if the relevant decay rates were known. The net effect of flip-flop transitions in this scheme will always be to increase the nuclear polarization, so the transitions that are neglected in equation 5.6 will not reduce the nuclear polarization. This effect can be seen as an alternative polarization technique that would be useful if RF radiation was not available, as described on page 60.

If the nuclear transition M_4 is inaccessible for some reason, CW DNP could be achieved by applying RF radiation at frequency M_3 or M_2 instead. This would produce lower polarizations. The above analysis can be repeated by replacing Equation 5.4 with $P[C]=P[D]$ or $P[A]=P[B]$. The resultant polarization would be α^{-2} for M_3 and α^{-1} for M_2. In each case, the nuclear polarization is as big as the electronic polarization that was used to align the nuclei. CW DNP is demonstrated in the next chapter using M_2 radiation, and the nuclear polarization achieved is compared with this model.

Partial CW DNP could also be achieved by applying RF radiation with frequency M_1. In this case the microwave radiation should have frequency G_1. Almost all of the total population is then split equally between the five levels $|00\rangle$, $|01\rangle$, $|A\rangle$, $|C\rangle$ and $|10\rangle$. Four of these levels contribute to the $|00\rangle$ level after waiting for the electronic spin-lattice relaxation. This will produce a nuclear polarization of no more than $\frac{4}{5} = 80\%$ for small α.

The populations described in equation 5.6 are practically perfect for QIP. For $\alpha = 0.02$, $\alpha^3 = 8 \times 10^{-6}$ which is negligible in experimental realizations of this scheme. Further, the equality of the three computational levels that are supposed to be empty is highly advantageous. The density matrix of the subsystem in the computational basis is

$$\rho = \frac{N}{1+3\alpha^3} \begin{pmatrix} 1 & 0 & 0 & 0 \\ 0 & \alpha^3 & 0 & 0 \\ 0 & 0 & \alpha^3 & 0 \\ 0 & 0 & 0 & \alpha^3 \end{pmatrix}, \tag{5.7}$$

for an ensemble of N 2-qubit computers. The entry in the top left corner of the matrix corresponds to the population of the $|00\rangle$ state, which is much larger than the populations of the three other eigenstates: $|01\rangle$, $|10\rangle$ and $|11\rangle$. The density matrix can be rewritten as

$$\rho = \alpha^3 \frac{N}{1+3\alpha^3} \begin{pmatrix} 1 & 0 & 0 & 0 \\ 0 & 1 & 0 & 0 \\ 0 & 0 & 1 & 0 \\ 0 & 0 & 0 & 1 \end{pmatrix} + (1-\alpha^3) \frac{N}{1+3\alpha^3} \begin{pmatrix} 1 & 0 & 0 & 0 \\ 0 & 0 & 0 & 0 \\ 0 & 0 & 0 & 0 \\ 0 & 0 & 0 & 0 \end{pmatrix}. \tag{5.8}$$

The first matrix here is the identity, which is unaffected by any applied pulses, and is hence invisible to measurements. The second matrix is the zero-temperature state which is the perfect state with which to begin a quantum computation. The reduction in size of this term leads to a reduced experimental signal. However, this reduction depends on α^3, which can be made negligible with experimentally accessible Boltzmann factors.

The CW DNP technique prepares all of the molecules in the ground state except for a negligible number that are invisible to the measurement apparatus. This is possible because α can be made much smaller than 1. This state is analogous to the 'pseudo-pure' states used for liquid-state NMR QC [49, 7]. However,

Section 2.4.2 showed that the state used in NMR QC is much weaker, and the size of the zero-temperature (useful) term becomes exponentially smaller as the number of qubits increases.

This limitation does not apply to ensemble QC schemes in which these DNP techniques can be used. Any number of interacting $^{15}N@C_{60}$ molecules can be initialized to the state shown in Equation 5.8. The amplitude of the pure-state term does not depend on the number of qubits.

5.2.2 Pulsed DNP

Pulsed techniques can also be used for DNP, and the degree of nuclear polarization is similar to that in CW DNP. However, the computational states that are supposed to be empty do not have equal populations, producing a small 'error' signal as well as the main signal that is used for QC.

Pulsed DNP is analogous to the CW variety described already, with π pulses replacing the CW radiation:

1. A microwave π pulse with frequency G_2 flips the electron spin of molecules with $I_z = -\frac{1}{2}$.

2. An RF π pulse flips the nuclear spin of these molecules.

3. The electron spins (but not the nuclei) are allowed to thermalize.

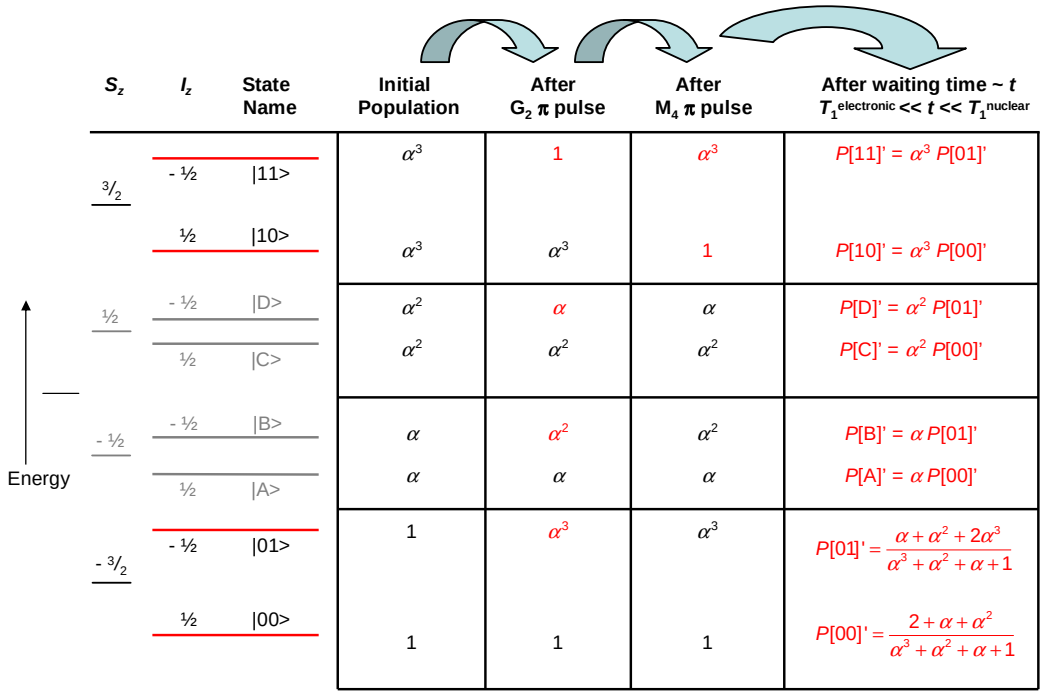
The largest polarizations are reached using M_4 for the nuclear pulse, and running this sequence several times. Radio frequencies M_3 and M_2 could be used also, but there is a double penalty for this: The electron polarization available is much smaller (as in CW DNP) and not all of the spins can be flipped from level $|01\rangle$ to $|B\rangle$ or $|D\rangle$.

For experimentally accessible combinations of temperature and magnetic field, the electronic Boltzmann factor $\alpha \approx 0.02$ and the initial nuclear polarization is very small: 50.01% of the nuclei are aligned with the field and 49.99% are anti-aligned. To calculate the polarizations introduced by pulsed DNP, these initial

populations can be taken to be equal, so that $P[00]$=$P[01]$. This assumes there is no initial nuclear polarization, which will tend to underestimate the success of the technique. Combining this assumption with Equation 5.5 (describing the populations of energy levels in $^{15}N@C_{60}$ at thermal equilibrium) gives

$$P[11] = P[10] = \alpha P[\mathrm{D}] = \alpha P[\mathrm{C}] = \alpha^2 P[\mathrm{B}] = \alpha^2 P[\mathrm{A}] = \alpha^3 P[01] = \alpha^3 P[00]. \quad (5.9)$$

Applying a π pulse with frequency G_2 swaps the populations of levels $|01\rangle$ and



S_z	I_z	State Name	Initial Population	After G_2 π pulse	After M_4 π pulse	After waiting time ~ t ($T_1^{electronic} \ll t \ll T_1^{nuclear}$)
3/2	-1/2	|11>	α^3	1	α^3	$P[11]' = \alpha^3 P[01]'$
	1/2	|10>	α^3	α^3	1	$P[10]' = \alpha^3 P[00]'$
1/2	-1/2	|D>	α^2	α	α	$P[D]' = \alpha^2 P[01]'$
	1/2	|C>	α^2	α^2	α^2	$P[C]' = \alpha^2 P[00]'$
-1/2	-1/2	|B>	α	α^2	α^2	$P[B]' = \alpha P[01]'$
	1/2	|A>	α	α	α	$P[A]' = \alpha P[00]'$
-3/2	-1/2	|01>	1	α^3	α^3	$P[01]' = \frac{\alpha + \alpha^2 + 2\alpha^3}{\alpha^3 + \alpha^2 + \alpha + 1}$
	1/2	|00>	1	1	1	$P[00]' = \frac{2 + \alpha + \alpha^2}{\alpha^3 + \alpha^2 + \alpha + 1}$

Figure 5.2: Three steps to pulsed DNP of $^{15}N@C_{60}$ in a strong magnetic field. Populations are shown in the table for each step, changing from left to right, with red text indicating the populations that just changed. This produces nuclear polarization of $\frac{P[00]'}{P[01]'} \sim \frac{2}{\alpha}$ for small α. Reapplying the same pulse sequence three more times produces nuclear polarization of $\sim \alpha^{-3}$.

$|11\rangle$, as shown in Figure 5.2. The effect of applying an RF π pulse at frequency M_4 is shown next, followed by the result of electron spin thermalization. The resulting populations are distinguished by a dash. Equation 5.5 remains valid for

these populations:

$$P[10]' = \alpha P[\mathrm{C}]' = \alpha^2 P[\mathrm{A}]' = \alpha^3 P[00]', \tag{5.10}$$

and the analogous expression applies to the molecules with $I_z = -\frac{1}{2}$:

$$P[11]' = \alpha P[\mathrm{D}]' = \alpha^2 P[\mathrm{B}]' = \alpha^3 P[01]'. \tag{5.11}$$

The nuclear polarization is the same for each of the four values of the electron spin:

$$\frac{P[00]'}{P[01]'} = \frac{P[\mathrm{A}]'}{P[\mathrm{B}]'} = \frac{P[\mathrm{C}]'}{P[\mathrm{D}]'} = \frac{P[10]'}{P[11]'}, \tag{5.12}$$

and takes the value

$$\frac{P[00]'}{P[01]'} = \frac{2+\alpha+\alpha^2}{\alpha+\alpha^2+2\alpha^3} \approx \frac{2+\alpha}{\alpha}, \tag{5.13}$$

where the final approximation is valid for small α. The error in this approximation is 0.05% for $\alpha = 0.02$. The same technique can then be applied again. The resulting populations are distinguished by two dashes. Equations 5.10 and 5.11 remain valid for any number of dashes, and so does Equation 5.12. The size of the polarization has now increased from Equation 5.13 to

$$\frac{P[00]''}{P[01]''} = \frac{(2+\alpha+\alpha^2)(1+\alpha+\alpha^2)+\alpha+\alpha^2+2\alpha^3}{(\alpha+\alpha^2+2\alpha^3)(\alpha+\alpha^2+\alpha^3)+\alpha^3(2+\alpha+\alpha^2)} \approx \frac{2+4\alpha}{\alpha^2}. \tag{5.14}$$

A third application of the DNP pulse sequence increases the polarization by another factor of α:

$$\frac{P[00]'''}{P[01]'''} \approx \frac{2+6\alpha}{3\alpha^3}. \tag{5.15}$$

Applying the same pulse sequence a fourth time increases the polarization by a

small amount:

$$\frac{P[00]''''}{P[01]''''} \approx \frac{1+\alpha}{\alpha^3}. \tag{5.16}$$

The last two approximate equations are accurate in the denominator to the leading order in α and terms in the numerator containing α to powers greater than one were dropped. To this level of accuracy, further applications of the pulse sequence do not increase the polarization. Exactly the same results can be achieved using pulsed DNP on different transitions. The first π pulse can be at frequency G_1, and then an RF π pulse should be applied at M_1. Equations 5.10 - 5.16 are all still valid, so this technique also reaches a polarization of $\sim \alpha^{-3}$ after four passes. Having multiple ways to polarize the system is useful if, for example, the power output of the RF coils in the apparatus depends strongly on frequency.

For small α, the result of four-step pulsed DNP is a nuclear polarization of α^{-3} for each electron spin level. This is slightly higher than the overall nuclear polarization due to CW DNP, where the two levels with $S_z = \frac{3}{2}$ have the same (negligible) population, as shown in Equation 5.6. In spite of this, CW DNP is more suitable for QIP because of the advantages arising from the equality of the populations of the computational basis states.

The error in the pulsed DNP state due to the non-equality of the populations of the $S_z = \frac{3}{2}$ level corresponds to a small spurious signal α^{-3} times smaller than the signal used for the computation. The relative size of the spurious signal should not grow as a result of performing the operations that make up the quantum algorithm. For $\alpha \approx 0.02$ the spurious signal is 100,000 times smaller than the computational signal, which is negligible for any two-qubit computation. This error could be significant for computers with more qubits or for larger values of α. A more significant error would be that due to the non-zero initial populations of levels $|A\rangle$, $|B\rangle$, $|C\rangle$ and $|D\rangle$. This error is present in CW and pulsed DNP, and is dealt with in Section 5.6.

5.2.3 Flip-Flop Transitions

It is also possible to polarize the nuclei in $^{15}N@C_{60}$ without using RF radiation. This technique is slower and produces lower polarizations, but is a significant effect that could be useful in spectrometers that do not have RF coils. After cooling the sample to polarize the electrons, radiation is applied at frequency G_2 to flip the electron spins of molecules that have anti-aligned nuclear spins. CW radiation or a π pulse would be suitable.

Consider first using a π pulse to flip the electron spin to $S_z = \frac{3}{2}$. After the pulse, spin-lattice relaxation events occur in which the electron spin reduces by one and the nuclear spin is unchanged. These are allowed dipolar transitions. The net directions in which these transitions occur moves the spin system toward thermal equilibrium. A few of these events will be due to the spontaneous emission of a photon. More commonly, the energy is lost to the lattice. Angular momentum must also be conserved, which generally results in some other spin flipping in the opposite direction to the electron. The ^{15}N nuclear spin that is hyperfine coupled to the flipping electron can act as this other spin. This 'flip-flop' transition[2] conserves angular momentum because a nuclear spin $\frac{1}{2}$ has the same angular momentum as a spin-half electron, even though they have very different magnetic moments.

Nuclear polarization occurs because of two asymmetries in the experiment. The more simple of these is that electron spins were flipped only if their nuclear spins were $I_z = -\frac{1}{2}$. The molecules left in state $|00\rangle$ do not make flip-flop transitions because they are in thermal equilibrium with the other $I_z = \frac{1}{2}$ states. The nuclear spin of the molecules that were excited by the G_2 π pulse are all aligned against the applied field, so any nuclear spin flips that they experience can only increase the nuclear polarization.

The second asymmetry is a property of the system: All flip-flop transitions

[2]Other authors define flip-flop transitions differently so that the second spin does not have to be the nucleus that is hyperfine coupled to the relaxing spin.

that reduce the energy in this system polarize the electron spin, and must therefore polarize the nuclear spin also. This can be traced back to the minus sign in the nuclear Zeeman term of the Hamiltonian. The three flip-flop transitions in this system end in states with $S_z = -\frac{3}{2}, -\frac{1}{2}$ and $\frac{1}{2}$. All of these go from states with $I_z = -\frac{1}{2} \rightarrow \frac{1}{2}$, polarizing the nuclei. This means that a π pulse with frequency G_1 would not generate any anti-polarization as the electron spins relaxed back to equilibrium.

In order to reach the maximum polarization, further G_2 π pulses should be applied after waiting a time on the order of the electronic T_1. The number of useful repetitions would increase with the fraction of T_1^e processes that are not polarizing. The flip-flop method of polarization will always be slower than the techniques employing RF radiation because only a fraction of the T_1^e transitions are flip-flops. In the previous schemes, all of the T_1^e transitions were useful. The fraction of the T_1^e transitions that are polarizing is equal to the ratio of these polarization speeds.

Flip-flop transitions can create nuclear polarization with CW radiation also. CW radiation at G_2 equalizes the four levels with $I_z = -\frac{1}{2}$, while the total population of these levels remains at $\frac{N}{2}$ for a sample of N molecules. Three of the four levels can experience polarizing flip-flop transitions, and as soon as any molecule does this, it will remain in the $I_z = \frac{1}{2}$ state. The rate of these flip-flop transitions will determine the rate at which the system polarizes. Experimental confirmations of flip-flop polarization (with G_2) and the lack of flip-flop anti-polarization (with G_1) are presented in the following chapter using CW radiation.

5.2.4 Summary of Initialization Techniques

The ideas that have been presented for polarizing nuclear spins are applicable to many other systems, including some which may be useful for QIP such as $^{15}N@C_{70}$, $^{14}N@C_{60,70}$ $Sc@C_{82}$ and $P@C_{60,70}$. The nuclear spin does not have to be $I = \frac{1}{2}$. These techniques would all work equally well with scaled up systems in

which large numbers of these molecules are interacting.

One limitation of this approach for scaled-up systems is the long time required to prepare the qubits in their ground state. To operate indefinitely, any scheme for large-scale QIP needs to fix the minor errors that inevitably creep into the computation during the calculation. There are various suggestions for quantum error correction codes to achieve this [18]. All of these ideas make use of a supply of 'cold' qubits in a given initial state. The DNP techniques for nuclear cooling presented here needs several electronic T_1 times to prepare cold qubits, which is less useful for QEC than a cooling technique that operates orders of magnitude faster.

5.3 Decoherence

Table 5.1 gives measurements of the electronic T_1 and T_2 times and the nuclear T_1 time of $N@C_{60}$. These experiments were made at the low temperatures where DNP can be used, as described in the following chapter. Nuclear spins have longer relaxation times because their smaller magnetic moments couple more weakly to the environment. The nuclear T_2 time is relevant for scaled-up schemes in which an array of nuclear spins are used to store quantum information that is processed in the corresponding electron spins, as described in Section 5.7.2. The nuclear T_2 has not been measured yet, but as it is much longer than the electronic T_2 it does not affect the operation of the two-qubit scheme described here.

Relaxation time	Value	Isotope	Solvent	Temperature (K)
Electronic T_1	4.5 minutes	^{14}N	amorphous sulphur	3.7
Electronic T_2	215 μs	^{14}N	amorphous sulphur	3.7
Nuclear T_1	$\sim$ 12 hours	^{15}N	deuterated toluene	4.2

Table 5.1: Relaxation times of $N@C_{60}$ at low temperatures. These measurements are described in Chapter 6.

The electronic T_2 of 215 μs is one of the longest electron dephasing times measured for any system[3]. It is as long as 10 nuclear π pulses, which are the slowest logic gates in this scheme for two-qubit QC. The following section will show that the Deutsch-Jozsa algorithm can be implemented in about 100 μs.

It is common in the spin-based QC literature to suppose that T_2 approaches T_1 when the unwanted nearby spins that are responsible for dephasing are removed. Preparing such spin-free environments is experimentally challenging but feasible[3]. With an electronic T_2 of the order of a minute, 3×10^6 nuclear operations could be performed, or 10^9 electronic operations. Both of these numbers are significantly higher than the 10^4 operations required for unlimited QEC [18].

5.4 Quantum Logic Gates

To be able to perform any quantum logic gate, it is sufficient to be able to perform all single qubit operations, as well as the 2-qubit CNOT gate [32]. This is the universal set of quantum logic gates that are used in this QC scheme.

5.4.1 CNOT Gates

CNOT is a conditional NOT gate in which one qubit (the target) is flipped if and only if some other qubit (the control) is in a particular state. The CNOT gate can entangle the two qubits and is actually the simplest gate to perform in this scheme. Two different CNOTs are possible because either the electron spin or the nuclear spin can act as the control qubit. The logic table is shown in Table 5.2 for the latter case: The electron spin is flipped if and only if the nuclear qubit is in the $|1\rangle$ state. The energy level diagram (Figure 5.1) shows that this gate is implemented by applying a π pulse at frequency G_2. This takes only 50 ns, so more than 4000 could be performed before the decoherence time was reached.

[3]Phosphorus atoms in isotopically ultra-pure silicon have the longest T_2^e times, measured as 14 ms at 7 K [124]

It will also be necessary to perform CNOT gates in which the nucleus acts as the target. A π pulse at frequency M_4 will flip the nuclear spin if and only if the electron qubit is in state $|1\rangle$. This nuclear pulse is much slower: On the order of 20 μs. Already it is clear that the time required to perform an algorithm in this scheme is dominated by the number of nuclear pulses. In realising this scheme, it may be convenient to define the CNOT gate differently, so that the target bit is flipped if and only if the control bit is in state $|0\rangle$.

Initial State		Final State	
Nuclear Qubit	Electron Qubit	Nuclear Qubit	Electron Qubit
$\|1\rangle$	$\|1\rangle$	$\|1\rangle$	$\|0\rangle$
$\|1\rangle$	$\|0\rangle$	$\|1\rangle$	$\|1\rangle$
$\|0\rangle$	$\|1\rangle$	$\|0\rangle$	$\|1\rangle$
$\|0\rangle$	$\|0\rangle$	$\|0\rangle$	$\|0\rangle$

Table 5.2: Logic table for a CNOT in which the electron spin is the target qubit: It is flipped if and only if the nuclear spin is in the $|1\rangle$ state.

5.4.2 Wavefunction Swaps

Combining the two different kinds of CNOT gates mentioned above makes it possible to swap the wavefunctions of the two qubits. This was done in the first three columns of the table in Figure 5.2, where the nuclear spins were polarized by swapping their wavefunction with that of the electrons. This was a particularly simple case because the nuclei started in a completely mixed state: Specifically the equality of $P[11]$ and $P[10]$ means that the wavefunction swap required only two CNOT gates. The first of these used the nuclei as the control and the second used the electrons.

Combining three CNOT gates can swap the wavefunctions of any general two qubit state [32]. The simplest way to show this is to consider the four levels in Figure 5.3. A SWAP gate should leave the population of the $|11\rangle$ and $|00\rangle$ states unchanged, and exchange the populations of the other two states, shown in blue

ovals. The three CNOT gates used to do this would be realised here with the pulse sequence G_2^π - M_4^π - G_2^π. The same result can be obtained by doing the RF pulse first, producing M_4^π - G_2^π - M_4^π. However, this sequence takes twice as long because it contains two nuclear pulses. Another sequence that is just as good as that in Figure 5.3 is G_1^π - M_1^π - G_1^π. Its slower cousin is M_1^π - G_1^π - M_1^π.

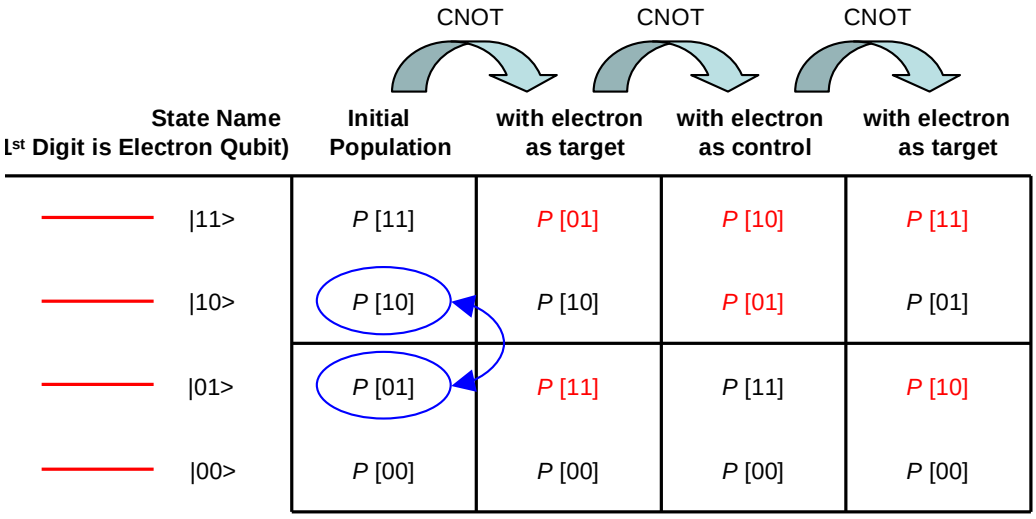


Figure 5.3: Three CNOT gates can always be used to swap the wavefunctions of a two-qubit system. This SWAP gate must leave the populations of the $|00\rangle$ and $|11\rangle$ states unchanged, while exchanging the populations of the other two states (identified with blue ovals). There are four routes to this, one of which is shown here.

The operations described in Figure 5.3 will now be referred to as the SWAP gate in this scheme. This takes as long as a single nuclear π pulse, and is necessary to perform general single-qubit operations to the electron spin.

5.4.3 Single-Qubit Gates complete the Universal Set of Logic Gates

It is possible to rotate each qubit from any point on the Bloch sphere to any other point.

The nuclear spin is naturally a qubit so RF pulses can be applied to perform single qubit operations on the nucleus. The resonant frequency must be used,

regardless of the state of the electron, so for a general nuclear state it is necessary to apply both M_1 and M_4 pulses. These should be applied simultaneously to save time, if the spectrometer has two RF channels, or sequentially otherwise. The two pulses rotate the qubit about the y-axis by an angle that is proportional to the power and the duration of the pulse. To rotate around different axes in the x-y plane, the radiation phase should be changed. A pulse with a $\frac{\pi}{2}$ phase change rotates the qubit about the x-axis. Adjusting the pulse length and phase is sufficient to apply any single qubit operation.

Levels $|A\rangle$, $|B\rangle$, $|C\rangle$ and $|D\rangle$ in Figure 5.1 are inconvenient for the purposes of performing single qubit operations to the electronic qubit. In order to change the electronic spin of the level $|00\rangle$, a pulse with frequency G_1 should be applied. However, such a pulse will move spins from $|00\rangle$ to $|A\rangle$ to $|C\rangle$ to $|10\rangle$, because of the degeneracy of these transitions. Appendix A shows that π pulses can be performed to this $\mathbf{S} = \frac{3}{2}$ system. If a rotation by some other angle is required then the SWAP gate must be used to exchange the nuclear and electronic qubits. The single qubit gate can then be applied to the nuclear spin before un-SWAP-ing the wavefunctions.

To implement a quantum logic gate, it is not sufficient to manipulate populations alone: The phases must also be manipulated correctly. In other words, the off-diagonal elements of the density matrix must be considered as well as the diagonal elements. Demonstrated quantum computing schemes commonly use resonant radiation to perform single-qubit manipulations to a spin-qubit [7]. This technique manipulates the off-diagonal elements in the correct way. Appendix A demonstrates that π pulses can be performed on the $S = \frac{3}{2}$ electron system in such a way that the phase is manipulated correctly. The CNOT gates described above must also manipulate the off-diagonal elements as required. To implement these logic gates, four separate radiation frequencies are required. Each of these four radiations must be coherent for the duration of the manipulations. The same requirements were met for NMR QC with seven qubits, each of which was ma-

nipulated with its resonant frequency [7]. In the present scheme, the frequency of the radiation manipulating the electrons is up to four orders of magnitude different to the nuclear radiation. The NMR QC experiment made use of frequencies around 125 MHz and 470 MHz. There is no clear reason why problems should be encountered by operating with more widely spaced frequencies.

It is clear from this description of the universal set of logic gates, that some are much easier than others. In practice, quantum algorithms can always be adapted to avoid those gates that are slow. In this case, nuclear pulses are three orders of magnitude slower than electron pulses, CNOT gates are twice as fast as single qubit flips, and single qubit rotations of the electron would be restricted to π pulses wherever possible.

5.4.4 Implementing the Deutsch-Jozsa Algorithm

The DJ algorithm was described in Section 2.4.3 as a convenient demonstration that an experimental system is suitable for QIP. Figure 2.2 shows that the first step is to perform a $\frac{\pi}{2}$ gate to the electron spins and a $-\frac{\pi}{2}$ gate to the nuclear qubit.

A general single-qubit rotation such as the $\frac{\pi}{2}$ gate consists of a selective pulse for each of the possible values of the other qubit. For example, two pulses at frequencies M_1 and M_4 rotate the nuclear spin qubit regardless of the state of the electronic qubit. However, after qubit initialization, the electron spin is known to be in the state $|0\rangle$. In this case, the nuclear spin can be rotated with just one pulse at frequency M_1. 90° pulses cannot be performed directly on the electronic qubit, so the required state must be prepared on the nucleus and SWAP-ed. The two-pulse SWAP gate can be used to prepare the electron qubit because the populations of levels $|10\rangle$ and $|11\rangle$ are the same and/or negligible after initialization.

The pulse sequence to apply a $\frac{\pi}{2}$ gate to the electron qubit and then a $-\frac{\pi}{2}$ gate

to the nuclear qubit is:

$$\underbrace{\underbrace{\mathrm{M}_1^{90}}_{\frac{\pi}{2}\text{ to }|N\rangle} - \underbrace{\mathrm{G}_2^{180} - \mathrm{M}_4^{180}}_{\text{SWAP}}}_{\frac{\pi}{2}\text{ to }|E\rangle} - \underbrace{\mathrm{M}_1^{-90} - \mathrm{M}_4^{-90}}_{-\frac{\pi}{2}\text{ to }|N\rangle}, \tag{5.17}$$

where M_1^{θ} is a pulse that produces a θ degree rotation about the y-axis for spins whose resonant frequency is M_1.

Implementing the function $\mathbf{U}_f$ requires up to two further pulses. There are four different gates that make up $\mathbf{U}_f$ corresponding to the four possible functions $f(x)$. These are shown in Table 5.3.

Classical Function	QC Function	Operation Required	Pulse(s)	Time Required (μs)
$f_{00}(x)$	$\mathbf{U}_{00}$	do nothing	none	0
$f_{01}(x)$	$\mathbf{U}_{01}$	CNOT: Flip nucleus if and only if electron is in state $\|1\rangle$	M_4^{180}	20
$f_{10}(x)$	$\mathbf{U}_{10}$	CNOT: Flip nucleus if and only if electron is in state $\|0\rangle$	M_1^{180}	20
$f_{11}(x)$	$\mathbf{U}_{11}$	180° pulse to nuclei	M_4^{180} and M_1^{180}	40 or 20

Table 5.3: QC implementations of the four different functions in the Deutsch problem. U_{11} can be implemented in 20 μs if the spectrometer can apply two nuclear pulses simultaneously, or 40 μs otherwise.

After any of the $\mathbf{U}_f$ operations, the nuclear qubit will be in the state $\frac{|0\rangle-|1\rangle}{\sqrt{2}}$. It is sometimes suggested in the literature that a further gate should then be applied to the nuclear qubit to return it to the state $|0\rangle$. This makes the algorithm more symmetrical, but adds nothing to the solution of the problem. It is more sensible to leave this step out as it increases the time required for the algorithm.

The next operation would therefore be to perform a $\frac{\pi}{2}$ gate to the electronic

qubit. This consists of a 90° rotation of the electronic spin which could be implemented by SWAP-ing to the nuclear qubit and performing the nuclear $\frac{\pi}{2}$ gate before SWAP-ing back. However, this last electronic $\frac{\pi}{2}$ gate can be left out, as it cancels the $\frac{\pi}{2}$ readout pulse that would follow. Section 5.5.2 describes the measurement of the electronic spin by recording the FID after a $\frac{\pi}{2}$ readout pulse. Leaving out the final $\frac{\pi}{2}$ gate in the DJ algorithm and the readout pulse means that the electronic spin finishes in the state $\frac{|0\rangle+|1\rangle}{\sqrt{2}}$ if $f(0) = f(1)$ and $\frac{|0\rangle-|1\rangle}{\sqrt{2}}$ otherwise. The first case will produce a positive FID qualitatively the same as would be recorded after applying a $\frac{\pi}{2}$ pulse to the polarized sample in an FID measurement. For $f(0) \neq f(1)$, a negative FID would be recorded such as would be measured if a $-\frac{\pi}{2}$ pulse were applied to the polarized sample.

The result $f(0) \neq f(1)$ means that the function $f(x)$ was balanced, and $f(0) = f(1)$ means that the function was constant.

A 180° nuclear pulse takes about 20 μs and all electron pulse times are negligible in comparison. So the time required to perform this algorithm is up to $10+20+10+10+20+20 = 90$ μs for a spectrometer without the ability to apply two RF pulses simultaneously. This is the time to apply the longest of the four U_f functions. The T_2^e time is 215 μs so a lot of the phase information will survive to the measurement.

5.5 Readout

As with initialization, qubit readout can be performed with pulsed or CW ESR. However, in this case a pulsed measurement is clearly superior because it measures both qubits simultaneously. CW ESR can measure only the nuclear qubit, but this is enough for most algorithms. If it were necessary to measure both qubits with CW ESR then the computation could be run a second time, swapping the electron state to the nuclear spin before measuring it.

5.5.1 CW Readout

A CW ESR scan of $^{15}N@C_{60}$ is shown in Figure 5.4. The two resonances correspond to the two states of the spin-half nucleus. When the nuclear magnetic moment adds to the applied field, the resonance condition for the electrons is met with a lower external field. So this scan provides a classical measurement of the ensemble of nuclear qubits. An equal superposition would look the same as a completely mixed state. After perfect nuclear polarization, only the $I_z = \frac{1}{2}$ state remains, so only the low-field resonance is expected. This experiment is presented in the following chapter.

A classical measurement of the nuclear spin should be performed in a time that is much shorter than the nuclear T_1. As Table 5.1 shows, this time is about half a day at the relevant temperature of 4.2 K. The CW ESR scan takes on the order of a minute, so errors due to nuclear flips during the scan time are negligible.

It is not possible to measure both qubits with this technique after a single computation, because the electron spin is changed in an unknown way by the CW scan that is used to measure the nuclear spin. If it were necessary to measure the electronic as well as the nuclear qubit, the experiment could be run again. This would double the time required for the computation which is never seen as a problem by QC theorists. There are many constant factors (like this factor of two) that determine the time required to run an algorithm. However, these factors can be much smaller than the exponential gains possible with QC.

5.5.2 Pulsed Readout

The maximum amount of information that can be obtained by measuring qubits is the classical values of the qubits. The nuclear and electronic qubits in this scheme can both be measured simultaneously by applying a hard 90° microwave pulse and recording the FID. This pulse must be hard enough to excite both transitions G_1 and G_2 which requires a higher microwave power than the selective pulses used so far. The FID, as usual, is an exponential decay modulated by one or more

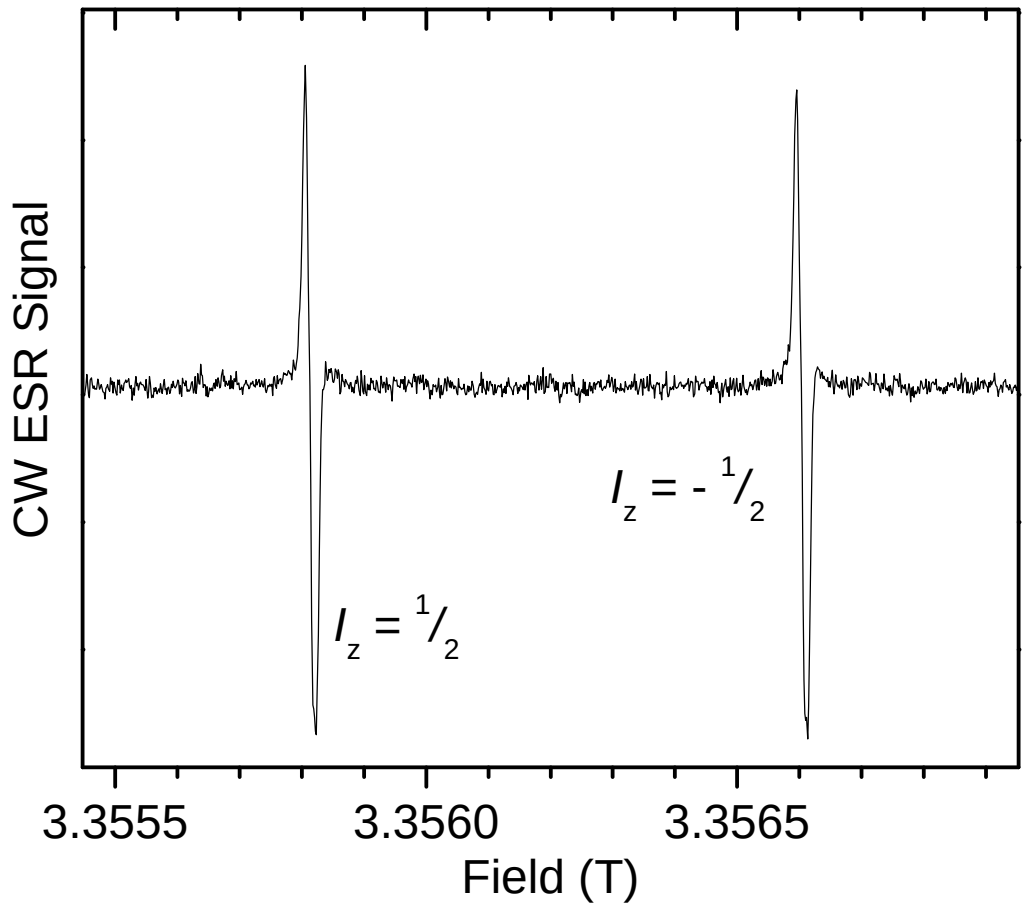


Figure 5.4: CW ESR scan of $^{15}N@C_{60}$ at W-Band. The frequency was 94.0427 GHz. The sample was dissolved in deuterated toluene solution at 260 K.

sinusoidal oscillations.

If the electronic qubit is in the $|0\rangle$ state, the signal is initially positive and then decays toward zero. This is a standard FID measurement. However, if the electron is in the $|1\rangle$ state, the signal is initially negative and decaying toward zero. This difference is the easiest conclusion that can be drawn from the data. The value of the nuclear spin lies in the same data: This is revealed by subtracting the exponential decay to leave the sinusoidal oscillations. Fourier transforming these oscillations produces a graph of the strength of each frequency that is present. This measurement is analogous to the CW scan used above. There are two possible resonances due to the two nuclear states of $^{15}N@C_{60}$. The higher frequency is due to molecules in which the nuclear magnetic moment is aligned with the applied

field, making the electron spin precess faster about this larger effective field. Hence this higher frequency signal corresponds to a measurement of the nucleus in the state $|0\rangle$. Molecules in the $|1\rangle$ state provide a resonance at lower frequency. The difference between the two frequencies is G_1 - $G_2 = A$, the hyperfine coupling.

Such a measurement must be made with a single pulse. Averaging is generally used to improve the signal-to-noise ratio in an ESR measurement, but it is only the first shot that contains the measurement of the quantum computation. Therefore, to improve the size of the signal, it would be necessary to average over the measurement of many such computational runs. Unfortunately, the qubit initialization time is the rate-limiting step here: The computation can only be run once every 30 minutes or so. Fortunately, the single-shot signal-to-noise can be good at low temperature with purified samples of $^{15}N@C_{60}$.

Pulsed ESR readout is demonstrated in the following chapter with W-band radiation. The sample used is $^{14}N@C_{60}$, which has three resonances that are spread over a larger frequency range than the two $^{15}N@C_{60}$ lines. The spectrometer provided pulses that were broadband enough to excite the three transitions of the ^{14}N so the resonances of ^{15}N will be more strongly excited.

5.6 Sources of Error

Section 5.2 showed how to make $P[01]$, $P[10]$ and $P[11]$ negligibly small compared to $P[00]$. Equation 5.8 and Figure 5.2 illustrate this for CW and pulsed DNP respectively. However, both techniques leave population in the 'unwanted' levels $|A\rangle$, $|B\rangle$, $|C\rangle$ and $|D\rangle$. In both cases $P[A] = \alpha P[00]$, providing an error signal only 5 times smaller than the QC signal at W-band (3.4 T). This error signal is straightforward to subtract from the final readout signal because the populations of states $|A\rangle$, $|B\rangle$, $|C\rangle$ and $|D\rangle$ are almost unaffected by the QC manipulations applied.

The RF pulses used are not resonant with transitions M_2 or M_3, so the un-

wanted signal in the nuclear qubit is unchanged by the computation. Before doing the QC, this unwanted signal can be measured by initializing the system and applying a M_1^{180} pulse. A measurement of this nuclear state will consist of a large signal corresponding to $I_z = -\frac{1}{2}$ and a smaller (unwanted) signal at $I_z = \frac{1}{2}$. Then the system should be reinitialized and the computation can be run, with the measurement of the unwanted signal subtracted from the result of the QC.

If it were necessary to measure the electronic qubit at the same time, pulsed readout should be used. In this case, an unwanted signal due to state $|\mathrm{A}\rangle$ appears again. Erroneous molecules in this $S_z = -\frac{1}{2}$ state look like a weaker version of $S_z = -\frac{3}{2}$, which would otherwise be interpreted as a measurement of the electronic qubit as $|0\rangle$. The only QC manipulation that affects this state is G_1^{180} pulses. The number of these pulses used in the algorithm should be counted up, and an even number will leave the unwanted signal unchanged. An odd number of these pulses will flip the unwanted population to level $|C\rangle$, where it will be responsible for an error signal of the same size and the opposite sign. To measure the initial unwanted signal, two initializations are needed. After the first, the electronic qubit should be measured with a hard pulse. Then, after reinitializing the system, the following pulse sequence should be applied: M_1^{180} - G_2^{180} - measure. The difference between the FID signals in these two cases is due to the unwanted signal from the $|\mathrm{A}\rangle$ state. This difference should then be subtracted from the result of the QC, or added if an odd number of G_1^{180} pulses were applied during the manipulations.

For CW and pulsed DNP, $P[\mathrm{A}] > P[\mathrm{C}] > P[\mathrm{B}] > P[\mathrm{D}]$, with the last two being at least as small as $P[01]$, which is negligible. If necessary, the errors due to any or all of these other unwanted levels could be subtracted with an analogous procedure to that described above for state $|\mathrm{A}\rangle$.

Errors in the rotation angle and the rotation axis due to a commercial pulsed ESR machine were measured by Morton *et al.* [125]. These errors were found to be significant, but systematic, so composite pulses [126] could be used whose improved accuracy was similar to those used to successfully demonstrate NMR

QC [127].

5.7 Scaling up to Many Qubits

It may be possible to use $^{15}N@C_{60}$ for three-qubit QC. The triple degeneracy of the electronic transitions is split by the second-order hyperfine interaction which depends on the hyperfine constant, A and the applied field, B as $\frac{A^2}{B}$. For $^{14}N@C_{60}$ at X-band, the splitting is 1.0 μT [128, 129]. $^{15}N@C_{60}$ has a larger A so the second-order hfs constant should be 1.9 μT at X-band. These transitions could be excited selectively with a 19 μs pulse which is significantly shorter than the longest T_2^e times. The populations of the four electronic levels can be controlled in this way, making a two-qubit system. The ^{15}N nucleus is a further qubit that can be manipulated with RF pulses of 20 μs duration. The first order hyperfine interaction couples the electronic and nuclear spins, producing a three-qubit system. Unfortunately it is difficult to initialize this system with an X-band magnetic field of just 0.33 T. To reach a pure state it would be necessary to cool to around 300 mK using a pumped ^3He refrigerator, and then use DNP. An alternative would be to work with pseudo-pure states at 170 K where the T_2^e reaches 240 μs [93].

To perform computations with four qubits or more will require a larger physical system than $N@C_{60}$. Arrays of these molecules could be made in one, two or three dimensions. Higher dimensional arrays would be more powerful computers, but are more difficult to construct. Qubits in higher dimensional arrays can communicate directly with more than two neighbors, which speeds up algorithms. Defects in a 1D array are a more serious problem than in higher dimensional systems. 1D arrays of $^{14}N@C_{60}$ and $Sc@C_{82}$ have been formed by filling a carbon nanotube, and will be described in more detail in Chapter 8. Pushing fullerenes around on surfaces with the tip of an STM is another way to make a 1D chain.

Fullerene chemistry can be used to form larger molecules, but no standard techniques have been demonstrated yet for high-yield synthesis of long chains of

specific fullerenes. Reactions at temperatures above 220°C cannot be used with $N@C_{60}$, as the nitrogen atom escapes from its cage at these temperatures [85]. It might be possible to attach $N@C_{60}$ to DNA fragments. These fragments can be made to join up in with each other in a variety of controllable geometries, leading to 2D arrays [130] and 3D structures [131].

5.7.1 Dimers: Potential Four-Qubit Systems

Chemically bonding two fullerenes creates a dimer, and this is the simplest way to begin to scale up the $N@C_{60}$ system. To do QC with dimers, the two ends should be separately addressable by their resonance frequencies. Five such end-molecules are $^{15}N@C_{60}$, $^{15}N@C_{70}$, $^{14}N@C_{60}$, $^{14}N@C_{70}$ and $Sc@C_{82}$[4]. These all have sharp resonances which do not overlap in a CW ESR scan. An asymmetric dimer (such as $^{15}N@C_{60}$-$^{14}N@C_{60}$) would be most suitable for QIP. Single qubit operations simply consist of pulses that affect just one of the ends.

Some synthesis techniques [97] have a higher yield when making dimers with identical ends, such as $(N@C_{60})_2$. This molecule would also be useful for QC, because it is still possible to address the ends individually. Within an ensemble of these molecules, a significant number will be made up of ends having two different nuclear spins. For $(^{15}N@C_{60})_2$, half of the dimers will contain one nuclear spin $+\frac{1}{2}$ and one nuclear spin $-\frac{1}{2}$. This subset of molecules can be used for QC, as long as the nuclear spin does not change. This condition means that the nuclear spin cannot be used for information storage in this scheme. The nuclear T_1 time is of the order of hours at 4.2 K, so the number of spontaneous flips is negligible.

The same approach could be used with the dimer $(^{14}N@C_{60})_2$. In this case, the molecules in which nuclear spin $I_z = 1$ and 0 are present could be used for the computation. Dimers containing $I_z = -1$ and 0 could just as well be used. Perhaps the third and final possibility is the best though: Those with I_z= -1

[4]Dimerization would probably destroy $P@C_{60}$ [85] and the T_2^e time has not been measured as being higher than 14 μs [33]. The chapter on $Sc@C_{82}$ describes a measurement of $T_2 = 13$ μs at 20 K.

and +1 are further separated in frequency, so the selective pulses could be made shorter. For each of these pairings, only $\frac{2}{9}$ of the total will meet the criteria, so the useful signal will be less than half as strong as for the symmetric ^{15}N dimer.

Aligning these dimers would be useful for QC. This could be achieved by growing a single crystal or possibly with a zeolite template. The system would be operated at low temperatures in a strong magnetic field, so as to access an almost pure starting state. The zero field splitting (see Section 4.1.1) would break the degeneracy of the electronic transitions, so each end of the dimer provides four levels: $S_z = \pm\frac{1}{2}$ and $\pm\frac{3}{2}$. The combined system has sixteen levels, with transitions that could be independently frequency-addressable. The dipolar coupling provides a strong interaction that can be used to perform conditional operations between the two $S = \frac{3}{2}$ systems. All quantum logic gates can then be performed on these sixteen levels, making a four-qubit quantum computer.

The dipolar coupling needs to be strong in this scheme, and it is. It must operate on a timescale that is much shorter than the decoherence time. This dipolar coupling broadens the CW resonances of N@C_{60} powders. Measurements of highly purified powders have found that the linewidth can reach 3.5 mT [132] - 6 mT [88]. Dipolar simulations predict even broader lines for pure material with 1 nm between molecules [132]. Exchange interactions are not expected to be strong here as less than 3% of a spin is transferred from the nitrogen atom to the cage [89]. However, the exchange interactions that do exist may be responsible for the observation of linewidths that are narrower than would be expected from purely dipolar simulations.

The two ends of a fullerene dimer are also separated by about 1 nm. The linewidth measured for powders (3.5-6 mT) corresponds to an interaction frequency of 100-170 MHz, which is an interaction time of as little as 6 ns. This time is 20,000 times shorter than the decoherence time which provides an excellent figure of merit. However, such a strong interaction that cannot be turned off is incompatible with many QC schemes. QC would be made easier by reducing the

strength of this interaction by going close to the 'magic angle'. When the crystal is oriented at the magic angle to the applied field, there is a reduced dipolar interaction. A convenient interaction time to choose might be 500 ns, as this is much longer than the time for an operation ($\sim$ 50 ns) and much shorter than the T_2^e time ($\sim$ 4500 ns for N@C_{60} powders). The dipolar interaction is Heisenberg-like which is slightly less convenient for QIP than an Ising-like interaction.

The measured result at the end of computations with a symmetric dimer will contain signals from the molecules that are not part of the computation. The pulse sequence used will always manipulate some of these, so it is not sufficient to simply subtract the signal measured before the computation begins. Instead it is necessary to create a model that predicts the response of each spin system to the pulses applied. The pulse sequence should be chosen to make the modeling simple. If this modeling is slow on a classical computer then the QC speedup may be lost. There would be no reason to build a scaled up version of this computer if it could only be measured with the help of a quantum computer to decide which parts of the signal should be subtracted!

In fact, this modeling is simple for the $(^{15}N@C_{60})_2$ computer. The unwanted signal comes from dimers in which both ends have the same nuclear spin. These molecules are easy to model because the two ends are in the same spin state throughout the manipulations. It is encouraging that the computation required to predict the behaviour of the unwanted molecules is significantly easier than the computation performed by the useful molecules. For $(^{14}N@C_{60})_2$, it might be possible to use the three asymmetric pairings as three separate QC systems. This is only feasible because a lot of information can be extracted by measuring these systems.

The electronic spin must be measured here, so CW scans are of no use. Instead, an FID should be used, as described in Section 5.5. In this case, the 90° pulses used should be selective, so as to excite just one transition. In this way, the relative populations can be found of any two adjacent levels in the sixteen-

level computer, without disturbing the other levels. Measuring all eight relative populations separately reveals the values of all four qubits.

If the dimers cannot be aligned, it may be possible to use them for QC in solution. The fast tumbling averages out the dipolar interaction, so another way is needed to entangle the two ends of the dimer. The exchange interaction would have to be used, which has not been measured or calculated for a $N@C_{60}$ dimer. This interaction is likely to be weak because there is only a weak interaction between the nitrogen atom and its cage. The spin density transfered to the cage is less than 3% [90]. The exchange interaction between the two nitrogen atoms of a $N@C_{60}$ dimer depends on this weak interaction squared, times the interaction between the two fullerene cages. This slow interaction must happen much faster than the T_2^e time.

The system could be initialized to create a pseudo-pure state, as in NMR QC. The electronic transitions would remain degenerate, so only two electronic qubits could be used. As long as the dimers are asymmetric, it would be possible to store information in the nuclear spin. Each ^{15}N nucleus would constitute a qubit. DNP would be used to initialize these nuclear spins.

5.7.2 Fully Scalable QC

There are two scientific breakthroughs that could enable this research to develop into QC with an unlimited number of qubits:

- Controlled chemical synthesis of large fullerene arrays.
- A technique that can measure the electron spin of a single molecule of $N@C_{60}$.

It is estimated that on the order of 100 logical qubits will be necessary to perform calculations that are intractable on a classical computer. With quantum error correction [18], one logical qubit might be coded into ten 'physical qubits'. If global addressing [37] is used, the number of logical qubits per physical qubits

drops further. So a system that does not require global addressing needs on the order of 1000 physical qubits to match the best classical computers.

Huge advances in fullerene chemistry would be necessary to build up from monomers through dimers to such large chains. This route was followed in NMR up to seven qubits, by synthesizing a hydrocarbon containing just 24 atoms. Progress was stopped by the pseudo-pure state preparation rather than by the chemistry. Preparing weak pseudo-pure states is avoided in ESR QC, but fullerene chemistry is not yet mature.

Current research aims to synthesize useful quantities of asymmetric dimers such as $^{14}N@C_{60}$-$^{15}N@C_{60}$. Joining these dimers in an ABAB... structure would be useful for QC as long as there were 10^{15} of these molecules with exactly equal length and no ESR signal from defects. Further, it would be necessary to align these long chains: In liquid solution, the chains would be much too long to tumble faster than the characteristic time of the microwaves. Hence the dipolar interaction would be significant and should be used to interact the qubits. Another reason not to work in liquid solutions is that pseudo-pure states cannot be prepared for so many qubits [132].

If it were possible to measure the electronic spin of a single $N@C_{60}$ molecule, the ensemble approach would not be necessary. Then it would suffice to create one perfect array of $N@C_{60}$ molecules. Nano-SQUIDS have reached a sensitivity of 40 electron spins per root hertz [43], and there are three electron spins in $N@C_{60}$. The electronic T_1 time is 4.5 minutes, so a negligible number of spins will decay in the four seconds required to reach 20 spin sensitivity. Hence a magnetometer is needed with an order of magnitude more sensitivity[5]. It is necessary to bring the magnetometer very close to the spin in question. Other magnetometers have higher sensitivity than nano-SQUIDS, but do not allow the fullerene molecule to get so close [41]. If a fullerene were found with an accessible optical transition as well as a long-lived electron spin, it may be possible to use an optical readout

[5]Alternatively, the spin could be magnified by SWAP-ing it out [133] to a single molecule magnet [134] which could have spin $S = 15$.

method similar to that employed to study nitrogen vacancy centres in diamond [135].

Assuming that readout were possible, many parts of the scheme presented in this chapter could be used in the full-scale quantum computer that results. In particular, DNP could be used to initialize the nuclear spins. The nuclear qubits would then be used to store quantum information because they have a very long decoherence time, but are slow to manipulate. This information could then be completely swapped onto the electronic qubit, to be manipulated in a calculation. The electronic qubit can be manipulated much faster but does not maintain its quantum state for as long as the nuclear spin. Twamley suggested a similar scheme in which the electron spins act as a bus for the nuclear qubits in an array of endohedral fullerenes [133].

If an unlimited number of $N@C_{60}$ molecules could be created in an interacting array and operated as a single quantum computer, it may not be necessary to use the nuclear spin for computations. In this case the nuclear spin could be used as a longer-term memory because of its longer T_2. Alternatively, for any quantum computer based on $N@C_{60}$ molecules, the ENDOR scheme can be used to double the number of physical qubits in the computer. A computer that can access one qubit for each of its N molecules of $N@C_{60}$ is an N-qubit computer. The $2N$-qubit QC that could be done by making use of the nuclear spin corresponds to an extra factor of 2^N in the number of eigenstates.

Chapter 6

ESR and ENDOR Experiments with $N@C_{60}$

Contents

6.1 $^{15}N@C_{60}$ QC Scheme 82

6.1.1 Initializing the Nuclei with DNP 82

6.1.2 Nuclear T_1 92

6.1.3 Qubit Readout 94

6.2 $N@C_{60}$ Decoherence 97

6.2.1 Sources of Decoherence 97

6.2.2 Spin Dephasing: T_2 Time 101

6.2.3 Spin-Lattice Relaxation: T_1^e Time 102

6.3 Conclusions 104

Experiments are presented showing the usefulness of $N@C_{60}$ for QIP. DNP initialization of $^{15}N@C_{60}$ was performed and measured with CW ENDOR, producing a nuclear polarization of 80%. Using amorphous sulphur as a solvent extends the elecronic dephasing time, T_2^e, to 215 μs and the electronic spin-lattice relaxation time, T_1^e, to 4.5 minutes at 3.7 K.

6.1 Partial Implementation of $^{15}N@C_{60}$ ENDOR QC Scheme

6.1.1 Initializing the Nuclei with DNP

These experiments were performed with high-field high-frequency (HFHF) ESR, as this provides higher polarizations. The spectrometer was built by J. van Tol, L.-C. Brunel and R. J. Wylde and uses CW microwave radiation with a frequency of 240 GHz, as described in reference [136]. $N@C_{60}$ has $g \sim 2$ so the resonant field is around 8.6 T.

$^{15}N@C_{60}$ was prepared by ion implantation [128] by K. Porfyrakis and J. Zhang in the Materials Department at the University of Oxford. ^{15}N ions are fired at empty C_{60} molecules emerging from an effusion cell. This technique produces approximately one molecule of $N@C_{60}$ for every 10,000 empty C_{60} cages. The sample was dissolved in toluene and purified several times with HPLC[1]. This removes many of the empty cages as well as oxides and higher fullerenes such as C_{70}. The final stage of HPLC was several runs in recycling mode, the last of which is shown in Figure 6.1. Integrating the area under the peaks reveals that more than 80% of the sample is $^{15}N@C_{60}$, and the remainder is mainly empty C_{60}. The accuracy of this measurement depends on the assumption that the UV-vis absorbtion of $N@C_{60}$ is the same as that of empty C_{60} at 312 nm, as found in reference [88].

The purified sample was dissolved in deuterated toluene from a freshly opened vial and put into an X-band ESR tube. The solvent was deoxygenated with three freeze-pump-thaw cycles and sealed under a dynamic vacuum[2]. A room temperature scan is shown in Figure 6.2. The fact that Gaussians give a better fit than Lorentzians indicates that the intrinsic linewidth is not being recorded here.

[1] A 'Buckprep-M' column was used and the flow rate of toluene through the column was 18 ml min^{-1}.

[2] The pump was left running while the tube was sealed with an oxygen blow torch.

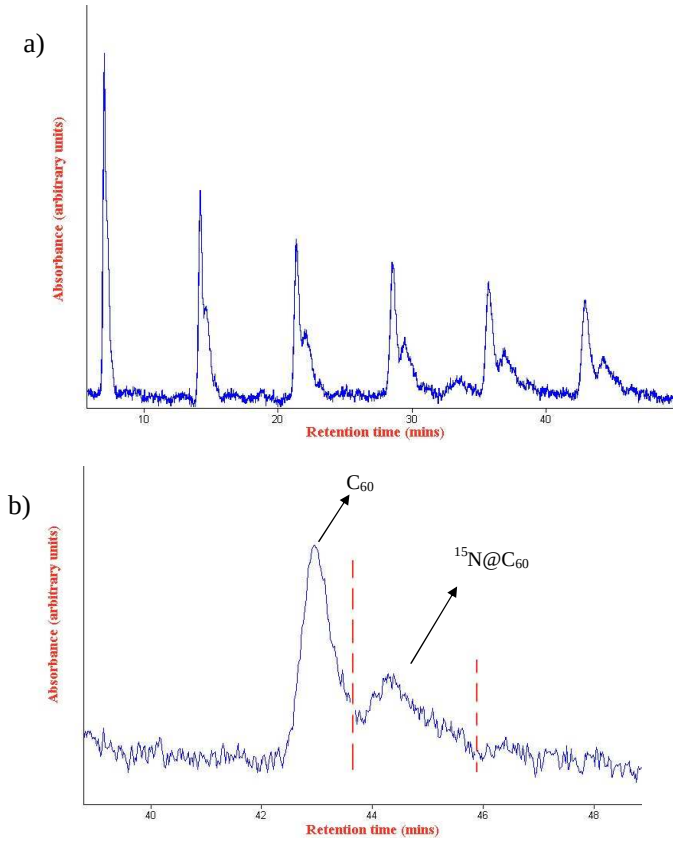


Figure 6.1: a) The final HPLC purification of ^{15}N@C_{60}. After several passes through the column, the ^{15}N@C_{60} peak becomes clearly distinguishable from the C_{60} peak. N@C_{60} takes about 15 seconds longer than C_{60} to pass through the column. b) Enlargement of the final pass. These figures are courtesy of J. Zhang.

It was necessary to choose a high modulation amplitude of 0.02 mT, in order to have a good signal to noise. This over-modulation increased the linewidth, and inhomogeneity in the applied magnetic field provided further line-broadening.

To make measurements at low temperatures it is necessary to flash-cool the sample in liquid nitrogen and then insert it into the pre-cooled spectrometer. Figure 6.3 shows a CW ESR scan at 4.2 K. At this temperature the T_1^e of N@C_{60} can be on the order of minutes, as shown in Section 6.2.3. With such a long T_1^e it was not possible to avoid saturating the spins with a CW scan. Even with a very low microwave power, scanning through resonance equalizes the populations of the electronic levels. Once the populations are equal, no more signal can be measured until spin-lattice relaxation polarizes the spins again. This is responsible for the

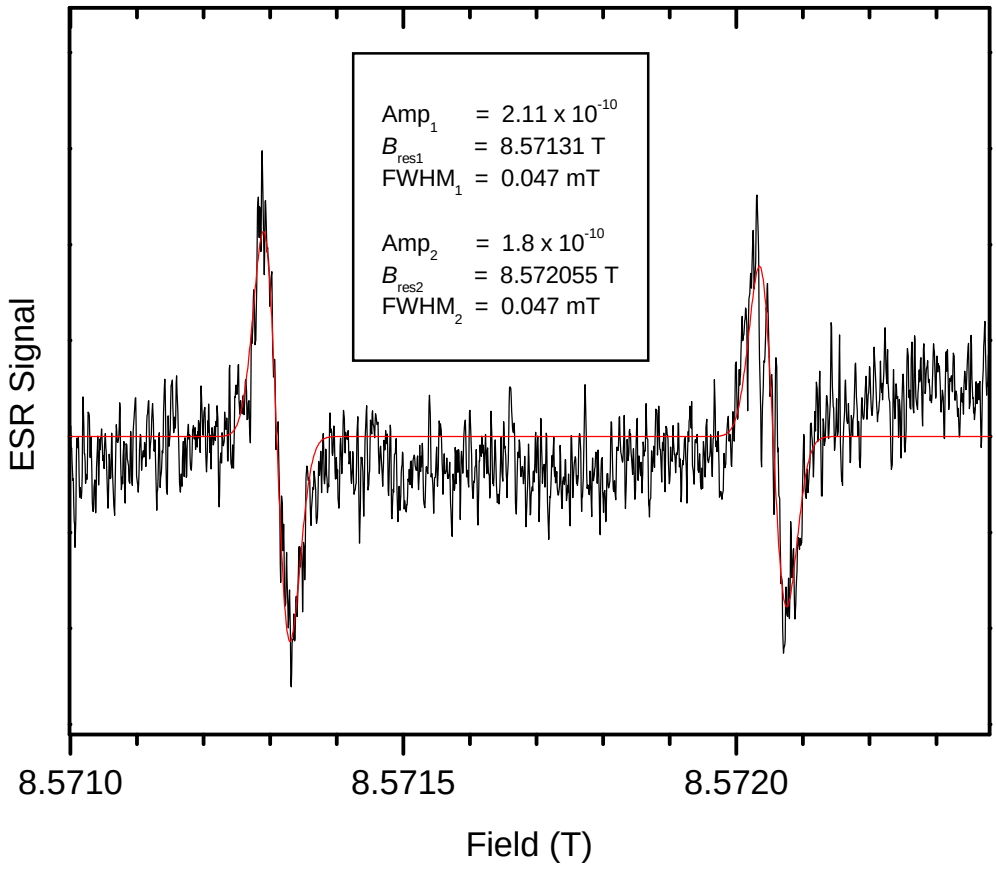


Figure 6.2: CW ESR of $^{15}N@C_{60}$ at room temperature. Four scans were averaged. The red line is a fit with two Gaussians using the parameters shown.

'absorption' lineshape present in all of the CW scans presented here at 3-5 K.

Flip-Flop Polarization

Radiation of frequency G_2 (as labeled in Figure 5.1) was applied for 2.5 hours by setting the magnetic field to the high-field resonance. Figure 6.4 shows the resultant nuclear polarization. This is due to the flip-flop transitions as described in Section 5.2.3. 57 % of the molecules are in the ground state with $S_z = -\frac{3}{2}$ and $I_z = \frac{1}{2}$. Performing the same experiment with G_1 radiation, (with the magnetic field set to the low-field resonance) produced no polarization. This shows that the polarization in Figure 6.4 is not due to a difference in the T_1^n times of the four nuclear transitions. If the nuclear T_1 time of the M_2, M_3 or M_4 transitions

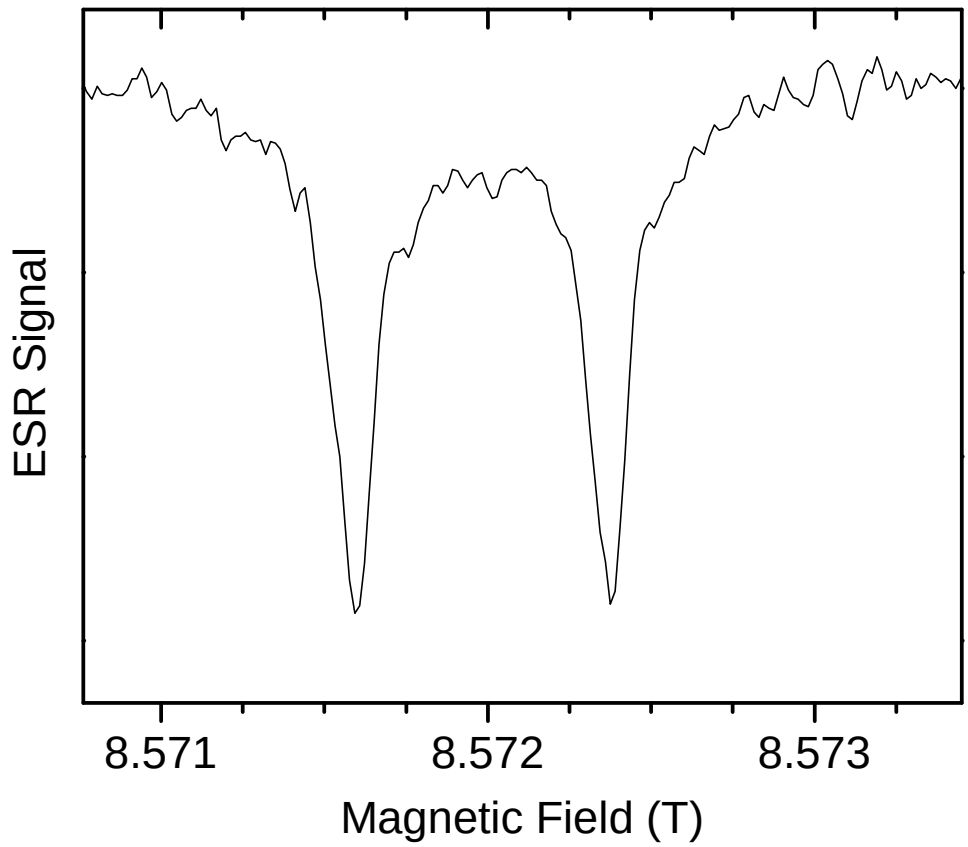


Figure 6.3: CW ESR scan of ^{15}N@C_{60} in deuterated deoxygenated toluene at 4.2 K. The unusual lineshape is due to saturation.

were much shorter than that of M_1, then it would be possible to polarize or anti-polarize the nuclei by exciting the electronic spins of anti-polarized or polarized nuclei respectively. Some difference in these nuclear T_1 times is expected because of the difference in their frequencies, but it seems that all of the nuclear T_1 transition rates are much smaller than the rates of flip-flop transitions.

CW DNP

The continuous-flow cryostat can reach 3 K where the electronic Boltzmann factor is 0.02. CW DNP was performed at 3 K as described in Section 5.2.1. It was possible to align the nuclei with or against the applied field. To align the nuclei with the applied field, the field was set to be on the high-field ESR resonance.

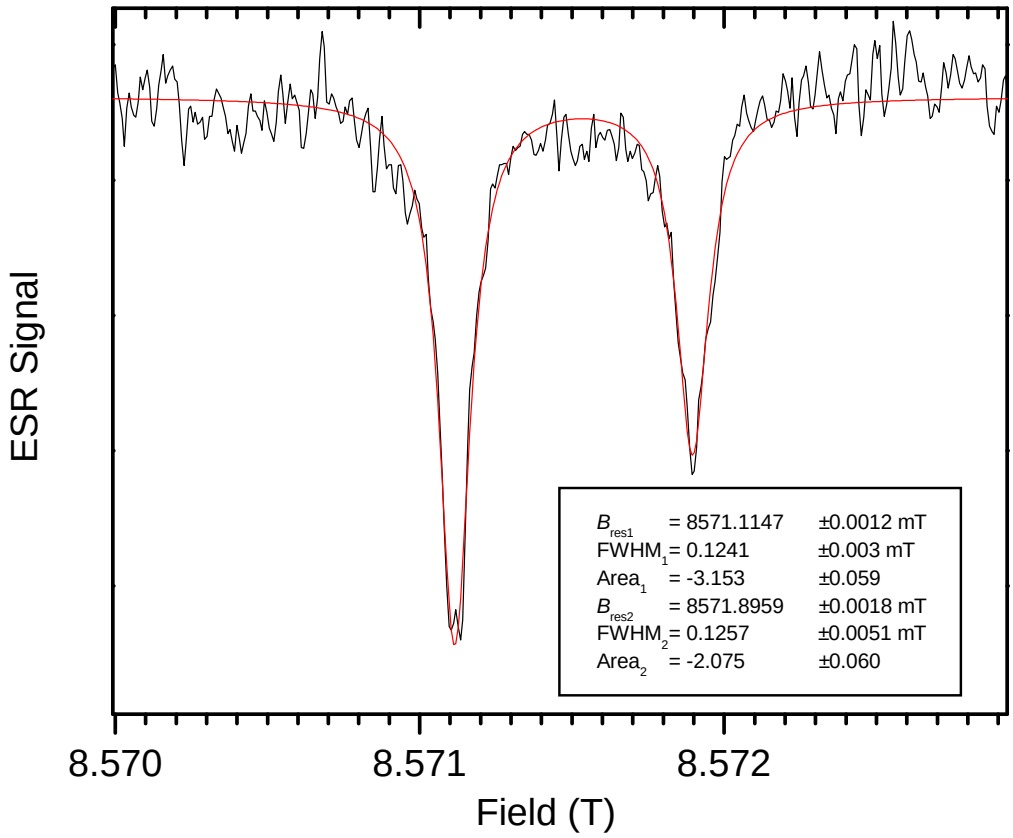


Figure 6.4: CW ESR scan of $^{15}N@C_{60}$ at 4.2 K after 2.5 hours G_2 radiation. The nuclear polarization is due to the flip-flop transitions. The red line is a fit with two Lorentzians, showing that 60% of the nuclei are polarized; 57% of the molecules are in the ground state of nuclear and electronic spin.

This excites the electron spin of molecules with anti-aligned nuclei, using radiation with frequency G_2. DNP was more effective when the CW modulation coils were used to sweep the magnetic field slightly. While applying this G_2 radiation, RF radiation was applied, repeatedly sweeping the frequency through one of the resonant frequencies $M_{2,3,4}$ predicted in Figure 5.1. Each of these ENDOR sweeps took about a minute. This slow sweeping was found to polarize more effectively than setting the RF frequency to some value and adding frequency modulation from the RF power supply. The power provided by the power supply depended strongly on the RF frequency. This may be influenced by the geometry of the RF coils as much as the design of the power supply.

The most effective polarization was produced by sweeping from 47.916 to 47.924 MHz. This corresponds to M_2 radiation, which was expected to produce less polarization than M_3, with M_4 being expected to be the most effective. It was certainly possible to polarize the nuclei with the other two frequencies, but the effect was smaller. The RF coils were not producing as much power at the lower frequencies, which provides a partial explanation for the poor polarization produced by M_3 and M_4.

The red trace in Figure 6.5 shows the polarization produced by applying G_2 and M_2 radiation for 13 minutes. No signal from the $I_z = -\frac{1}{2}$ line remains, but the signal to noise is not as high as the 4.2 K scan. The black trace then shows the effect of using the same RF while applying G_1 radiation. This anti-polarizes the nuclei, leaving only a very small low-field resonance.

The signal to noise ratio can be improved by averaging, but the resonances are made less sharp by the slight field drifts. These field drifts do not affect the area under the peak, which is used to measure the relative number of molecules in each of the two nuclear spin states. DNP was applied again, as before, to polarize the nuclei and four CW scans were averaged to produce Figure 6.6. The best fit line was found by constraining the width of the weak high-field peak to be the same as that of the low-field line where the signal to noise is much higher. The areas of the resonances depend on the nuclear polarization of the entire system:

$$\frac{P[I_z = \frac{1}{2}]}{P[I_z = -\frac{1}{2}]} = \frac{\text{Area}_1}{\text{Area}_2} = \frac{15.87}{3.71} = 4.28. \tag{6.1}$$

This polarization means that 81% of the nuclei are polarized.

To compare this polarization with the model in Chapter 5, Equation 5.4 should be rewritten for the case where M_2 radiation is applied, so that

$$P[\text{A}] = P[\text{B}]. \tag{6.2}$$

Equations 5.3 and 5.5 still apply. This model predicts that the nuclear polarization

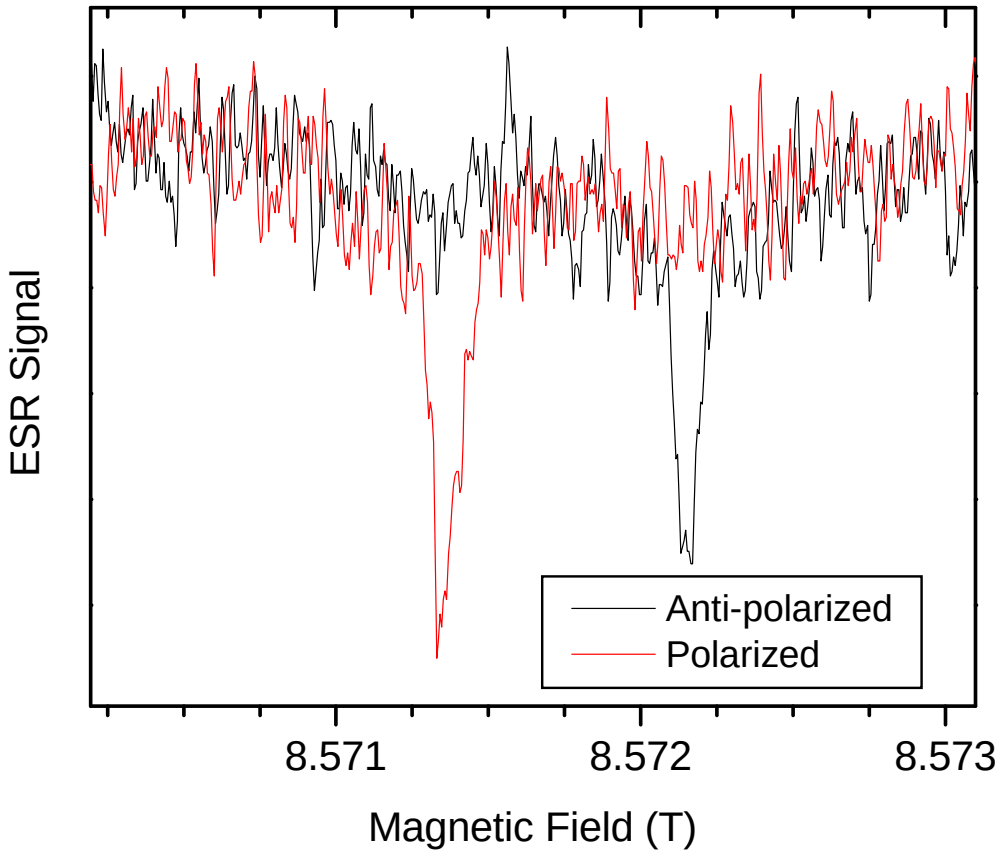


Figure 6.5: CW ESR scans of $^{15}N@C_{60}$ at 3 K after DNP polarization for 13 minutes (red trace). The system was then anti-polarized (black trace) with the same technique for 21 minutes, using G_1 radiation instead of G_2.

of the entire system is:

$$\frac{P[I_z = \frac{1}{2}]}{P[I_z = -\frac{1}{2}]} = \frac{\frac{1}{\alpha} + 1 + \alpha + \alpha^2}{4} = 11.9, \tag{6.3}$$

for $\alpha = 0.022$. This is larger than the measured polarization of 4.3.

One reason for this discrepancy could be that the CW scan is too saturated to accurately reflect the true nuclear polarization. A reliable CW scan should sweep the field much slower than the electronic T_1, so that the system is always close to equilibrium. The scans in Figure 6.6 lasted just 85 seconds, which is much shorter than the electronic T_1 of 4.5 minutes at 3.7 K. This regime is known as 'fast passage', and the lineshape recorded is a classic example of this: An absorption

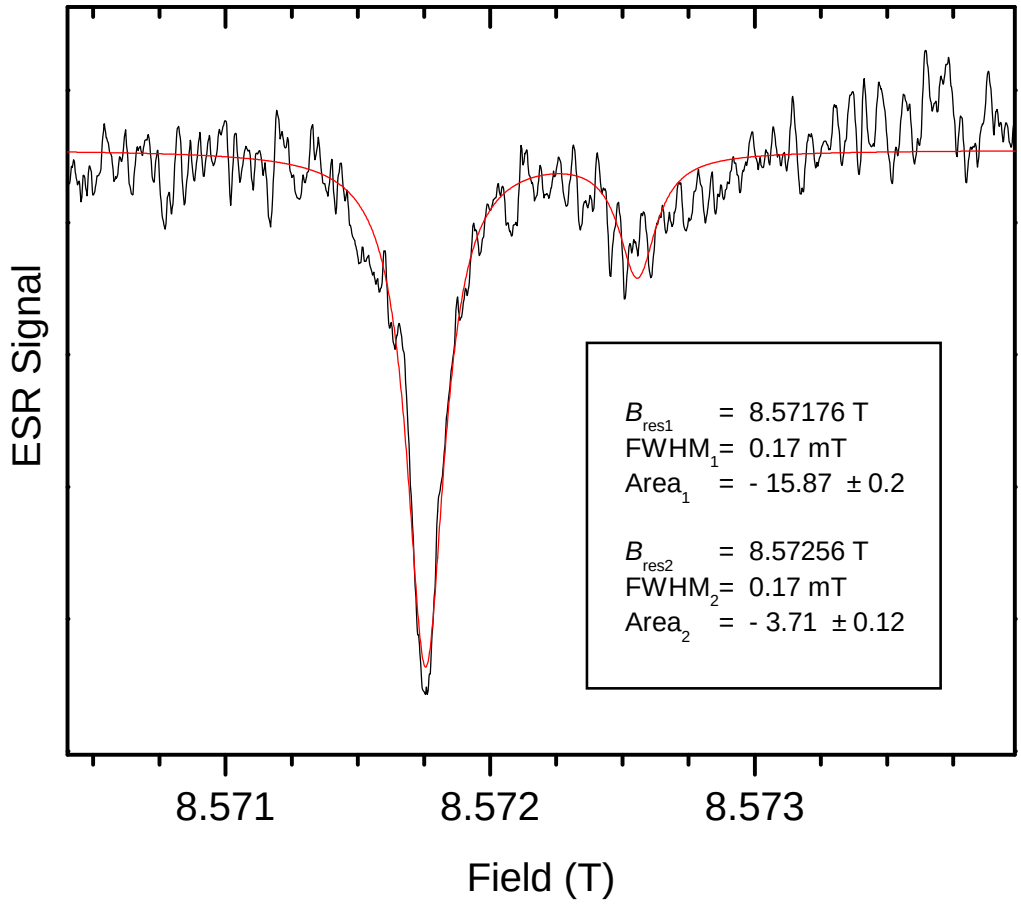


Figure 6.6: Averaged CW ESR scan of $^{15}N@C_{60}$ at 3 K after DNP polarization. The red line is the bi-Lorentzian best fit with the parameters given. The linewidth of the two peaks was set to be the same.

line is recorded instead of the derivative line found from an adiabatic scan (Figure 5.4 is an example of an adiabatic passage). The derivative lineshape should be integrated to get an absorption line, and then the area under that is proportional to the number of spins making up the resonance. It is not meaningful to integrate the data in Figure 6.6 twice, so this procedure was replaced by simply finding the area under the peak. The saturation problem should affect the two resonances equally, so this does not provide an explanation for measuring a reduced polarization.

Another explanation might be that the electronic T_1 is so long at 3 K that the DNP was not applied for long enough. The T_1^e has been measured as 4.5 minutes at 3.7 K, but it is possible that cooling to 3 K increases the T_1^e significantly.

However, DNP was performed many times during these experiments with a wide variety of durations, and using more than 12 minutes did not generally produce a larger effect. Figure 6.5 shows two such attempts: The anti-polarization was performed for 21 minutes without producing a bigger effect than the 13 minute polarization. Leaving the DNP radiation on for longer would have increased the polarization, but certainly not by enough to agree with the prediction of the model above.

If the temperature was higher than 3 K then this could explain the observed polarization. The temperature was measured as 3.00 ± 0.02 K, which corresponds to a measurement of $\alpha = 0.0215 \pm 0.0005$. This is only enough error to justify a polarization of 11.6, rather than 11.9.

Instead, the measurement of a much weaker polarization is probably due to two complementary problems:

- If the RF power is too low then Equation 6.2 does not apply because the transition is not saturated.
- If the RF power is too high then the sample heats up and α is higher than would be thought from the thermometer reading.

This experiment was deliberately performed with an RF power that is a compromise between these problems, so both are likely to play a part. The RF coils are wrapped around the sample to maximize the amount of RF delivered. Unfortunately the thermometer is further away from the sample, so local heating due to the RF coils will affect the sample more than the thermometer. The RF power used here was always kept at 40 W or less to minimize sample heating. This power was certainly not enough to saturate the M_2 transition, resulting in a lower polarization than that predicted by the model. The amount of heat dissipated in the sample due to the RF is much less than 40 W: Most of this energy comes back out of the fridge, but some of it will be dissipated in the coils that surround the sample. The cooling power of the fridge is not known, but the heat leak due

to 40 W of RF is known to be significant from previous experiments with this spectrometer. Pumping on ^{4}He reduced the measured temperature to 3 K, but the cooling power of this evaporating helium is probably too low to deal with the continuously applied RF. Above 4.2 K, the helium bath is capable of coping with the RF heat load. However, there may still be a thermal gradient between the sample and the bath, so the sample could warm above 4.2 K. For a temperature of 4.2 K the model presented here predicts that the nuclear polarization of the entire system should be 4.1, in agreement with the measured polarization. Taking into account the fact that the nuclear transition was probably not saturated, it is more likely that the temperature rose by a smaller amount.

The DNP used so far constitutes a measurement of the M_2 transition frequency as 47.92 $\pm$0.004 MHz. This can be used to calculate the nuclear g-factor using the expression given in Figure 5.1:

$$g_N = \frac{h\,M_2 - \frac{A}{2}}{\mu_N B}. \tag{6.4}$$

The hfs constant, A, is measured as 0.781 $\pm$ 0.003 mT from Figure 6.4. This is lower than the value of 0.790 $\pm$ 0.005 mT found from W-band measurements of the same sample, shown in Figure 5.4. The W-band measurement agrees with the value of 0.795(5) mT quoted in the literature [128], so it is likely that there is a small error in the calibration of the field of the 240 GHz spectrometer. Using the hyperfine constant from the 240 GHz spectrometer gives a value of $g_N = 0.566$. Using the hyperfine constant from the W-Band spectrometer would reduce this by 0.002, and the error due to the other parameters are smaller than this. The accepted value of g_N for the ^{15}N nucleus is 0.566 [137], in excellent agreement with these measurements.

The frequencies of the other nuclear transitions can be calculated from this g-factor, as shown in Table 6.1. The measured transition frequencies agree well with these calculations. It is only surprising that applying M_3 and M_4 produced such small nuclear polarizations. This was partially due to the weakness of the

applied RF at these lower frequencies. The power supply reading was 40 W for the M_4 radiation, but only 23 W was provided for the M_3 radiation. These powers must have been reduced further, relative to the M_2 radiation, by poor frequency-dependent coupling to the sample.

Nuclear Transition	Frequency Calculated from M_2 Transition (MHz)	Measured Frequency (MHz)	Measuring Technique
M_1	69.80 ± 0.13	$69.875 \rightarrow 69.900$	Unpolarization
M_2	N/A	$47.916 \rightarrow 47.924$	DNP
M_3	26.03 ± 0.04	$25.9 \rightarrow 26.1$	weak DNP
M_4	4.15 ± 0.13	$3.8 \rightarrow 4.8$	weaker DNP

Table 6.1: Comparison of measured and calculated frequencies of nuclear transitions in $^{15}N@C_{60}$. The transitions are labeled in Figure 5.1. The ranges indicated in the calculated frequencies are due to the uncertainty in the hyperfine constant. The measurement of 0.781 $\pm$0.003 mT, at 240 GHz was used. The range in the measured frequencies corresponds to the sweep range used.

Applying M_1 radiation is a useful way to unpolarize the nuclei, equalizing the size of the two resonance lines, as shown in Figure 6.7. The magnetic field is set to be away from the ESR resonances. Unpolarization was most effective when the frequency was swept from $69.875 \rightarrow 69.900$ MHz. This resonance was much wider than M_2, where it was possible to identify an 8 kHz window outside of which there was no DNP effect.

6.1.2 Nuclear T_1

After DNP, the nuclei relax back to thermal equilibrium at the spin-lattice relaxation rate, T_1^{-1}. No value is available for this in the literature, but it is certainly much slower than the spin-lattice relaxation rate of the electrons.

The first attempt to measure the nuclear T_1 was at 4.2 K after the flip-flop polarization, producing Figure 6.8. ESR scans were taken approximately every 12

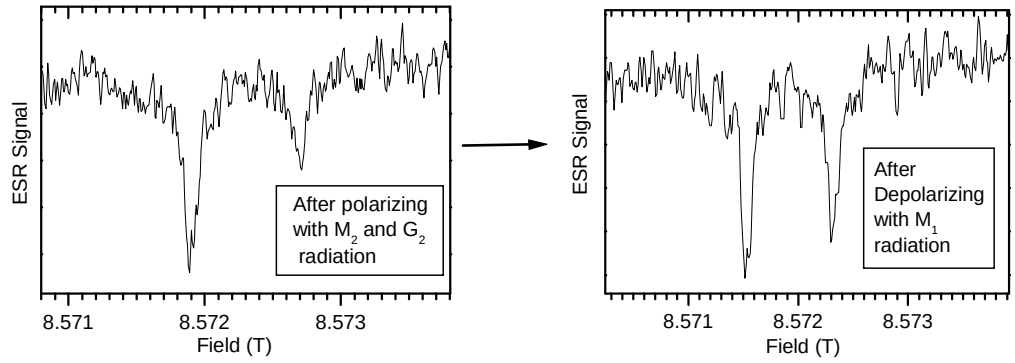


Figure 6.7: CW ESR scans of ^{15}N@C_{60} at 4.2 K after DNP polarization (G_2 and M_2 radiation) followed by depolarization with M_1 radiation only.

minutes, yielding a biexponential decay with $T_1^a = 30 \pm 12$ minutes and $T_1^b \gg 3.6$ hours. However, the repeated measurements may have artificially speeded up the decay in this experiment.

Another measurement was made by starting with the high polarization of Figure 6.6, and leaving the system undisturbed for 11.5 hours at 4.2 K. The resulting scan is shown in Figure 6.9: The polarization has almost halved. With only two measured points it is impossible to accurately infer the T_1^n: The general rule for a good exponential fit is that the data should extend to at least 3 T_1. However, the thermal equilibrium state is also known: The nuclear spin populations will be equal (within experimental error) after a long enough time. This information is represented by a horizontal line on the graph of nuclear polarization versus time. The shape of the decay is not known, but it may be assumed that this will be a sum of exponential decays. With the further assumption that one decay time dominates it is possible to obtain an order of magnitude for the nuclear T_1 time. For ^{15}N@C_{60} at 4.2 K this is on the order of twelve hours.

The very long nuclear T_1 excludes the possibility that nuclear spin flips are a relevant electronic T_2 process at low temperature. The nuclear T_1 of ^{14}N@C_{60} is expected to be of the same order of magnitude, so the low-temperature electronic T_2 of ^{14}N@C_{60} and ^{15}N@C_{60} should be the same. All of the relaxation times in this chapter are expected to be about the same for both ^{14}N@C_{60} and ^{15}N@C_{60}.

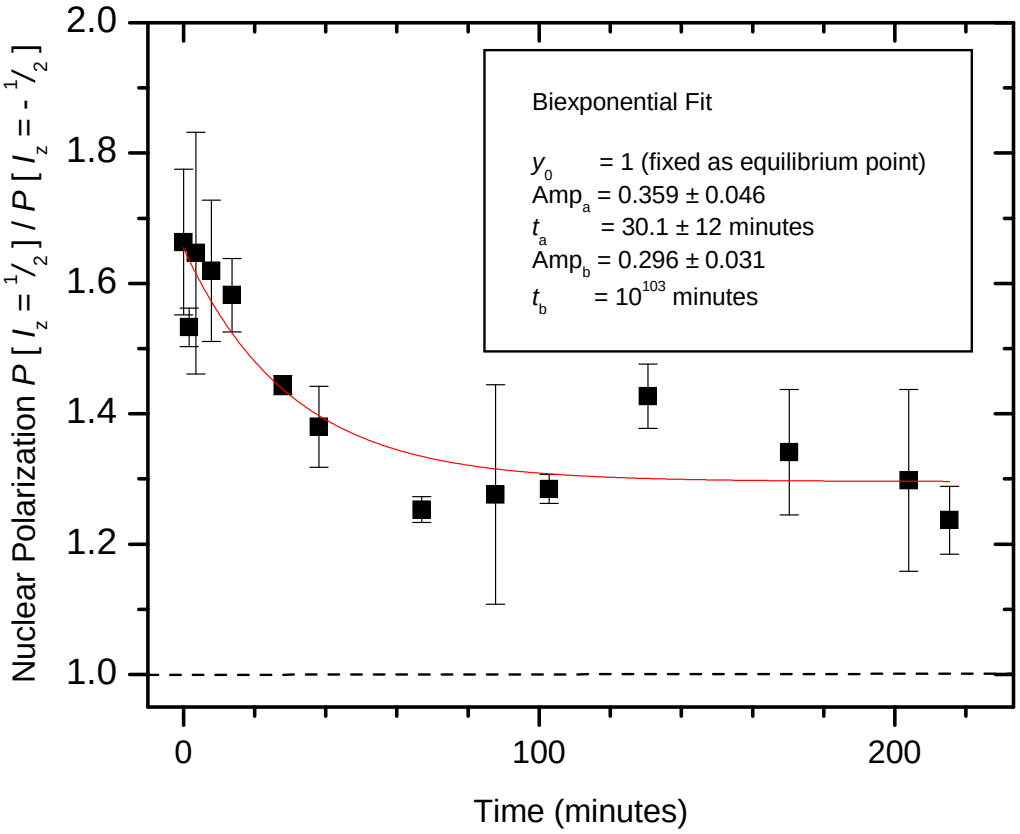


Figure 6.8: Decay of nuclear polarization increased by repeated ESR scans at 4.2 K. The polarization was measured as the ratio of the areas of the low-field to the high-field resonance. The data are fit with a biexponential decay, one component of which is much longer than the measurement time of 3.6 hours. This slow decay time cannot be estimated from these data, so the fitting parameter $t_b = 10^{103}$ minutes should be interpreted as $t_b \gg 3.6$ hours.

6.1.3 Qubit Readout

The measurements presented up to this point demonstrate the use of CW ESR scans for measuring the nuclear spin qubit as described in Section 5.5.1.

Pulsed readout was demonstrated on a W-band spectrometer at a field of 3.4 T. The nuclear spin of ^{14}N@C_{60} was measured, which is more difficult than using ^{15}N@C_{60} because the three hyperfine lines due to ^{14}N are spread over 1.2 mT while the two ^{15}N lines cover just 0.8 mT. A hard 90° pulse is applied that must cover a wide enough frequency range to excite all of the spins. The commercial W-band spectrometer used was made by Bruker. The maximum microwave power is still

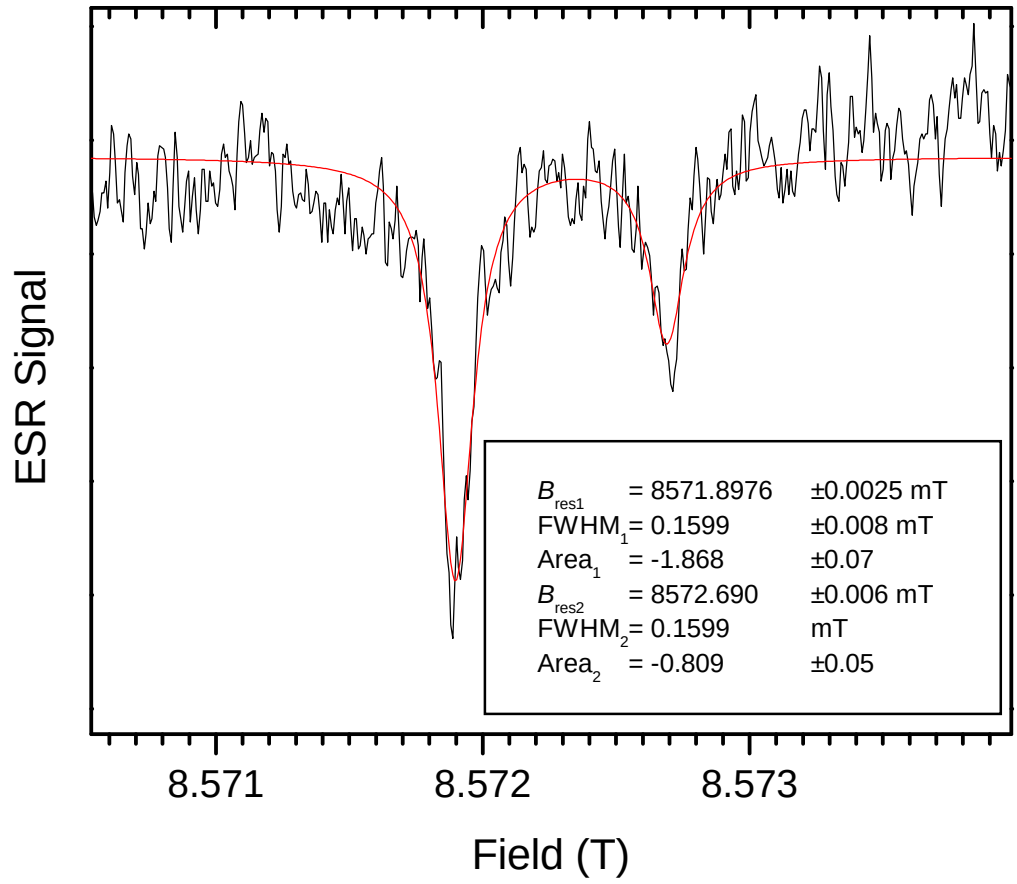


Figure 6.9: CW ESR scan of $^{15}N@C_{60}$ at 4.2 K 11.5 hours after DNP polarization. In this time, the polarization has fallen from 4.3 (see Figure 6.6) to 2.3. The red line is the bi-Lorentzian best fit with equal line-widths.

quite low, so the 90° pulse at 3.2 K lasted 124 ns. This maximum-power pulse was broadband enough to excite all of the spins.

The free induction decay (FID) that was recorded is shown in Figure 6.10. The fact that the decay begins positive shows that the electrons are polarized with the applied field. This would define a measurement of $|0\rangle$ for the electronic qubit. Real QC measurements would then be compared to this reference.

The nuclear spin can be found from further analysis of these data. Subtracting the exponential decay shown reveals three sinusoidal oscillations with different frequencies. The Fourier transform of these data is shown in Figure 6.11. The three resonances are analogous to a CW scan and reveal the relative populations

of the three nuclear spin manifolds. The central peak is larger because the hard pulse is still stronger at the central frequency than at the other resonances. As with the electronic qubit, this measurement should be taken as a reference. It corresponds to equal populations of all three levels.

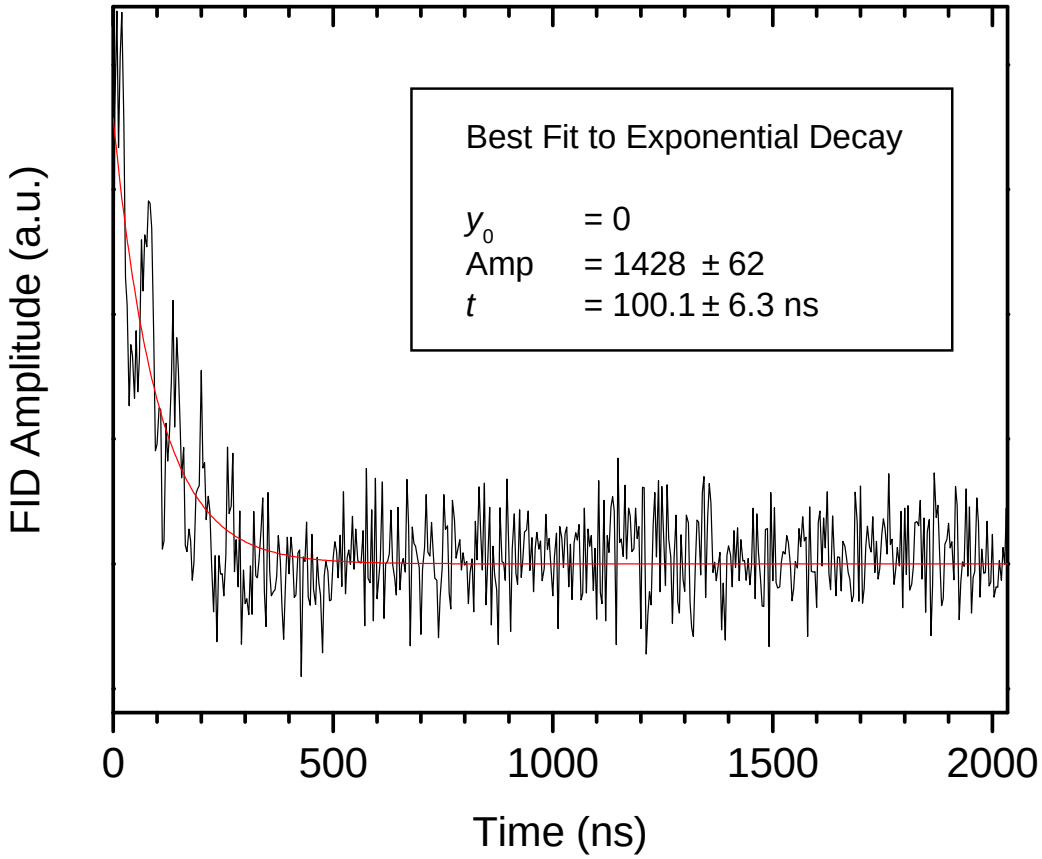


Figure 6.10: FID of $^{14}N@C_{60}$ in deuterated, deoxygenated decalin at 3.2 K. The fact that the signal is positive and falls towards zero indicates that the electronic spin is aligned with the applied field. This would constitute a measurement of the electronic qubit as $|0\rangle$.

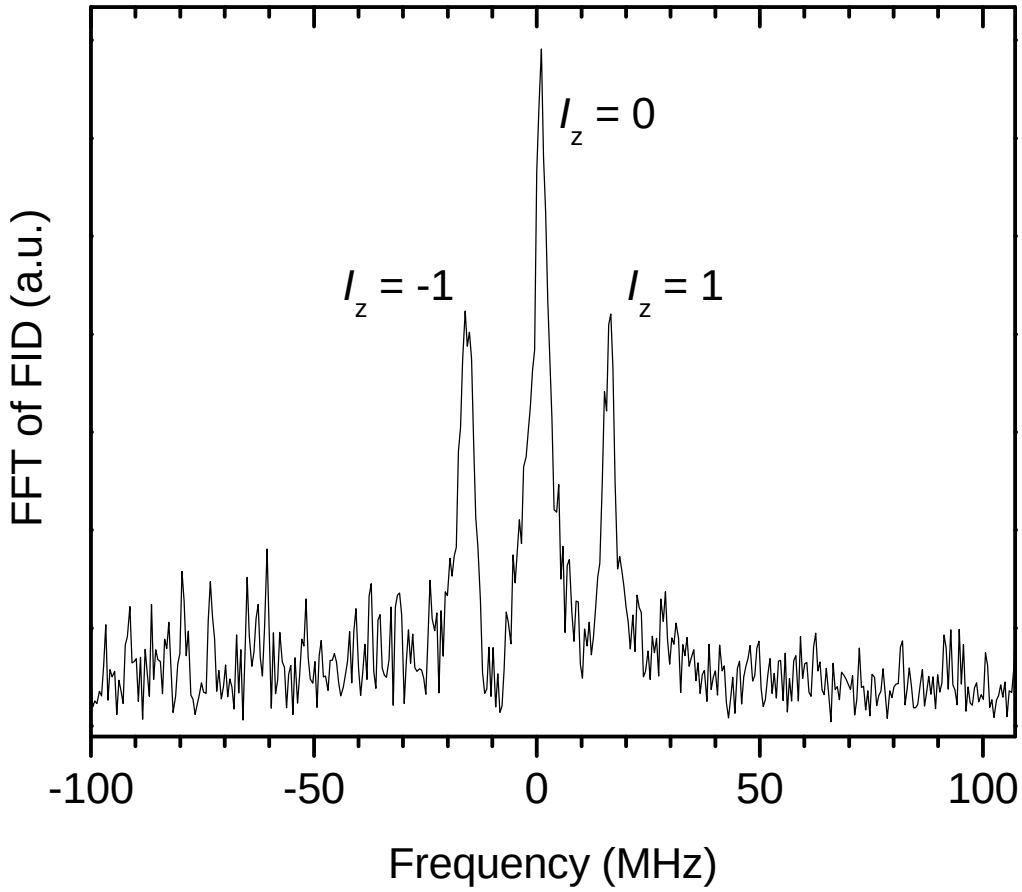


Figure 6.11: Fast Fourier transform (FFT) of the FID from ^{14}N@C_{60} at 3.2 K. The three nuclear spin manifolds are equally populated, despite the different intensities of their resonances. The resonances are separated by 16 MHz, which is the hfs constant of ^{14}N@C_{60}.

6.2 Electronic T_1 and T_2 Decoherence of N@C_{60} in Amorphous Sulphur

6.2.1 Sources of Decoherence

The energy of a spin interacting with a magnetic field is split into two or more possible states. The quantum states of the ^{15}N atom in ^{15}N@C_{60} are well described in Figure 5.1 by the three strongest interactions: The electronic and nuclear Zeeman interactions and the hyperfine interaction. All of the molecules in the ensemble experience these interactions, which can be understood as spins whose energies

depend on the local magnetic field. The 2nd order hyperfine interaction modifies this picture slightly, (see page 74) but it is so weak that it can be neglected. All other interactions will cause the spin system to behave in ways not predicted by this scheme for QC. The spin system can become coupled to some other spins in the environment, and these other spins should be incorporated into the model to completely understand the behavior of any part of the new, larger system. Ignoring these other spins means that information is lost to them, from the computation. This is the general mechanism of decoherence in the quantum computer described here[3].

It is necessary to ignore these other spins because they are at random positions with respect to the qubits. Each ^{15}N atom experiences a different interaction due to its spin environment, but ensemble QC remains possible because these interactions are weak enough to be ignored. Electron spin decoherence is best quantified by measuring the T_2 with pulsed ESR.

The decohering spins present in real experiments are:

1. ^{13}C nuclear spins in the C_{60} cage.
2. Nuclear spins in the solvent molecules.
3. Impurity spins such as organic radicals or metal ions.
4. The electron spins of other N@C_{60} molecules.
5. The nuclear spin of the parent nitrogen nucleus.

The measurements of the long nuclear T_1 of N@C_{60} presented above shows that item 5 is certainly not significant at low temperatures, and probably not at room

[3]When N@C_{60} is dissolved in liquid solution it collides with other dissolved molecules that cause deformations to the shape of the fullerene cage. This results in a fluctuating zero-field splitting tensor. It has been suggested that this could be a significant decoherence mechanism at room temperature [77, 89]. However, for the QC ideas described in this thesis, low temperatures are always used to polarize the electron spins. In this regime, the solvents are always solid so there are no molecular collisions, but phonons may cause similar cage deformations.

temperature either. Spontaneous nuclear flips are so rare that they are always dominated by other sources of decoherence.

HPLC purification removes some impurity spins, and there are none present in the samples studied here. Dissolved oxygen molecules in solution are removed with a freeze-pump-thaw cycle as these are paramagnetic.

If there are other N@C_{60} molecules nearby then these can provide the dominant decoherence mechanism. A powder containing just one molecule of N@C_{60} per 10,000 empty C_{60} cages brings the nitrogen atoms close enough for this to be the case [132]. The same may be true of concentrated solutions. The T_1^e and T_2^e of a dilute solution of N@C_{60} in deoxygenated CS_2 are long at room temperature and increase significantly on cooling. However, the T_2^e in solutions has been found to drop sharply when the solvent freezes. This may be due to large numbers of N@C_{60} molecules being brought together at the domain boundaries in the crystallized solvent. Avoiding this problem requires a solvent that is amorphous rather than crystalline. Toluene is a good fullerene solvent that can form an amorphous solid when flash-frozen. However, the protons present have nuclear magnetic moments that seem to reduce the electronic T_2. Using deuterated toluene increases the T_2^e somewhat, as the nuclear spin is weaker.

A mixture of cis- and trans-decalin is glassy when frozen, and is a good fullerene solvent. It also contains protons, so the deuterated version is preferred. N@C_{60} in a deoxygenated, deuterated mixture of cis- and trans-decalin was studied at W-band at low temperatures. The T_2 was 9.1 ± 0.3 μs at 5 K. This is probably limited by the nuclear spins in the deuterium atoms.

In the search for a glassy solvent with no nuclear spins, sulphur seemed like an improbable choice because it is solid at room temperature. The suggestion came from A. N. Khlobystov and it transpired that heating sulphur produces a liquid that is a good fullerene solvent. Upon further heating, the yellow liquid turns red, and flash-freezing this is known to produce an amorphous rubbery yellow material. Less than 1% of sulphur atoms have nuclear spins, and isotopically pure

versions are available which are nuclear-spin silent.

A chemistry textbook [138] recommended heating the sulphur to 300°C for five minutes and then pouring the liquid into ice water. This much heating would destroy many of the $N@C_{60}$ molecules, but it proved possible to use 220°C for 30 seconds, which does not cause many nitrogen atoms to escape from their cages. Plunging an ESR tube of molten sulphur into ice water proved as effective as pouring the molten sulphur directly into the water. Crystalline sulphur is soluble in CS_2, so $N@C_{60}$ was added to this solution, and the CS_2 was evaporated. This provided an excellent mixture of the two powders in an ESR tube. The tube was pumped on to remove the oxygen, and sealed under approximately half an atmosphere of argon. This tube was placed into a cylindrical ceramic furnace at 220°C for 30 seconds[4]. The molten solution at this temperature was red, or dark red if a lot of fullerene was used. This was immediately plunged into ice water, forming a yellow (dark yellow if enough fullerene was present) rubber. The rubber would crystallize within five minutes if exposed to the air and touched. Alternatively, samples kept sealed under argon in the freezer remained rubbery for one or two weeks. Pressure is also known to be a relevant parameter when making amorphous sulphur, but this was not explored systematically.

The technique was used many times in Oxford and London without any problems. Surprisingly, the same technique did not initially work in Tallahassee, Florida in July 2004. The red liquid could be produced, and sometimes this formed a glass upon flash-cooling, but recrystallization took place within a minute even while submerged in ice water. Subsequently, in March 2005, amorphous sulphur samples were successfully made in Tallahassee. The relaxation times of $^{14}N@C_{60}$ in amorphous sulphur were measured in University College, London, using a pulsed X-band Bruker spectrometer.

[4]With tubes sealed under vacuum, the sulphur recondensed on a cooler part of the tube when placed into the furnace.

6.2.2 Spin Dephasing: T_2 Time

The T_2 of this sample was measured with the standard Hahn echo sequence $\frac{\pi}{2}$ - τ - π - τ - echo. The area under the echo is plotted against the time, τ, between the two pulses, and this decays exponentially with time constant T_2. This measurement is straightforward at temperatures above 30 K, where $T_1 < 1$ s. Typical data are shown in Figure 6.12 for 240 K. The x-axis shows τ, so the fitted time constant is multiplied by two to find the T_2. The PulseSpel program (provided by Bruker with their spectrometers) was used to perform 16-step phase cycling. This is not crucial as the FID will have decayed long before the echo in this case. A 56 ns pulse was used as a $\frac{\pi}{2}$ to selectively excite the central line, so 'electron spin echo envelope modulation' (ESEEM) is not seen [129].

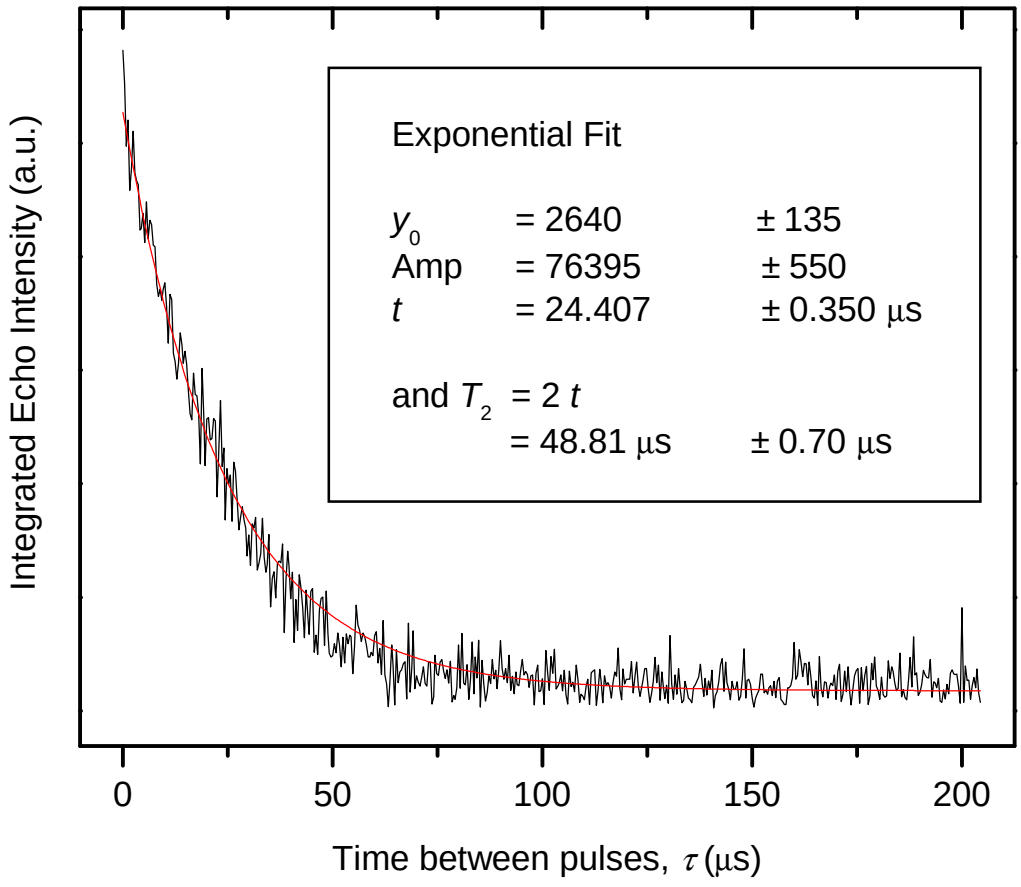


Figure 6.12: Hahn echo T_2 measurement of ^{14}N@C_{60} in amorphous sulphur at 240 K.

The convenient automation provided by PulseSpel programs allows a 16-step phase-cycled T_2^e measurement to be left running unattended. To benefit from this facility the shot repetition time (Srt) must remain longer than the T_1^e, or the signal drops to zero. At temperatures below about 30 K, the T_1^e becomes comparable with a second, which is the maximum value the Srt can be set to. This inconvenience was avoided by rewriting the PulseSpel program to include the 'sleep' command. This makes the spectrometer inactive for a chosen amount of time, during which the spins can repolarize in time for the next shot.

The sleep command was used to measure the T_2 at 3.7 K $\pm$0.2, as shown in Figure 6.13. This measurement was made on samples with isotopically pure ^{32}S and sulphur containing the natural abundance of nuclear spins. In both cases the T_2 was 215 μs at 3.7 K. This shows that the nuclear spins in the sulphur are not the dominant decoherence mechanism at 3.7 K and higher temperatures.

Figure 6.14 shows the T_2 of ^{14}N@C_{60} in amorphous sulphur at temperatures between 3.7 K and room temperature. This graph can be used to test models of the dominant decoherence mechanisms in N@C_{60}. The signals from these samples are very strong, indicating that there are a lot of N@C_{60} molecules in the ESR tube. This makes it likely that interactions between nitrogen spins is still a relevant source of decoherence.

6.2.3 Spin-Lattice Relaxation: T_1^e Time

Figure 6.15 shows a T_1^e measurement of the same sample at 280 K. A standard inversion recovery sequence was used: A π pulse followed by a Hahn echo readout sequence.

The low temperature T_1^e time of N@C_{60} has been studied before, but the only result in the literature is $T_1^e > 1$ s [33]. The reason for the lack of a more precise measurement may be instrumental: Such long relaxation times are very unusual in electron spin systems, and Bruker spectrometers are not designed to measure them. An inversion recovery measurement could be made here if the

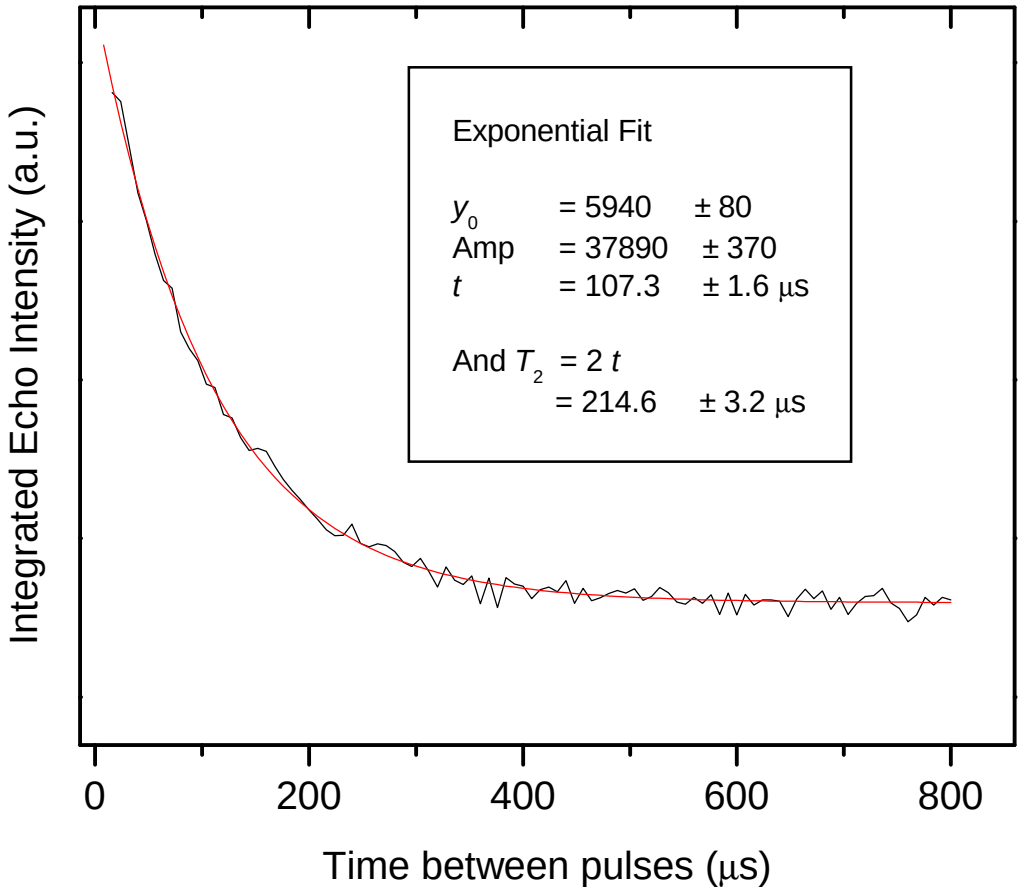


Figure 6.13: Hahn echo T_2 measurement of ^{14}N@C_{60} in amorphous isotopically pure ^{32}S at 3.7 K. No phase cycling has been used.

sleep command were used to increase the Srt to about two minutes.

Instead, another technique was used that extracts the desired information directly from the problematic behaviour. By using a standard pulse sequence, but varying the time between applications of it, the measured signal depends on how well the system has repolarized during the pause. Plotting this signal against the pause-time produces the familiar exponential decay, and the time constant is the T_1^e as desired. This is a variation on the saturation recovery measurement. The inversion recovery sequence was used, with echo detection. After each pause, only the first shot contains the desired information, so the sample must be strong enough to give a good single-shot signal. This sample had excellent single-shot signal to noise, easily satisfying the hope expressed in Section 5.5.2 for pulsed

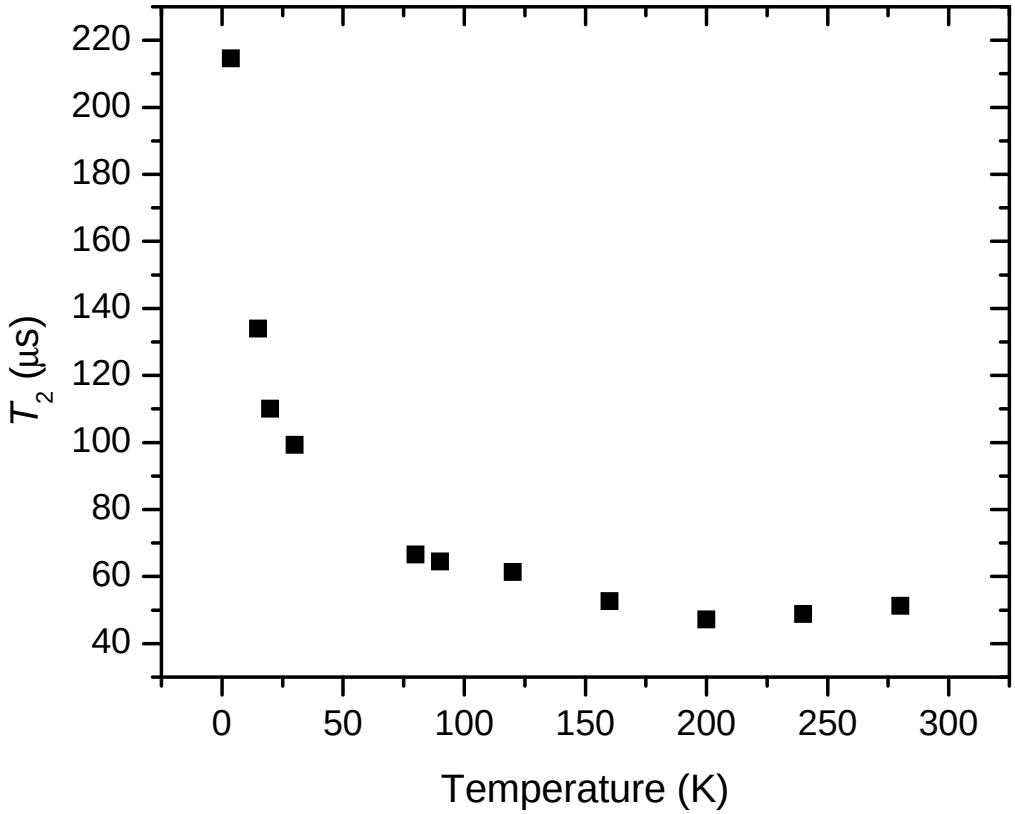


Figure 6.14: T_2 of ^{14}N@C_{60} in amorphous sulphur at various temperatures. The error bars are no bigger than the square markers.

QC readout. The polarization achieved at low temperatures increases the signal greatly, as long as a measurement is made that does not suffer from saturation.

The measurement is shown in Figure 6.16, yielding $T_1 = 4.5$ minutes. Such a long time increases the chance of performing single-spin readout of N@C_{60} as discussed in Section 2.4.4.

6.3 Conclusions

In summary, DNP has been used to create an 80% nuclear spin polarization in ^{15}N@C_{60}. This demonstrates the initialization that is the first step in a quantum computation with this molecule. Using amorphous sulphur as a solvent has made it possible to measure the T_2 of N@C_{60} as 215 μs, which is long enough for a

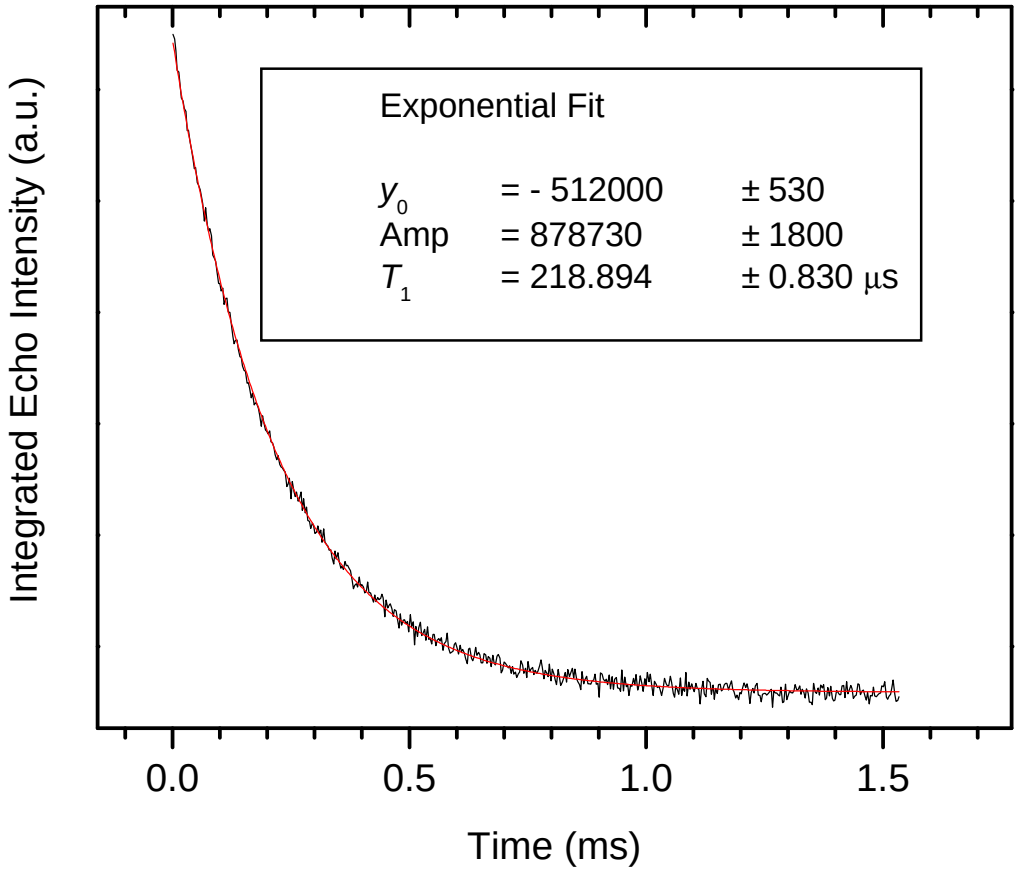


Figure 6.15: Inversion recovery T_1^e measurement of ^{14}N@C_{60} in amorphous sulphur at 280 K.

pulsed ESR machine to perform the Deutsch-Jozsa algorithm. Pulsed and CW readout techniques have been demonstrated for measuring the result of a computation. Doing these things in the same experiment would make it possible to solve Deutsch's problem with a single function call.

The nuclear T_1 of N@C_{60} has been measured using DNP to be on the order of 12 hours at 4.2 K, making it attractive for long-term storage of quantum information. The electronic T_1 has been measured as 4.5 minutes at 4 K, improving the chances of a vector measurement of this molecule's single electron spin.

These results show that N@C_{60} can be used for simple QIP and may be suitable for fully scalable QC.

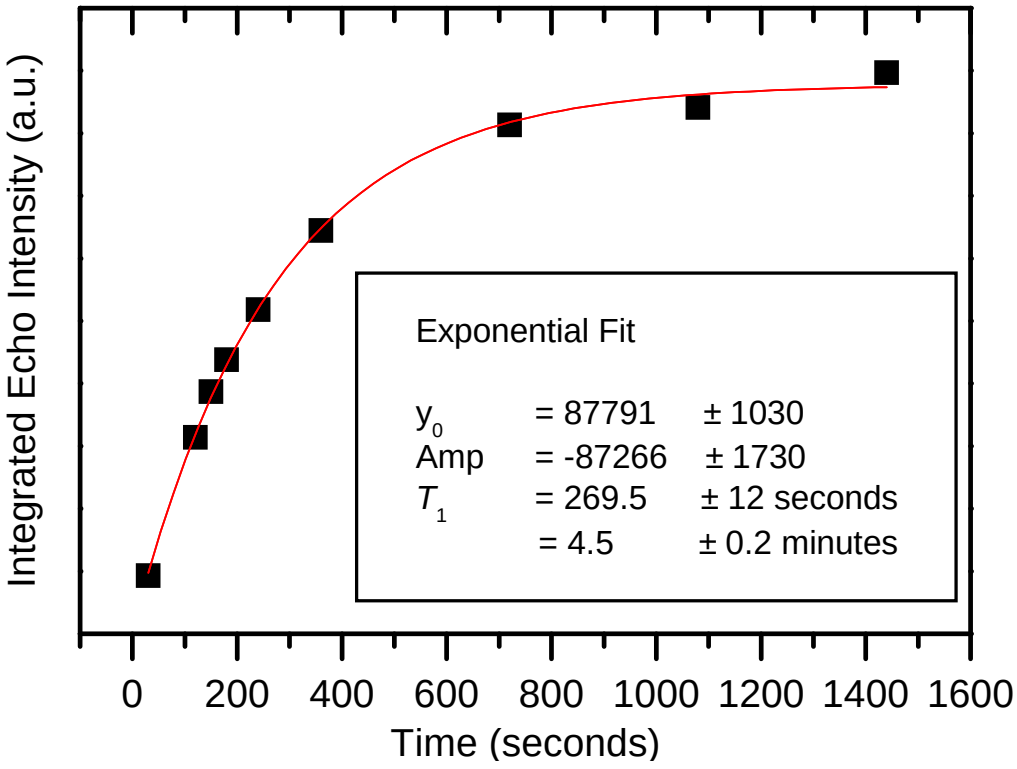


Figure 6.16: T_1^e measurement of ^{14}N@C_{60} in amorphous sulphur at 3.7 K.

Chapter 7

Sc@C_{82}

Contents

7.1 Sample Preparation 107

7.2 Electronic T_1 and T_2 Decoherence 109

7.2.1 Room Temperature 109

7.2.2 A Frozen Solution 114

7.3 Understanding Anisotropy with DFT 117

7.3.1 Summary 128

Sc@C_{82} is shown to be a useful qubit because it has long electron spin decoherence times. N@$C_{60,70}$ is the only endohedral fullerene for which the measured T_2^e times are significantly longer than Sc@C_{82}. A comparison of density functional theory (DFT) modeling with ESR experiments reveals the hyperfine and electronic structure of this molecule.

7.1 Sample Preparation

Sc@C_{82} was produced and purified by K. Porfyrakis and T. J. S. Dennis. The DC arc discharge method was used with a graphite rod doped with 0.8% Sc, following the procedure described in the literature [63]. The fullerenes were extracted from

the soot in a soxhlet extraction apparatus during several hours of operation, using boiling N,N-Dimethylformamide (DMF) as solvent. A two-stage HPLC method was employed to isolate Sc@C_{82}. In the first stage, the DMF extract was dissolved in toluene and the solution was passed through a 5-PYE (pyrenyl ethyl) column (20 x 250 mm) with pure toluene eluent. Figure 7.1(a) shows the HPLC chromatogram for the first stage of purification. During this stage C_{60}, C_{70} and higher fullerenes such as C_{78} and C_{84} were separated from Sc-containing endohedral metallofullerenes. Mass spectrometry showed that the peak eluting around 19 minutes contained mainly Sc@C_{82}. In the second stage, recycling HPLC was used to isolate Sc@C_{82}, as shown in Figure 7.1(b). Mass spectrometry (MALDI) confirmed the high purity of the material (Figure 7.1(c)).

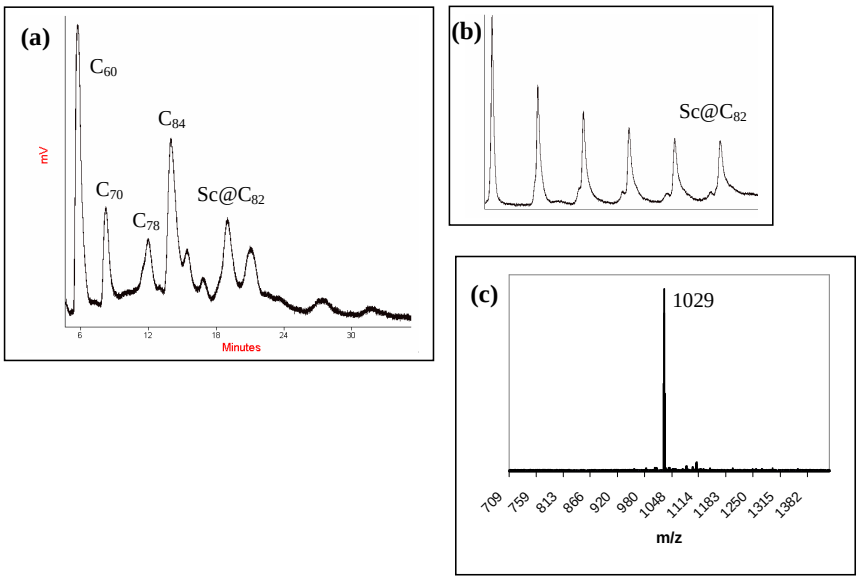


Figure 7.1: (a) HPLC chromatogram for the purification of Sc@C_{82}. The peak that elutes at around 19 minutes contains Sc@C_{82}. (b) This fraction was passed again through HPLC in recycling mode. After several cycles, pure Sc@C_{82} was acquired. (c) Mass spectrum (MALDI) of the isolated Sc@C_{82} peak. All figures courtesy of K. Porfyrakis.

This purified sample was dissolved in deuterated toluene and deoxygenated in an X-band ESR tube with three freeze-pump-thaw cycles. The ESR tube was sealed under a dynamic vacuum.

7.2 Electronic T_1 and T_2 Decoherence

Sc@C_{82} has lower symmetry than N@C_{60} because the Sc atom is chemically bound to the inside of the cage wall. Instead of simplifying the g- and A-tensors to their scalar values, anisotropy must be considered, as described below in Section 7.3.

7.2.1 Room Temperature

At room temperature, in liquid solution, the molecules tumble fast: The rotational correlation time is estimated as 5 ps [69]. For comparison, the characteristic time of the g- and A-anisotropies is estimated as ~ 50 ns from the linewidths in Figure 7.8. In this 'motional narrowing' regime, molecular anisotropy is averaged away, and Equation 4.2 remains a valid approximation.

The scandium nucleus has spin $I = \frac{7}{2}$, and Sc@C_{82} is thought to have electron spin $S = \frac{1}{2}$, on the basis of DFT calculations [66] such as those in Section 7.3. In the fast tumbling limit, this spin system has the energy levels shown in Figure 7.2, in a strong magnetic field. As shown in this figure, eight equally spaced lines are expected in a CW ESR scan.

A Bruker pulsed X-band spectrometer was used to obtain the measurements in this chapter. The room temperature CW spectrum is shown in Figure 7.3, which is consistent with Figure 7.2. The hfs constant is 0.38 mT, identifying the sample as Sc@C_{82}(I) rather than the less common Sc@C_{82}(II) [70]. Zooming in on the 4th-lowest-field line produces Figure 7.4, where the satellite features due to the hyperfine coupling to the natural abundance of ^{13}C can be seen more clearly. These are analyzed in Section 7.3. The intrinsic linewidth of the main peak is 13 μT, suggesting that the relaxation times are on the order of 3 μs. This approximate conversion is valid because the linewidth is not broadened by inhomogeneities or over-modulation.

The same sample was studied in pulsed mode. The room temperature T_1^e was measured with an inversion recovery sequence, as shown in Figure 7.5(a),

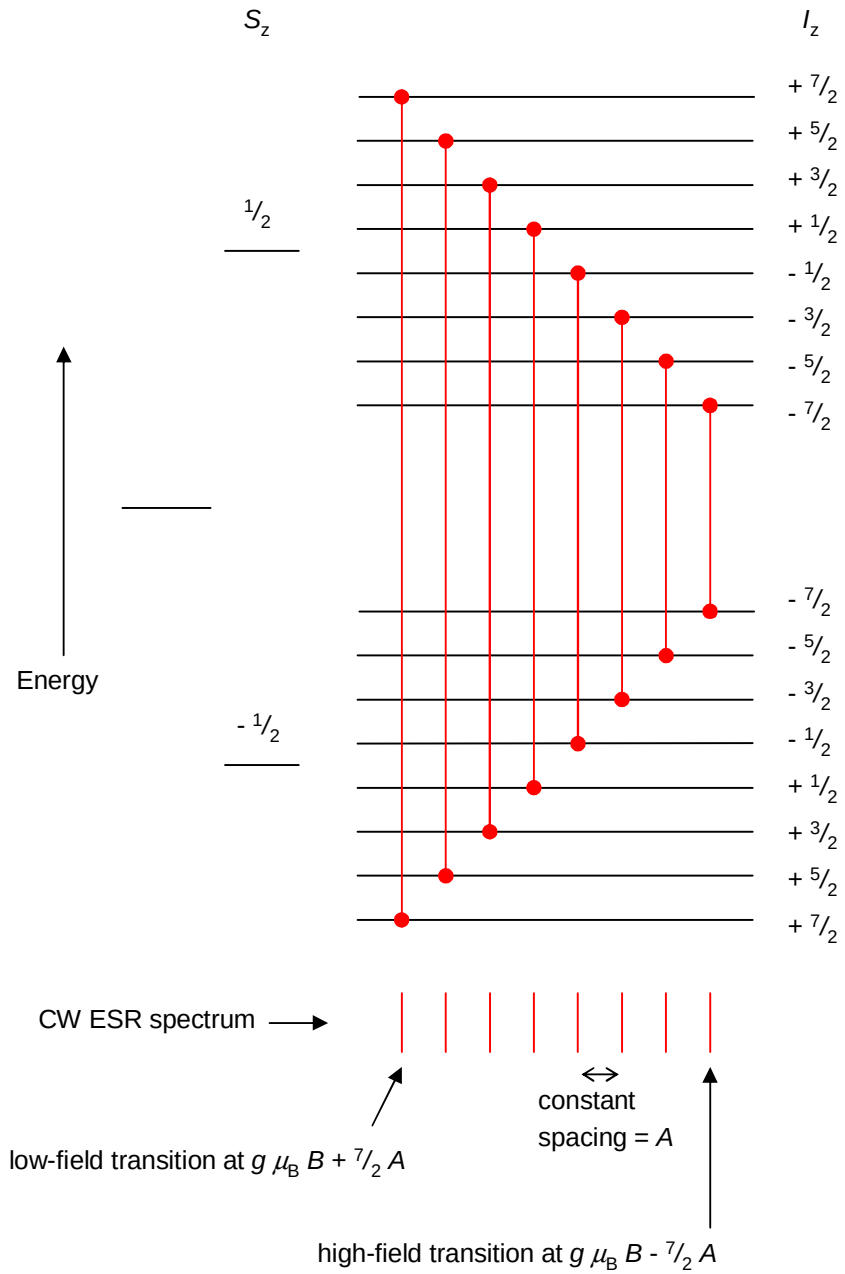


Figure 7.2: Energy levels of Sc@C_{82} tumbling fast in a strong magnetic field. The Hamiltonian used is $B(g\mu_{\mathrm{B}}S_z - g_{\mathrm{N}}\mu_{\mathrm{N}}I_z) + AS_zI_z$, with hfs constant $\frac{A}{h} = 10.67$ MHz and nuclear Zeeman frequency $\frac{Bg_{\mathrm{N}}\mu_{\mathrm{N}}}{h} \sim 3.4$ MHz at 0.33 Tesla (X-band). Eight equally spaced resonances are expected in CW ESR.

producing $T_1^e = 2.0$ μs. T_2^e was measured as 1.50 μs at room temperature with a Hahn echo sequence as shown in Figure 7.6(b). The fact that T_2^e is almost as long as T_1^e is characteristic of this motional narrowing regime. This indicates that the dephasing is dominated by spin-spin processes in which the electron spins of two $Sc@C_{82}$ molecules flip in opposite directions, according to pages 212-213 in reference [139].

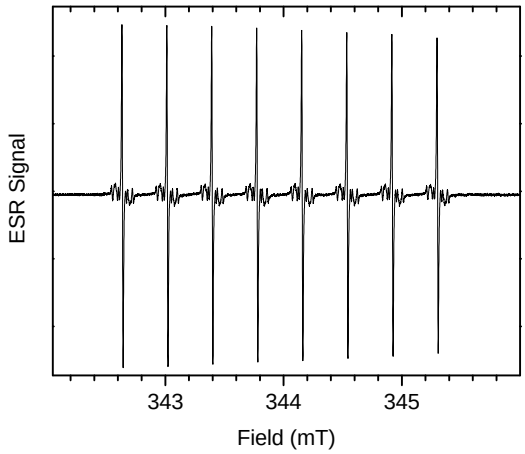


Figure 7.3: CW ESR of Sc@C_{82} in deoxygenated deuterated toluene at room temperature, as explained in Figure 7.2. Fitting with eight differentiated Lorentzians reveals that the isotropic hfs constant is 0.381 ± 0.006 mT. The microwave frequency was 9.638431 GHz, the power was 20 μW and the modulation amplitude was 0.01 mT.

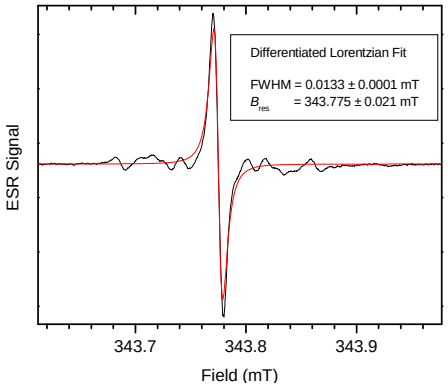


Figure 7.4: CW ESR of 4th-lowest-field resonance of Sc@C_{82} at room temperature. The satellite peaks are due to hyperfine coupled ^{13}C nuclei naturally present in the cage. These are fitted in Figure 7.13. Fitting with a single differentiated Lorentzian gives as intrinsic linewidth of 13.3 ± 0.1 μT. The microwave frequency was 9.638318 GHz, the power was 6.3 μW and the modulation amplitude was 3 μT.

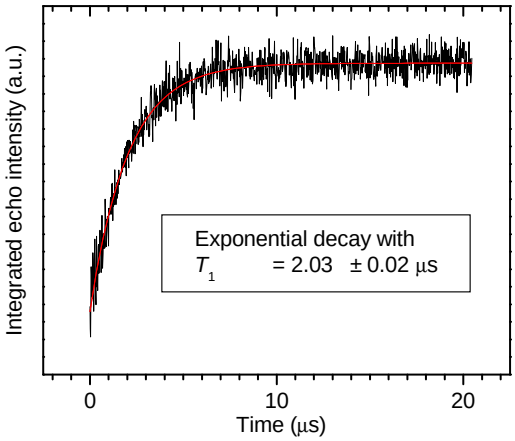


Figure 7.5: Room temperature measurement of Sc@C_{82} longitudinal relaxation time in deoxygenated deuterated toluene. The inversion recovery shows T_1^e=2.0 μs. Non-selective hard pulses were used exciting all eight lines.

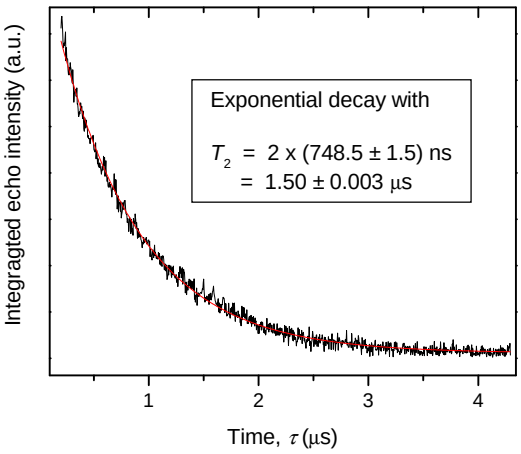


Figure 7.6: Room temperature measurement of Sc@C_{82} transverse relaxation time in deoxygenated deuterated toluene. The Hahn echo decay shows $T_2^e = 1.50$ μs. Non-selective hard pulses were used exciting all eight lines.

Rabi Oscillations at 260 K

Rabi oscillations from $Sc@C_{82}$ dissolved in deoxygenated CS_2 solvent are shown in Figure 7.7. The integrated FID intensity at 260 K is plotted against the length of a single applied pulse. The dotted green curve shows that decreasing the pulse power reduces the frequency of the Rabi oscillations. Fitting to the black curve shows that with 18 dB microwave attenuation, a π pulse is 148 ns. Higher powers would be used for QC to reduce the length of the π pulse, but these hard pulses excite more than one of the eight lines, reducing the FID signal-to-noise. Rabi oscillations are commonly measured to demonstrate that single qubit rotations can be performed. This kind of measurement in a pulsed ESR experiment suffers from a decay that would not occur in ESR QC. The signal falls with T_2^*, which is dominated by experimental inhomogeneities such as that of the microwave field. This time is shorter than the true dephasing time, T_2^e, measured with a Hahn echo. In this case, $T_2^* = 684$ ns.

7.2.2 A Frozen Solution

Freezing the sample prevents molecular tumbling, bringing out anisotropy in the g- and A-tensors of Equation 4.1. The sample is a powder, because the molecular orientation is random. This anisotropy is interpreted in Section 7.3 but the relaxation times of the powder sample can be measured without understanding the anisotropy. The blue trace in Figure 7.8 is the CW spectrum at 20 K. The resonances are inhomogeneously broadened by anisotropy in the g- and A-tensors; this broadening is not determined by the relaxation times. The same figure shows the CW spectrum at room temperature as a black trace. The field axis of these data has been scaled by the ratio of microwave frequencies, as the resonant frequency of the cavity changes significantly with such a large change of temperature. The amplitude of the room temperature data has been scaled by a factor of $\frac{1}{3}$ for clarity. This change in signal size is due to the different microwave power, field modulation amplitude, Boltzmann factor and cavity Q-factor. The significant

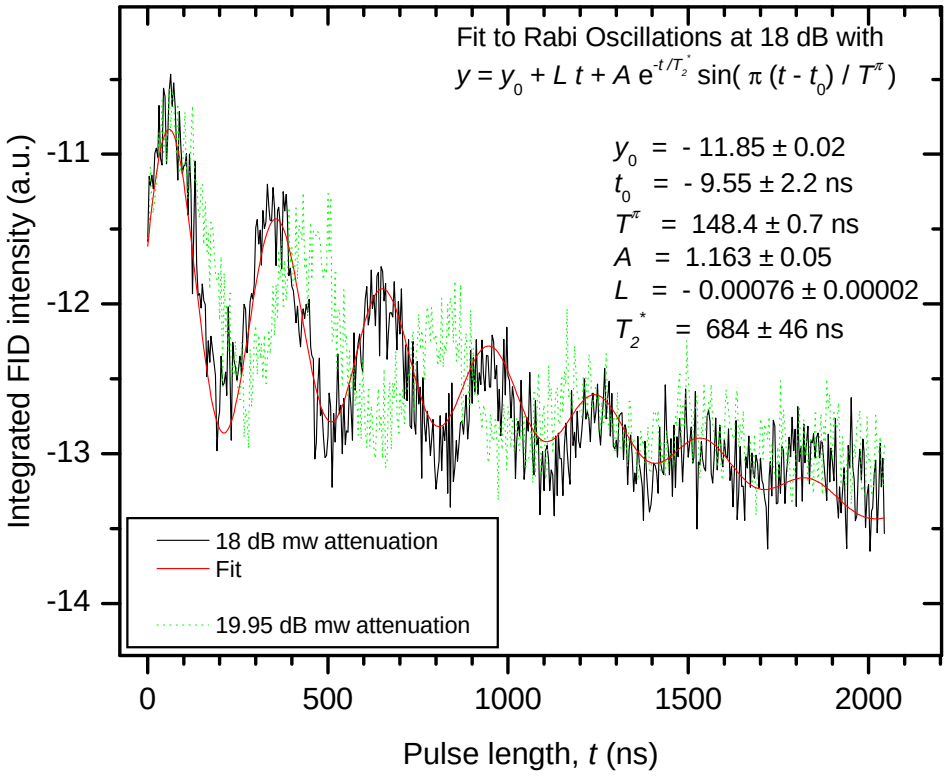


Figure 7.7: FID-detected Rabi oscillations of Sc@C_{82} in deoxygenated CS_2 at 260 K.

conclusion here is simply that these two spectra are produced by the same spin system, because they resonate in the same field range.

The green trace in the same figure is the echo-detected field-sweep (Edfs) at 20 K. The field axis has again been scaled to be comparable with the other two data-sets. As before, the information that is useful here is that resonance occurs over the same field range for all three scans. This is good evidence that these spectra are all due to the same spin system: Sc@C_{82}.

This conclusion contradicts the opinion expressed in reference [140]. An Edfs of Sc@C_{82} at 20 K found the same 3 mT plateau shown in Figure 7.8, with an extra feature: A sharper peak superimposed on the plateau. The sharper line was attributed to Sc@C_{82}, while the plateau was described as a background signal. It seems more likely that the sharper feature was an impurity that is not present in the sample described here.

The T_2^e of this plateau was measured as 13 μs at 20 K from Figure 7.9. This decoherence time is already 300 times longer than a π pulse and similar to T_2^e measurements of P@C_{60}[1]. Much longer T_2^e times should be possible, by working at lower temperatures, and with a nuclear-spin free solvent such as amorphous sulphur.

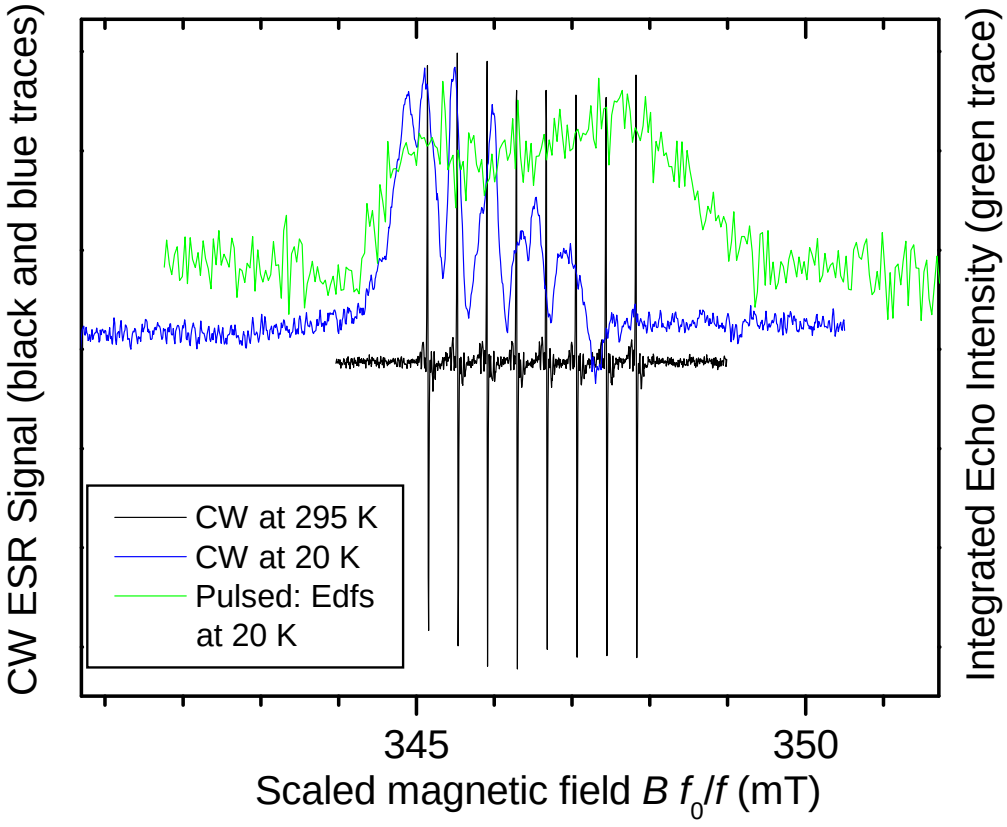


Figure 7.8: Field Sweeps of Sc@C_{82}. The blue CW spectrum at 20 K was taken with 0.2 μW microwave power at frequency $f_0 = 9.714158$ GHz, and field modulation amplitude of 0.1 mT. The black CW spectrum at room temperature used 20 μW power at 9.669895 GHz, with 0.01 mT modulation amplitude. The field axis has been scaled with the ratio of microwave frequencies $\frac{f_0}{f_{295\,\mathrm{K}}}$, to enable comparison with the 20 K spectrum. The green line is an echo-detected field-sweep at 20 K, using a frequency of 9.715360 GHz. The field axis has been similarly scaled making all three scans comparable.

Figure 7.10 shows that at 60 K, the longitudinal relaxation can be fit by a biexponential decay with time-constants 431 and 20 μs. The origin of the two

[1] P@C_{60} has $T_2^e = 14$ μs at 5 K [33].

distinct decay constants is not known. Figure 7.11 was recorded at 10 K, where T_1^e is inconveniently long: One of the time constants is 1 ms, and the other is certainly greater than 40 ms. At 4 K, the T_1^e is longer than a second and very inconvenient to measure. The sleep command mentioned in Section 6.2.2 should be used in this situation.

The T_2^e should approach these very long T_1^e times when all unwanted nearby spins are removed. This would fulfill the promise that Sc@C_{82} shows as a qubit.

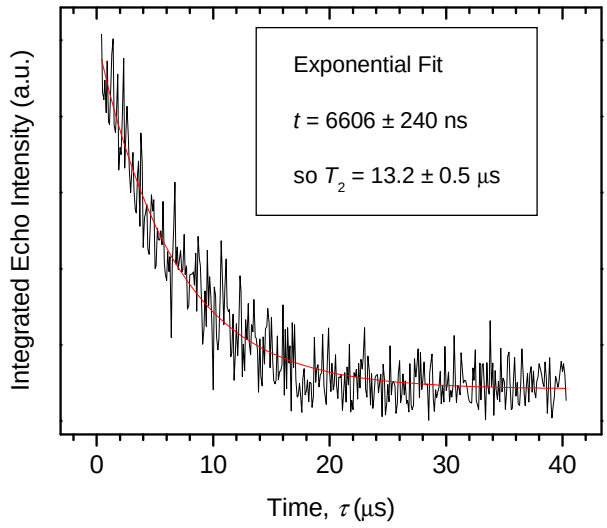


Figure 7.9: Hahn echo measurement of Sc@C_{82} at 20 K.

7.3 Understanding Anisotropic ESR with DFT Modeling

The electron spin g- and hyperfine tensors of Sc@C_{82} are anisotropic. Using ESR spectroscopy and density functional theory (DFT) modeling, their principal axes can be related to the coordinate frame of the molecule. The hfs tensor is almost axially symmetric, while the g-tensor is not. DFT calculations find that the Sc bond with the cage is partly covalent and partly ionic, as confirmed by ESR measurements of the ^{13}C and ^{45}Sc hyperfine coupling. The electron spin

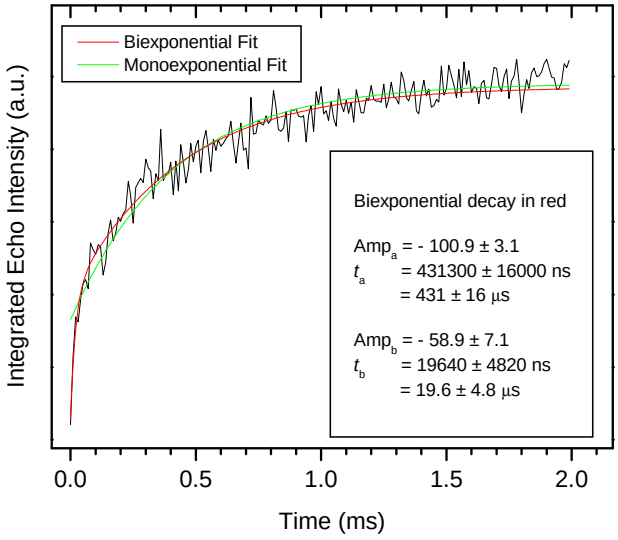


Figure 7.10: Inversion recovery measurement of Sc@C_{82} at 60 K.

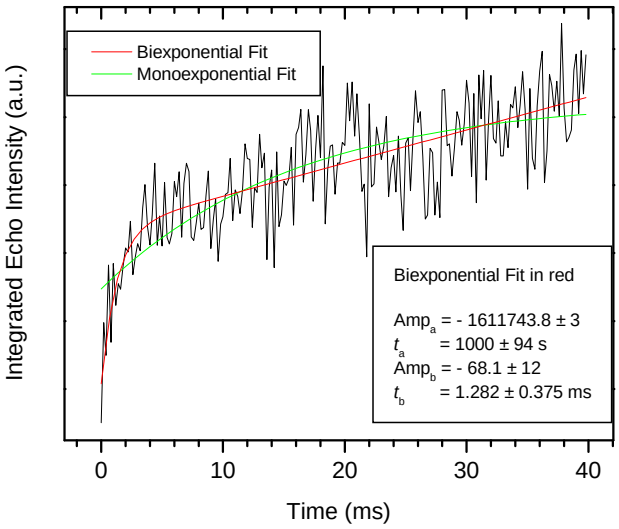


Figure 7.11: Inversion recovery measurement of Sc@C_{82} at 10 K. The signal to noise is poor because the T_1^e has become longer than the shot-repetition time, saturating the spins. The decay has not reached its baseline value, so $t_a = 1000$ s should be interpreted as $t_a >> 40$ ms.

density is distributed mainly around the carbon cage, but 5% is associated with the scandium d_{yz} orbital and this drives the observed anisotropy.

The reports of a scandium atom being trapped in fullerenes [67, 68] raised fundamental questions about the electronic and geometric structures of these species [66, 69, 70, 71, 72, 73, 74]. The initial characterization of the most stable molecule, Sc@C_{82}(I), was with electron spin resonance [67, 68]. It was found that the hyperfine coupling between the Sc nucleus and the unpaired electronic spin is only 0.38 mT, and the g-factor is close to the free electron value. These results were interpreted as evidence for the transfer of three electrons away from the metal atom to the cage. This conclusion was later supported by the small value for the nuclear quadruple interaction measured by temperature-dependent ESR [71]. Other studies have suggested less electron transfer. Hartree-Fock calculations [72, 73] described the electronic state as $Sc^{2+}C_{82}^{2-}$, which was consistent with ultraviolet photoelectron spectroscopy [74] and absorption spectroscopy with UV-vis-NIR radiation [70]. Analyzing synchrotron powder diffraction with the maximum entropy method [141] provided a value of 2.2 e^- for this charge transfer.

More recently, DFT calculations [66] have provided a compromise: Strong hybridization was found between the d valence orbitals of the Sc atom and the π orbitals of the C_{82} cage. This is similar to the hybridization that gives significant La character to the occupied part of the valence band of La@C_{82} in resonant photoelectron spectroscopy [142].

The extraordinarily long spin lifetimes exhibited by Sc@C_{82} mean that it could serve as a qubit in as-yet-unbuilt quantum information processing devices. In order to further assess the potential of this molecule, the nature of the spin state and its coupling to the molecule must be understood.

A systematic study was performed of the hyperfine structure of the endohedral metallofullerene Sc@C_{82} using all electron DFT calculations and ESR measurements. There are nine cage isomers of Sc@C_{82} that satisfy the isolated pentagon rule (IPR). DFT modeling reveals that only the isomer with C_{2v} symmetry has

isotropic ^{45}Sc and ^{13}C hyperfine splitting (hfs) constants that are consistent with ESR measurements. This confirms prior experimental observations [141] and theoretical predictions [73]. The calculated anisotropy of the hfs-tensor is in good agreement with the low temperature ESR spectrum and allows the axes of the tensor to be identified with the coordinate frame of the molecule. The spin density distribution modeled by DFT provides a value for the Sc orbital population that is in agreement with the measured ^{45}Sc isotropic hfs constant.

DFT modeling was carried out by two groups in the University of Oxford. B. J. Herbert and J. C. Green in the Inorganic Chemistry Laboratory used the facilities of the Oxford Supercomputing Centre. S. M. Lee, D. Nguyen-Manh, R. Scipioni and D. G. Petiffor used the Materials Modeling Laboratory in the Materials Department.

The energy was calculated for all the nine IPR isomers of Sc@C_{82}. DFT was used within the local density approximation (LDA) and the generalized gradient approximation (GGA) as implemented in the DMol^3 code [143]. Several different Sc positions were calculated in order to confirm the stable geometry of each isomer. The first row in Table 7.1 shows that the isomer with C_{2v} symmetry was the most stable as has been found previously. The endohedral Sc atom lies off-centre along the C_2 symmetry axis close to the C_{82} cage as shown in Figure 7.12. These calculations confirm the earlier findings of Lu *et al.* [66] that in this off-centre position there is considerable hybridization between the Sc orbitals and the C π orbitals. The distances between Sc and the nearest carbon atoms within the different isomers are given in the second row of Table 7.1.

The isotropic hfs constants were evaluated [145] within the Amsterdam density functional (ADF) code [144] using the optimized structures from DMol as input without further relaxation of the atoms. Although similar ADF calculations underestimate the hfs constants for the first row transition metals by 20-30% [146, 147, 148], the trends across the isomers should be reliable. The isotropic hfs constants for scandium are shown in the third row of Table 7.1. The stable C_{2v}

Isomer	$C_2(1)$	$C_2(2)$	$C_2(3)$	$C_s(1)$	$C_s(2)$	$C_s(3)$	C_{2v}	$C_{3v}(1)$	$C_{3v}(2)$
Relative Energy (eV)[a]	1.13	1.19	0.46	0.32	1.25	0.35	0.00	1.47	2.81
Sc-C Distance (nm)[a]	0.228	0.229	0.228	0.233	0.226	0.233	0.228	0.227	0.241
^{45}Sc hfs (mT)[b]	0.92	0.95	0.30	0.52	0.59	0.19	0.27	0.01	5.60
^{13}C hfs (mT)[b,c]	0.45	0.37	0.25	0.38	0.39	0.34	0.15	0.29	0.25

Table 7.1: DFT calculated relative energies, nearest-neighbour Sc-C distances, and ^{45}Sc and ^{13}C isotropic hfs constants for the nine Sc@C_{82} isomers.
[a] DMol^3 results using GGA functionals [143].
[b] ADF results using GGA functionals [144].
[c] Maximum value for each isomer is listed.

isomer has an hfs coupling of 0.27 mT which is 30% smaller than the experimental value. The Sc hfs was also calculated for non-aufbau occupancies of the C_{2v} isomer with the unpaired electron promoted to a series of orbitals above the Fermi level. Those with predominant d character gave hfs constants an order of magnitude larger, and when the unpaired electron was in a $4s$-based orbital the hfs constant was two orders of magnitude larger.

The carbon hfs constants for the different isomers of Sc@C_{82} were also calculated, the maximum values of each being shown in the fourth row of Table 7.1. Large hfs constants reflect the spin density becoming more localized. The small maximum value for the C_{2v} isomer indicates that the spin density is distributed over the cage rather than being localized on a given carbon atom. Figure 7.12(b) shows the spin density in the C_{2v} isomer. A number of the C atoms have very low spin density; this is a consequence of the relatively high symmetry of the molecule leading to the orbital nodes coinciding with carbon centres.

These predicted hfs constants for the C_{2v} isomer may be compared directly with values from room-temperature ESR experiments. The deoxygenated sample of Sc@C_{82} in deuterated toluene, for which relaxation times are given above, was used for these measurements. The continuous wave ESR spectra are shown in

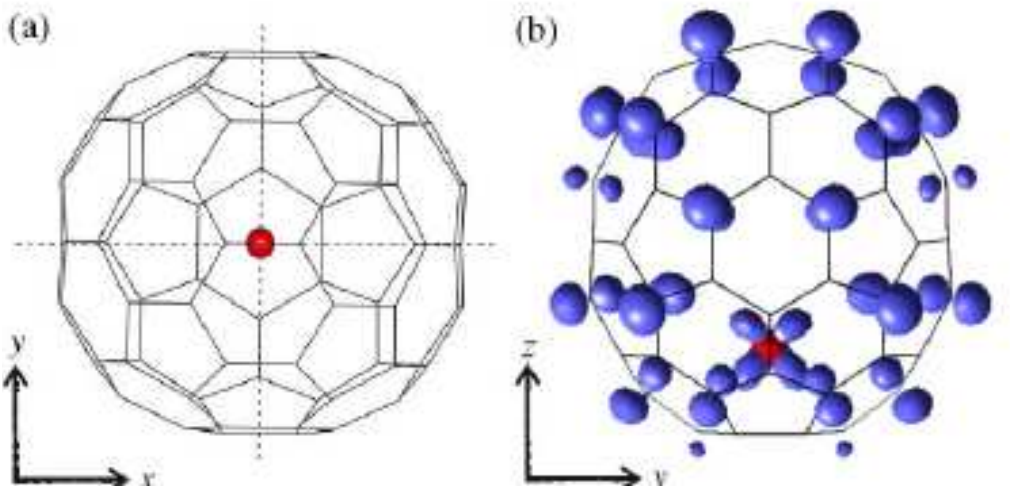


Figure 7.12: (a) Fully optimized geometry of the stable C_{2v} isomer of Sc@C_{82}. The ball is the Sc atom and the dotted lines indicate the mirror planes of C_{2v} symmetry. (b) Calculated spin density with isovalue of 0.10 μ_BÅ^{-3}. The axes define the orientation of the tensors in Equations 7.2-7.4. These figures are courtesy of J. C. Green.

Figure 7.13. The $I = \frac{7}{2}$ ^{45}Sc nucleus provides eight resonances equally spaced by an hfs constant of 0.381 mT. The sharpness of the lines indicates that the Sc atom is stationary with respect to the cage over the timescale of the ESR measurement. The electronic T_2 is 1.5 μs at room temperature, which is much longer than the length of a π pulse at these microwave powers. Therefore the relevant experimental timescale here is the length of the π pulse, which is on the order of 100 ns.

Each ^{45}Sc hyperfine line has a series of satellite lines arising from the hyperfine coupling with ^{13}C atoms on the cage. Since the natural abundance of ^{13}C is 1.1%, over half of the Sc@C_{82} molecules contain one or more ^{13}C atoms, and of these 63% contain only one. Hence the ^{13}C hyperfine structure is dominated by coupling to a single $I = \frac{1}{2}$ ^{13}C nucleus, which can be in various positions that can give different hyperfine splittings. In Figure 7.13(b) the red curve gives the best fit to the hyperfine structure using five pairs of Lorentzian lines equally split about their centre. Fewer than five pairs produced a poor fit, while more than five did not improve it. The fitted hfs constants and their weightings are given in Table 7.2.

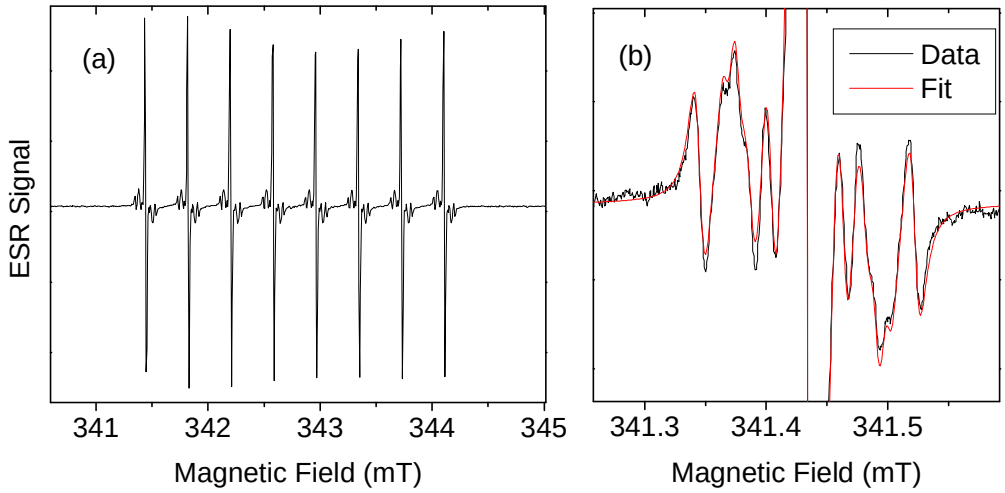


Figure 7.13: Room temperature CW ESR spectra of Sc@C_{82}: (a) full spectrum; (b) enlargement of lowest-field line, and the best fit with five Lorentzian curves, using the hfs constants in Table 7.2. The measurement shown in Figure 7.3 used a different resonant cavity with a different resonant frequency, so resonance occurs at different fields. The slight variations in the resonant amplitudes with I_z are different for these two eight-line scans. This shows that the variations are merely due to the small number of points (∼7) taken while passing through the sharp resonances with these broad scans.

^{13}C hfs (mT)	0	0.06	0.09	0.11	0.13	0.18
% of molecules	52.42	13.38	19.65	6.14	2.55	5.86

Table 7.2: The hfs constants for the experimental fit in Figure 7.13(b). Zero coupling corresponds to no ^{13}C atoms in the fullerene cage or ^{13}C in sites with negligible spin density.

These ESR measurements may be directly compared with the calculated DFT results in Table 7.1. The measured ^{45}Sc hyperfine constant is comparable with the calculated values for the $C_2(3)$ and the C_{2v} symmetries, though as expected the calculations somewhat underestimate the strength of the coupling. The ambiguity between these two isomers is removed by the ^{13}C coupling. The largest experimental value that can be taken from the measurements in Table 7.2 is 0.18 mT. The calculated value for C_{2v} is 17% less than this, but the calculated value for $C_2(3)$ is 67% greater. Assuming the ADF calculations are giving consistently low values for the hfs constant, the isomer used for ESR experiments must indeed

have C_{2v} symmetry, as expected.

The anisotropy of the hfs-tensor was measured by freezing the solvent. This removes the isotropic averaging which was present in the room temperature ESR spectra. Figure 7.14 shows the resultant ESR spectrum at 80 K for the same sample of Sc@C_{82} that was measured at room temperature in Figure 7.13. Without the motional averaging due to molecular tumbling, the eight lines that were sharp in Figure 7.13(a) are broadened by the anisotropy. This experimental spectrum was fitted with the effective spin Hamiltonian

$$H = \mathbf{S} \cdot \mathbf{g} \cdot \mathbf{B} + \mathbf{S} \cdot \mathbf{A} \cdot \mathbf{I}, \tag{7.1}$$

where $S = \frac{1}{2}$ and $I = \frac{7}{2}$, with the g- and A-tensors restricted to being diagonal. The six fitted parameters were optimized using standard numerical iteration techniques producing the red curve in Figure 7.14. This procedure yielded a g-tensor

$$\mathbf{g} = \begin{pmatrix} 1.9968 & 0 & 0 \\ 0 & 2.0033 & 0 \\ 0 & 0 & 1.9998 \end{pmatrix} \tag{7.2}$$

and an hfs-tensor

$$\mathbf{A} = \begin{pmatrix} 0.55 & 0 & 0 \\ 0 & 0.28 & 0 \\ 0 & 0 & 0.26 \end{pmatrix} \text{ mT}. \tag{7.3}$$

The g-tensor is not axially symmetric, even though the hfs-tensor may be regarded as approximately axial. Previously the g-tensor had been obtained from experiment by assuming that it is axial and using the Kivelson equations to determine the two unknown constants from a series of ESR spectra obtained at a range of temperatures. This yielded differences between the constants of 0.0128 [149] and more recently 0.005 [69], which may be compared with the r.m.s. dif-

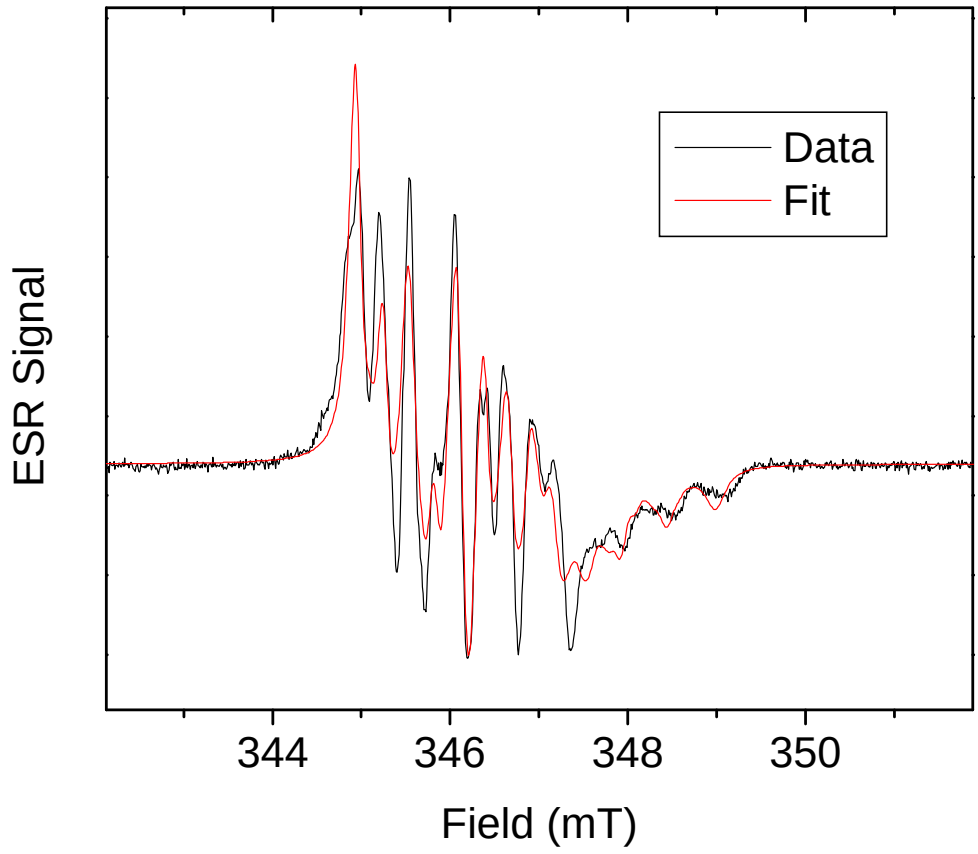


Figure 7.14: ESR scan of Sc@C_{82} at 80 K in frozen solution. The data were fitted using the g-tensor given in Equation 7.2 and the hfs-tensor given in Equation 7.3. The slight change in resonant field compared with Figure 7.13 arises from retuning the microwave frequency following the change in the cavity temperature.

ference of 0.0033 between the two pairs of adjacent constants in the non-axial g-tensor, Equation 7.2. The non-axiality confirms that Sc@C_{82} does not have C_{3v} symmetry, since this higher symmetry would produce an axial g-tensor.

The hyperfine tensor of the C_{2v} isomer was calculated using the ADF code [144] for a single molecule with a known geometry and orientation. In the coordinate system shown in Figure 7.12, the hfs-tensor is

$$\mathbf{A} = \begin{pmatrix} 0.47 & 0 & 0 \\ 0 & 0.23 & 0 \\ 0 & 0 & 0.19 \end{pmatrix} \text{ mT} \tag{7.4}$$

which is comparable with the experimentally determined tensor in Equation 7.3, with an underestimation by the usual factor of ∼20%. The anisotropy factors ($\Delta A = A_{zz} - \frac{A_{xx}+A_{yy}}{2}$) may also be compared: The DFT tensor in Equation 7.4 and the ESR tensor in Equation 7.3 both have $\Delta A = 0.26$ mT; previous measurements of temperature-dependent ESR linewidths provided $\Delta A = 0.3$ mT [69] and 0.31 mT [149], by assuming $A_x = A_y$.

The relationship between the calculated and measured hfs tensors enables the principal axes of both of the experimental tensors to be related to the molecular orientation indicated in Figure 7.12. This is convenient because the hfs tensor calculated by DFT underestimates the true coupling strength, and it is particularly difficult for DFT to calculate the g-tensor.

The spin density on the Sc site in Figure 7.12(b) is associated with the $3d_{yz}$ orbital, which is found to account for 5% of the semi-occupied molecular orbital (SOMO), corresponding to the spin $\frac{1}{2}$ eigenstate of Sc@C_{82}. This controls the anisotropy of the g- and hfs-tensors: Figure 7.15 shows that the d_{yz} orbital (lower right) is symmetrical with regard to the following four transformations:

- 180° rotation about the x-axis
- reflection in the plane $x = 0$
- reflection in the plane $z = y$
- reflection in the plane $z = -y$

All of these symmetries are possessed (to a good approximation) by the experimental hfs tensor, Equation 7.3, as it is almost axial about the x-axis. The small deviation from axiality in Equation 7.3 is consistent with the DFT finding that there is a small amount of Sc spin density which is not associated with the $3d_{yz}$ orbital

Mulliken population analysis of the calculated Sc valence orbitals assigns a charge of +0.8 to Sc, and other methods of charge estimation give slightly lower

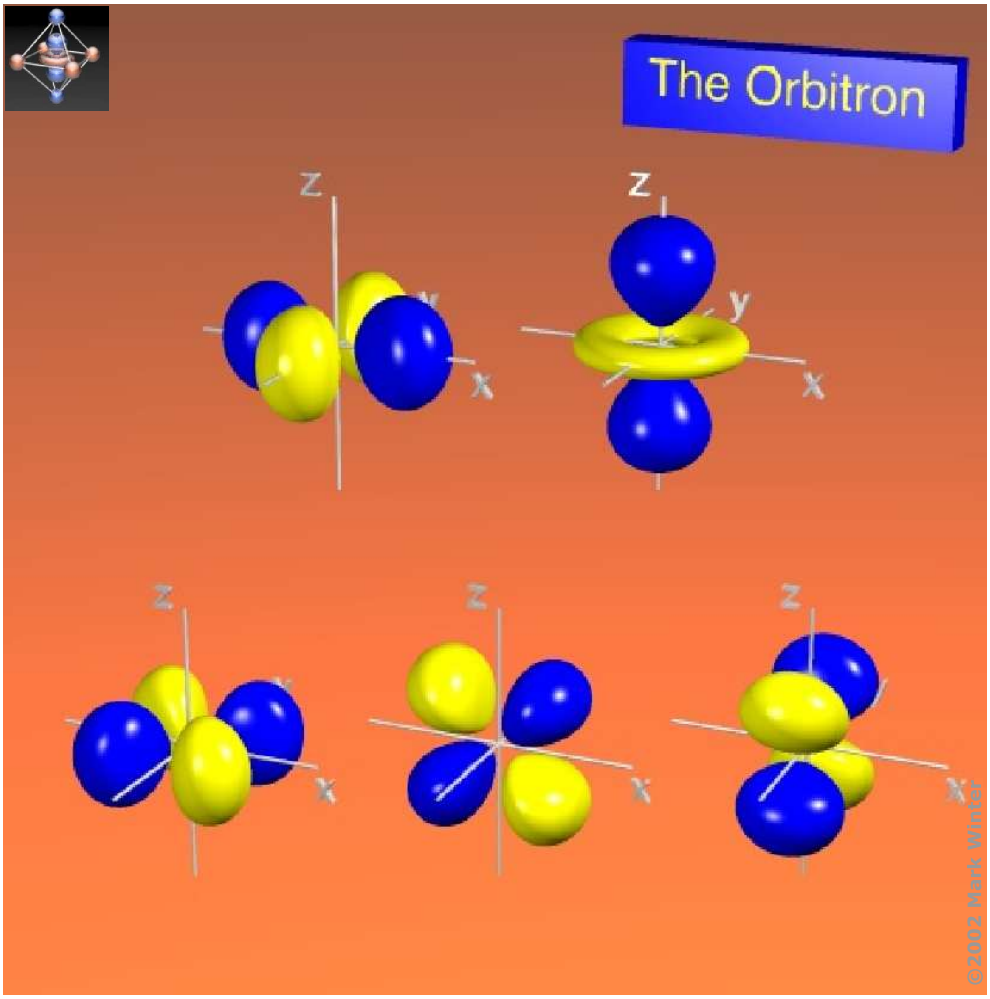


Figure 7.15: The shapes of the five different $3d$ orbitals. From left to right, the top row shows $3d_{x^2-y^2}$ and $3d_{z^2}$, while the bottom row shows $3d_{xy}$, $3d_{xz}$ and $3d_{yz}$. The d_{yz} orbital contains most of the spin density present on the Sc atom in Sc@C_{82} as found in DFT calculations. This picture is copyright Mark Winter 2002 [137].

values. The combined electron density in the $4s$ and $4p$ orbitals is 0.56, with the d-orbitals containing a further 1.53 electrons. Most of the spin density on Sc is contained in the d orbitals, with the major contributor being the d_{yz} orbital. This orbital contributes ∼5% to the SOMO.

ESR measurements of Sc^{2+} ions substituted for Ca^{2+} in a CaF_2 crystal found the hfs constant to be 6.92 ± 0.05 mT [150]. To facilitate comparison with this, the hfs constant of an isolated Sc ion was calculated as a function of the number of spin-polarized d electrons using the programme for the linear combination of

atomic orbitals (PLATO) [151]. The dependence is approximately linear from zero $3d$ electrons up to one, as shown in Figure 7.16 for both a Sc^{2+} ion and a Sc ion with combined electron density in the $4s$ and $4p$ orbitals of 0.56. The discrepancy between the Sc^{2+} calculation and the experimental point is 23%, which arises from the spherical approximation for the atom, neglect of the environment, and the local spin density approximation for exchange and correlation. However, the approximately linear trend is more reliable than the absolute values. Linear interpolation between 6.92 mT and the origin converts the measured hfs constant of Sc@C_{82} into a d orbital occupancy of 5.5%, in excellent agreement with the 5% spin density calculated for the Sc d_{yz} orbital.

7.3.1 Summary

The hyperfine and g-tensors of Sc@C_{82}(I) have been written in the coordinate frame of the molecule by combining information from both theory (DFT) and experiment (ESR). Although the hfs-tensor is almost axially symmetric, the g-tensor is not (in contrast to previous assumptions). The symmetry of Sc@C_{82}(I) has been confirmed as C_{2v}, with the metal atom lying far off-centre along the symmetry axis, adjacent to a six-membered carbon ring. This results in strong hybridization between the Sc d orbitals and C π orbitals, so that the bond is partially covalent, partially ionic with a Mulliken charge of +0.8 on the Sc site. The electron spin density is distributed mainly around the carbon cage with 5% of the spin eigenstate associated with the Sc d_{yz} orbital, which determines the anisotropy of the resultant g- and hfs-tensors.

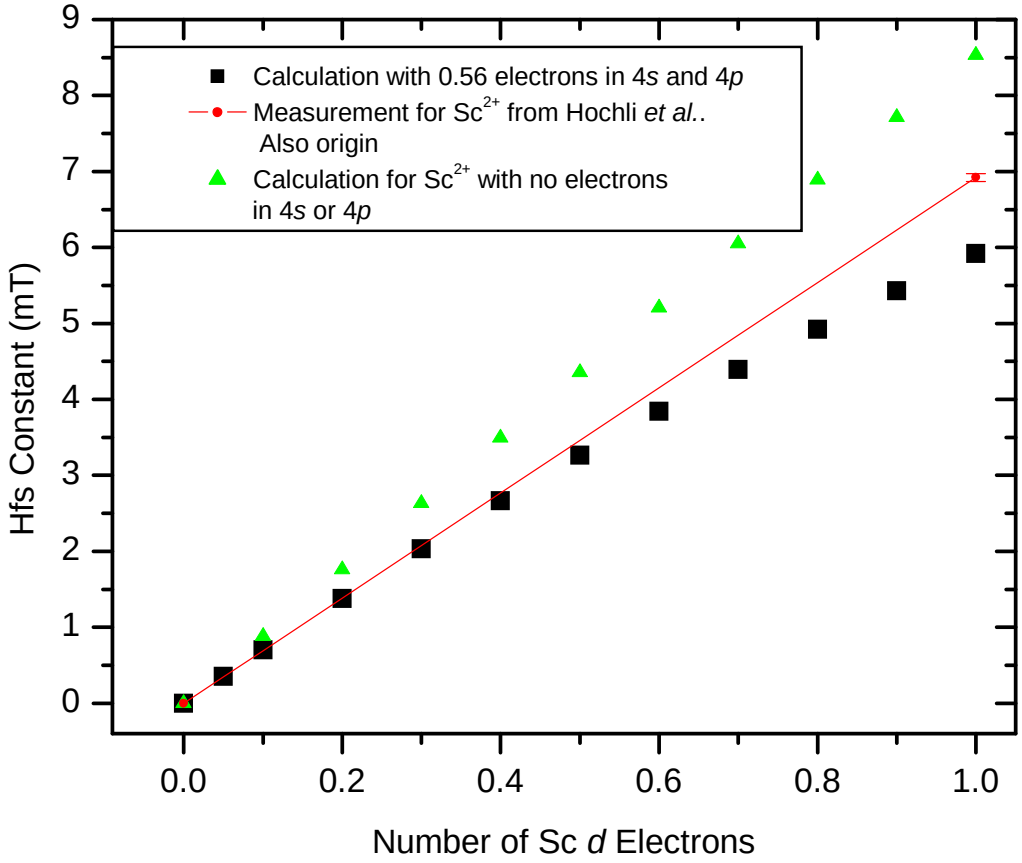


Figure 7.16: Dependence of the hfs constant for an isolated Sc ion on $3d$-orbital occupancy. The black and the green points were calculated from DFT with GGA (using the PLATO code [151]) for the sp occupancies shown. Both of these calculations find approximately linear relations. The green point for one d electron can be compared with the experimental measurement shown as a red dot with error bars. The straight red line joins this experimental point to the origin, which is assumed to be a reliable point. This line is shown only as a guide to the eye. It was used to interpolate the d orbital occupancy of Sc@C_{82} using the measured value of the isotropic hfs constant, $A = 0.381$ mT. This figure is courtesy of A. P. Horsfield.

Chapter 8

Two Spin-Active Endohedral Peapods

Contents

8.1 Nanotubes 131

8.1.1 Solution ESR 133

8.2 N@C_{60} Peapods 134

8.2.1 Modeling the Dipolar Interaction between N@C_{60} molecules in SWNTs 141

8.3 Sc@C_{82} 143

8.3.1 ESR of Sc@C_{82} Powders 144

8.3.2 Peapod Synthesis 145

8.3.3 Pure Sc@C_{82} Peapod Powders 147

8.3.4 Samples Dispersed in CCl_4 156

8.4 Conclusions 162

The one-dimensional cavity inside single-walled carbon nanotubes (SWNTs) has been exploited as a nanoscale container for a range of species [152]. When fullerenes such as C_{60} are encapsulated the resulting structures are known as peapods. Structures of this kind employing functionalized or endohedral fullerenes have been proposed as candidates for scalable quantum information processing

(QIP) applications [35]. Global addressing [38] or local gating [35] architectures could be used to control these one dimensional arrays of qubits. Both of these approaches to QIP would require a technique for vector measurements of a single electron spin in order to readout the result of the computation.

8.1 Single Walled Nanotubes

The SWNTs studied in this chapter were purchased from Carbolex [153] and purified to remove catalyst impurities. The purification consisted of air anneals at 315-410°C, heating in a kitchen microwave, and refluxing in 37% HCl [132, 154]. This process also reduces the number of different nanotube diameters from about five to two as measured with Raman spectroscopy [132]. The nanotube diameters after purification were 1.49 nm and 1.36 nm. Significantly smaller SWNTs are too narrow to accept fullerenes.

The purified sample was baked at 300°C in an ESR tube, while pumping to remove water and oxygen, before sealing the tube. The ESR spectrum of this sample has an extremely broad feature, shown in Figure 8.1. This Lorentzian resonance has been attributed to catalytic impurity particles such as nickel and yttrium remaining from the nanotube growth [132]. The inset shows a zoom of the smaller feature at $g \sim 2$, which is attributed to conduction electrons. This resonance has been fit with a linear term (to account for the broad impurity) added to a Lorentzian. The line is 1.6 mT wide, and the g-factor has previously been estimated as 2.003 ± 0.002 [132].

The paramagnetic impurities that produce the broad feature are likely to provide a very significant decoherence mechanism for any other spins in the sample, broadening their lines in CW ESR. However, the broadness of this resonance means that it can often be ignored when looking at small CW scans near $g = 2$. In Figure 8.1 the inclusion of a linear term improved the fit of the 1.6 mT wide conduction-electron-resonance, but this would not be necessary for resonances

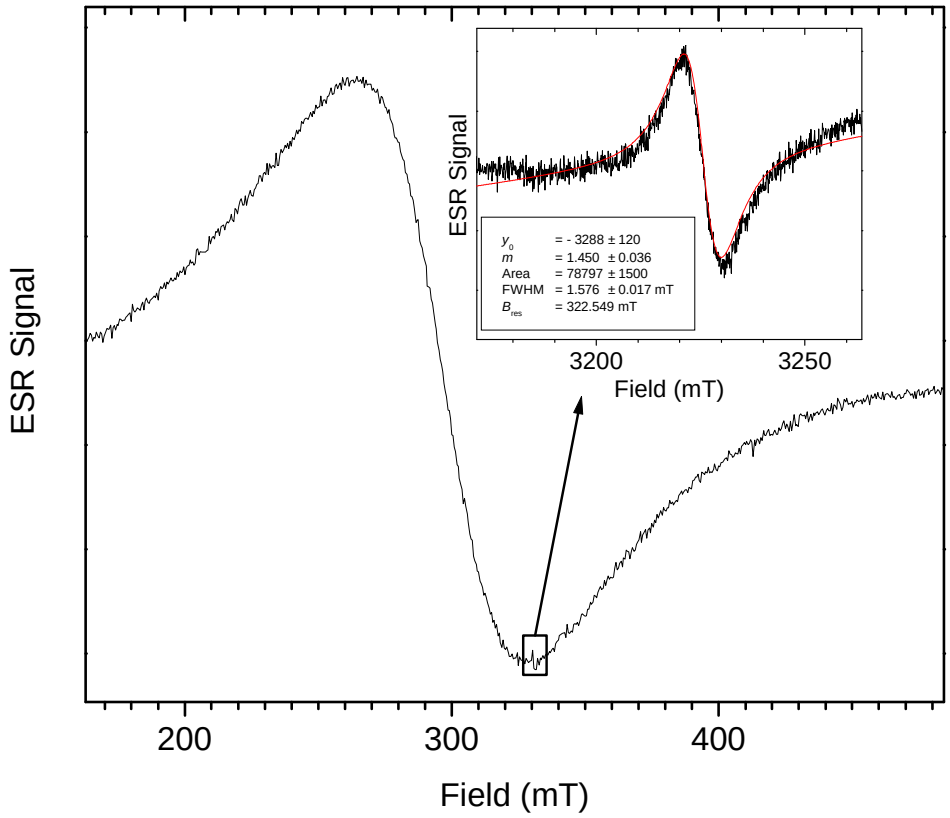


Figure 8.1: Broad ESR spectrum of purified SWNTs at room temperature. This was an eight minute sweep with a power of 12.5 mW and a modulation amplitude of 0.1 mT. Inset shows the smaller resonance at $g \sim 2$ due to conduction electrons in the metallic SWNT. This scan lasted 16 minutes with 10 mW power and 0.4 mT modulation. This feature was fit with a linear term, of gradient m (to account for the very broad feature), added to a Lorentzian of width 1.58 mT. These measurements were made at 9.1 GHz on the CW JEOL spectrometer in University College London, with the permission of M. C. W. Evans.

that are significantly sharper. Both of the resonances in the SWNT spectrum are distinguished by their resistance to saturation. Using a microwave power of 10 mW would saturate most ESR signals (including manganese ions, the nitroxyl radical TEMPO, $N@C_{60}$, $Sc@C_{82}$, $Nd@C_{82}$), but increasing the power to 100 mW is not sufficient to saturate the broad impurity resonance. The great width of this feature corresponds to very short relaxation times, which is why a particularly high power would be needed to produce saturation.

8.1.1 Solution ESR

ESR of nanotubes is complicated by their electrical conductivity and tendency to coalesce into ropes. The conducting ropes affect the microwave distribution, significantly reducing the quality factor of the cavity, and shielding any paramagnetic species that are encapsulated. In practice, these factors restrict the amount of material that can be used in ESR experiments to about 0.3 mg, corresponding to a very small quantity of the encapsulated paramagnetic species. In order to permit the use of larger quantities, in excess of 0.5 mg, the SWNTs were dispersed in CCl_4. This partially breaks apart the ropes, making them less thick. The solvent was deoxygenated with three freeze-pump-thaw cycles, and then the ESR tube was sealed under a dynamic vacuum.

The spectrum of this sample around $g = 2$ is shown in Figure 8.2. The single conduction-electron-resonance has been replaced by many features that are sharper than 1.6 mT. These features are clearly much smaller than the conduction-electron-resonance in the powder: The latter could be seen in Figure 8.1 without any zooming. Again a high power was used: 19.78 mW, without saturating these SWNT features.

The electronic properties of a sample of SWNTs are complex because various diameters and chiralities are generally present, leading to a variety of bandgaps. It is possible that Figure 8.2 shows the separate resonances of the different nanotubes present because the ropes are dispersed. A rope of many different nanotubes could be expected to behave like a single conductor with a lower electrical resistance than single tubes: The electrons in a rope have more freedom to move.

In the remainder of this chapter, the goal is to find resonances due to the spin-active endohedral fullerenes that have been inserted into these SWNTs.

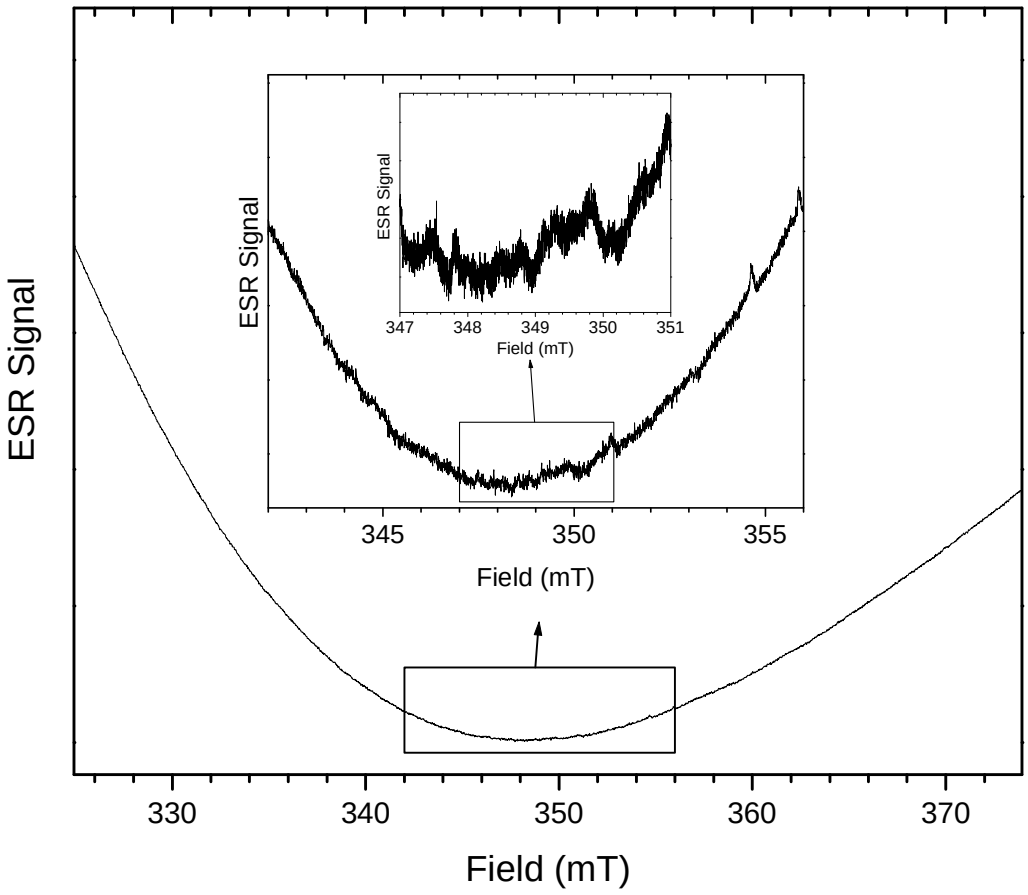


Figure 8.2: ESR spectrum of purified SWNTs dispersed in deoxygenated CCl_4 at room temperature. The trough of the broad feature in Figure 8.1 is shown, with a zoom and a zoom-zoom of $g = 2$.

8.2 N@C_{60} Peapods

Among all endohedral fullerenes, N@C_{60} has the longest spin coherence times, making it the most promising candidate qubit. Chapters 5 and 6 showed that there are excellent prospects for QC with this molecule. The N@C_{60} peapods in this chapter were all made with ^{14}N@C_{60}, but ^{15}N@C_{60} could just as well have been used.

The conventional approach to making peapods involves heating a dry mixture of fullerenes and SWNTs such that vapourized fullerenes diffuse into the nanotubes at temperatures of several hundred degrees centigrade [118]. This method cannot be used for filling with N@C_{60} because of its poor stability at temperatures

much above room temperature [85]. As an alternative, a highly efficient technique for producing peapods at moderate temperatures was used [100, 122], employing supercritical fluids (SCFs) [155] as a fullerene solvent.

The low viscosity and absence of surface tension of SCFs, combined with the low solvation effect of solvent molecules interacting only weakly with the solute provide a high diffusivity approaching that of the gas phase. Supercritical carbon dioxide ($scCO_2$) was chosen as the SCF medium as it has a critical temperature of 31°C [155], well below the decomposition temperature of N@C_{60} [85].

Raw N@C_{60} in C_{60} was produced by C. Meyer, W. Harneit and A. Weidinger at HMI-Berlin. The 'glow discharge' method was used [86] to make a sample in which about 0.01% of the cages were filled. HPLC followed by recycling HPLC was used to enrich this raw material to greater than 0.25% purity. The enriched sample was dissolved in CS_2 and mixed with SWNTs. The CS_2 solvent was then quickly evaporated at room temperature. The resulting dry nanotube-fullerene mixture was immersed in $scCO_2$ in a high-pressure cell at 35 - 50°C under 150 bar for 10 days. After depressurisation, non-encapsulated fullerenes were removed from the nanotube surface by repeated sonication in CS_2 and filtration. This material was examined by high-resolution transmission electron microscopy (HRTEM) revealing that about 60% of the SWNTs were filled, as shown in Figure 8.3. The SCF-filling was performed by A. N. Khlobystov at Nottingham University in M. Poliakoff's laboratory.

This sample was studied with a CW Bruker X-band ESR spectrometer in Warwick University with M. Newton and R. Crudace. The spectrum obtained under these conditions is shown in Figure 8.4 as a black trace. The characteristic N@C_{60} triplet is the dominant feature. The green trace shows the spectrum of unfilled SWNT from the same batch. The field axis of this SWNT scan has been scaled to allow for the slightly different microwave frequency used. The amplitude of the SWNT scan has been reduced to allow comparison of features in the green and black traces. This was necessary because the unfilled SWNT sample contained

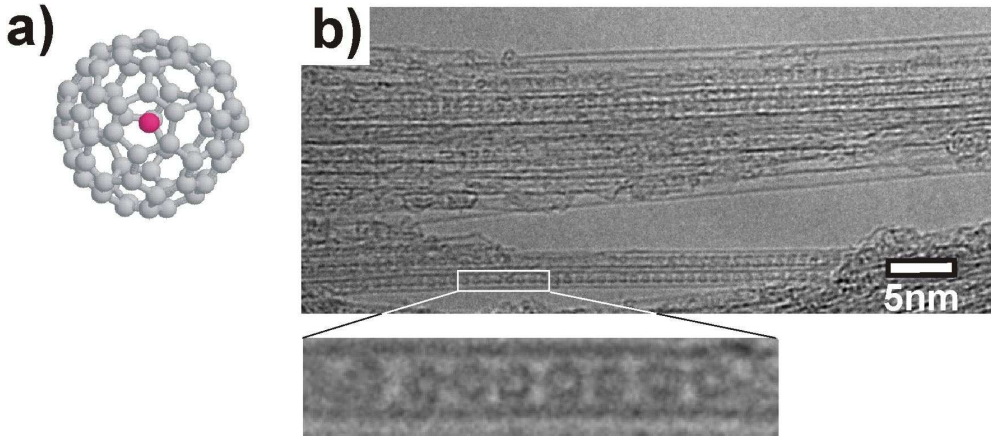


Figure 8.3: a) Structure of N@C_{60} b) HRTEM micrographs of SWNTs filled with ^{14}N@C_{60} using scCO_2 at room temperature, courtesy of A. N. Khlobystov.

more material. The red curve is a Lorentzian fit to the broad feature in the black N@C_{60} peapod scan. This feature probably arises from the nanotubes, as it can also be seen in the spectrum of unfilled SWNT. The yellow curve is a fit to a resonance that does not seem to be present in the SWNT scan. It is possible that this is a SWNT feature that has moved to a different g-factor as a result of interactions with the N@C_{60} molecules.

The black trace in Figure 8.5 shows the N@C_{60} peapod spectrum again. The red trace in this figure is the spectrum of N@C_{60} from the same batch that was used to fill the SWNTs. This sample was dissolved in deoxygenated CCl_4. The lineshape appears saturated even though the microwave power was only 20 μW. This may be due to fullerene clustering as the solubility of C_{60} in CCl_4 is significantly lower than in toluene. With this enriched N@C_{60}, clustering will produce significant line-broadening. The field axis of this spectrum has been scaled to allow comparison with the peapod spectrum. The two spectra have about the same g-factors and hyperfine splittings. These parameters are given in Table 8.1, after scaling each field axis with respect to a known reference sample: Nitrogen defects in a single diamond crystal were used, whose g-factor is 2.0024(1). Measuring this reference sample revealed that the spectrometer magnet is actually 1.385 mT

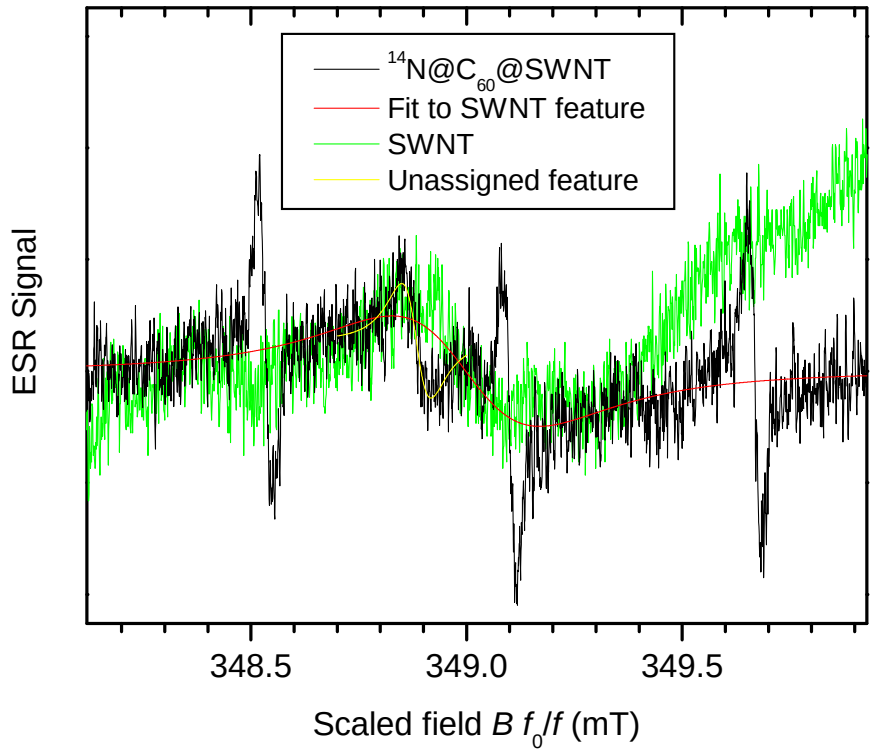


Figure 8.4: CW ESR spectrum of N@C_{60}@SWNT (black trace) and SWNT (green trace), both dispersed in deoxygenated CCl_4. The N@C_{60} triplet is clearly seen from inside the nanotubes. The red curve is a Lorentzian fit to the SWNT feature in the N@C_{60} peapod. This occurs at $g = 2.0049$ and the FWHM is 0.59 mT. The field axis of the SWNT data has been scaled to allow comparison with the peapod scan at a slightly different frequency. The yellow curve is a Lorentzian fit to the small unassigned feature present in the peapod spectrum. This resonance occurs at $g = 2.0055$ and the FWHM is 0.085 mT.

lower in field than it claims to be.

After the SWNT filling process, non-encapsulated fullerenes were removed from the nanotube surface by repeated sonication in CS_2 and filtration. The efficiency of this washing was checked by preparing a control sample of N@C_{60} mixed with SWNTs in CCl_4; its EPR spectrum is shown in Figure 8.5 as a green trace. Owing to the low solubility of N@C_{60} in CCl_4, the fullerenes are likely to aggregate on the surface of nanotubes due to van der Waals forces, but peapods do not spontaneously form. This is confirmed by the fact that washing a mixture prepared in this way removed the N@C_{60} and produced a sample without the characteristic N@C_{60} ESR spectrum. The spectrum of this washed sample is shown in Figure

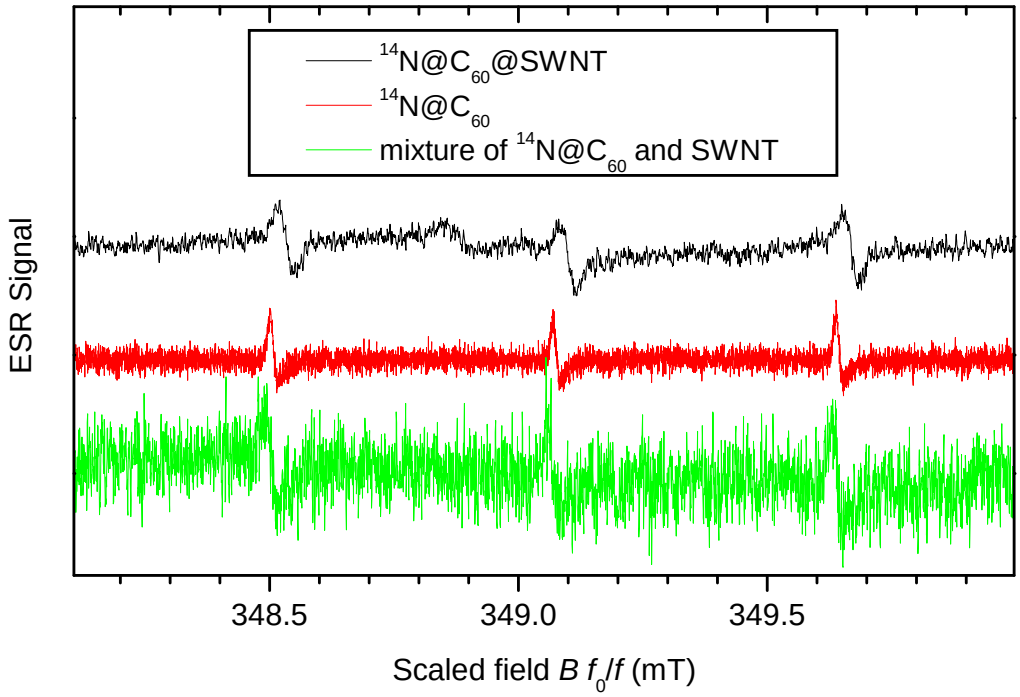


Figure 8.5: CW ESR spectrum of N@C_{60}@SWNT (black), N@C_{60} (red) and a mixture of N@C_{60} and SWNT (green). The nanotube samples are dispersed in deoxygenated CCl_4 and the fullerene is dissolved in the same solvent. The field axes of the red and green traces have been scaled to allow comparison with the peapod scan at a slightly different frequency. The traces are vertically offset for clarity.

8.6 as a black trace. The peapod signal is shown as a light blue trace to indicate the N@C_{60} pattern qualitatively. These two signals were recorded on different spectrometers, so their amplitudes cannot be compared directly: They were simply scaled for convenient viewing. The field axis was scaled for the difference in the microwave frequency, but the uncertainty in the frequency of the spectrometer used to scan the washed sample corresponds to 1 mT.

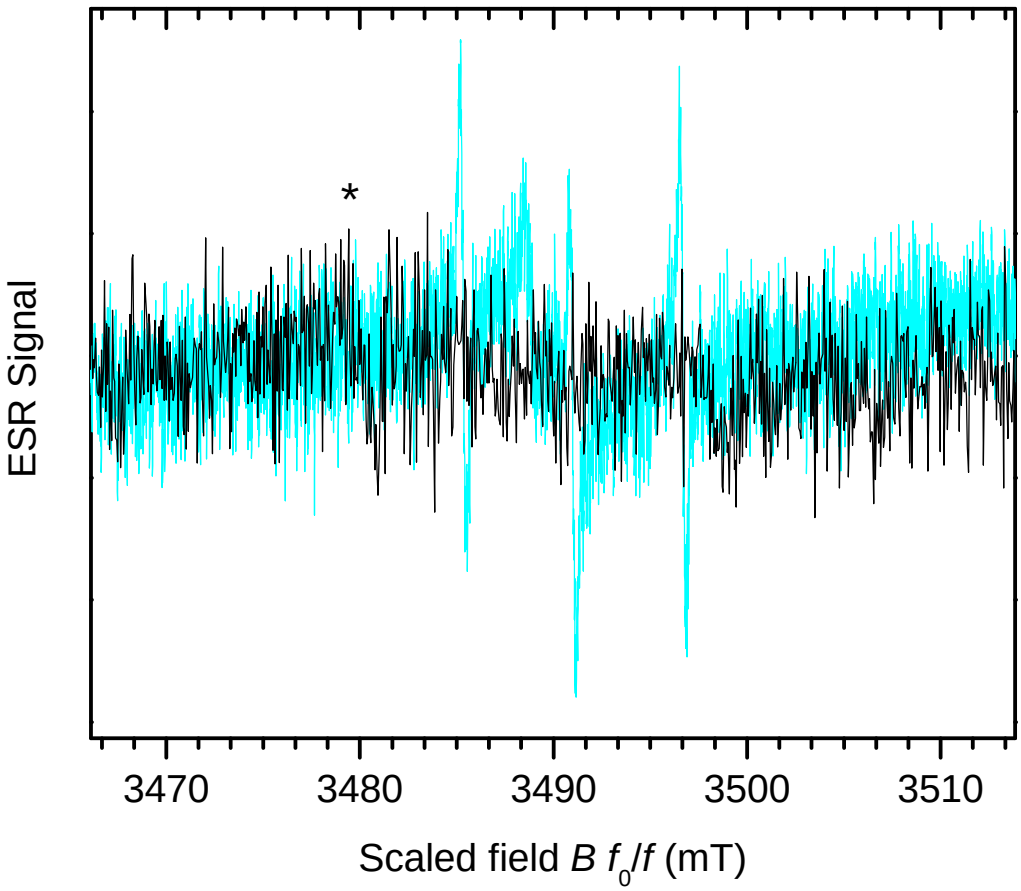


Figure 8.6: CW ESR spectrum of a washed mixture of N@C_{60} (black trace). The light blue trace is the spectrum of N@C_{60}@SWNT peapods after the same washing procedure: Repeated sonication in CS_2 and filtration. The characteristic N@C_{60} ESR spectrum is not present in the sample that did not experience SCF-filling. The two spectra can only be compared qualitatively as the black line was recorded on a different spectrometer. The feature marked with a star is assigned to the SWNTs.

	N@C_{60}@SWNT	N@C_{60} + SWNT	N@C_{60}	N@C_{60}
Microwave Frequency (GHz)	9.754(1)	9.7207(5)	9.72905(5)	
Modulation Amplitude (μT)	5	5	5	
Gain ($\times 10^5$)	2	2	1	
Number of Scans	695	317	4	
Power (μW)	198	198	19.8	
g-factor	2.0020(3)	2.0022(2)	2.0021(2)	2.0030(2)$^{(a)}$
Linewidth (μT)	49	41	23	$<2^{(b)}$
Hyperfine Splitting (mT)	0.567(35)	0.567(17)	0.5670(17)	0.5619$^{(a)}$

Table 8.1: Measurement parameters above parameters calculated from ESR spectra of: N@C_{60}@SWNT peapods, a N@C_{60} + SWNT mixture and N@C_{60}. All measurements were made in deoxygenated CCl_4. The g-factor, Lorentzian linewidth and hyperfine splitting were calculated from fits to the scans in Figure 8.5, using the magnetic field calibration from nitrogen defects in a diamond crystal. The errors in the peapod measurements are dominated by the frequency drift during the two-day acquisition. The total drift was 2 MHz, which corresponds to 70 μT. The fact that the measured linewidth is below 70 μT is because the frequency was almost constant for most of the scan and only drifted significantly at the end. For comparison, published values are shown for N@C_{60} in $^{(a)}$ toluene [12] and $^{(b)}$ CS_2 solution [129].

8.2.1 Modeling the Dipolar Interaction between N@C_{60} molecules in SWNTs

A computer program has been used in a previous publication to simulate the dipolar broadening inside a N@C_{60} powder [132]. Each spin is treated as a classical magnetic moment. This program was altered to simulate peapods by moving from three dimensions to one. The program is written in Python and behaves as follows:

1. Generates $2N$ sites on a 1D lattice from -N to +N. There is no site at the origin. The separation of C_{60} molecules in SWNTs is 1.0 nm [156].
2. Populates these sites randomly with a probability p.
3. Randomly assigns a dipole direction for populated sites.
4. Samples the magnetic field at the origin.
5. Bins the magnitude of this field and starts again.
6. After following this loop a chosen number of times, the output gives the frequency with which the field lay in each bin.

The program was initially run with occupation probability of 0.25%, which is the concentration of the N@C_{60} molecules (in empty C_{60}) estimated from the UV absorption spectrometer attached to the HPLC equipment. This simulation was run with 4000 lattice sites, as shown in Figure 8.7. The broadening is much smaller than that seen experimentally, showing that other broadening mechanisms dominate here. This agrees with the observation that the linewidth of the mixture (green trace in Figure 8.5) is almost as large as that of the peapod.

Even if the concentration of N@C_{60} were ten times greater, the dipolar broadening remains insignificant. Figure 8.8 shows that the dipolar width is still much less than 1 μT for $p = 2.5\%$. The line is not well fit by the Lorentzian, and a Gaussian would be worse. This is due to two satellite peaks arrising from the nearest-neighbour site that are explained further in Section 8.3.4.

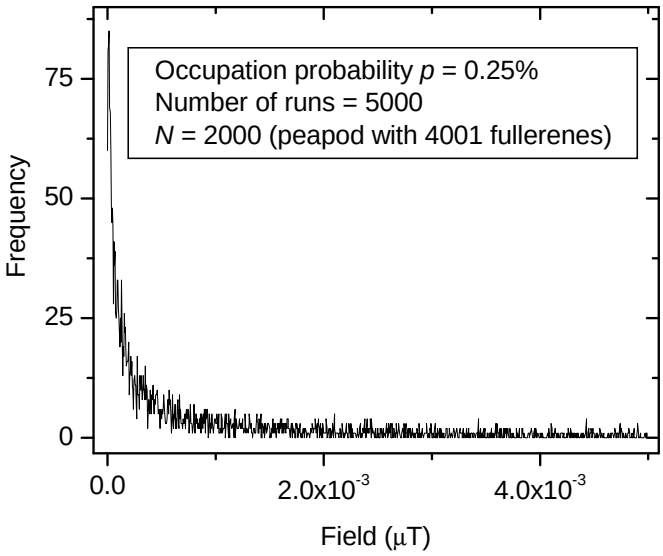


Figure 8.7: Classical simulation of dipolar broadening for SWNT peapods made with 0.25% pure N@C_{60}. The width of this peak is insignificantly small in an ESR experiment.

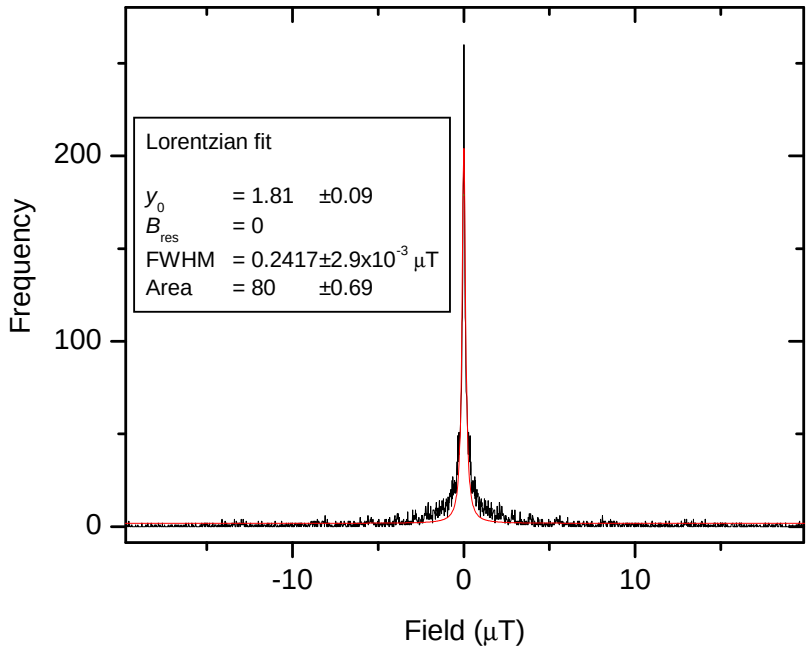


Figure 8.8: Classical simulation of dipolar broadening for SWNT peapods made with 2.5% pure N@C_{60} in C_{60}. 5000 runs were used with 4000 lattice sites. The width of this peak is still insignificantly small in an ESR experiment, so other broadening mechanisms would dominate.

8.3 Interactions between Sc@C_{82} Molecules

The strength of interactions between qubits is a crucial parameter in a quantum computer. Adjacent Sc@C_{82} molecules would be expected to have a stronger exchange interaction than adjacent N@C_{60} molecules because of their different spin density distributions. $\sim 95\%$ of the Sc@C_{82} spin is on the cage (see Section 7.3), while only $\sim 3\%$ of the N@C_{60} spin is on the cage [90].

Powder ESR measurements provide a simple way to study the exchange interaction between adjacent Sc@C_{82} molecules. A pure powder and a powder diluted with empty C_{82} were examined. The ESR spectra of pure and dilute Sc@C_{82} peapods are presented after the powder experiments. They provide further information about the inter-fullerene interactions. All dilutions were with empty C_{82} cages.

ESR spectra of Sc@C_{82} peapods were recorded for three different concentrations of Sc@C_{82} in C_{82}. The most concentrated sample was close to 100% pure and was only studied as a dry powder. These data are compared with the measurements of dry SWNT powders. Diluting the pure Sc@C_{82} with empty C_{82} produced 20% and 1% pure Sc@C_{82} samples which were also inserted into SWNTs. These were only studied in a CCl_4 suspension, so their spectra are compared with the spectra of SWNTs in CCl_4. It is expected that the suspension will reduce the tendency of the SWNTs to bundle together. Table 8.2 summarises the ESR data that were collected with Sc peapods and powders.

Sample	Concentration of Sc@C_{82} in C_{82}
Dry Sc@C_{82} Powder	$\sim 100\%$ and 21%
Dry Sc@C_{82} Peapod Powder	$\sim 100\%$
Sc@C_{82} Peapod Suspended in CCl_4 Solvent	1% and 20%

Table 8.2: Summary of the CW ESR measurements that were made with Sc@C_{82} powders and peapods. Inter-fullerene interactions are relevant for these samples.

8.3.1 ESR of Sc@C_{82} Powders

A sample of pure Sc@C_{82} powder was prepared in an ESR tube by baking at 120°C and pumping away the gases before sealing in a dynamic vacuum. The X-band ESR spectrum of this sample was recorded at room temperature over a wide range of fields, microwave powers and modulation amplitudes. No spectrum is shown here because no resonances were found. If the resonances had been severely broadened by dipolar interactions, then this would have been found as a broad line. This broadening would not be expected to be larger than that of pure N@C_{60} powder, where lines up to 6 mT have been measured [88, 93]. These broad N@C_{60} powder lines are due to the strong dipolar interaction, but are narrower than would be expected from a dipolar simulation. This narrowing may be due to exchange interactions.

The lack of ESR signal in pure Sc@C_{82} powder could be explained by antiferromagnetic ordering due to a negative exchange interaction[1]. With no unpaired spins the ESR signal disappears. This ordering occurs below the Néel temperature, which is proportional to the strength of the exchange interaction experienced by a spin [51]. This interaction would be much stronger in three dimensions than in one. Hence it is possible that pure Sc@C_{82} powder is antiferromagnetically ordered at room temperature, while the same spins in a peapod do not order in this way, even at much lower temperatures.

A less concentrated sample of Sc@C_{82} powder was prepared in the same way by diluting with C_{82} until only 21% of the fullerenes were filled. The ESR spectrum of this sample has eight distinct, broadened lines as shown in Figure 8.9. This looks similar to the solution spectum, with some extra relaxation mechanisms associated with the solid state. The anisotropy seen in Figure 7.14 is not evident, so the molecules must be tumbling. C_{60} molecules in powder form rotate freely at room temperature [90]. Relevant relaxation processes will be phonons distorting the cage and the dipolar interaction with other Sc@C_{82} molecules.

[1]Discussions with K.-P. Dinse on this topic were useful.

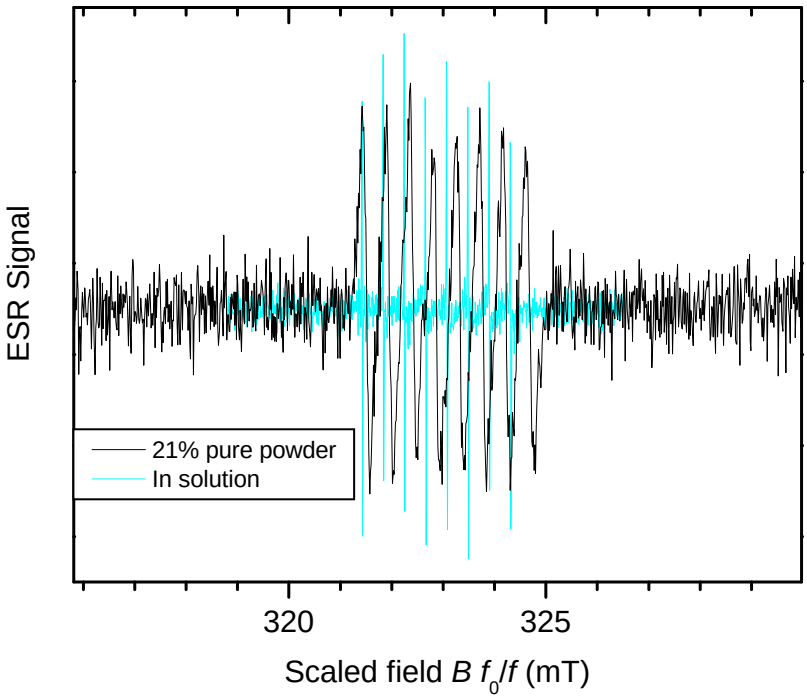


Figure 8.9: Room-temperature CW ESR spectrum of 21% Sc@C_{82} in C_{82} powder. The familiar solution spectrum is very similar with a slightly smaller hyperfine coupling. The field axis of the solution scan has been scaled upfield by 4.4% (a 40 MHz difference in the applied frequency, corresponding to 1.5 mT) for convenience because the g-factors are expected to be the same and the microwave frequencies of the two scans are only known ± 50 MHz. The microwave bridge used here only specifies the frequency as ~ 9.1 GHz.

The sample of 21% Sc@C_{82} in C_{82} powder cannot behave as an antiferromagnet because of the random spatial distribution of spins, and the ESR spectrum is certainly not spin-silent. This is consistent with the hypothesis that antiferromagnetic ordering is responsible for the spin-silence of 100% pure Sc@C_{82} powder.

8.3.2 Peapod Synthesis

Unlike N@C_{60}, Sc@C_{82} is stable up to $\sim$ 800^{o}C, so the conventional method of peapod synthesis can be used [118]. Pure Sc@C_{82} was used from the same batch as the samples in the previous chapter. A dry mixture of Sc@C_{82} and SWNT in a quartz ampule was pumped down to about 10^{-6} mbar and sealed at room temperature. The ampule was heated to 400°C for 4 days. The endohedral

fullerenes vaporize and diffuse into nanotubes, which is an exothermic process because of the extra van der Waals interactions that are possible inside the tubes. HRTEM images are shown in Figure 8.10. The number of filled and empty SWNTs were counted in fifty HRTEM images, each 100 nm square. Around 80% of the nanotubes were filled completely, and most of the others were empty.

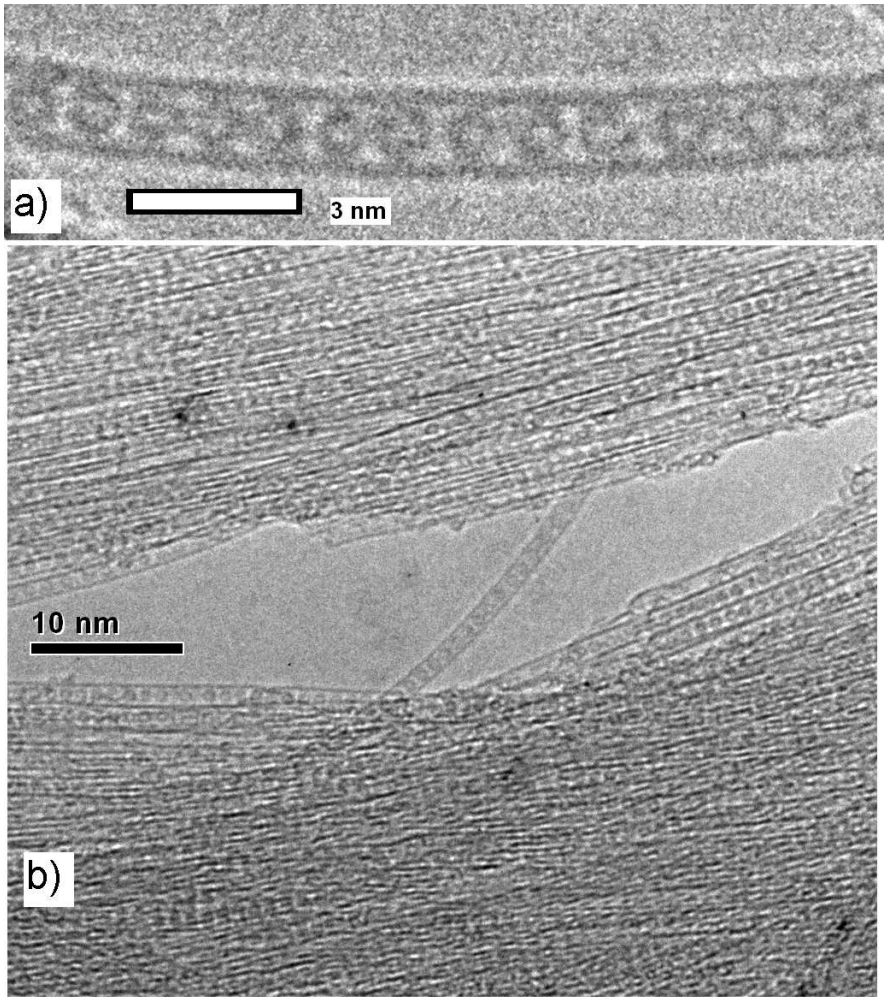


Figure 8.10: High-resolution TEM micrographs of Sc@C_{82}@SWNT. Figure a) is a close-up view in which the Sc atoms are just about visible as dark spots inside the fullerenes. b) is a zoomed out view showing the high degree of filling. Images courtesy of A. N. Khlobystov.

8.3.3 Pure Sc@C_{82} Peapod Powders

Room-Temperature ESR Measurements

These Sc@C_{82} peapods were put into an ESR tube and baked at 120°C while alternately pumping and then flushing with inert gas (argon). The tube was sealed in a dynamic vacuum. The ESR spectrum of this sample was recorded at a range of microwave powers as shown in Figure 8.11. This should be compared with the spectrum of dry SWNTs shown in the inset of Figure 8.1. Each spectrum in the power series contains two resonances; the larger one is not saturated, while the other is heavily saturated at 6.25 mW. Each spectrum was recorded with four times more power than the one below it, providing twice as much signal ($\sqrt{4} = 2$) in the absence of saturation. This doubling was compensated by halving the detector gain, so an unsaturated resonance does not change in size.

It was mentioned earlier that resistance to saturation is a signature of SWNT resonances, and the broader feature here is due to the SWNTs. The lowest power spectrum is fitted in Figure 8.12. The SWNT feature is well described (green curve) by a linear term for the very broad ($\sim$ 100 mT) resonance added to a Lorentzian, as was found in the inset of Figure 8.1. The linewidth of the $g \sim 2$ SWNT resonance in the Sc@C_{82} peapod is only 0.72 mT: Much smaller than in the empty SWNTs, where it was 1.6 mT wide.

To fit the full spectrum it is necessary to use an extra Lorentzian that was not needed for the SWNT sample. This extra feature is attributed to the Sc@C_{82} spins and is shown in Figure 8.13 by subtracting the green line in Figure 8.12 from the data. There is a 0.4 mT resonance[2]. How can this resonance be attributed to the same spins that produced the much wider spectra in Figure 7.8? That figure was used to show that Sc@C_{82} resonates over a field range (of about $7 \times 0.38 = 2.7$ mT) due to the eight hyperfine lines. Finding a narrower resonance from Sc@C_{82} can be explained if the hyperfine constant has become smaller, such as if the

[2]Other features may also be present, which could result from molecular anisotropy.

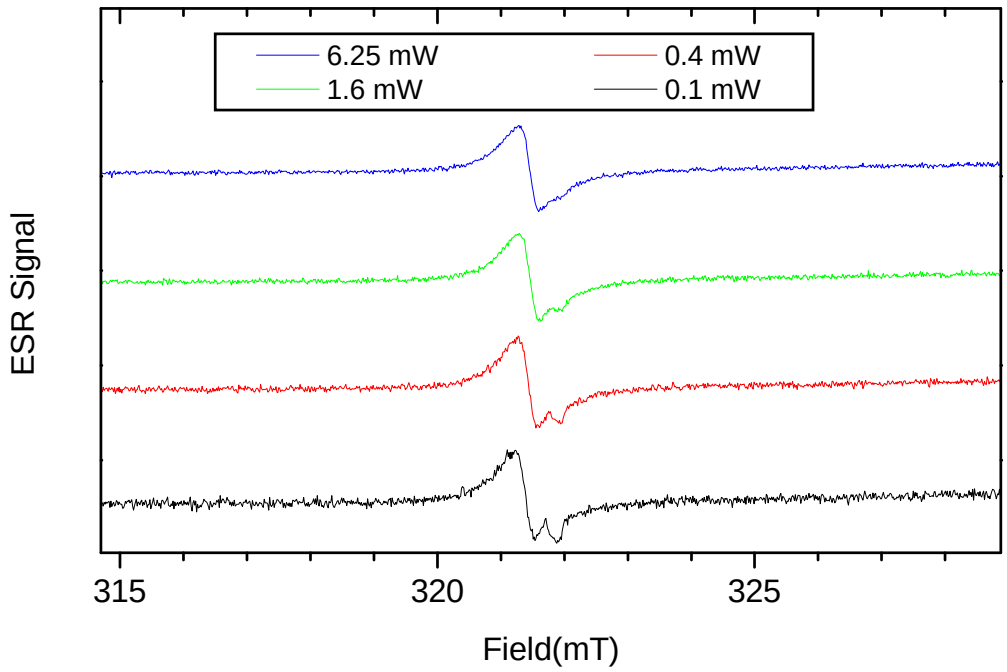


Figure 8.11: ESR spectra of degassed Sc@C_{82}@SWNT powder at room temperature in JEOL 9.1 GHz spectrometer. Moving up the figure, the power increases by a factor of four each time, and the gain is halved. The traces are offset for clarity. The fact that the larger, broader feature is the same size in each scan shows that it is not saturating, so it is attributed to conduction electrons in the SWNT. The smaller feature is reduced by saturation at 0.4 mW, suggesting that it is due to a different spin system. It is attributed to the Sc@C_{82} spins and is shown more clearly in Figure 8.13. Figure 8.12 shows a fit to the 0.1 mW scan.

unpaired electron was spending less time near the ^{45}Sc nucleus. This suggests charge transfer from the fullerene to the nanotube, which is possible because, as shown in Section 7.3, the unpaired Sc@C_{82} spin is located mainly on the carbon cage. The same effect would not be expected in N@C_{60} peapods where there is only ∼3% spin density on the C_{60} cage [90].

Dipolar Modeling of Dry Sc@C_{82} Peapod Powders

The classical dipolar Python program introduced in Section 8.2.1 was used to simulate Sc@C_{82} peapods. The magnitude of the dipoles were reduced by a factor of three to μ_B as Sc@C_{82} has electron spin $S = \frac{1}{2}$ rather than $\frac{3}{2}$. Also, the

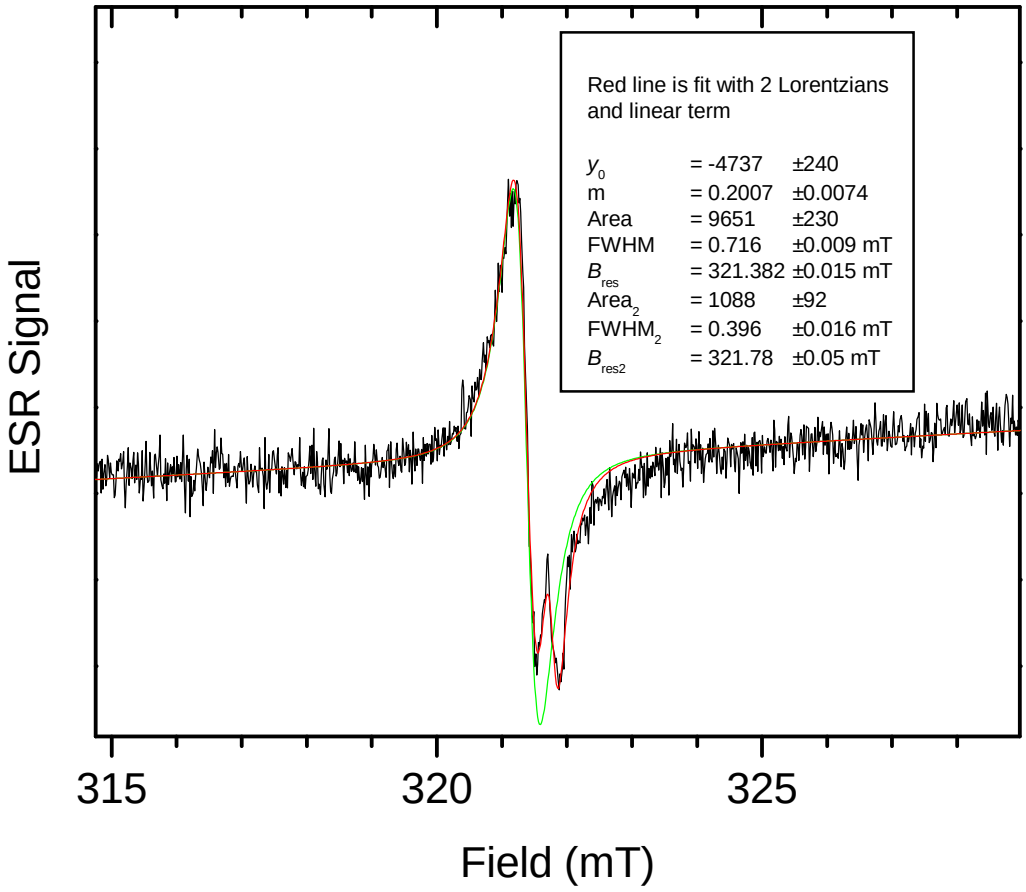


Figure 8.12: ESR spectra of degassed Sc@C_{82}@SWNT powder at room temperature. The data were fit with two Lorentzians and a linear term, as shown by the red line. The linear term accounts for the ∼100 mT resonance shown in Figure 8.1 and the broader of the Lorentzians is due to conduction electrons in the SWNT. The sharper Lorentzian is due to Sc@C_{82} spins. This is shown in Figure 8.13 by subtracting the two SWNT features (green line) from the data.

separation of the spin sites was increased to 1.1 nm, as the C_{82} cages are larger than C_{60} [156]. The program is not expected to simulate these asymmetric molecules as well as the N@C_{60} molecules for which every spin is sitting in the middle of its cage. Sc atoms are attached to the wall of the C_{82} cage, and can move about. This allows the peapod to be arranged in many ways, while the simulation assumes that each unpaired spin (and hence each Sc atom) in the chain is at the same point within the cage. This assumption may be valid in two significant regimes:

1. High temperature:

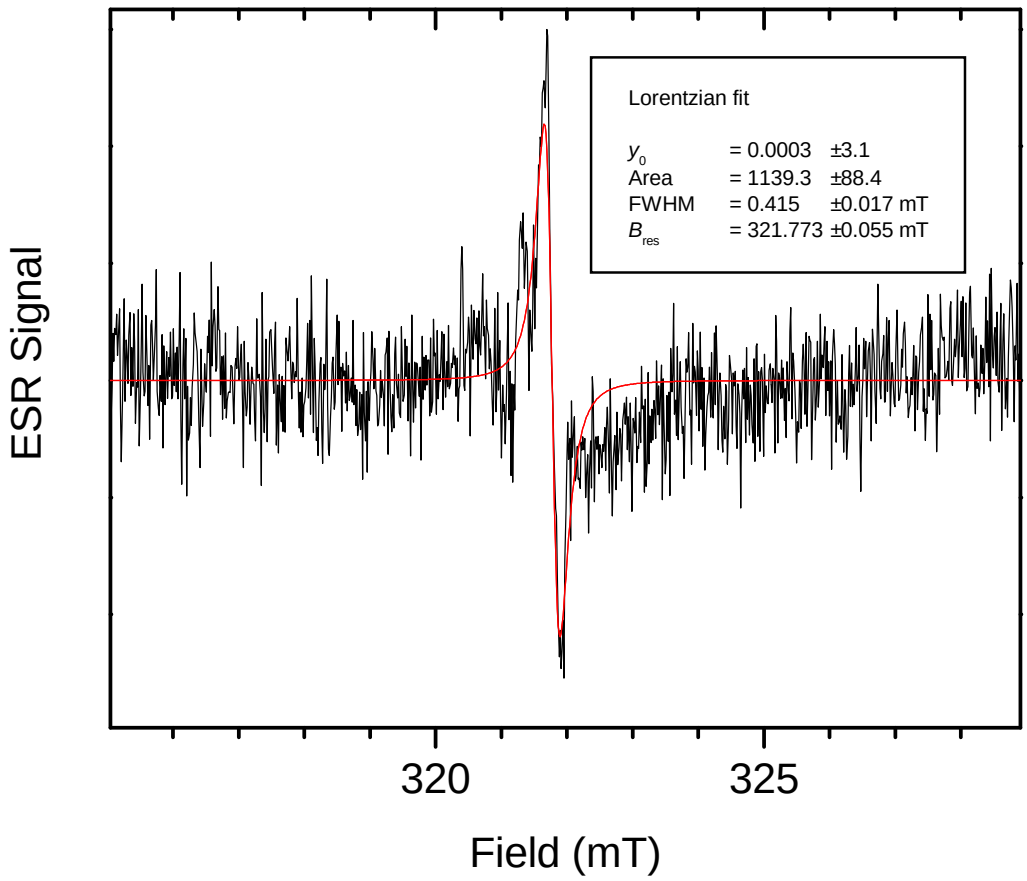


Figure 8.13: ESR spectrum of Sc@C_{82}@SWNT after subtracting fit to SWNT features. The 0.4 mT resonance is due to the Sc@C_{82} spins, with the hfs constant reduced by a factor of 6.5. This reduction could be a result of charge transfer from the C_{82} cage to the SWNT.

- When the cages are rotating faster than the characteristic time of the ESR experiment, each Sc@C_{82} molecule contributes a spherically symmetric spin distribution co-centred with the cage. C_{60} cages in an FCC lattice only cease rotating at 258 K [90], but C_{60} has a higher symmetry and the lattice is a higher symmetry environment, so Sc@C_{82} cages in SWNT would be expected to cease their rotations at a higher temperature.

- Almost the same effect would be produced by the Sc atom hopping fast within the cage. However, the previous chapter showed that at room temperature the Sc atom is stationary within the cage during the

characteristic timescale of a CW ESR experiment.

2. Low temperature: The Sc@C_{82} molecule has an electric dipole so an ordered head-to-tail pattern may result when the thermal energy is lower than the Coulomb repulsion [120].

Sequential HRTEM images were recorded, but these do not contain enough information to resolve this question. The Sc atoms can be seen to move between scans, but they are difficult to resolve in the images. Also the electron beam provides an unknown amount of energy to the molecules being imaged, so the effective temperature is not known. Molecules of Sc_2@C_{84} do not rotate freely at room temperature [157]. It is therefore unlikely that Sc@C_{82} molecules can rotate in SWNTs at room temperature.

Another approximation within the dipolar program is that it treats each spin as a point. Section 7.3 showed that the unpaired spin is actually delocalized over the Sc@C_{82} molecule. The electrons could also be further delocalized onto the nanotube, as is suggested by the reduced hyperfine coupling measured in Figure 8.13

The program was run with a $p = 100\%$ chance of spin occupation and the result is shown in Figure 8.14. Again, the line is intriguingly non-Lorentzian, and a Gaussian fit would again be worse. Two Lorentzians would provide a better fit. Studying this lineshape further may reveal that it is characteristic of 1D, but remembering the many approximations used, the important result here is simply that the linewidth is comparable to that of the experimental resonance.

The simulated linewidth is about 1 mT, more than twice as broad as the measured line in Figure 8.13. The fact that point-like spins have been assumed increases the discrepancy, as the spin separation in the model is actually the maximum possible separation, where the dipolar interaction is minimized. The delocalized spins in the experiment are closer together, which is significant for the dipolar coupling which depends on separation^{-3}.

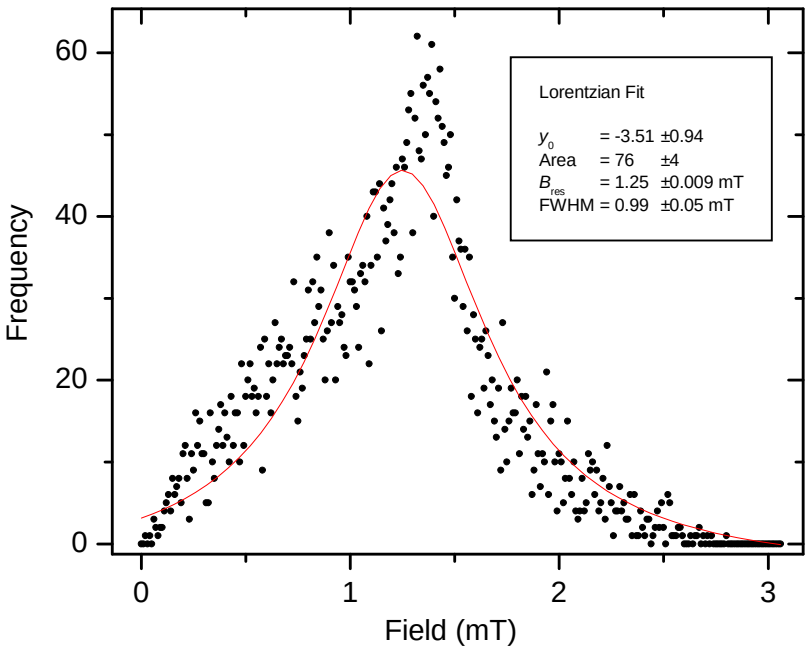


Figure 8.14: Simulation of dipolar broadening due to a 1D chain of pure Sc@C_{82}.

Exchange narrowing could provide an explanation for the discrepancy [158]. The spins in adjacent cages interact directly and indirect exchange via the conduction electrons in the nanotube could be relevant, particularly for less concentrated peapods. DFT could be used to calculate the exchange interaction between Sc@C_{82} molecules inside a SWNT. These calculations are underway but the large number of atoms that must be considered makes this more computationally demanding than for the Sc@C_{82} molecule.

Sc@C_{82} Peapod Powders at Lower temperatures

The pure Sc@C_{82} peapod powder was studied at lower temperatures. ESR spectra were recorded between 97 and 103 K, with a liquid nitrogen continuous-flow cryostat. Changing to liquid helium enabled a measurement at 4 K, and these scans are all shown in Figure 8.15. Cooling to 100 K does not significantly reduce the size of the Sc@C_{82} feature with respect to the SWNT feature. The Sc feature is still clearly visible at 4 K, but it is now significantly smaller with respect to the SWNT resonance. For this to be a fair comparison, the Sc resonance must not be

saturated. Figure 8.16 shows that this is the case: The SWNT resonances in this plot are all the same size because they are certainly not saturated. The Sc feature does not get smaller when the power is increased from 0.01 mW to 0.024 mW, so both of these powers are acceptable. For the 4 K spectrum in Figure 8.15, the data at 0.01 mW were used for extra confidence.

ESR measurements of identically prepared empty SWNT samples have suggested that the intensity of the SWNT conduction electron resonance would grow by two orders of magnitude between room temperature and 4 K, in the absence of saturation [132]. This would mean that the Sc feature is also growing significantly on cooling, even though it does not keep up with the SWNT feature. This could be explained by an increased polarization at low temperatures, implying that these spins are paramagnetic rather than antiferromagnetic.

In the traces at 4 K, 97 K and room temperature, the possibility of a smaller resonance at a slightly lower field than the main Sc feature cannot be ruled out. The signal to noise is not good enough to accurately see the lineshape of the Sc feature(s), but it is possible that this could reveal an anisotropic powder spectrum. The fullerenes are not expected to be rotating freely at room temperature, which should broaden the spectra and perhaps separate out $g_{x,y}$ from g_z.

The conclusion of these low temperature measurements is that the Sc feature is still present at 4 K, possibly even becoming stronger. This suggests that the Sc@C_{82} peapods are not behaving antiferromagnetically, even thought Sc@C_{82} powder may well be. The absence of antiferromagnetism in 1D is compatible with a significant exchange coupling, that could reduce the simulated dipolar linewidth to agree with the measured value.

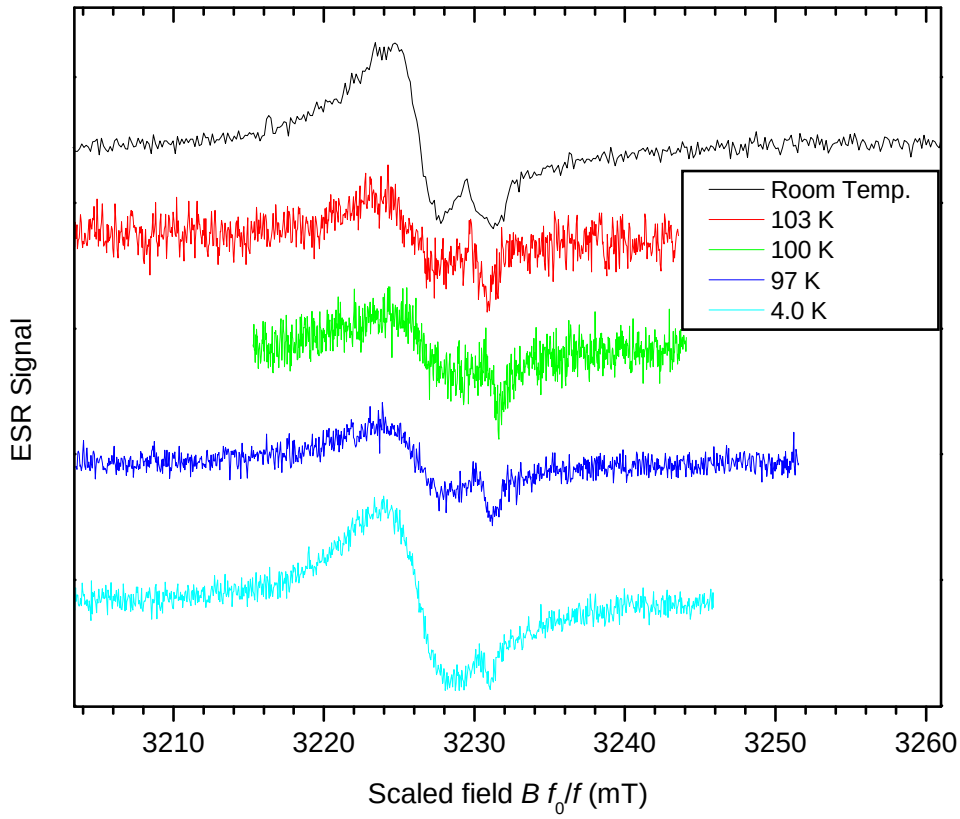


Figure 8.15: CW ESR spectra of pure Sc@C_{82}@SWNT between room temperature and 4 K. The size of the smaller Sc@C_{82} feature with respect to the broader SWNT can be compared. The Sc feature is relatively weaker at 4 K, but still present. The spectra are offset for clarity. The field axis was scaled approximately for the different frequencies used by assuming that the g-factors of the features do not change. This implies that the frequency changed by 50 MHz in cooling from room temperature to 4 K, which is reasonable.

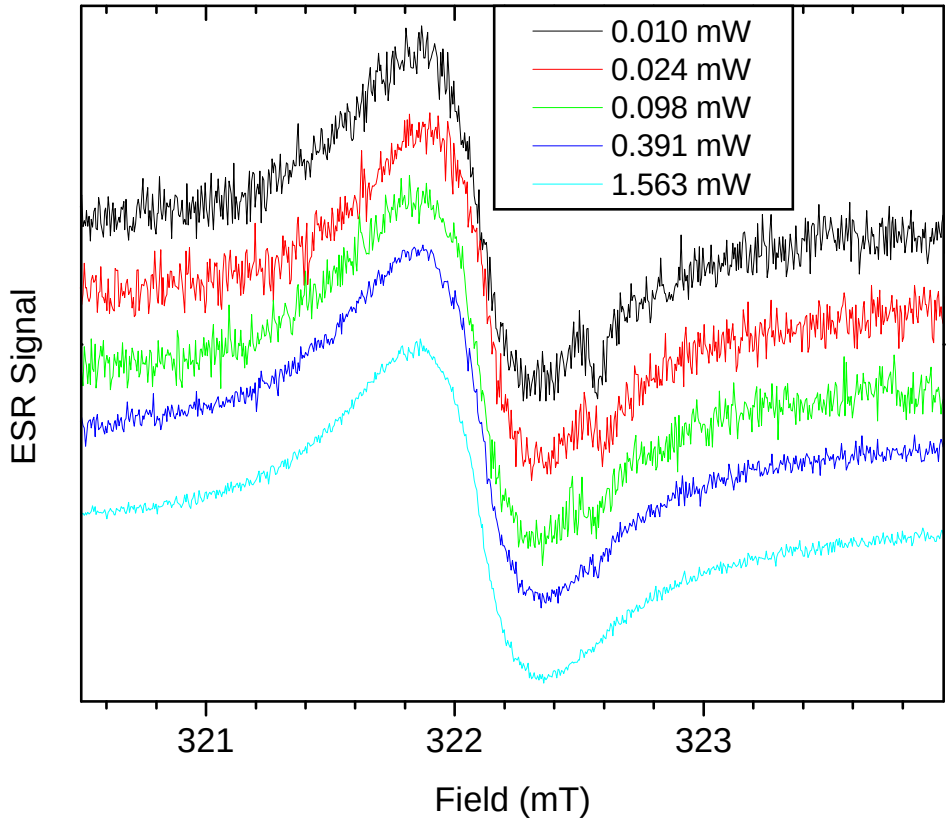


Figure 8.16: CW ESR spectra of pure Sc@C_{82}@SWNT at 4 K with a range of applied microwave powers. For powers greater than 0.024 mW, the Sc@C_{82} resonance is saturated. The spectra are offset for clarity.

8.3.4 Samples Dispersed in CCl_4

Two samples of Sc@C_{82} peapods were prepared in deoxygenated CCl_4: One sample had a concentration of 0.5-1% Sc@C_{82} in C_{82} and the other was 20% pure.

Peapods Dispersed in Solvent: 20% Pure Sc@C_{82} in C_{82}

Figure 8.17 shows the spectrum of the 20% pure peapod at room temperature, after subtraction of the background spectrum due to an empty ESR tube. Figure 8.2 shows that no sharp $g = 2$ resonance is found in SWNTs dispersed in CCl_4, so all of the signal in Figure 8.17 can be attributed to Sc@C_{82}. The lineshape is not Lorentzian (or Gaussian), and has an increased g-factor of 2.0068. A central Lorentzian and two satellites were used to get the fit shown. A broader field-sweep would be desirable to fit this line more accurately.

This sample was modeled with the classical dipolar program used in Section 8.3.3 and the results are shown in Figure 8.18. The non-Lorenzian lineshape seen experimentally is partially reproduced: Again the best fitting function consists of a central Lorentzian with a pair of Lorentzians split about the centre. The fit in Figure 8.17 was obtained by starting with the simulation value of $\Delta B_{res} =$ 0.742 mT, and this value remained after numerical optimization. The satellites correspond to arrays in which the nearest neighbour site is populated with a spin. The discreet spacing in real space produces discreet satellite peaks in the ESR spectrum. This was confirmed by calculating the maximum magnetic field due to a spin located 1.1 nm away: This is 0.70 mT, which equals the lowest field at which the satellites appear in the simulations. Increasing the lattice constant decreased the field position of the satellites as expected.

This satellite field does not depend on the concentration, as shown in Figure 8.19, but the linewidth increases with concentration. The relative size of the satellites is compared in Table 8.3. The measured sample would need to be more concentrated to be explained completely by the dipolar simulations. It is possible that Sc@C_{82} molecules enter nanotubes preferentially over empty C_{82} cages, as

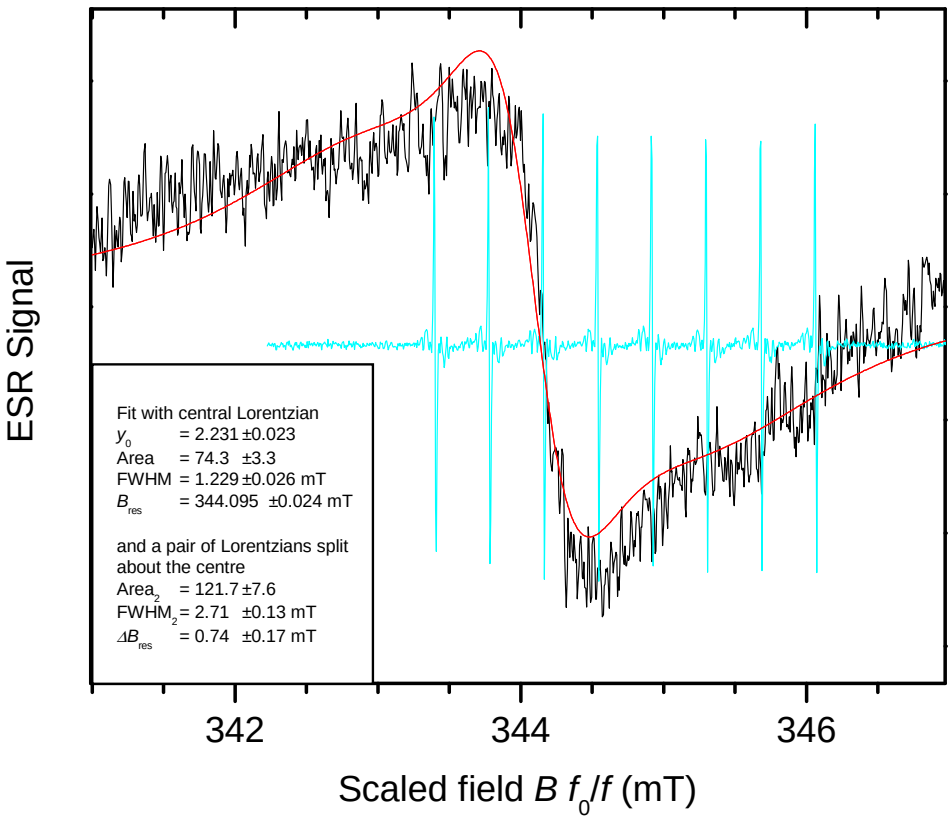


Figure 8.17: Black trace is room temperature CW ESR spectrum of Sc@C_{82}@SWNT made with 20% pure Sc@C_{82} in C_{82}. The spectrum of Sc@C_{82} in toluene is included as a light blue trace to compare the peapod g-factor and linewidth with previous measurements. The field axis of the solution spectrum was accurately scaled to allow for the different frequencies used. The reference frequency was $f_0 = 9.665001$ GHz. The red line is a fit with a central Lorentzian and a pair of Lorentzians equally spaced on either side.

the endohedral atom donates electrons to the cage. If the concentration in the measured peapod was actually $\sim 50\%$, then the relative areas may agree.

The linewidths in the experimental fit are much larger than in the simulation. This merely shows that dipolar interactions are not the dominant line-broadening mechanism. The satellites in the simulation are certainly not Lorentzian: They spread out asymmetrically to higher fields. This is a consequence of the averaging over all possible spin directions.

These satellites are not resolved in the simulations of a 1D array of pure Sc@C_{82} (broad peak in Figure 8.19) or the opposite limit of highly diluted spin

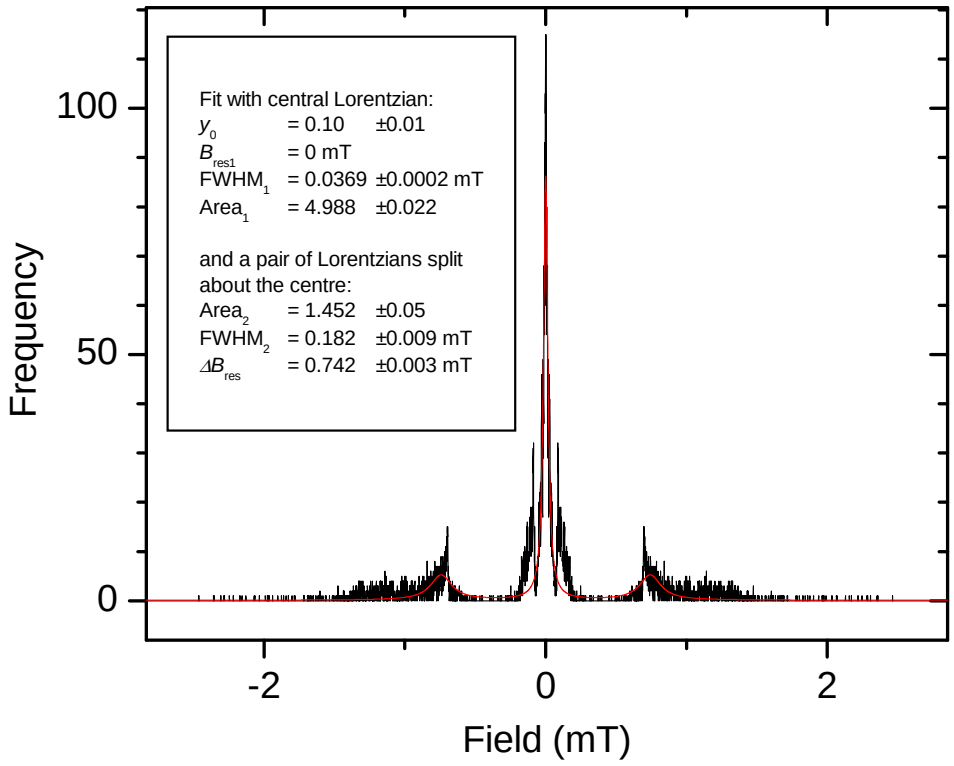


Figure 8.18: Classical dipolar simulation of the field experienced in a 1D spin-half array with 20% purity (black trace). The red curve is a fit with a central Lorentzian and a pair of Lorentzians split about the central line. There is extra structure on the central peak that is not fitted because it will be washed out by the line-broadening that is seen in the experiments. The satellites are due to arrays in which the nearest-neighbour site contains a spin.

chains (Figure 8.7 for 0.25% and Figure 8.8 for 2.5%). This lineshape may be characteristic of 1D arrays with an intermediate spin concentration.

Sc@C_{82} Peapods Dispersed in Solution: 1% Pure Sc@C_{82} in C_{82}

The most dilute Sc peapods studied were of a similar concentration to the N@C_{60} peapods. About 336 μg of these 0.5-1% Sc@C_{82} peapods were dispersed in CCl_4 and studied with CW X-band ESR. A fairly wide scan is shown in Figure 8.20, showing the trough of the very broad SWNT/impurity resonance and some of the resonances due to the SWNTs. The sharper feature at $g \sim 2$ is not present in scans of SWNTs in CCl_4, so it is attributed to the Sc@C_{82} spins.

A zoom of the sharp resonance from Figure 8.20 is shown in Figure 8.21. The

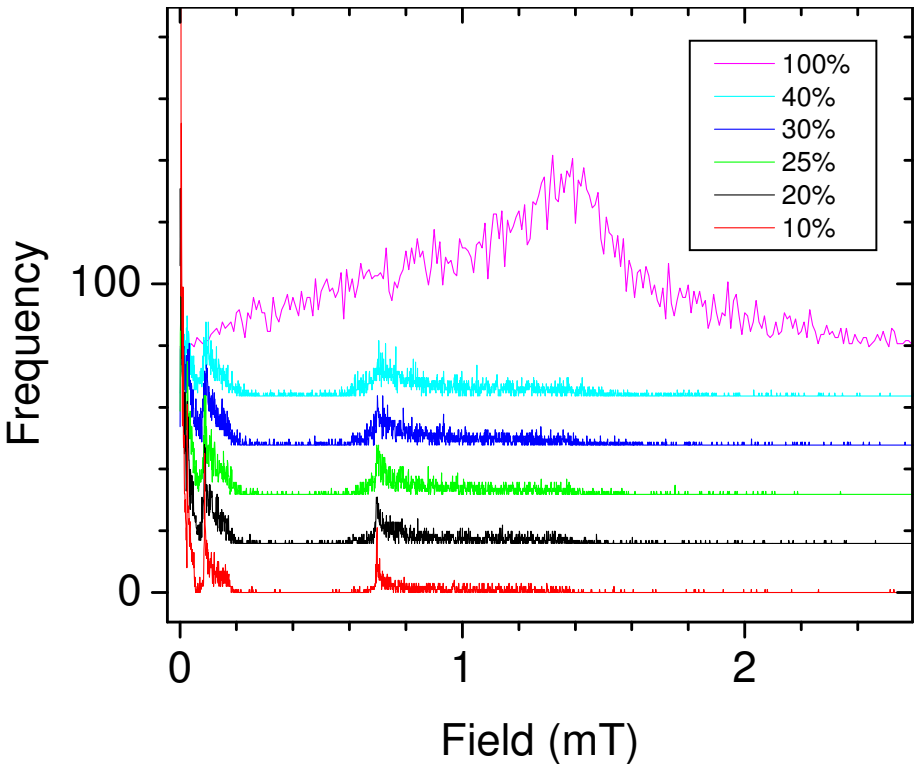


Figure 8.19: Classical dipolar simulation of the field experienced in a 1D spin-half array with the purities shown. The satellites at 0.7 mT are due to nearest-neighbour interactions.

dispersed nanotubes tumble too slowly for motional narrowing to be observed, and the fullerenes are not expected to tumble fast at room temperature [90]. In these conditions, powder anisotropy becomes relevant, and Figure 8.21 is a fairly classic powder spectrum. The effective spin Hamiltonian, Equation 7.1 can therefore be applied. The Lorentzian fit shown in red uses the following tensors:

Sample Concentration	Central Peak Area
20% (simulated)	65.2%
30% (simulated)	50.7%
40% (simulated)	37.6%
20% (measured)	23%

Table 8.3: Area of the central peak as a percentage of the total area of the central peak and the two satellites.

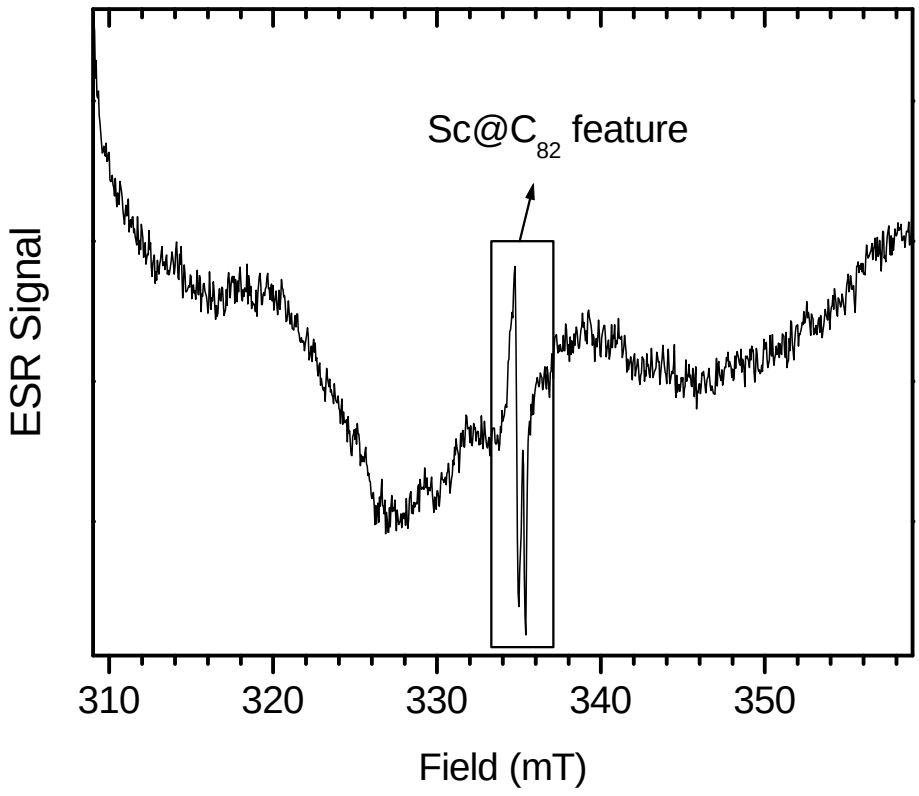


Figure 8.20: CW ESR spectrum of Sc@C_{82}@SWNT made from 1% pure Sc@C_{82} in C_{82}. The sample was dispersed in deoxygenated CCl_4. Part of the trough of the very broad SWNT/impurity resonance can be seen, with smaller resonances due to the SWNT. The sharp features in the rectangle are attributed to Sc@C_{82} and a zoom of this region is shown in Figure 8.21.

$$\mathbf{g} = \begin{pmatrix} 2.0239 & 0 & 0 \\ 0 & 2.0209 & 0 \\ 0 & 0 & 2.0178 \end{pmatrix} \tag{8.1}$$

and

$$\mathbf{A} = \begin{pmatrix} 0.0898 & 0 & 0 \\ 0 & 0.0140 & 0 \\ 0 & 0 & 1 \times 10^{-14} \end{pmatrix} \text{ mT}. \tag{8.2}$$

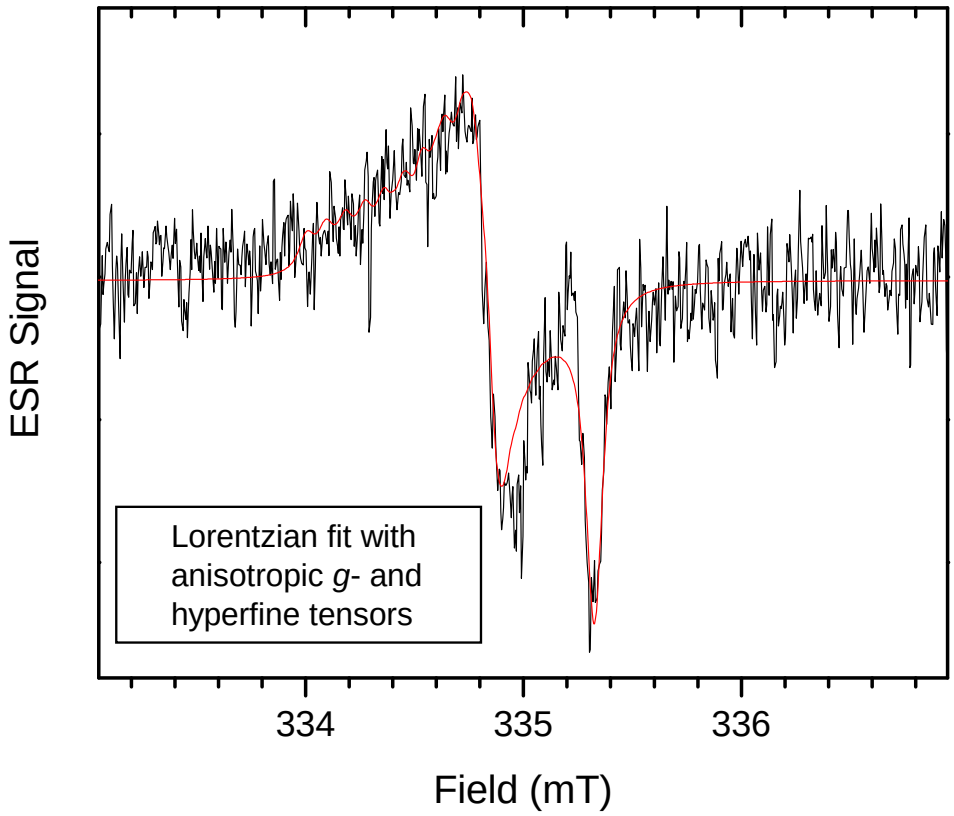


Figure 8.21: CW ESR spectrum of Sc@C_{82}@SWNT made from 1% pure Sc@C_{82} in C_{82}. The sample was dispersed in deoxygenated CCl_4. The features are attributed to Sc@C_{82} and are fit with the anisotropic g- and hyperfine tensors shown in the text. The Lorentzian lines have a homogeneous width of 0.087 mT.

This hfs tensor would correspond to an isotropic hfs constant of 0.035 mT, which is more than ten times smaller than the value for isolated Sc@C_{82} measured in the previous chapter. This reduction may be due to transfer of spin density from the C_{82} cage to the SWNTs. The same argument was used with the pure sample shown in Figure 8.13 where the effective hfs constant was $\frac{0.42}{7} = 0.06$ mT. This large reduction in the hfs constant was not seen in the sample made from 20% pure Sc@C_{82} in C_{82}.

The anisotropic model explains the data for the 1% pure sample. There are two possible sources of anisotropy:

- The C_{82} molecules are probably not free to rotate in SWNT at room temperature, in which case the anisotropic cage would provide a powder spectrum

similar to that modeled by DFT in the previous chapter.

- Even if the fullerenes are spinning in their nanotubes, the spin-environment is anisotropic due to the nanotube and the other fullerenes. Interactions between Sc spins are a part of this anisotropy that is relevent for QIP.

The Sc@C_{82} molecule is certainly anisotropic, but it is expected to rotate in powders at room temperature: This is probably required to explain the eight-line spectrum due to the 21% pure powder in Figure 8.9. Anisotropy is expected at low temperatures, and it is possible that it is also present in the Sc@C_{82} peapod spectra at room-temperature, because the signal to noise is not high enough to rule out powder spectra such as those in Figure 8.21.

The dipolar program was run for this sample and the result was qualitatively the same as for the dilute N@C_{60} peapods described above: A single line too sharp to affect an ESR spectrum.

8.4 Conclusions

SWNTs can be used to encapsulate and form one-dimensional arrays of spin-active N@C_{60} and Sc@C_{82} molecules. The characteristic ESR triplet of N@C_{60} remains after encapsulation. Since the filling process occurs at low temperatures, the concentration of N@C_{60} in the resulting structure can be made arbitrarily high, depending only on the starting concentration. This constitutes an important step in the fabrication of molecularly self-assembling functional nanomaterials. Such materials may find applications in nanoelectronics and QIP.

The ESR spectrum of peapods made from Sc@C_{82} is more complex than that of N@C_{60} peapods. Nitrogen atoms are independent of their isotropic environment at the centre of a C_{60} cage [90], while Sc atoms are strongly bound to the walls of their C_{82} cages [66, 159]. These differing environments explain why the spectrum of N@C_{60} retains its atomic characteristics inside a SWNT, while the fundamental shape of the Sc@C_{82} spectrum is radically changed by SWNT encapsulation.

These results are summarized in Table 8.4.

The isolated position of a nitrogen atom inside C_{60} gives it long relaxation times, and SWNT encapsulation does not destroy this isolation. It is likely that the T_2^e time of N@C_{60}@SWNT is still excellent for QIP. The Sc@C_{82} molecules inside SWNTs interact more strongly with their neighbours which could be very useful as long as the interaction with other qubits is stronger than that with sources of decoherence. If these interactions could be controlled, Sc@C_{82} may have a role in a future SWNT quantum information processor.

	Spin Conc.	State	Temperature	Resonance Width (mT)	Notes
SWNT		Dry Powder	Room Temp	~ 100	impurities
				1.58	conduction electrons
		Dispersed in CCl_4	Room Temp	~ 100	impurities
				various	small features around $g \sim 2$
$N@C_{60}$ @SWNT	0.25%	Dry powder	Room temp. and 4 K	none	metallic tubes destroy cavity Q
	0.25%	Dispersed in CCl_4	Room temp.	0.049	same hfs
$Sc@C_{82}$ @SWNT	100%	Dry powder	Room temp.	0.4	at $g \sim 2$
			97-103 K	~ 0.4	does not disappear
			4.0 K	~ 0.4	
	20%	Dispersed in CCl_4	Room temp.	1.6	with 2 satellites
	1%	Dispersed in CCl_4	Room temp.	0.087	anisotropic fit

Table 8.4: Summary of the ESR signals seen from N and Sc peapods.

Chapter 9

Conclusions

Contents

9.1 ^{15}**N@C$_{60}$ Two-Qubit Scheme** **165**

9.2 **Sc@C$_{82}$** **166**

9.3 **Peapods** **166**

9.4 **Future Research** **167**

9.1 ^{15}N@C$_{60}$ Two-Qubit Scheme

In Chapter 5 a new scheme was described for complete two-qubit QC with atoms having electronic and nuclear spin. Dynamic nuclear polarization (DNP) is used to initialize the spin system. The efficiency of several DNP techniques were evaluated, producing algebraic expressions for the polarization achieved as a function of the ratio of applied magnetic field to temperature. Potential routes to scaling this approach up were suggested and evaluated.

In Chapter 6 parts of the ENDOR scheme were implemented. The DNP initialization was demonstrated at helium temperatures with an 8.6 T magnet. The polarization achieved was not as high as had been predicted in the previous chapter because the RF radiation was heating the sample and not saturating the nuclear spin transitions. Nuclear spin readout suitable for the end of a QC

was demonstrated with CW and pulsed ESR. The nuclear polarization produced allowed the nuclear T_1 to be estimated as on the order of 12 hours. If the nuclear T_2 is close to this order of magnitude, the nuclear spin may be very useful as a quantum memory while operations are carried out with the electron spins.

Electronic relaxation times of N@C_{60} were measured in amorphous sulphur. The electronic T_1 time was found to be 4.5 minutes at 4 K, where previously it had only been measured as being longer than one second. The longer time increases the chance of single-spin measurement. The electronic T_2 time reached 215 μs at 4 K, which is long enough for the Deutsch-Jozsa algorithm to be performed in the ENDOR QC scheme. The increased T_2^e time was attributed to the absence of nuclear spins in the solvent, and the absence of crystallites.

9.2 Sc@C_{82}

In Chapter 7 the electronic relaxation times of Sc@C_{82} were measured. The T_1^e was on the order of a second at 4 K and the T_2^e was 13 μs at 20 K. These times are long enough to make Sc@C_{82} a promising candidate qubit. Understanding the anisotropic behaviour of the individual molecule is necessary for QC applications at low temperatures, and when ensembles are not used. The g- and A-tensors were written in the coordinate frame of the molecule by comparing ESR measurements with DFT simulations. The g-tensor is not axial, while the A-tensor is approximately axial. 95% of the spin density is located on the cage.

9.3 Peapods

ESR spectra of two spin-active endohedral peapods were presented in Chapter 8. N@C_{60} molecules in SWNTs maintain their atomic behaviour, exhibiting the characteristic three-line spectrum. Only 0.25-0.5% of the fullerenes contained spins, so the dipolar coupling was much weaker than other line-broadening interactions. Finding out the relaxation times and mechanisms for these species will be a key

test of their suitability for QIP.

$Sc@C_{82}$ peapods were also examined with CW ESR. Exchange interactions were invoked to explain the fact that the resonance in a pure $Sc@C_{82}$ peapod is sharper than would be expected from dipolar interactions. This conclusion was backed up by the spin-silence of $Sc@C_{82}$ powders. Exchange interactions could be used to entangle neighbouring qubits. Satellite lines due to 1D nearest-neighbour interactions were found in the dipolar simulations of peapods with spin concentrations between 10% and 50%. This feature was measured in a sample made from 20% pure $Sc@C_{82}$.

9.4 Future Research

High magnetic fields will continue to provide opportunities to initialize ESR quantum computers. A 330 GHz pulsed spectrometer in Tallahassee will be particularly suitable for these experiments.

New samples will continue to make new ESR QIP experiments possible. Asymmetric $N@C_{60}$ dimers and single crystals offer the chance for multi qubit systems. Fullerenes that are optically active as well as ESR-active could provide a way to readout the results of a QC. New architectures such as 2D and 3D arrays could offer rewarding challenges for ESR spectroscopists. A magnetometer that is sensitive to a single electron spin per root hertz would enable fast progress in ESR QC.

The wider field of QIP continues to attract interest in a variety of academic journals as well as the popular press and commercial long-term plans. This vibrant mix makes it a lively topic for research.

Appendix A

π Pulses in a Spin $\frac{3}{2}$ System

Contents

A.1 Pauli Matrices 168

A.1.1 Pauli Matrices for Spin $\frac{3}{2}$ 169

A.2 Time Evolution 171

Rabi oscillations in three-level systems have been treated in textbooks [160, 161], and the general case with four and five levels has been solved numerically [162, 163]. Here a simple analytic solution is presented for a four level system in which all of the levels are equally spaced. This was written as a program in Maple by A. Ardavan, in discussion with J. J. L. Morton and B. W. Lovett. The generalization to higher spin-states is straightforward.

A.1 Pauli Matrices

The two-by-two Pauli matrices

$$\sigma_0 \equiv I \equiv \begin{pmatrix} 1 & 0 \\ 0 & 1 \end{pmatrix} \tag{A.1}$$

$$\sigma_1 \equiv \sigma_x \equiv \begin{pmatrix} 0 & 1 \\ 1 & 0 \end{pmatrix} \tag{A.2}$$

$$\sigma_2 \equiv \sigma_y \equiv \begin{pmatrix} 0 & -i \\ i & 0 \end{pmatrix} \tag{A.3}$$

$$\sigma_3 \equiv \sigma_z \equiv \begin{pmatrix} 1 & 0 \\ 0 & -1 \end{pmatrix} \tag{A.4}$$

describe the dynamics of a qubit, such as a spin-half in a magnetic field. As long as there is no g-anisotropy, applying a magnetic field $\mathbf{B}$ produces the following term in the Hamiltonian:

$$H_B = g\mu_{\mathrm{B}}(B_x\sigma_x + B_y\sigma_y + B_z\sigma_z). \tag{A.5}$$

A.1.1 Pauli Matrices for Spin $\frac{3}{2}$

The behaviour of a spin $\frac{3}{2}$ in a magnetic field can be conveniently solved by using a generalization of the Pauli matrices above to their four-by-four analogues. The σ_0 and σ_z matrices can be immediately written down:

$$\sigma_0(S=\frac{3}{2}) \equiv I(S=\frac{3}{2}) \equiv \begin{pmatrix} 1 & 0 & 0 & 0 \\ 0 & 1 & 0 & 0 \\ 0 & 0 & 1 & 0 \\ 0 & 0 & 0 & 1 \end{pmatrix} \tag{A.6}$$

and

$$\sigma_3(S=\frac{3}{2}) \equiv \sigma_z(S=\frac{3}{2}) \equiv \begin{pmatrix} 3 & 0 & 0 & 0 \\ 0 & 1 & 0 & 0 \\ 0 & 0 & -1 & 0 \\ 0 & 0 & 0 & -3 \end{pmatrix}. \tag{A.7}$$

The two remaining four-by-four Pauli matrices can be found with the raising and lowering operators which are defined [51] as

$$\sigma_+ = \sigma_x + i\sigma_y \tag{A.8}$$

$$\sigma_- = \sigma_x - i\sigma_y. \tag{A.9}$$

The standard commutation relation should be transferred to the four-by-four case, so that

$$[\sigma_z, \sigma_x] = i\sigma_y. \tag{A.10}$$

Combining this relation with the definition of the raising and lowering operators produces another commutation relation

$$[\sigma_z, \sigma_+] = \sigma_+. \tag{A.11}$$

From here, σ_+ can be written down, and hence σ_-. The four-by-four σ_x and σ_y matrices follow:

$$\sigma_1(S=\frac{3}{2}) \equiv \sigma_x(S=\frac{3}{2}) \equiv \begin{pmatrix} 0 & \sqrt{3} & 0 & 0 \\ \sqrt{3} & 0 & 2 & 0 \\ 0 & 2 & 0 & \sqrt{3} \\ 0 & 0 & \sqrt{3} & 0 \end{pmatrix} \tag{A.12}$$

$$\sigma_2(S=\frac{3}{2}) \equiv \sigma_y(S=\frac{3}{2}) \equiv \begin{pmatrix} 0 & -\sqrt{3}i & 0 & 0 \\ \sqrt{3}i & 0 & -2i & 0 \\ 0 & 2i & 0 & -\sqrt{3}i \\ 0 & 0 & \sqrt{3}i & 0 \end{pmatrix} \tag{A.13}$$

Applying a microwave pulse to the $\frac{3}{2}$ system causes a rotation about the x-axis, because the pulse provides a magnetic field that is constant and in the x-direction. This simple description of the microwave pulse is valid here in the rotating frame.

A.2 Time Evolution

The next step is to consider the time evolution of the spin $\frac{3}{2}$ as a result of the Hamiltonian

$$H_{B_x} = g\mu_{\mathrm{B}} B_x \sigma_x (S=\frac{3}{2}). \tag{A.14}$$

The time-evolution operator $\mathrm{e}^{-i\frac{Ht}{\hbar}}$ can be used by applying it to a wavefunction describing the state at $T=0$. Using the initial wavefunction

$$\left|-\frac{3}{2}\right\rangle = \begin{pmatrix} 0 \\ 0 \\ 0 \\ 1 \end{pmatrix} \tag{A.15}$$

corresponds to starting with the perfectly initialized, zero-temperature state. The evolution of this state with the applied pulse is shown in Figure A.1. After a π pulse, all of the population has been transferred from the $S_z = -\frac{3}{2}$ state to the state with $S_z = \frac{3}{2}$. The populations of the other levels have increased, but then returned to zero. Performing the same calculation with the initial wavefunction

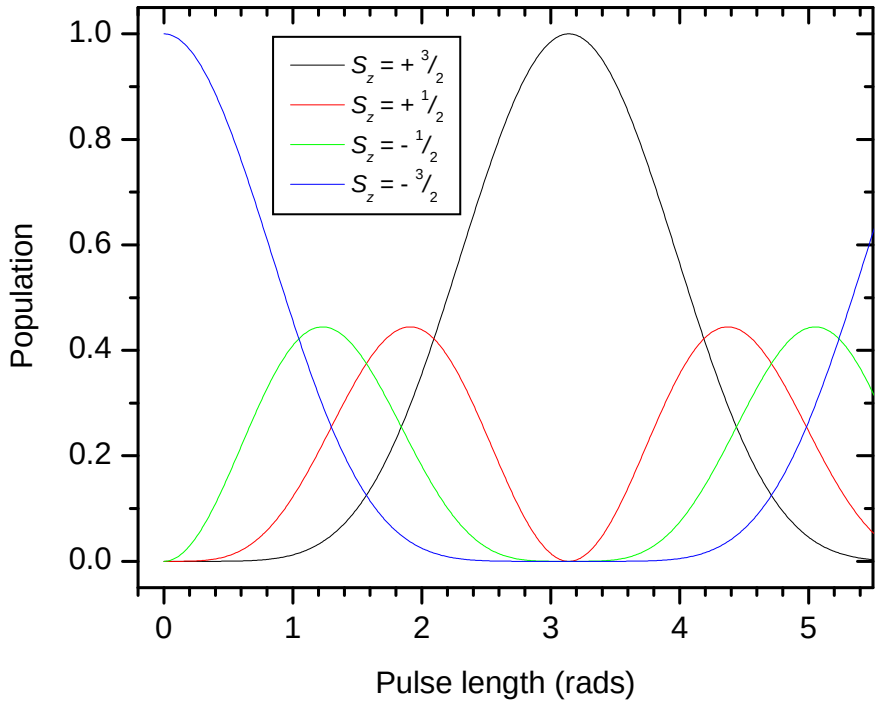


Figure A.1: Evolution of $S = \frac{3}{2}$ spin system excited by the common resonant frequency of all of the allowed transitions. The system was started off in the $S_z = -\frac{3}{2}$ state, and reached the $S_z = +\frac{3}{2}$ state after a π pulse.

$$\left|-\frac{1}{2}\right\rangle = \begin{pmatrix} 0 \\ 0 \\ 1 \\ 0 \end{pmatrix} \tag{A.16}$$

corresponds to beginning entirely in the $S_z = -\frac{1}{2}$ state. The evolution of this state is shown in Figure A.2. The perfect π pulse lasts for the same time as in the previous figure, with the population moving completely to the $S_z = +\frac{1}{2}$ state, with no net leakage to the other states.

These calculations show that a perfect π pulse exists for a spin-$\frac{3}{2}$ system, just as it does in the more standard spin-$\frac{1}{2}$ system. The Rabi oscillations have two frequency components, differing by a factor of two.

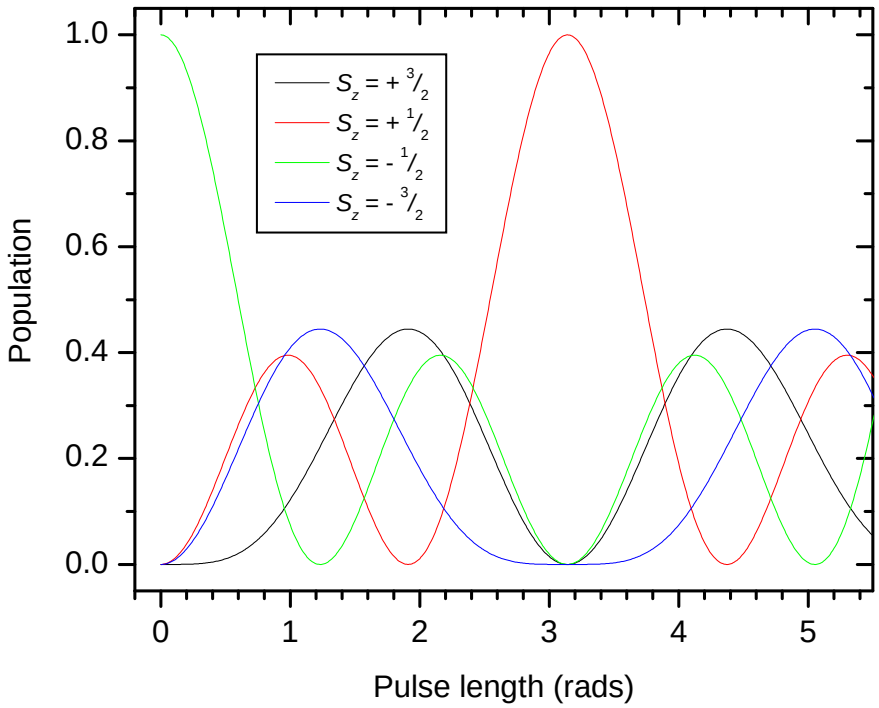


Figure A.2: Evolution of $S = \frac{3}{2}$ spin system excited by the common resonant frequency of all of the allowed transitions. The system was started off in the $S_z = -\frac{1}{2}$ state, and reached the $S_z = +\frac{1}{2}$ state after a π pulse.

Bibliography

[1] P. Benioff. *J. Stat. Phys.*, 22:563, 1980.

[2] D. Deutsch. *Proc. Roy. Soc. London A*, 400:97, 1985.

[3] P. W. Shor. *Proceedings of the 35th Annual Symposium on the Foundations of Computer Science, Santa Fe, NM, Nov 20-22nd 1994 (IEEE Computer Society Press)*, page 124, 1994.

[4] P. W. Shor. *e-Print archive*, quant-ph/9508027, 1996.

[5] L. Grover. *e-Print archive*, quant-ph/9605043, 1996.

[6] L. Grover. *Proceedings, 28th Annual ACM Symposium on the Theory of Computing*, pages 212–219, May 1996.

[7] L. M. K. Vandersypen, M. Steffen, G. Breyta, C. S. Yannoni, M. H. Sherwood, and I. L. Chuang. *Nature*, 414:883, 2001.

[8] E. K. Zavoisky. *J. Phys. USSR*, 9:211, 245, 1945.

[9] R. J. Blume. *Phys. Rev.*, 109:1867, 1958.

[10] H. W. Kroto, J. R. Heath, S. C. O'Brien, R. F. Curl, and R. E. Smalley. *Nature*, 318:162, 1985.

[11] J. R. Heath, S. C. O'Brien, Q. Zhang, Y. Liu, R. F. Curl, H. W. Kroto, F. K. Tittel, and R. E. Smalley. *J Am Chem Soc*, 107:7779, 1985.

[12] T. Almeida Murphy, Th. Pawlik, A. Weidinger, M. Höhne, R. Alcala, and J. M. Spaeth. *Phys. Rev. Lett.*, 77:1075, 1996.

[13] S. Iijima. *Nature*, 354:56, 1991.

[14] B. W. Smith, M. Monthioux, and D. E. Luzzi. *Nature*, 396:323, 1998.

[15] D. Deutsch. *The Fabric of Reality*, Allen Lane, 1997.

[16] D. S. Abrams and S. Lloyd. *Phys. Rev. Let.*, 79:2586, 1997.

[17] R. P. Feynman. *Intl. Journ. Th. Phys.*, 21:467, 1982.

[18] A. Steane. *e-Print archive*, quant-ph/0207119, 2002.

[19] D. DiVincenzo. *Fortschr. Phys.*, 48:771, 2000.

[20] R. Raussendorf and H. J. Briegel. *Phys. Rev. Lett.*, 86:5188–5191, 2001.

[21] R. Raussendorf, D. E. Browne, and H. J. Briegel. *Phys. Rev. A*, 68:022312, 2003.

[22] D. J. Wineland, C. Monroe, W. M. Itano, D. Leibfried, B. E. King, and D. M. Meekhof. *J. Res. Natl. Inst. Stand. Tech.*, 103:259, 1998.

[23] J. S. Tsai, Y. Nakamura, and Y. Pashkin. *Physica C*, 367:191, 2002.

[24] T. Yamamoto, Yu. A. Pashkin, O. A. Astafiev, Y. Nakamura, and J. S. Tsai. *Nature*, 425:941, 2003.

[25] B. E. Kane. *Fortschr. Phys.*, 48:1023, 2000.

[26] M. S. Anwar, D. Blazina, H. A. Carteret, S. B. Duckett, and J. A. Jones. *Chem. Phys. Lett.*, 400:94–97, 2004.

[27] D. G. Cory, R. Laflamme, E. Knill, L. Viola, T. F. Havnel, N. Boulant, G. Boutis, E. Fortunato, S. Lloyd, R. Martinez, C. Negrevergne, M. Pravia, Y. Sharf, G. Teklemariam, Y. S. Weinstein, and W. H. Zurek. *Fortschr. Phys.*, 48:875, 2000.

[28] T. D. Ladd, J. R. Goldman, F. Yamaguchi, and Y. Yamamoto. *Phys. Rev. Lett.*, 89:017901, 2002.

[29] J. A. Jones and M. Mosca. *J. chem. Phys*, 109:1648–1653, 1998.

[30] R. Cleve, A. Ekert, C. Macchiavello, and M. Mosca. *Proc. Roy. Soc. London A*, 454:339–354, 1998.

[31] A. Tapp. Reference [32] states that unpublished work by Tapp is the same as the ideas in Reference [30], 1998.

[32] M. A. Nielsen and I. L. Chuang. *Quantum Computation and Quantum Information*, Cambridge University Press, 2000.

[33] W. Harneit. *Phys. Rev. A*, 65:032322, 2002.

[34] D. Suter and K. Lim. *Phys. Rev. A*, 65:052309, 2002.

[35] A. Ardavan, M. Austwick, S.C. Benjamin, G. A. D. Briggs, T. J. S. Dennis, A. Ferguson, D. G. Hasko, M. Kanai, A. N. Khlobystov, B. W. Lovett, G. W. Morley, R. A. Oliver, D. G. Pettifor, K. Porfyrakis, J. H. Reina, J. H. Rice, J. D. Smith, R. A. Taylor, D. A. Williams, C. Adelmann, H. Mariette, and R. J. Hamers. *Phil. Trans. R. Soc. Lond. A*, 361:1–13, 2003.

[36] S. C. Benjamin. *Phys. Rev. A*, 61:020301, 2000.

[37] S. C. Benjamin. *Phys. Rev. A*, 64:054303, 2001.

[38] S. C. Benjamin. *Phys. Rev. Lett.*, 88:017904, 2002.

[39] J. Kohler, J. A. J. M. Disselhorst, M. C. J. M. Donckers, E. J. J. Groenen, J. Schmidt, and W. E. Moerner. *Nature*, 363:242, 1993.

[40] J. Wrachtrup, C. Vonborczyskowski, J. Bernard, M. Orrit, and R. Brown. *Nature*, 363:244, 1993.

[41] I. K. Kominis, T. W. Kornack, J. C. Allred, and M. Romalis. *Nature*, 422:596–599, 2003.

[42] M. Pannetier, C. Fermon, G. Le Goff, J. Simola, and E. Kerr. *Science*, 304:1648–1650, 2004.

[43] J. Gallop, P. W. Josephs-Franks, J. Davies, L. Hao, and J. Macfarlane. *Physica C*, 368:109–113, 2002.

[44] M. Jamet, W. Wernsdorfer, C. Thirion, D. Mailly, V. Dupuis, P. Mélinon, and A. Pérez. *Phys. Rev. Lett.*, 86:4676, 2001.

[45] K. J. Bruland, J. Krzystek, J. L. Garbini, and J. A. Sidles. *Rev. Sci. Instr.*, 66:2853, 1995.

[46] G. P. Berman, G. D. Doolan, P. C. Hammel, and V. I. Tsifrinovich. *Phys. Rev. B*, 61:14694, 2000.

[47] D. Rugar, R. Budakian, H. J. Mamin, and B. W. Chui. *Nature*, 430:329, 2004.

[48] H.-A. Engel and D. Loss. *Phys. Rev. Lett.*, 86:4648, 2001.

[49] S. L. Braunstein, C. M. Caves, R. Jozsa, N. Linden, S. Popescu, and R. Schack. *Phys. Rev. Lett.*, 83:1054, 1999.

[50] C. Poole. *Electron Spin Resonance (second edition)*, Dover, 1996.

[51] S. J. Blundell. *Magnetism in Condensed Matter*, Oxford University Press, 2001.

[52] A. Schweiger and G. Jeschke. *Principles of Pulse Electron Paramagnetic Resonance*, Oxford University Press, 2001.

[53] W. Kratschmer, K. Fostiropoulos, and D. R. Huffman. *Chem. Phys. Lett.*, 170:167, 1990.

[54] H. W. Kroto. *www.sussex.ac.uk/Users/kroto/FullereneCentre/*, Website of the Sussex Fullerene Research Centre.

[55] J. Stankowski and J. Martinek. *Solid State Comm.*, 100:717, 1996.

[56] R. Konenkamp, G. Priebe, and B. Pietzak. *Phys. Rev. B*, 60:11804, 1999.

[57] A. Hamed, Y. Y. Sun, Y. K. Tao, R. L. Meng, and P. H. Hor. *Phys. Rev. B*, 47:10873, 1993.

[58] S. G. Kukolich and D. R. Huffman. *Chem. Phys. Lett.*, 182:263, 1991.

[59] T. Kato, T. Kodama, M. Oyama, S. Okazaki, T. Shida, T. Nakagawa, Y. Matsui, S. Suzuki, H. Shiromaru, K. Yamauchi, and Y. Achiba. *Chem. Phys. Lett.*, 186:35, 1991.

[60] M. Baumgarten, A. Gugel, and L. Gherghel. *Advanced Materials*, 5:458, 1993.

[61] A. Stasko, V. Brezova, S. Biskupic, K.-P. Dinse, R. Gross, M. Baumgarten, A. Gugel, and P. Belik. *Journal of Electroanalytic Chemistry*, 423:131, 1997.

[62] S. Kawata, K. Yamauchi, S. Suzuki, K. Kikuchi, H. Shiromaru, M. Katada, K. Saito, I. Ikemoto, and Y. Achiba. *Chem. Lett.*, 9:1659, 1992.

[63] H. Shinohara. *Rep. Prog. Phys.*, 63:843–892, 2000.

[64] Y. Chai, T. Guo, C. Jin, R. E. Hauffler, L. P. F. Chibante, J. Fure, L. Wang, J. M. Alford, and R. E. Smalley. *J. Phys. Chem.*, 95:7564, 1991.

[65] R. D. Johnson, M. S. Devries, J. Salem, D. S. Bethune, and C. S. Yannoni. *Nature*, 355:239–240, 1992.

[66] J. Lu, X. Zhang, X. Zhao, S. Nagase, and K. Kobayashi. *Chem. Phys. Lett.*, 332:219–224, 2000.

[67] H. Shinohara, H. Sato, M. Ohkohchi, Y. Ando, T. Kodama, T. Shida, T. Kato, and Y. Saito. *Nature*, 357:52–54, 1992.

[68] C. S. Yannoni, M. Hoinkis, M. S. Devries, D. S. Bethune, J. R. Salem, M. S. Crowder, and R. D. Johnson. *Science*, 256:1191–1192, 1992.

[69] M. Rübsam, P. Schweitzer, and K.-P. Dinse. *J. Phys. Chem.*, 100:19310, 1996.

[70] M. Inakuma and H. Shinohara. *J. Phys. Chem. B*, 104:7595, 2000.

[71] M. Rübsam, P. Schweitzer, and K.-P. Dinse. *Chem. Phys. Lett.*, 263:540, 1996.

[72] S. Nagase and K. Kobayashi. *Chem. Phys. Lett.*, 214:57, 1993.

[73] K. Kobayashi and S. Nagase. *Chem. Phys. Lett.*, 282:325, 1998.

[74] S. Hino, K. Umishita, K. Iwasaki, T. Miyamae, M. Inakuma, and H. Shinohara. *Chem. Phys. Lett.*, 300:145–151, 1999.

[75] K. Furukawa, S. Okubo, H. Kato, H. Shinohara, and T. Kato. *J. Phys. Chem. A*, 107:10933–10937, 2003.

[76] A. Bartl, L. Dunsch, and U. Kirbach. *Sol. State Comm.*, 94:827–831, 1995.

[77] C. Knapp, N. Weiden, H. Kass, K.-P. Dinse, B. Pietzak, M. Waiblinger, and A. Weidinger. *Molecular Physics*, 95:999–1004, 1998.

[78] A. Weidinger, M. Waiblinger, B. Pietzak, and T. Almeida Murphy. *App. Phys. A*, 66:287, 1998.

[79] J. Lu, X. Zhang, and X. Zhao. *Chem. Phys. Lett.*, 312:85, 1999.

[80] J. C. Greer. *Chem. Phys. Lett.*, 326:567, 2000.

[81] J. J. BelBruno. *Fullerene Nanotubes and Carbon Nanostructures*, 10:23, 2002.

[82] E. Dietel, A. Hirsch, B. Pietzak, M. Waiblinger, K. Lips, A. Weidinger, A. Gruss, and K.-P. Dinse. *J Am. Chem Soc.*, 121:2432, 1999.

[83] S. Melchor, J. A. Dobado, J. A. Larsson, and J. C. Greer. *J Am. Chem Soc.*, 125:2301–2306, 2002.

[84] This is the case in the experience of the present author.

[85] M. Waiblinger, K. Lips, W. Harneit, A. Weidinger, E. Dietel, and A. Hirsch. *Phys. Rev. Lett.*, 63:045421; reprinted with typographical corrections in 64:159901, 2001.

[86] B. Pietzak, M. Waiblinger, T. Almeida Murphy, A. Weidinger, M. Höhne, E. Dietel, and A. Hirsch. *Chem. Phys. Lett.*, 279:259–263, 1997.

[87] K. Porfyrakis and T. J. S. Dennis. *Personal communication*, 2002.

[88] P. Jakes, K.-P. Dinse, C. Meyer, W. Harneit, and A. Weidinger. *Phys. Chem. Chem. Phys.*, 5:4080–4083, 2003.

[89] C. Knapp, K.-P. Dinse, B. Pietzak, M. Waiblinger, and A. Weidinger. *Chem. Phys. Lett.*, 272:433, 1997.

[90] N. Weiden, H. Kass, and K.-P. Dinse. *J. Phys. Chem. B*, 103:9826–9830, 1999.

[91] A. L. Buchachenko. *J. Phys. Chem.*, 105:5839, 2001.

[92] J. F. Reichert and N. C. Jarosik. *Phys. Rev. B*, 27:2710, 1983.

[93] G. W. Morley, J. J. L. Morton, M. R. Austwick, A. N. Khlobystov, K. Porfyrakis, M Kanai, T. J. S. Dennis, S. M. Lee, D. A. Britz, A. Ardavan, D. G. Pettifor, and G. A. D. Briggs. *Solid State Quantum Information Processing Conference*, Amsterdam, Holland, 2003.

[94] N. Weiden, B. Goedde, H. Kass, K.-P. Dinse, and M. Rohrer. *Phys. Rev. Lett.*, 85:1544, 2000.

[95] C. Meyer, W. Harneit, K. Lips, A. Weidinger, P. Jakes, and K.-P. Dinse. *Phys. Rev. A*, 65:61201, 2002.

[96] P. C. Chow, X. Jiang, G. Reiter, P. Wochner, S. C. Moss, J. D. Axe, J. C. Hanson, R. K. McMullan, R. L. Meng, and C. W. Chu. *Phys. Rev. Lett.*, 69:2943, 1992.

[97] B. Goedde, M. Waiblinger, P. Jakes, N. Weiden, K.-P. Dinse, and A. Weidinger. *Chem. Phys. Lett.*, 334:12–17, 2001.

[98] M. Bockrath, D. H. Cobden, J. Lu, A. G. Rinzler, R. E. Smalley, L. Balents, and P. L. Mceuen. *Nature*, 397:598, 1999.

[99] L. C. Qin, X. L. Zhao, K. Hirahara, Y. Miyamoto, Y. Ando, and S. Iijima. *Nature*, 408:50, 2000.

[100] D. A. Britz, A. N. Khlobystov, J. Wang, A. S. O'Neil, M. Poliakoff, and G. A. D. Briggs. *Chem. Commun.*, 2:176–177, 2004.

[101] D. S. Bethune, C. H. Kiang, M. S. Devries, G. Gorman, R. Savoy, J. Vazquez, and R. Beyers. *Nature*, 363:605, 1993.

[102] J. W. Mintmire, B. I. Dunlap, and C. T. White. *Phys. Rev. Lett.*, 68:631, 1992.

[103] J. W. G. Wildoer, L. C. Venema, A. G. Rinzler, R. E. Smalley, and C. Dekker. *Nature*, 391:59, 1998.

[104] S. G. Lemay, J. W. Janssen, M. van den Hout, M. Mooij, M. J. Bronikowski, P. A. Willis, R. E. Smalley, L. P. Kouwenhoven, and C. Dekker. *Nature*, 412:617, 2001.

[105] R. Saito, G. Dresslhaus, and M. S. Dresselhaus. *Physical Properties of Carbon Nanotubes*, Imperial College Press (London), 1998.

[106] J. P. Lu. *Phys. Rev. Lett.*, 74:1123, 1995.

[107] P. Petit, E. Jouguelet, J. E. Fischer, A. G. Rinzler, and R. E. Smalley. *Phys. Rev. B*, 56:9275, 1997.

[108] S. Bandow, S. Asaka, X. Zhao, and Y. Ando. *App. Phys. A*, 67:23, 1998.

[109] Y. Chen, J. Chen, H. Hu, M. A. Hamon, M. E. Itkis, and R. C. Haddon. *Chem. Phys. Lett.*, 299:532, 1999.

[110] K. D. Ausman, R. Piner, O. Lourie, and R. S. Ruoff. *J. Phys. Chem. B*, 104:8911, 2000.

[111] H. Zhang, S. Liu, A. Wei, Y. He, X. Tang, X. Xue, L. Liang, and C. Wu. *J Phys. Chem. Sol.*, 61:1123, 2000.

[112] D. J. Hornbaker, S. J. Kahng, S. Misra, B. W. Smith, A. T. Johnson, E. J. Mele, D. E. Luzzi, and A. Yazdani. *Science*, 295:828, 2002.

[113] T. Pichler, H. Kuzmany, H. Kataura, and Y. Achiba. *Phys. Rev. Lett.*, 87:267401, 2001.

[114] B. Burteaux, A. Claye, B. W. Smith, M. Monthioux, D. E. Luzzi, and J. E. Fischer. *Chem. Phys. Lett.*, 310:21, 1999.

[115] S. Berber, Y. K. Kwon, and D. Tomanek. *Phys. Rev. Lett.*, 88:185502, 2002.

[116] X. Liu, T. Pichler., M. Knupfer, M. S. Golden, J. Fink, H. Kataura, Y. Achiba, K. Hirahara, and S. Iijima. *Phys. Rev. B*, 65:45419, 2002.

[117] L. A. Girifalco, M. Hodak, and R. S. Lee. *Phys. Rev. B*, 62:13104, 2000.

[118] K. Hirahara, K. Suenaga, S. Bandow, H. Kato, T. Okazaki, H. Shinohara, and S. Iijima. *Phys. Rev. Lett.*, 85:5384, 2000.

[119] J. Lee, H. Kim, S. J. Kahng, G. Kim, Y. W. Son, J. Ihm, H. Kato, Z. W. Wang, T. Okazaki, H. Shinohara, and Y. Kuk. *Nature*, 415:1005, 2002.

[120] A. N. Khlobystov, K. Porfyrakis, M. Kanai, D. A. Britz, A. Ardavan, H. Shinohara, T. J. S. Dennis, and G. A. D. Briggs. *Angew. Chem. Int. Ed.*, 43:1386–1389, 2004.

[121] F. Simon, H. Kuzmany, H. Rauf, T. Pichler, J. Bernardi, H. Peterlik, L. Korecz, F. Fülöp, and A. Jánossy. *Chem. Phys. Lett.*, 383:362–367, 2004.

[122] A. N. Khlobystov, D. A. Britz, J. Wang, S. A. O'Neil, M. Poliakoff, and G. A. D. Briggs. *J. Mat. Chem.*, 14 (19):2852–2857, 2004.

[123] G. W. Morley, A. Ardavan, J. J. L. Morton, and A. N. Khlobystov. *UK Patent*, 0421456.5:filed on 29 September, 2004.

[124] A. M. Tyryshkin, S. A. Lyon, A. V. Astashkin, and A. M. Raitsimring. *Phys. Rev. B*, 68:193207, 2003.

[125] J. J. L. Morton, A. M. Tyryshkin, A. Ardavan, K. Porfytakis, S. A. Lyon, and G. A. D. Briggs. *http://arxiv.org*, quant-ph:0403226, 2004.

[126] S. Wimperis. *J. Mag. Res. A*, 109:221–231, 1994.

[127] H. K. Cummins and J. A. Jones. *New J. Phys.*, 2:6.1–6.12, 2000.

[128] K. Lips, M. Waiblinger, B. Pietzak, and A. Weidinger. *Phys. Stat. Sol.*, 177:81–91, 2000.

[129] J. J. L. Morton, A. M. Tyryshkin, A. Ardavan, K. Porfytakis, S. A. Lyon, and G. A. D. Briggs. *http://arxiv.org*, quant-ph:0412002, 2004.

[130] A. J. Turberfield. *Phys. World*, 16 no.3:43, 2003.

[131] W. B. Sherman and N. C. Seeman. *Nano. Lett.*, 4(7):1203–1207, 2004.

[132] M. A. Austwick. *University of Oxford Materials Department*, D.Phil Thesis, 2004.

[133] J. Twamley. *Phys. Rev. A*, 67:052318, 2003.

[134] M. Leuenberger and D. Loss. *Nature*, 410:789, 2001.

[135] F. Jelezko, T. Gaebel, I. Popa, A. Gruber, and J. Wrachtrup. *Phys. Rev. Lett.*, 92:076401, 2004.

[136] J. van Tol, L.-C. Brunel, and R. J. Wylde. *Rev. Sci. Inst.*, 2005.

[137] M. Winter. *Webelements* ™, www.webelements.com.

[138] A. F. Cotton and G. Wilkinson. *Advanced Inorganic Chemistry.*

[139] A. Schweiger and G. Jeschke. *Principles of Pulse Electron Paramagnetic Resonance*, Oxford University Press:212–214, 2001.

[140] S. Knorr, A. Grupp, M. Mehring, U. Kirbach, A. Bartle, and L. Dunsch. *Appl. Phys. A*, 66:257–264, 1998.

[141] E. Nishibori, M. Takata, M. Sakata, M. Inakuma, and H. Shinohara. *Chem. Phys. Lett.*, 298:79–84, 1998.

[142] B. Kessler, A. Bringer, S. Cramm, C. Schlebusch, W. Eberhardt, S. Suzuki, Y. Achiba, F. Esch, M. Barnaba, and D. Cocco. *Phys. Rev. Lett.*, 79:2289, 1997.

[143] A. D. Becke. *J. Chem. Phys.*, 88:2547, 1988.

[144] E.J. Baerends (ed). *Scientific Computing and Modelling*, NV Vrije Universiteit: Amsterdam, 2002.

[145] E. van Lethe, A. van der Avoird, and P. E. S. Wormer. *J. Chem. Phys.*, 108:4783, 1998.

[146] D. A. Braden and D. R. Tyler. *Organometalics*, 17:4060, 1998.

[147] P.J. Carl, S.L. Isley, and S.C. Larsen. *J. Phys. Chem. A*, 105:4563, 2001.

[148] P. Novak and F. R. Wagner. *Phys. Rev. B.*, 66:184434, 2002.

[149] T. Kato, S. Suzuki, K. Kikuchi, and Y. Achiba. *J. Phys. Chem.*, 97:13425, 1993.

[150] U. T. Höchli and T. L. Estle. *Phys. Rev. Lett.*, 18:128, 1967.

[151] S. Kenny, A. P. Horsfield, and H. Fujitani.

[152] M. Monthioux. *Carbon*, 40:1809–1823, 2002.

[153] Carbolex Inc. http://carbolex.com.

[154] M. R. Austwick, G. A. D. Briggs, and A. N. Khlobystov. *Purification of Nanotubes*, International Patent Number WO2004/052781A1:Filed 24th June, 2004.

[155] M. A. McHugh and V. J. Krukonis. *Supercritical Fluid Extraction: Principles and Practice, 2nd ed.*, Butterworth-Heinemann, Boston:176–177, 1994.

[156] K. Hirahara, S. Bandow, K. Suenaga, H. Kato, T. Okazaki, H. Shinohara, and S. Iijima. *Phys. Rev. B*, 64:115420, 2001.

[157] M. Takata, E. Nishibori, B. Umeda, M. Sakota, E. Yamamoto, and H. Shinohara. *Phys. Rev. Lett.*, 78:3330–3333, 1997.

[158] J. H. Van Vleck. *Phys. Rev.*, 74:11681183, 1948.

[159] G. W. Morley, B. J. Herbert, S. M. Lee, K. Porfyrakis, T. J. S. Dennis, D. Nguyen-Manh, R. Scipioni, J. van Tol, A. P. Horsfield, A. Ardavan, D. G. Pettifor, and G. A. D. Briggs. *submitted to Phys. Rev. Lett.*, 2005.

[160] P. Meystre and M. Sargent III. *Elements of Quantum Optics*, Springer-Verlag, 1990.

[161] S. M. Barnett and P. M. Radmore. *Methods in Theoretical Quantum Optics*, Oxford University Press, 1997.

[162] K. Fujii, K. Higashida, R. Kato, and Y. Wada. *http://arxiv.org*, quant-ph:0307066, 2003.

[163] K. Fujii, K. Higashida, R. Kato, and Y. Wada. *http://arxiv.org*, quant-ph:0312060, 2003.